Illuminating the Role of *Cul3* in Autism Spectrum Disorder Pathogenesis

by

Jasmin Morandell

October, 2020

A thesis presented to the
Graduate School of the
Institute of Science and Technology Austria, Klosterneuburg, Austria
in partial fulfillment of the requirements
for the degree of
Doctor of Philosophy

The dissertation of Jasmin Morandell, titled '*Illuminating the Role of Cul3 in Autism Spectrum Disorder Pathogenesis'*, is approved by:

Supervisor: Gaia Novarino, IST Austria, Klosterneuburg, Austria

Signature: _____

Committee Member: Simon Hippenmeyer, IST Austria, Klosterneuburg, Austria

Signature: _____

Committee Member: Harald Sitte, Institute of Pharmacology - Medical University of Vienna, Vienna, Austria

Signature: _____

Exam Chair: Michael Sixt, IST Austria, Klosterneuburg, Austria

Signature: _____

signed page is on file

IST Austria Thesis, ISSN: 2663-337X

I hereby declare that this dissertation is my own work and that it does not contain other people's work without this being so stated; this thesis does not contain my previous work without this being stated, and the bibliography contains all the literature that I used in writing the dissertation.

I declare that this is a true copy of my thesis, including any final revisions, as approved by my thesis committee, and that this thesis has not been submitted for a higher degree to any other university or institution.

I certify that any republication of materials presented in this thesis has been approved by the relevant publishers and co-authors.

Signature: _____

Jasmin Morandell

October 7, 2020

signed page is on file

Abstract

The development of the human brain occurs through a tightly regulated series of dynamic and adaptive processes during prenatal and postnatal life. A disruption of this strictly orchestrated series of events can lead to a number of neurodevelopmental conditions, including Autism Spectrum Disorders (ASDs). ASDs are a very common, etiologically and phenotypically heterogeneous group of disorders sharing the core symptoms of social interaction and communication deficits and restrictive and repetitive interests and behaviors. They are estimated to affect one in 59 individuals in the U.S. and, over the last three decades, mutations in more than a hundred genetic loci have been convincingly linked to ASD pathogenesis. Yet, for the vast majority of these ASD-risk genes their role during brain development and precise molecular function still remain elusive.

De novo loss of function mutations in the ubiquitin ligase-encoding gene *Cullin 3* (*CUL3)* lead to ASD. In the study described here, we used *Cul3* mouse models to evaluate the consequences of *Cul3* mutations *in vivo.* Our results show that *Cul3* heterozygous knockout mice exhibit deficits in motor coordination as well as ASD-relevant social and cognitive impairments. *Cul3*$^{+/-}$, *Cul3*$^{+/fl}$ *Emx1-Cre* and *Cul3*$^{fl/fl}$ *Emx1-Cre* mutant brains display cortical lamination abnormalities due to defective migration of post-mitotic excitatory neurons, as well as reduced numbers of excitatory and inhibitory neurons. In line with the observed abnormal cortical organization, *Cul3* heterozygous deletion is associated with decreased spontaneous excitatory and inhibitory activity in the cortex. At the molecular level we show that *Cul3* regulates cytoskeletal and adhesion protein abundance in the mouse embryonic cortex. Abnormal regulation of cytoskeletal proteins in *Cul3* mutant neural cells results in atypical organization of the actin mesh at the cell leading edge. Of note, heterozygous deletion of *Cul3* in adult mice does not induce the majority of the behavioral defects observed in constitutive *Cul3* haploinsufficient animals, pointing to a critical time-window for *Cul3* deficiency.

In conclusion, our data indicate that *Cul3* plays a critical role in the regulation of cytoskeletal proteins and neuronal migration. ASD-associated defects and behavioral abnormalities are primarily due to dosage sensitive *Cul3* functions at early brain developmental stages.

Acknowledgments

The work presented in this thesis was carried out at the Life Science department of the Institute of Science and Technology (IST) Austria and was financially supported by the Austrian Science Fund (FWF) to Gaia Novarino (W1232-B24 and SFB F7807-B). I am thankful to the MolTag Doctoral Program for offering me the financial support that allowed me to participate at a large number of national and international conferences and symposia.

I am very grateful to my supervisor, Gaia Novarino, for helping me to grow not only as a scientist but also as a person, for teaching me the importance of creativity, critical thinking and how to stay optimistic when times get challenging. Thank you for guiding this project with so much interest and enthusiasm.
Further, I would like to thank my external and internal thesis committee members, Harald Sitte and Simon Hippenmeyer, for taking the time to read, to evaluate and to suggest improvements for my PhD thesis, as well as for inviting me to speak at the Joint Meeting of Austrian Neuroscience Consortia in Alpbach in 2018 and the 16th Austrian Neuroscience Association Meeting in Innsbruck in 2019, respectively. In addition, I want to acknowledge my former internal committee member, Anna Kicheva, for participating in the annual progress review meetings and her feedback and interest in this project.

Many people have contributed to this work, by either active collaboration and sharing of data, or through informal brain-storming sessions, by teaching and supporting me over these last years. Specifically, I would like to express my sincere gratitude to all the collaborators on this project, to Lena Schwarz, Bernadette Basilico, Saren Tasciyan, Georgi Dimchev, Caroline Kreuzinger, Christoph Dotter, Lisa Knaus, Zoe Dobler, Emanuele Cacci, as well as Florian Schur, and Johann Danzl. In addition, I would like to especially thank Armel Nicolas from the Proteomics and Christoph Sommer from the Bioimaging Facilities for the data analysis, and to thank the team of the Preclinical Facility, especially Sabina Deixler, Angela Schlerka, Anita Lepold, Mihalea Mihai and Michael Schun for taking care of the mouse line maintenance and their great support.

I also want to thank all of the current and former Novarino group members, who helped me with their expertise on different methods and techniques, for the nice working atmosphere and collegial environment, for the collaborations, constructive criticism and suggestions. Over the years many of them became much more than simply colleagues, they became close friends. Through their support and kindness they helped me to navigate and overcome the challenges of the graduate student life. Thank you so much for your friendship Christoph, Lisa, Roberto, Eva, Elena, Barbara, Lena and Laura.

Lastly, I want to thank my family, my brother Simon, my mum Rosmarie and my partner Christian, for their unconditional love and patience. I dedicate this work to you, thank you for giving me love, recognition and courage, for always being there for me, for making me smile, for helping me to keep going and, so often, for waiting for me.

About the Author

Jasmin Morandell obtained a BSc in Biology from the Leopold-Franzens University Innsbruck in 2012, before moving to Vienna and completing the MSc in Biomedicine and Biotechnology at the University of Veterinary Medicine, Vienna in 2015. During the practical work for her Master thesis at the Institute of Molecular Pathology (IMP) in the group of David A. Keays she first studied and uncovered her passion for the developing mammalian brain. She published her Master thesis work in the Journal of Comparative Neurology in 2015 and in the same year joined the IST Austria as a graduate student. During the following five years she worked in the group of Gaia Novarino, investigating the molecular and cellular causes underlying neurodevelopmental disorders. She was involved in a study on the role of *Setd5* in Intellectual Disability, published in 2018 in Nature Neuroscience, and completed her PhD investigating the role of the E3-ubiquitin ligase Cul3 in the pathogenesis of ASD.

List of Publications

1. **Morandell J.**, Schwarz L.A., Basilico B., Tasciyan S., Nicolas A., Sommer C., Kreuzinger C., Dotter C.P., Knaus L.S., Dobler Z., Cacci E., Danzl J.G., Novarino G. (2020). **Cul3 regulates cytoskeleton protein homeostasis and cell migration during a critical window of brain development**. BioRxiv, doi:10.1101/2020.01.10.902064.

2. Basilico B., **Morandell J**., Novarino G. (2020). **Molecular mechanisms for targeted ASD treatments**. Current Opinion in Genetics & Development, 65:126-137, doi:10.1016/j.gde.2020.06.004.

Table of Contents

List of Figures

List of Supplementary Figures

List of Supplementary Tables

List of Symbols/Abbreviations

AS	Angelman Syndrom
ASD	Autism Spectrum Disorder, occasionally also ‘autism’ for brevity
BCAA	Branched Chain Amino Acids
BrdU	Bromodeoxyuridin
CDC	Center for Disease Control and Prevention
CFC	Contextual fear conditioning
CNS	Central nervous system
CNV	Copy number variants
CP	Cortical plate
CRL	Cullin-RING-ubiquitin ligases
DD	Developmental delay
DSM-5	Diagnostics and Statistics Manual 5
E	Embryonic day
ECM	Extracellular matrix
EPM	Elevated plus maze
GW	Gestational week
hESC	Human embryonic stem cells
ID	Intellectual disability
IEI	Interevent interval
INM	Interkinetic nuclear migration
iPSC	Induced pluripotent stem cells
IUE	*In utero* electroporation
IZ	Intermediate zone
loF	Loss of Function
MO	Anti-sense morpholino nucleotides
MRI	Magnetic resonance imaging
NE	Neuroepithelial (cells)
NPC	Neural progenitor cells
OHDH	Olfaction Habituation Dishabituation test
PPI	Pre-pulse inhibition
qRT-PCR	Quantitative real-time polymerase chain reaction
RG	Radial glia
sEPSC	Spontaneous excitatory postsynaptic currents
sIPSC	Spontaneous inhibitory postsynaptic currents
SNP	Single nucleotide polymorphism
sPSC	Spontaneous postsynaptic currents
STED	Stimulated emission depletion
SVZ	Subventricular zone
UPS	Ubiquitin proteasome system
VZ	Ventricular zone

1. INTRODUCTION

1.1. The Autism Spectrum Disorders

The term Autism Spectrum Disorder (ASD) describes a common, etiologically and phenotypically heterogeneous group of disorders sharing the core symptoms of social interaction and communication deficits and restrictive and repetitive interests and behaviors. The most recent study by the Center for Disease Control and Prevention (CDC) found that 16.8 per 1000 (one in 59) children, aged 8 years, was affected by an ASD in the US in 2014. Although reliable diagnosis can usually be made by the age of 18 month, the median age of the earliest ASD diagnosis in these cases was 52 month (4.3 years) and the prevalence in boys was significantly higher than in girls (prevalence ratio: 4.0, $p<0.01$) [1]. Interestingly, over the last twenty years ASD frequency has increased dramatically from 6.6 in 1000 (one in 152) children in 2000-2002 to almost triple the incidence today [2]. While this steep rise in ASD incidence is concerning, some evidence suggests that changes in diagnostic and reporting practices, the availability of services, the age of diagnosis and increased public awareness can account for a large proportion (60%) of the observed increase in ASD cases [3].

1.1.1. A historical perspective

The Austrian-American psychiatrist and physician Leo Kanner was the first to publish a systematic description of the common characteristics observed in eleven children with “autistic disturbance of affective contact” in 1943. He defined these common characteristics as “autistic aloneness” and “an obsessive insistence on persistent sameness”, additionally to difficulties in verbal and non-verbal communication as well as stereotypical and repetitive patterns of behaviors [4]. Only one year later, in 1944, he confirmed his initial observations now in twenty patients, first defining the diagnostic term “early infantile autism”. In this study he also acknowledged the large heterogeneity associated with the disorder “[…] in the manifestation of specific features, and in the step by step development in the course of time” [5]. Yet, the initially described lack of interest and engagement in social interaction and restricted and repetitive behaviors continued to remain core features of the disorder and were replicated in the scientific literature of the following years. Only in 1980 however, was the term “infantile autism” formally entered in the Diagnostics and Statistics Manual (DSM-3) of the American Psychiatric Association as a distinct disorder, separate from schizophrenia [6].

1.1.2. DSM-5

Today, ASD is most often diagnosed based on the criteria of the Diagnostics and Statistics Manual (DSM-5) of the American Psychiatric Association, released in 2013 [7]. ASDs are here defined by two core groups of behavioral abnormalities (Fig. 1a), affecting the most complex

aspects of human nature, namely social interactions, language and the capacity to adapt to unfamiliar environments:

1) Defects in social communication and interaction: these defects are characterized by abnormal social-emotional reciprocity, deficits in verbal and nonverbal communication in social interactions, as well as difficulties in building and maintaining relationships; for example, autistic individuals may find it difficult to engage in and carry on a conversation, maintain eye contact and understand social rules.

2) Restrictive and repetitive behaviors and interests: these can include abnormal motor routines, the unusual use of objects, or speech, the insistence on sameness, restricted interests and hyper-or hyporeactivity to sensory inputs; for example, patients may develop an overwhelming interest in a certain topic, they may follow inflexible routines or rituals, they may make repetitive body movements, or they may be hypersensitive to certain sounds.

A more personal perspective on autism, in the form of a small collection of real stories from individuals living with ASD can be found on the CDC homepage (https://www.cdc.gov/ncbddd/autism/stories.html accessed: 10.02.2020).

For an ASD diagnosis, the above described core symptoms have to be present already early on in development and persist throughout life, although they might only fully manifest when social demands exceed the limited capabilities, and they may be masked by learned strategies later in life. With respect to symptom severity, three different ASD severity scores can be assigned when a patient is diagnosed [7]. Furthermore, in addition to the above described ASD core features, a number of frequently occurring comorbidities can be observed in affected individuals.

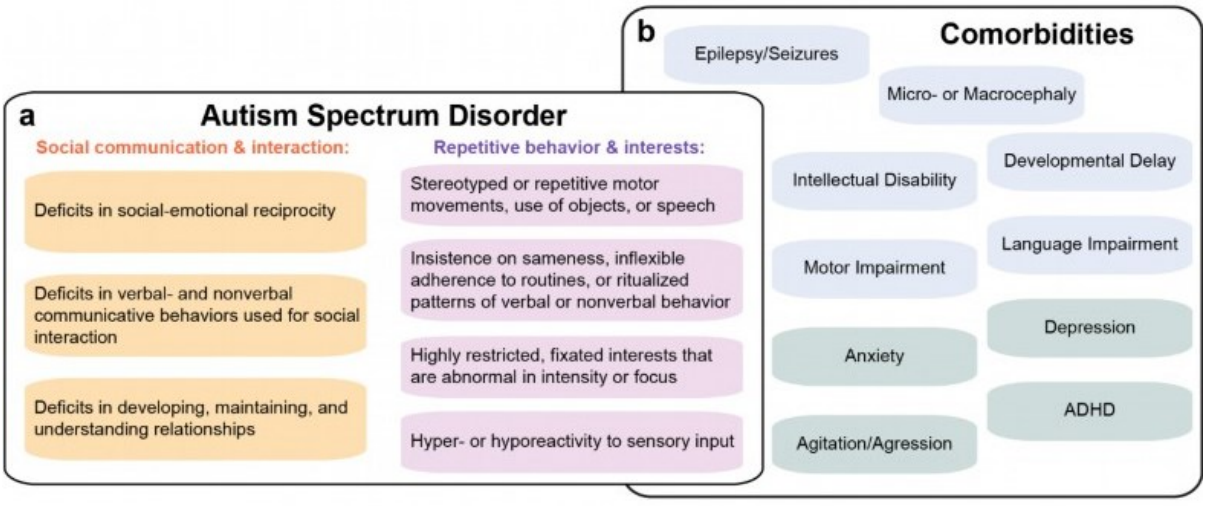

Figure 1: Autism Spectrum Disorder core symptoms and comorbidities. a, According to the DSM-5, autism spectrum disorders are defined by the core features of impaired social interactions and communication (orange) and repetitive and stereotyped behaviors (purple). **b**, In addition, autistic patients often suffer from a large variety of psychiatric (green) or neurological comorbidities (blue).

1.1.3. ASD comorbidities

Patients with ASD often present with co-occurring physical and mental health conditions that can significantly complicate ASD diagnosis and, more importantly, strongly impact their quality of life (Fig. 1b). These comorbidities can persist throughout life but may also appear or diminish at different developmental stages. ASD patients can have one or several of the listed comorbidities simultaneously or consecutively, and they can both mask or amplify the severity of the patient's symptoms. Below, some of the most frequent co-morbidities will be described more in detail.

Epilepsy and seizure disorders: Autism very frequently co-occurs with epilepsy. One study suggests that half of all autistic patients might have epileptic seizures, whereas in large study cohorts the prevalence lies at around 10% [8-10]. That close link between the disorders also points to a shared underlying pathophysiology. Indeed, certain genetic conditions associated with autism, such as tuberous sclerosis or Phelan-McDermid syndrome, also present with epilepsy. Furthermore, certain gene mutations, exemplified by the sodium channel family (*SCN1A*, *SCN2A* and *SCN3A),* confer risk to autism, epilepsy or both [11, 12]. Biologically, an abnormal interplay of excitation-inhibition (E:I) in the brain has been proposed as an underlying mechanism for both, potentially explaining the overlap. While there is plenty of evidence from mouse models and human patients supporting the idea of neuronal hyper-excitability caused by decreased inhibition in epilepsy [13], investigations in the ASD context yielded relatively heterogeneous results [14]. Today, the concept of 'E:I balance' is seen as a useful framework to investigate circuit derangements in autism, in which the many possible E-I imbalances should be classified into some tractable categories, biomarkers for E-I imbalances should be identified and the link between these forms of circuit derangement and behavior should be further investigated [15]. These points will be imperative when considering potential drug therapies for ASDs.

Micro- or Macrocephaly and structural brain malformations: Abnormal head-size is often observed in ASD patients, with about 20% of patients having increased head size, macrocephaly, and approximately 15% of patients showing microcephaly [16]. While in most cases the underlying pathophysiology is unknown, in some of these patients a phenotype-genotype connection could be established [17]. For instance, mutations in the genes *PTEN* [17, 18], *CHD8* [17, 19] and *NSD1* [20] have been associated with macrocephaly. Whereas microcephaly in ASD patients was linked to *DYRK1A5* [21], *CDKL510* [22] and *ASX1L* [17] truncating mutations. In addition, patients with 16p11.2 microdeletion- and duplication-syndrome and autistic features have opposing head sizes, a deletion is associated with increased head size, whereas the duplication is associated with decreased head size [23].

In addition to brain over- or undergrowth, other brain structure abnormalities and malformations identified by MRI studies have also been associated with ASD. For example, some autistic patients have been described with increased volumes of the prefrontal cortex and basal ganglia (e.g. the caudate), while in others the volumes of cerebellum and corpus callosum appear reduced [24]. Furthermore, various types of heterotopias (nodules of

neurons abnormally located in the brain), focal cortical dysplasia as well as abnormal cortical gyrification have been frequently reported in ASD patients (reviewed here [25]).

Intellectual Disability (ID) and/or Developmental Delay (DD): The distinction between autism, ID and DD can be especially difficult, as there is a strong overlap between the three neurodevelopmental disorders. This differentiation is important, as the DSM-5 mandates that ASD should *not* be diagnosed if symptoms can be explained by ID or general DD [26]. However, as many of the social communication deficits that define ASD represent a failure to acquire developmentally expected skills, these same deficits can occur to some extent in all individuals with intellectual disability and developmental delay, significantly complicating clinical diagnosis. ID severity as well as the patients age, when first assessed by a clinician, can thereby strongly impact the diagnostic outcome and subsequent access to health care services. For instance, children with extremely low IQ scores could be non-verbal, independently of ASD, while young children with ASD might score low in IQ-assessment as a consequence of their autism symptoms [26].

Motor impairment: Autistic patients can have a wide variety of motor abnormalities, from poor coordination or clumsy walking to fine-motor difficulties. These motor defects can be present already very early on in life and, to some degree, even predict ASD diagnosis [27, 28]. While it is clear that motor deficits are very prevalent in individuals with ASD [29], standardized testing, also taking individual cognitive abilities into account, is not yet established [30]. Having such assessments would help understand why motor difficulties occur in autism and how they affect core autism traits. Improving motor skills in autistic individuals is likely to also improve their psychosocial interactions and could target multiple areas of development [31].

Language impairment: The relationship between language and autism is somewhat complicated as the language abilities from autistic patients can vary over a large severity range: from minimally-verbal individuals [32] to normal or even excellent verbal competences [33]. Yet, also patients with fluent language can have abnormal language patterns; they can struggle to set a context for the subject matter of a conversation; they can overuse figures of speech; they can lack the ability to discuss subjects with coherence, so their conversations tend to run off in unexpected directions; they can make overly literal interpretations of idioms and they can struggle to initiate or sustain conversations. These aspects of language and speech typically associated with autism have so far centered around three phenomena, namely “pronoun reversal”, “echolalia”, and a “production-comprehension lag”. Yet, none of these aspects is unique to autism and cannot serve as sole basis for autism diagnostics, as also clarified in the DSM-5 [7, 34].

Psychiatric comorbidities (Fig. 1b green)*:* The most frequent psychiatric comorbidities of individuals with an ASD diagnosis are anxiety (39.6% [35]), attention deficit and hyperactivity disorder (ADHD, 40-70% [36]), agitation and aggression (20-70% [37]), as well as depression (22-72% [38]). Diagnosis of psychiatric comorbidities can be especially challenging in ASD patients, due to cognitive and language impairments, compromised reporting of emotions,

overlapping symptoms, and unique behavioral expressions of emotional states [39]. These increased mental health issues in individuals with autism may underlie their greater risk for suicide. Recent studies show higher than average rates of suicidal thoughts and behaviors, highlighting the need of improved psychiatric diagnostics and interventions for people with ASD [40].

1.2. ASD etiology

Already Leo Kanner observed a tendency towards autistic behaviors manifesting predominantly in certain families and described “infantile autism” as an “innate disorder”. This was, to some degree, a revolutionizing idea in a time during which Freudian Psychology mostly considered psychiatric disorders as consequence of unresolved emotional conflicts in the individual’s environment. With respect to autism, this is best exemplified by the “refrigerator mother” hypothesis of Bruno Bettelheim during the 1950s. He suggested that infantile autism was rooted in cold and unemotional parenting of mothers, leading to abnormal social bonding in children [41]. In the following decades, based on the assessment of brain function and cognition as well as the first twin studies, this notion was continuously challenged and eventually autism was conceptualized as a highly heritable neurodevelopmental disorder with underlying abnormal cognitive features [42-44]. Yet, it is important to highlight that environmental risk factors have also been shown to significantly contribute to ASD risk [45].

1.2.1. Environmental risk factors

Considering the vulnerability of the developing brain to external factors, such as alcohol or lead exposure, a causative link between environment and autism is biologically plausible [46]. Accordingly, current evidence suggests that environmental risk factors make up 40-50% of ASD liability [45] (Fig. 2a). These factors include advanced maternal (>40 years) and paternal (>50 years) age [47], birth trauma and especially hypoxia, in addition to maternal obesity, gestational diabetes, immune activation [48], as well as short intervals between pregnancies [45, 49]. However, it is necessary to consider that none of these factors can be considered causative alone, they could be reactive, independent or contributory to ASD risk. In addition, studies that did not find any connection between a specific environmental factor and autism risk are equally, if sometimes not even more, important to be considered for environmental health and safety guidelines. There is no better example for that than the clear evidence that autism is not associated with childhood vaccinations [50].

1.2.2. Genetic Architecture of the Autism Spectrum Disorders

The ASD phenotypic heterogeneity is mirrored by its large complexity in genetic architecture. Advances in genomic technologies over the last three decades together with the availability of large study cohorts, have led to the identification of an extensive number of different types

of genetic changes associated with autism. They include chromosomal abnormalities, copy number variants (CNV), rare inherited and *de novo* mutations, as well as rare combinations of common variants (as measured from single nucleotide polymorphisms, SNP) [51-59]. Taken together, this large amount of data best fits a model in which additive effects of common genetic variants make up the largest genetic contribution to ASD risk (around 49%), whereas contributions from *de novo* mutations and rare inherited variations are smaller (3%, respectively, Fig. 2a) [55, 57]. Furthermore, the observation that parental carriers of deleterious mutations usually show milder phenotypes, and patients with multiple hits are more severely affected supports a multifactorial model of risk [58]. The large number and diversity of genes affected by ASD *de novo* mutations predict a large variety of biologic functions involved in ASD pathology. In fact, based on the SFARI human gene database, more than 400 different genes (with SFARI scores < 3) have now been convincingly linked to ASD and its comorbidities (Fig. 2b).

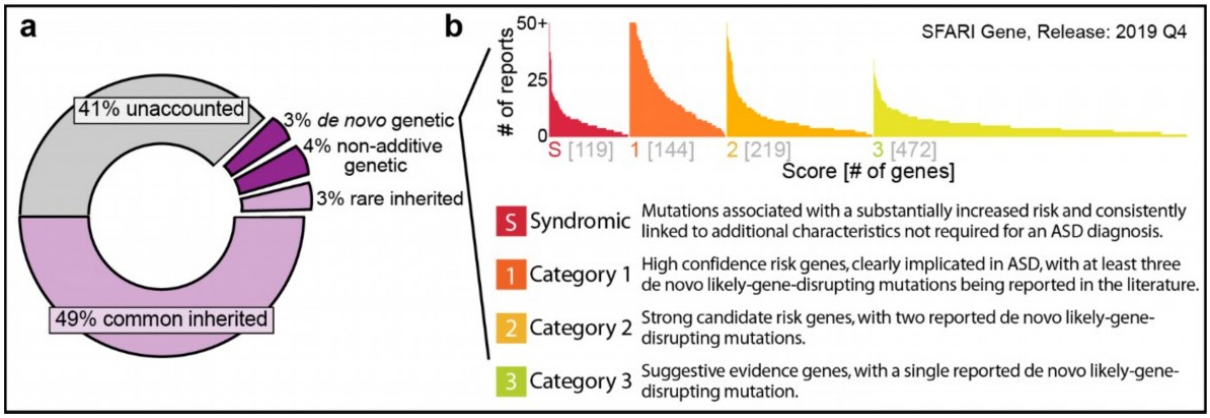

Figure 2: Etiology and genetic architecture of ASD. a, Contributions of environmental factors (in grey) and genetic variants (in purple) to ASD risk (adapted from [56]). **b**, To date rare *de novo* mutations in almost 1000 genes have been linked to ASD. They can be categorized according to the number of described gene-disrupting mutations and the number of reports in the literature into "Syndromic" genes, "Category 1" High confidence risk genes, "Category 2" Strong candidate risk genes, and "Category 3" Suggestive evidence genes; the SFARI Gene database is a thoroughly curated list of genes that have been described in the context of autism (adapted from the SFARI website https://gene.sfari.org/; access: 20.03.2020).

2. AUTISM AS NEURODEVELOPMENTAL DISORDER

2.1. Introduction

ASDs are paradigmatic neurodevelopmental conditions. Neurodevelopmental disorders typically manifest early in development, often before a child enters school, and are characterized by deficits and delays in achieving expected developmental milestones of personal, social, academic, or occupational functioning [7]. With that in mind, it is worth to first discuss normal brain development to understand when, where and how problems during this complex series of dynamic and adaptive processes can drive the pathophysiological changes underlying the manifestation of the core symptoms of ASDs in early childhood. The human central nervous system (CNS) follows the overall principles and developmental processes characteristic of all mammals [60]. It starts as a simple neural tube separating from the embryonic ectoderm in the first gestational weeks (GW), GW 3-4, and gradually acquires mature organizational features through immensely complex and strictly regulated molecular and cellular processes. The development of the CNS extends through childhood, adolescence and into young adulthood, and arguably, it even continues throughout the entire life [60, 61].

2.2. Brain developmental milestones relevant for ASD

Most patients receive a reliable ASD diagnosis usually in early or late childhood, when a number of crucial developmental processes are occurring or were already completed during embryonic and fetal development (Fig. 3). For example, this is true of the generation of the vast majority of neurons in the human telencephalon [62], since neocortical excitatory neuron production begins around GW 7 and ends around GW 27 [63] (Fig. 3). However, on the contrary some neocortical and striatal interneurons as well as neurons of the hippocampal dentate gyrus are generated after this time period, with their neurogenesis extending in part even postnatally [64-66].

Upon neuronal migration, post-mitotic neurons start forming the cortical plate (CP) in the rostral telencephalon at around GW 8-9 [67]. Following the neurogenic period, the production of cells of the macro-glial linage begins (Fig. 3). At first, during late fetal development and peaking around birth, astrocytes differentiate from radial glial (RG) cells, and only later during childhood, oligodendrocytes are formed after differentiating from oligodendrocyte precursor cells [68-70]. Although a few immature synapses can already be detected upon cortical plate formation [71], the majority of synapses are formed during the late fetal period with synaptic density peaking during early infancy, at one to two years of age [72] (Fig. 3). Three years after birth, the growth of the brain slows and processes such as myelination [73] and synaptic maturation and/or pruning predominate. These specifications and refinements of brain circuits occur throughout adolescence and can persist even into early adulthood [60, 72] (Fig. 3).

In the light of ASD, a recent focus has been put on the identification of the most relevant spatiotemporal convergence points of developmental processes. These efforts have

highlighted the importance of the mid-fetal developmental period for autism, when glutamatergic neurons are born and populate, initially, deep [74] and later, superficial [75] cortical layers. Spatially, in addition to abnormalities in prefrontal, visual and somatosensory circuits [76], also striatal [77] and cerebro-cerebellar circuits [78] have been linked to ASD pathophysiology.

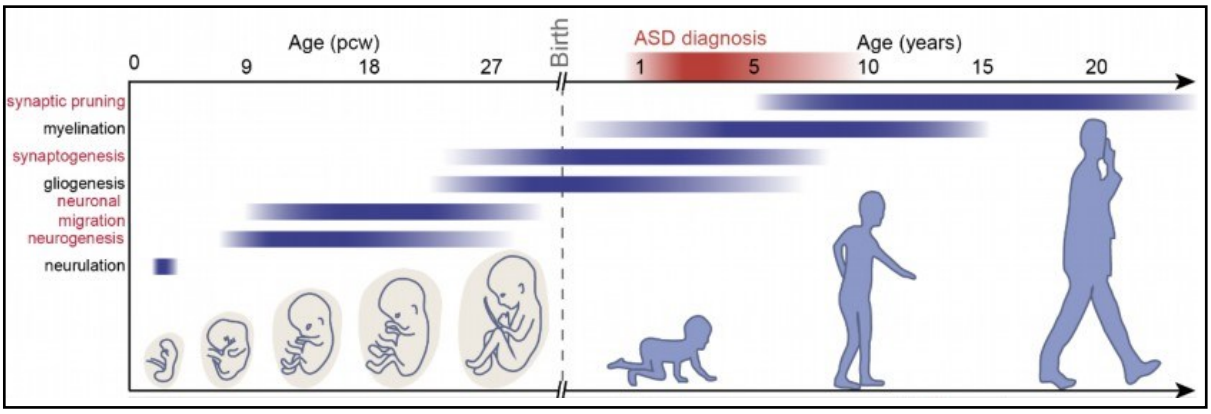

Figure 3: Timing of human brain developmental milestones relevant for ASDs. Human brain development starts around GW 3-4 with the closure of the neural tube. At neurulation the rudimental structures of the CNS, the brain (rostral structures) and the spinal cord (caudal structures), but also of the peripheral nervous system, the neural crest cells, are defined. Subsequent to neural tube closure, neurogenesis and neuronal migration start, peaking around the mid-fetal stage. The neurogenic period is followed by gliogenesis, first astocytes and then oligodendrocytes are produced, which then start to myelinate neural axons soon after birth. Synapses form and begin to mature, with a peak in synaptic density around one to two years after birth. Later, through adolescence and into adulthood neural circuits are refined through synaptic pruning and learning induced mechanisms. In red: neurodevelopmental processes that have been linked to ASD pathogenesis.

2.2.1. Neurogenesis and neuronal migration

Initially, the neural tube, including its most anterior part which will give rise to the cerebral cortex, is lined by a single layer of pseudostratified neuroepithelium in which the neuroepithelial (NE) cells undergo symmetric cell divisions and dramatically increase the neural stem cell pool (Fig. 4) [60]. It is characterized by apico-basal polarity, interkinetic nuclear migration (INM) and apical mitosis [79-81]. INM describes the dynamic movement of the cell nucleus through the different phases of the cell-cycle in elongated cells of pseudostratified epithelia [82]. In the neuroepithelium the nucleus migrates towards the basal lamina during G1-phase, undergoes S-phase at the basal surface of the neuroepithelium to then, throughout G2 phase, move back to the apical surface where it undergoes mitosis (Fig. 4a) [81].

Eventually, the NE cells acquire RG cell identity and the asymmetric neurogenic cell divisions can be observed at the apical surface of the ventricles around GW 7 (Fig. 3) [60]. While NE and RG cells share many molecular and morphologic features, they differ in the architecture of the basal process during M-phase. Recent live cell imaging experiments in human embryonic tissues showed that NE cells continuously retract their basal process during G2-

phase, the cells completely round up during mitosis, and upon cytokinesis the two daughter NE cells regrow a basal process and the cycle continues (Fig. 4a) [81]. RG cells instead, although undergoing the characteristic INM in the ventricular zone (VZ) (Fig. 4b), retain a very thin process to the pial surface throughout M-phase. Following mitosis, the fiber is retained by one of the two RG daughter cells and thickens, while the other RG daughter generates its own basal fiber, using the basal fiber of the sister cell as a guide [81]. At GW 9-10 roughly 30% of the RG cells undergo asymmetric cell divisions, giving rise to other types of progenitors, e.g. intermediate progenitor cells and outer radial glia cells (oRG) populating the subventricular zone (SVZ), or directly differentiate into excitatory pyramidal neurons. Thereby, the basal process maintained by the RG sister cell serves as a stable scaffold for the radial migration of these diverse cell types towards their target location (Fig. 4b,c) [81].

During development, the cerebral cortex gets populated by two main groups of neurons: excitatory projection neurons and inhibitory interneurons. They are generated in the proliferative VZs and SVZs adjacent to the lateral ventricles of the immature brain and subsequently migrate towards their final position in the cortex (Fig. 4d) [83].

Post-mitotic excitatory neurons in the developing cortex are born in the VZ and SVZ of the neocortex and use a variety of different modes for radial migration towards the pial surface and into the cortical plate [84-86]. During initial corticogenesis, early-born excitatory neurons employ radial glia-independent somal translocation. These neurons extend a long, leading process radially from the point of their origin in the VZ and attach it to the pial surface. Subsequently, the cell body is pulled towards the basal surface by a progressive shortening of this leading process to eventually form the transient preplate [85]. Later born neurons then split this preplate into marginal zone and subplate, first defining the developing cortical plate. These later born neurons initially exhibit a multipolar migration mode [86, 87]. Multipolar cells do not show any fixed cell polarity but rather dynamically extend and retract multiple processes as they slowly move from their birth place towards the apical margin of the intermediate zone (IZ). There, they change morphology and undergo a multipolar-to-polar transition. Now, they show a bi-polar cell morphology and continue their journey by using the radial glia basal processes as a scaffold for their migration [85]. Locomoting neurons have a thick leading process and a thin trailing process, while the entire cell moves along the radial fiber that extends across the entire thickness of the developing cerebral cortex [85]. Many of these locomoting neurons switch to somal translocation, also called terminal translocation, as soon as their leading process touches the pial surface, in order to reach their final position in the developing cortex [88].

Cortical inhibitory interneurons, instead, perform yet another mode of migration. Interneurons are derived from the lateral and medial ganglionic eminence (LGE and MGE, respectively) in the subcortical telencephalon and migrate tangentially into the developing cortex [89-91]. These cells are characterized by a leading process tipped with growth cones and a trailing process. They initially migrate in two streams over long distances tangentially and then switch to radial migration to integrate into the various cortical layers (Fig. 4d) [90].

This tangential migration is, among many other factors, dependent on the expression of the homeodomain proteins DLX-1 and DLX-2 [90].

Currently, the most widely accepted view of cortical neurogenesis is based on the observation that RG cells are multipotent and can generate all types of excitatory neurons. They progress through a coherent neurogenic program in which their proliferative potential diminishes over time and produce a highly predictable neuronal output [92]. Mathematical modeling, instead, suggests that the multipotent RG progenitor cells follow a more stochastic mode of cortical neurogenesis: as RG cells divide, they undergo a sequence of probabilistic decisions – in each division the cells have a certain probability to generate a specific type of neuron [93]. Consequently, the resulting cell lineages of different RG cells are rarely identical or contain all types of excitatory projection neurons, but collectively they generate the full diversity of pyramidal neurons in the cortex [93]. According to both models however, cortical neurogenesis follows a temporal inside-out pattern in which early born neurons predominantly populate deep layers and later born neurons populate more superficial cortical layers (Fig. 4c) [94]. Over time, the proliferative output of RG cells decreases and eventually they switch from producing neurons, to the direct or indirect production of cells belonging to the macroglial linage, astrocytes and oligodendrocytes (Fig. 4c) [95].

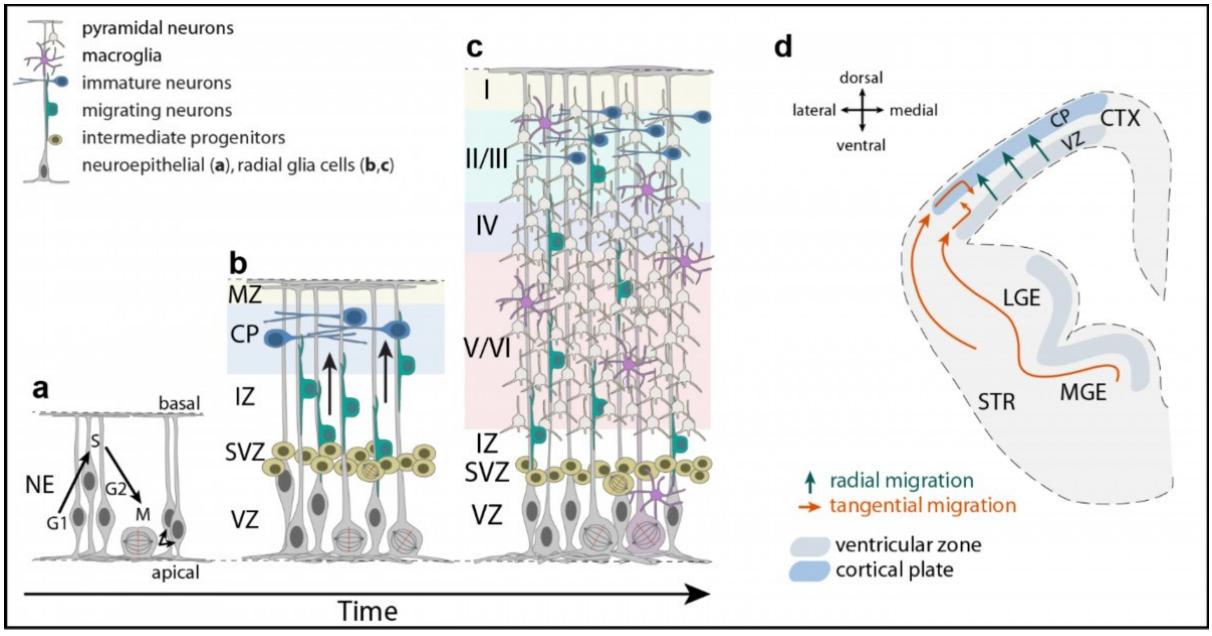

Figure 4: Neurogenesis, migration and differentiation in the mammalian neocortex. a, Cells in the single layered, pseudostratified neuroepithelium (NE) undergo multiple rounds of interkinetic nuclear migration during the cell cycle (from G1 to M-phase) and produce, through symmetric divisions at the apical surface, a large pool of neural stem cells that will give rise to the entire mammalian CNS. **b**, Later their progeny, the radial glia cells, will start with asymmetric neurogenic divisions in the ventricular zone (VZ), producing intermediate progenitor cells populating the subventricular zone (SVZ) and post-mitotic neurons that migrate along the radial glial processes and through the intermediate zone (IZ) into the developing cortical plate (CP) which assembles just below the marginal zone (MZ), the precursor of cortical layer I. There, these immature neurons will then differentiate. **c**, The six layered cerebral cortex is formed in an inside-out fashion, i.e. early born neurons will compose the pyramidal neurons of the deep layers, while later born neurons will migrate, guided by the radial glia's basal processes, through the entire cortical thickness to form the superficial cortical projection neurons (I-

VI, cortical layers). Upon the neurogenic period, the radial glial cells change morphology and will give rise to the macro-glial cell linages, the astrocytes and oligodendrocytes (not shown). **d**, Schematic of a coronal section of the developing anterior telencephalon showing cortical neurogenesis and the main migratory routs of excitatory neurons (radial migration, dark turquoise) and inhibitory neurons (tangential migration, orange) from their place of origin, the ventricular zone of the cortex (CTX) or of the lateral and medial ganglionic eminence (LGE and MGE) of the striatum (STR), respectively (adapted from [83]).

2.2.2. Neuronal differentiation, synaptogenesis, pruning and synaptic plasticity

Neuronal differentiation starts as soon as the neuroblast arrives in the cortical plate. Accordingly, layer V and layer VI neurons have differentiated into recognizable pyramidal cells even before layer II neurons have reached their target position [96]. Mature neurons of the cortex are highly polarized cells with functionally and structurally different processes: axons and dendrites. This polarization mediates the directional information flow in neural networks and is established early during development [97]. Neuroblasts acquire a highly polarized morphology already during migration towards their target location. The basal, thicker, leading process will later give rise to the branched dendrites that extend radially towards the pia, while the thin trailing process will become the axon, projecting into the opposite direction [86, 95]. The growing tips of these developing processes, the neurites, are called growth cones. They are the path finders for connections to target cells and are guided through cell-cell contacts, interactions with the extracellular matrix (ECM) and secreted extracellular guidance cues that can be both, attractant or repellant [96]. When a growth cone comes in contact with its target, a synapse is formed [96, 98].

Synapses are specialized asymmetric cell-cell contacts which permit the controlled transfer of electrical or chemical signals between a pre-synaptic neuron and a post-synaptic target cell, i.e. neuronal or muscle cells [98]. At chemical synapses in the CNS, neurotransmitters such as amino acids or peptides, are released from synaptic vesicles into the synaptic cleft in response to action potentials, and trigger a post-synaptic response (Fig. 5a). Although synapse formation occurs throughout life, it is especially predominant during brain development (Fig. 3) [98]. Pre-synaptic and post-synaptic differentiation is initiated at axodendritic contacts through cell adhesion proteins, such as the pre-synaptic neurexins coupling to the post-synaptic neuroligins [99-102]. This is followed by a stabilization of the intercellular contact and synapse maturation through recruitment of pre-synaptic scaffolding proteins as well as post-synaptic components, such as postsynaptic density proteins and neurotransmitter receptors [98]. Modulation of these newly formed synapses can then occur through altering the organization or composition of synaptic proteins, as well as post-translational modifications to achieve its required physiological responsiveness [103].

Differentiating neurons initially form an excessive number of synapses, many of which are subsequently removed during synaptic pruning [104]. Microglia, a cell type of the mesodermal linage, are essential for this process. They engulf and phagocyte pre-synaptic and post-synaptic elements (i.e. axonal terminals and dendritic spines) during developmental periods of network maturation and mediate appropriate brain connectivity (Fig. 5b) [105,

106]. Furthermore, programmed cell death of both pyramidal excitatory and inhibitory neurons in the postnatal brain plays an important role during circuit refinement and amoeboid microglia have been shown to phagocytose the apoptotic neurons [107-109]. In the adult, microglia directly interact with neurons, making frequent but brief contacts with synapses, surveilling the homeostatic brain and eliminating synapses for refinement when needed, enabling plasticity (Fig. 5b) [110, 111].

Also immature astrocytes are involved in neural network formation, for instance by secreting the trans-synaptic organizers Thrombospondins [112, 113], or the glia-derived neurotrophic factor GDNF that enhances synaptic adhesion [114] (Fig. 5). Oligodendrocytes, instead, are the myelinating cells of the CNS. They produce the myelin sheath, essential for the rapid and efficient conduction of the electrical impulses along the axons, and for preserving axonal integrity (Fig. 5) [115].

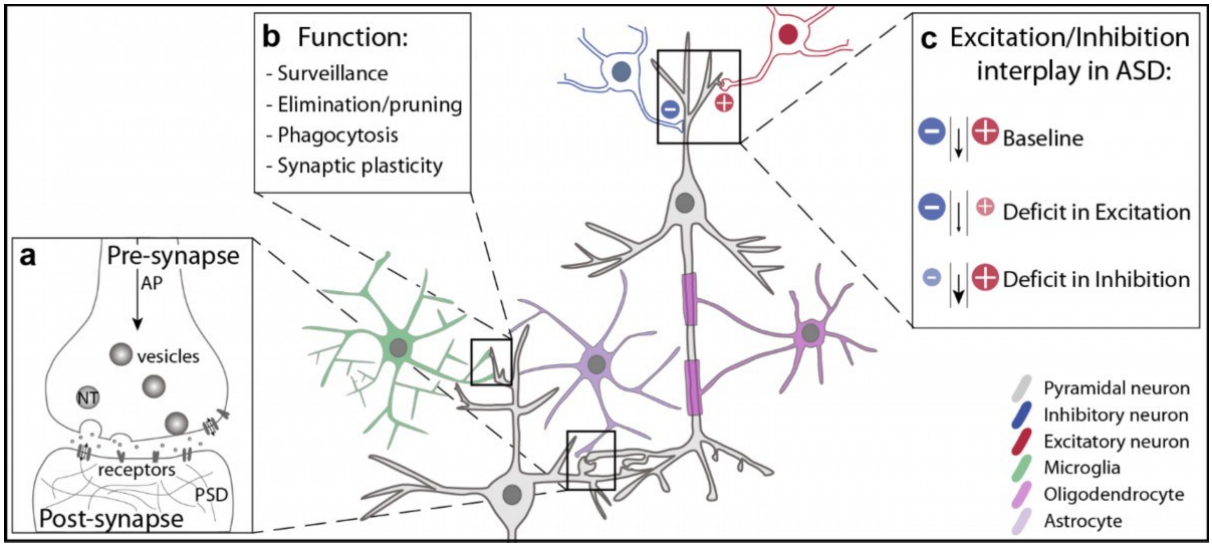

Figure 5: Cell composition and connectivity in the mature neocortex. a, Schematic of a synapse, consisting of an axonal pre-synaptic terminal, a synaptic cleft and a dendritic post-synapse. Arriving action potentials (AP) in the pre-synapse trigger the fusion of vesicles containing neurotransmitters (NT) with the pre-synaptic membrane, NT are released into the synaptic cleft and trigger a response in the post-synapse. **b**, Microglia (green) play an important role during development of neural circuits and adult brain homeostasis, but also plasticity. **c**, Mature pyramidal neurons receive excitatory (red) and inhibitory inputs (blue). Abnormal interplay of this excitation and inhibition might lead to "noise" in neural networks, a core concept of contemporary ASD research.

Correct wiring and appropriate circuit refinement provide the basis for normal brain function and higher cognitive abilities in mammals. Over the last years, a number of reports have put forward the hypothesis that abnormal 'noise' in the brain might underlie certain forms of ASD, a concept now widely known as 'E:I imbalance' [15]. At the level of a single pyramidal neuron, the number of excitatory and inhibitory synapses are highly-regulated, generating a relatively stable ratio of E:I synapses across dendritic segments [116-118]. As mentioned above, at the level of cortical circuits, the ratio of excitatory to inhibitory cortical neurons is similarly strictly controlled by a diverse range of developmental processes [108, 119]. Thus,

on a conceptual and oversimplified level, this means that if excitation exceeds inhibition due to pathophysiological changes in the brain, then activity will increase. Conversely, if inhibition exceeds excitation, activity will decrease, resulting in an imbalanced state (Fig. 5c). Hence, whenever circuit refinement or the homeostatic mechanisms that maintain E:I balance are disturbed, an altered E:I interplay might lie at the root of the behavioral and cognitive abnormalities observed in ASD [15].

2.3. Cytoskeleton organization in neurodevelopment

The cytoskeleton, its interacting proteins and dynamic changes are crucially involved in all major brain developmental processes, ranging from regulating INM [82] and cell division [120], over the regulation of migration of newborn neurons to neural differentiation [121-123] (Fig. 6a-c).

The neural cytoskeleton is composed of three major classes of filaments, the microtubules, filamentous (F-) actin and neurofilaments, i.e. specialized intermediate filaments (Fig. 6d) [121, 124, 125]. Neurofilaments contain three domains: a conserved α-helical core domain flanked by intrinsically disordered N-terminal head-, and C-terminal tail-domains; the core domain drives coiled-coil interactions and co-assembly with other subunits to form dimers, tetramers, and filaments [125]. Instead, F-actin and microtubule polymers assemble from ATP-bound G-actin monomers (in the brain one β- and two γ-isoforms are predominant) and GTP-bound α–β-tubulin heterodimers (formed from six α- and seven β-isotypes), respectively. For both, microtubules and actin filaments, polymerization occurs mainly at one end of the polarized structures - the plus end of microtubules and the barbed end of actin (Fig. 6d) [121, 124].

During INM in RG cells, basal movement of the nucleus is achieved by the exertion of direct force onto the nucleus by microtubule associated kinesin motor proteins as well as by apically located actomyosin contractility [126]. In contrast, return to the apical surface is mediated through dyneins and the microtubule-associated protein Tpx2 [127]. During M-phase at the apical surface, sister chromatids are separated by the mitotic spindle that is organized by the centrosomes (Fig. 6a). The dynamic microtubule ends generate the separation force together with dynein and kinesin motor proteins (Fig. 6d) [128]. In addition, cytokinesis requires tightly controlled accumulation of actin in the cleavage furrow [129].

Neuronal migration requires the generation, maintenance, and remodeling of the leading process that marks the direction of locomotion [130] (Fig. 6b). The leading process is defined during the multipolar to bipolar transition in the IZ, when a complex signaling cascade converges on the actin and microtubule cytoskeleton to mediate the required changes in cell shape [131]. Stabilization of the leading process is mediated by microtubules, and it is tipped by structures that are very similar to the growth cones of growing axons. These “growth-cone-like” structures are thought to play an important role in sensing the surrounding microenvironment and contributing to the chemotactic guidance of neurons [88, 130, 132].

The Arp2/3 (actin-related protein 2/3) complex, which initiates the nucleation of new actin filaments (F-actin) (Fig. 6d), is essential to promote the growth of branched actin networks composing filopodia and lamellipodia at these leading edges, mediating neurite extension [131]. Now, the nucleus moves, in a saltatory fashion, into the leading neurite - a process called nucleokinesis. To this end, microtubules form a cage around the nucleus by extending from a basally located microtubule organizing center, then microtubule motors and the actomyosin cytoskeleton generate the required force to move it in a stepwise fashion into the cortical plate (Fig. 6b) [123, 133, 134].

As excitatory neurons settle in the developing forebrain, differentiation programs are initiated. They form large dendritic trees, connecting to other neurons and from the trailing neurite, the axon is generated. Morphologically, developing axons are similar to the neurites formed during migration [97]. The extending axonal neurite is stabilized by parallel microtubule bundles while the axon growth cone is composed of F-actin based lamellipodia and filopodia. In addition, complex interactions between the actin and microtubule cytoskeleton mediate the continuous dynamic remodeling of the growing axon (Fig. 6c) [124].

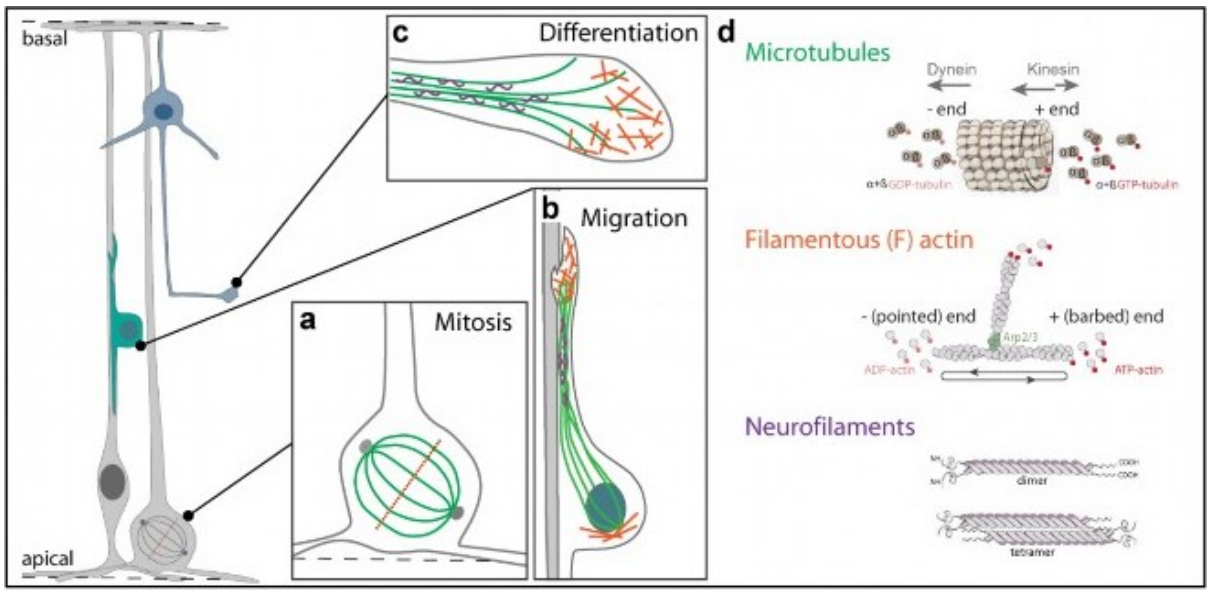

Figure 6: The neural cytoskeleton during brain development. a, The microtubule spindle is essential for cell divisions during neurogenesis. **b**, All cytoskeletal components, microtubules (green), F-actin (orange) and intermediate filaments (purple) are involved in mediating neural polarization and migration. **c**, The cytoskeleton furthermore regulates axon-growth, dendritic branching and differentiation of immature neurons. **d**, Organization, assembly and disassembly of the main cytoskeletal components of the nervous system.

While the functional roles of the microtubule and actin-cytoskeleton during brain development are quite well understood, the contribution of intermediate filaments remains comparatively little described. Intermediate filaments in general provide mechanical strength to cells and interestingly, intermediate filaments in the CNS follow a sequential expression pattern throughout neuronal development and maturation [125, 135]. For example, early expression of the intermediate filament Nestin is characteristic of neural stem cells and is

down-regulated after differentiation [136, 137]. Vimentin is transiently expressed in neuro-progenitors, while in newly born neurons, Vimentin is continuously replaced by the neurofilament classes of more mature neurons, i.e. the triplet of light, medium and heavy molecular mass neurofilaments (NF-L, NF-M and NF-H, respectively), α-internexin and peripherin [138]. α-Internexin expression can be detected in all differentiated neurons but decreases postnatally, when it is replaced by the triplet neurofilament classes. NF-L, NF-M and NF-H have been shown to be the targets of post-translational modifications, to interact with other cytoskeletal components, especially microtubules, and to mediate axonal stability in mature neurons [139].

3. CONVERGENCE IN ASD AND IMPLICATIONS FOR TREATMENT

3.1. Introduction

Due to the challenges of the large phenotypic and etiologic complexity in ASD (see chapter 1), today there are virtually no approved treatments available that target its core symptoms. While a large body of work on monogenic ASDs have provided valuable insights into the underlying pathophysiologic mechanisms of specific mutations, more recently a number of studies have focused on convergence [56, 74, 75, 140-144]. This scientific approach aims to uncover points of commonality across different ASD-risk genes to identify shared pathophysiological mechanisms underlying the disorder. Indeed, several initial studies have revealed important general characteristics, such as that a large number of ASD-risk genes are involved in synaptic structure and function or chromatin modification and regulation of gene expression [140, 145-147]. More recently, additional shared biological pathways, including neurogenesis and migration, synaptogenesis and synaptic plasticity, and activity-dependent transcription and translation have also begun to emerge as common motives at the root of autism and will be discussed in detail below (Fig. 7a). The idea that the large number and diverse set of ASD-risk genes might converge along a smaller number of molecular functions carries the promise to eventually simplify treatment developments, adding big value to the effort of identifying these points of commonalities. Although this endeavor may be complicated by the fact that a number of ASD-genes may function as master regulators of multiple developmental processes and/or are temporally and spatially ubiquitously expressed, when it comes to the identification of potential treatments, this approach grants the advantage to focus on a smaller number of molecular functions rather than a large number of genes and conditions. Thus, allowing to move from complicated and costly personalized medicine approaches to the treatment of larger subsets of patients.

3.2. Regulation of gene transcription

Dynamic changes of gene expression patterns coordinate brain development and function, from neurogenesis to adult neural plasticity (reviewed in [148]). Over the last few years, mutations in genes encoding transcription factors (e.g. *TBR1, FOXP2, ADNP, RAI1* and *DEAF1)* or chromatin modifiers (e.g. *CHD2*, *CHD7*, *CHD8*, *ARID1B*, *POGZ, SETD5, MECP2, KMT5B, KDM6B*) have been consistently identified in ASD patients [145]. Furthermore, analyses of global DNA methylation [149-152] as well as histone modifications [153, 154] revealed altered epigenetic signatures among patients with idiopathic ASDs.

To date, the most-studied transcriptional regulator associated with a condition presenting clinical features overlapping with ASDs is *MECP2*, whose mutations are the main cause of Rett syndrome (RTT). *MECP2* was shown to play multiple roles in the nucleus, ranging from transcriptional repression [155] to microRNA processing [156] and regulation of RNA splicing [157]. In the brain, *Mecp2* is expressed throughout development and adulthood [158, 159]. Constitutive *Mecp2* loss of function (loF) is associated with reduced morphological complexity

in neurons, altered neuronal connectivity, synaptic transmission and plasticity. Conditional *Mecp2* ablation in adulthood causes similar synaptic defects, suggesting that *Mecp2* participates in maintaining neuronal functions in the adult brain (reviewed in [160]). *Mecp2* rodent models recapitulate clinical features observed in RTT patients, such as seizures, motor and cognitive defects, social deficits and anxiety-like behaviors. Excitingly, by employing these models, it has been demonstrated that the neurological and behavioral phenotypes associated with *Mecp2* mutations are reversible [161, 162]. Thereafter, a number of groups have proposed potential therapeutic interventions, ranging from manipulation of neurotrophin levels [163-166] to gene therapies [167-171]. These approaches ameliorate phenotypic severity, extend mouse survival and recover the synaptic defects together with some of the RTT-associated behavioral abnormalities. While promising, these therapeutic strategies still have to overcome many challenges, such as identification of the specific cell type to target, toxicity of vehicles and side effects related to gene over dosage.

As opposed to *MECP2*, most ASD-linked genes have been identified only recently. One such example is the gene *CHD8,* which is also one of the most frequently mutated genes in ASD patients. *CHD8* heterozygous deletion results in defects of neural proliferation, differentiation and function [172, 173], however, the underlying molecular mechanisms are still a matter of debate. Sparse *in utero* knockdown of *Chd8* in mouse leads to downregulation of canonical Wnt-β-catenin signaling, premature neurogenesis and abnormal behavior. Activation of Wnt-signaling by expression of a stable form of β-catenin rescues the premature cell-cycle exit and behavioral abnormalities [174]. Constitutive *Chd8* haploinsufficiency, in contrast, leads to a slight activation of the Wnt-β-catenin pathway, whereas the over-activation of REST, a suppressor of neural gene transcription, has been proposed as the main pathophysiological driver [172]. These discrepancies suggest distinctive cell-autonomous and non-cell-autonomous and/or dosage-dependent mechanisms of *Chd8* mutations and need to be taken into consideration when moving towards clinical applications.

Heterozygous mutations in *ARID1B*, encoding a component of the BAF chromatin-remodeling complex, have been associated with the Coffin-Siris syndrome, characterized by growth retardation, facial dysmorphism, ID and ASD [175-177]. *Arid1b* heterozygous deletion in mice leads to abnormal cognitive and social behaviors, as well as growth retardation phenotypes [178, 179]. ASD-relevant behaviors are associated with a reduced number of cortical parvalbumin-positive interneurons and a consequent alteration of the excitation/inhibition ratio. Treatment with clonazepam, a positive allosteric modulator of $GABA_A$ receptors, rescues ASD behaviors, although information about the duration and age of treatment onset are missing [179]. Complementary manipulation of the GHRH-GH-IGF1 axis, a key modulator of growth and metabolism, by chronic GH supplementation is sufficient to rescue growth retardation and muscle weakness, but not behavioral phenotypes [178]. These findings emphasize the importance of combining multi-level therapeutic interventions when treating complex disorders, such as ASDs, to ameliorate different aspects of the disease.

While this class of ASD-genes has been continuously expanding in the last few years, for some of them establishing the molecular function has been less straightforward than for others. A

notable example is *SETD5.* Although Setd5 belongs to a family of histone methyl-transferases [180], three independent studies have found no experimental evidence of such catalytic activity of the protein [181-183]. Instead, Setd5 regulates gene transcription via its interaction with the Hdac3 and Paf1 complexes [183]. This regulatory function appears important in response to learning, to adjust synaptic gene expression and, potentially, network activity. Because the brain architecture is not affected by *Setd5* heterozygous deletion, these findings suggest that interventions targeting the activity-dependent regulatory function of *Setd5* may be sufficient to ameliorate the associated behavioral defects, an emerging concept potentially applicable to other genes belonging to this class.

In summary, the above-mentioned examples illustrate that chromatin interacting and modifying proteins play a key role in ASD pathogenesis during brain development and in adulthood. Since most of the genes belonging to this group are often ubiquitously expressed, many of them (such as *CHD8, TBR1, ADNP*) may orchestrate expression of several gene networks at multiple time points [184-187]. While their broad regulatory action may complicate the development of very specific treatments, the understanding gained from detailed functional analysis of downstream effects and interactions, as exemplified above by *Mecp2*, may lead to effective treatment strategies.

3.3. Proteostasis

Another emerging convergence point of ASD, central to this thesis, is the regulation of protein homeostasis in the brain. The fine control of protein synthesis and degradation is central for the assembly of brain circuits and synaptic plasticity [188-190]. Accordingly, genes encoding regulators of protein synthesis (e.g. *TSC1/2*, *PTEN, NF1*, *FMR1*) and degradation (e.g. *UBE3A*, *TRIP12*, *CUL3*) represent another common motive in ASDs.

For instance, the mammalian target of rapamycin (mTOR) signaling cascade is one of the major pathways regulating local protein synthesis and it is involved in a number of processes in the brain (reviewed in [191]). Mutations resulting in abnormal activation of the mTOR pathway, such as the ones identified in *TSC1/2, PTEN* and *CNTNAP2*, are linked to ASD. Therefore, over the last few years a number of modulators of the mTOR complex 1 have been tested as potential treatments for these conditions [192, 193]. In mouse models, these compounds not only yielded promising results in ameliorating ASD-associated phenotypes, but were also valuable to identify time-dependent effects [194-197]. For instance, inhibition of the mTOR pathway in animal models of tuberous sclerosis highlighted that early treatment completely prevents both neuroanatomical and behavioral phenotypes [194, 196]], whereas manipulation of the same pathway in adult animals is less successful [195]. These studies demonstrate that even when potential therapeutic targets are identified, correction of ASD core symptoms may be time-sensitive; therefore, temporal windows should be carefully considered when designing clinical trials.

Similarly to RTT, fragile-X-syndrome (FXS) represents another disorder with autistic features extensively studied in the past. FXS is caused by the expansion of a trinucleotide repeat

sequence at the promoter of the gene encoding the fragile X mental retardation protein (FMRP). As a consequence, abnormal activation of group 1 metabotropic glutamate receptors leads to exaggerated protein synthesis at the synapse [198, 199]. Several mGluR5 antagonists (e.g. MPEP, CTEP, fenobam) have been successfully tested in mice ([200-203], reviewed in [204]) and inhibiting protein synthesis rescues some FXS symptoms, as demonstrated by lovastatin administration in mice [205, 206] and humans [207]. As more and more targets of FMRP are emerging, however, it becomes evident that FXS patients will require a life-long multi-target pharmacological approach rather than a single treatment.

Since protein synthesis depends on the availability of amino acids, it was intriguing to find that abnormal regulation of branched chain amino acid (BCAA) levels is also associated with the development of autism core symptoms. In particular, homozygous loF mutations in genes regulating BCAA transport and catabolism (*SLC7A5* and *BCKDK* respectively) are linked to ASDs. Studies of *Slc7a5* and *Bckdk* animal models revealed that the neurological defects caused by mutations in these genes can be ameliorated by elevating brain BCAA levels, either by ventricular injections or diet supplementation [208, 209]. Encouragingly, dietary intervention successfully improved neurological symptoms also in patients carrying *BCKDK* mutations [210], supporting the idea that the detection of precise molecular causes of ASDs is the first step toward the identification of ad-hoc treatments.

Finally, several studies have linked defects in protein degradation to ASD, identifying mutations in genes encoding components of the ubiquitin proteasome system (UPS) (such as *UBE3A*, *CUL3, TRIP12* and *USP7*) in patients. For instance, loF of the *UBE3A* gene is the major cause of Angelman syndrome (AS). AS-causing mutations affect the maternally inherited allele, since the paternal allele is silenced by an *UBE3A* antisense transcript (*UBE3A-ATS*). In a mouse model of AS, the reduction of *Ube3a-ATS* levels via intra-hippocampal injection of antisense oligonucleotides results in partial restoration of Ube3a protein levels and improvement of some neurobehavioral abnormalities [211]. The efficacy of this treatment is time-sensitive: while embryonic restoration of *Ube3a* expression fully prevents neurological phenotypes, reinstatement of *Ube3a* later in development only achieves a partial rescue [212, 213]. Although gene therapy still faces major limitations in humans, these results point towards concrete opportunities for the treatment of AS.

As outlined above, protein homeostasis in the central nervous system is achieved by a fine-tuned interplay of protein synthesis and protein degradation, in response to both intra- and extracellular stimuli. Targeting this central player may therefore be a promising route to ASD treatment.

3.4. Cytoskeleton dynamics

Several ASD-genes encode proteins implicated, either directly or indirectly, in the regulation of cytoskeletal organization (e.g. *DLX1/2, AUTS2, WDFY3, NDE1, RELN, NEXMIF, TBR1, PTEN*) [214]. In the developing brain, mutations in these genes are associated with defects in neuronal migration and differentiation, as well as axon guidance, causing alterations in brain

cyto-architecture. For instance, reduced expression of the high-risk ASD-gene *RELN* has been linked also to lissencephaly and cerebellar hypoplasia [215, 216]. Animal studies have shown that Reln is essential to regulate the microtubule and actin cytoskeleton, orchestrating multiple steps in neuronal migration [217], and later on to modulate synaptic plasticity [218, 219] and promote dendrite and spine development [220, 221]. Migration is also affected by mutations in *NEXMIF* or *DLX1/2* genes, which, in mouse, lead to abnormal positioning of glutamatergic and GABAergic neurons, respectively, and neuronal morphology. These defects are associated with impaired actin organization, due to elevated levels of RhoA, in the case of *Nexmif*, or by increased expression of *Pak3,* in *Dlx1/2* mutants [222-225]. Similarly, activity of PTEN, another ASD-associated protein, is essential to control neuronal polarity through actin organization [226, 227] and to down-regulate the level of detyrosinated microtubules, preventing excessive axon outgrowth [228].

The observation of brain structural defects in animal models with mutations in this class of genes, poses the problem of how to correct these abnormalities later in life. Interestingly, Manent and colleagues reported that postnatal re-expression of *Dcx* rescues subcortical band-heterotopia in *Dcx* knockdown rats and reduces seizure threshold [229]. These results are encouraging and hold the promise that activation of developmental programs later in life could be beneficial for ASDs as well.

Alternatively, early genetic testing could lead to embryonic treatments. For example, prenatal treatment with Tubastatin A, a specific inhibitor of HDAC6, rescued the migration phenotype and behavioral defects associated with CAMDI deficiency [230]. Along the same line, a recent study showed rescue of neuronal migration and neurite outgrowth deficits in cells lacking the ASD-gene *CTNNA2* by inhibition of ARP2/3, a regulator of actin cytoskeleton [231].

To conclude, functional studies and treatment for ASDs associated with abnormal regulation of the cytoskeleton are still limited. Much more, however, is known about these dysfunctions in the framework of other diseases (e.g. cell migration in cancer [232]) and some of the treatments identified in that context may be employed to ameliorate ASD symptoms.

3.5. Synaptic development and plasticity

Genes encoding synaptic proteins (e.g. *NLGNs, NRXNs, DLG4/PSD-95, ANK2, SYNGAP1* and *SCN2A*) were among the first to be associated with ASDs. While it is now clear that this class of genes is not the only driver of molecular defects in autism, it remains a central focus of the scientific community working on ASDs.

De novo SYNGAP1 mutations are associated with ID, epilepsy and ASD. Syngap1 is localized at excitatory synapses, where it regulates AMPA receptors trafficking [233] and synaptic plasticity [234-237]. In the developing brain, *Syngap1* haploinsufficiency leads to the premature maturation of spine structures [238, 239] causing persistent deficits in neuronal network connectivity, cognition and behavior [234, 237, 238, 240-242]. Interestingly, *Syngap1* heterozygous mice show also elevated activation of Ras and ERK1/2 pathways, with a consequent increase in basal protein synthesis [234, 237, 243]. Pharmacological manipulation

of mGluR5 and Ras/ERK signaling, strategies already employed to rescue FXS symptoms, restores the exaggerated levels of protein synthesis in *Syngap1* mice [243].

Similarly, mutations in *SCN2A* have been associated with ASD, ID and epilepsy. *SCN2A* encodes the $Na_v1.2$ channel, primarily expressed in the axon initial segment of glutamatergic neurons and in a subset of interneurons [244, 245]. During early development, the $Na_v1.2$ channel contributes to action-potential generation and propagation, thus influencing neuronal excitability [244, 246]. A recent study demonstrated that *Scn2a* plays a double role in synaptic development. While *Scn2a* haploinsufficiency impairs axonal excitability during the first postnatal week, it affects dendritic excitability later in development, leading to an excess of immature spines and impaired synaptic plasticity [246]. The synaptic defects are also associated with behavioral abnormalities, such as reduced sociability and anxiety-behavior, and marked hyperactivity [246, 247]. Recently, one study reported the reversibility of hyperactive behavior through manipulation of glutamatergic transmission [247].

The trans-synaptic NLGN/NRXN complex promotes synaptic assembly, maturation and maintenance [248]. Mutations in *NRXNs* and *NLGNs* genes are associated with strong impairments of synaptic transmission, leading to changes in excitation/inhibition ratio and ASD core symptoms [249]. Transgenic mice overexpressing mutant Nrxn1β protein show repetitive behaviors and impaired sociability, as well as an abnormal excitation/inhibition ratio. Inactivation of transgene expression promotes behavioral rescue in juvenile and adult animals, suggesting that the effects of *Nrxn* mutations are reversible [250]. Among the *NLGN* family, *Nlgn3* has been extensively studied in the context of ASDs and phenotypic reversibility. Several studies demonstrated that genetic reinstatement of *Nlgn3* in juvenile and adult mice ameliorates sociability and synaptic plasticity defects [251-254]. Conversely, pharmacological interventions targeting the NLGN/NRXN pathway are still missing. To date, the only pharmacological example is the manipulation of the endocannabinoid system. In mice, conditional triple *Nrxn*β KO impairs excitatory synaptic transmission. Application of the CB1R-antagonist AM251 and inhibition of 2-arachidonoylglycerol synthesis restored the synaptic phenotype [255]. Similarly, the abnormal striatal synaptic transmission observed in mice carrying the human R451C mutation in the *NLGN3* gene is partially rescued by manipulating the endocannabinoid system [256]. This evidence identifies a potential signaling pathway that may exert beneficial effects on some aspects of the pathology.

SHANK proteins participate in regulating dendritic spine structure. Studies on *Shank* mutant mice revealed the possibility to reverse some of the observed ASD-phenotypes in adulthood by restoration of gene expression [257-259] and pharmacological interventions [260-263]. For instance, enhancing NMDA receptor function or using mGluR5 allosteric modulators rescue both synaptic physiology and ASD-phenotypes observed in *Shank2* [259, 261] and *Shank3* mutant mice [264, 265]. These findings have led to concrete clinical interventions in humans. Patients carrying *SHANK3* mutations are currently treated with IGF1 and show significant improvement in both social impairment and restrictive behaviors [266, 267]. Moreover, recent evidence linked *Shank3* deficiency to abnormally low levels of histone acetylation, resulting from HDAC2 upregulation, and consequent aberrant transcription of downstream

target genes, including NMDAR subunits and key actin regulators. In juvenile mice, brief treatment with a low dose of romidepsin, a brain-permeable HDAC inhibitor already approved for cancer treatment, leads to robust and long-lasting rescue of social deficits [268].

It is important to observe that synaptic plasticity is tightly linked to the other molecular processes discussed above such as the activity in the nucleus, protein synthesis and cytoskeleton organization. Therefore, the development of effective treatments for one ASD subgroup may also be useful for ameliorating defects in other ASDs.

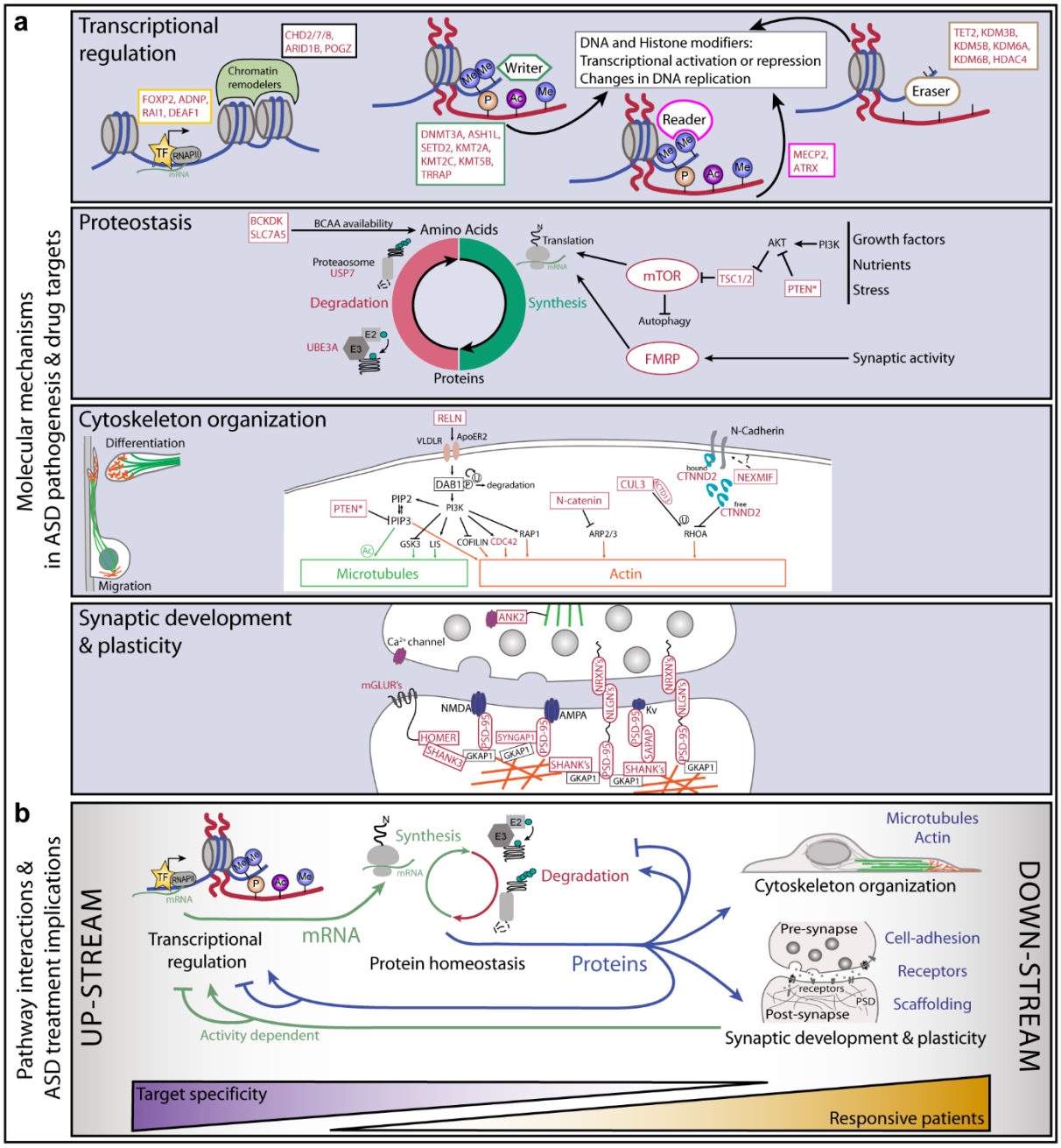

Figure 7: Convergence of molecular pathways in ASD. a, A number of biologically diverse ASD-subtypes can be identified. Transcriptional regulation: the ASD-risk genes (red) belonging to this category are transcription factors (TF), chromatin modifiers and genes regulating DNA and histone modifications. Those can further be classified into "writers" (catalyzing the post-translational modification), "readers" (recognizing and interacting

with specific variants) and “erasers” (removing epigenetic marks). Proteostasis: protein homeostasis is controlled by the interplay of protein synthesis, regulated by different stimuli that activate intracellular signaling cascades (e.g. mTOR and FMRP), and protein degradation, regulated by the UPS. Protein abundance is further limited by the availability of amino acids, such as BCAA. ASD-genes encoding regulators of protein homeostasis are indicated in red, PTEN* appears twice. Cytoskeleton organization: cytoskeleton dynamics regulate fundamental brain developmental processes, such as neural migration and differentiation. Several ASD-genes (red) participate in intracellular molecular pathways that converge on the regulation of microtubules (green) and actin (orange) organization. Synaptic development and plasticity: a large number of cell-adhesion and post-synaptic density proteins have been implicated in the etiology of ASD. These proteins create an interconnected molecular network stabilizing both inhibitory and excitatory synapses. **b,** Although ASDs can be grouped in molecularly distinct subtypes, the underlying pathways are interconnected. Treatments for ASDs may either target specifically affected molecular hubs (up-stream) or intervene on general physiological processes (down-stream).

3.6. Discussion

Over the last three decades, detailed studies on the consequences of monogenic ASD-risk gene mutations in both, rodent models and human cell culture systems, have highlighted common pathologic mechanisms underlying this group of neurodevelopmental conditions. Thus, allowing the division of ASD-risk genes into functionally distinct groups. Since developing targeted treatments for each single form of ASD seems currently out of reach, this approach of targeting common mechanisms, together with systematic studies, may prove a valuable means by which patients can be classified into meaningful treatment groups, with an idea of when and how is best to treat them. This task, however, is complicated by the fact that several ASD-genes are pleiotropic, meaning that these groups are functionally interconnected and that often mutations in one gene lead to the abnormal expression of other ASD-genes (Fig. 7b).

Furthermore, given the multiplicity of phenotypes observed and the complexity of the molecular mechanisms involved, it is becoming increasingly obvious that even monogenic forms of ASD will require multi-level pharmacological approaches. Alternatively, the development of precise targeted interventions, such as the use of oligonucleotide and CRISPR-mediated gene correction techniques, may lead to some valuable tools to correct defects associated with single gene mutations. Yet, the precise time points for these interventions remain unclear. To further complicate the picture, frequently, ASDs are caused by rare combinations of common mutations. Thus, how can we model such complexity? And how can we develop treatments for these patients? While single gene studies are important starting points, there will be the need to develop screening-based strategies that allow the investigation of the molecular pathways affected in a case-by-case manner. Based on this concept, it will become more common to repurpose known drugs to treat ASDs, an approach already showing some successful results [268-270]. Overall, despite the hurdles, advancements in knowledge and technology promise a rapid increase in the diversity and availability of ASD treatments and an improvement in the life quality of affected individuals and their families.

4. ILLUMINATING THE ROLE OF *CUL3* IN ASD PATHOGENESIS

4.1. Introduction

Abnormal regulation of protein abundance during development and in the mature brain has emerged as a common pathway at the root of ASD pathogenesis in recent years (see chapter 3.3 – Proteostasis). However, the developmental and cellular functions, as well as the molecular targets of the majority of the identified ASD-risk genes in this group remain poorly understood. One of these high risk ASD-genes encodes the E3-ubiquitin ligase Cullin 3 (Cul3), a protein at the center of the ubiquitin-proteasome system (Fig. 8a).

The Cullin family proteins are principal members of the Cullin-RING-ubiquitin Ligases (CRLs), the most common type of E3-ubiquitin ligases currently known and composed of eight protein members. Each Cullin forms a distinct class of structurally different CRLs, consisting of different adaptors and/or substrate recognition subunits [271]. Through the selective degradation of target proteins these multimeric complexes are involved in various cellular processes, including protein quality control, cell growth, cell signaling, cell cycle regulation, transcription regulation, as well as many others [271]. The activity of CRLs is controlled via the reversible conjugation of the small ubiquitin-like protein Nedd8 to the highly conserved neddylation domain of the Cullins. Binding of Nedd8 is essential for the association of the E2-enzyme (E2) with the CRL complex and subsequent ubiquitination of target proteins (Fig. 8a) [272, 273]. In addition to the highly conserved Cullin-homology domain, which interacts with the RING proteins (Rbx1 or Rbx2) and recruits the ubiquitin-conjugating enzyme (E2), and the C-terminal neddylation domain, Cul3 is characterized by the N-terminal Cullin-repeat (CR1, CR2 and CR3) domain. Through interaction with a substrate recognition protein, typically containing a N-terminal BTB-domain (from bric a brac, tramtrack, and broad complex), the Cullin-repeat domain mediates target specificity (Fig. 8b) [274].

Over the last decade multiple rare *de novo* variants in *CUL3* have been identified in patients with ASD and/or global developmental delay (Fig. 8b) [145, 146, 275-281]. In addition to these core symptoms, these patients can present with several comorbidities including varying levels of ID, ADHD, sleep disturbances, motor deficits, facial dysmorphic features and epileptic seizures [280-283]. The ASD-associated genetic variants in *CUL3* are most often *de novo* missense, frameshift or loF mutations resulting in haploinsufficiency. They are dispersed throughout the entire gene and affect distinct protein domains [145, 146, 275-281]. In contrast, certain splice site variants and mutations clustering around exon 9 of *CUL3* cause a severe form of pseudohypoaldosteronism type II (PHA2E) [284-291]. PHA2E is a rare endocrine disease with autosomal dominant inheritance, featuring hypertension, hyperkalemia, and metabolic acidosis but not ASD [284, 287, 291]. All the PHA2E variants described lead to a skipping of exon 9, causing an in-frame 57 amino acid deletion (CUL3Δ403-459) in the Cullin-homology domain (Fig. 8b). The resulting mutant protein acts in a dominant negative fashion in the kidney, promoting PHA2E [291].

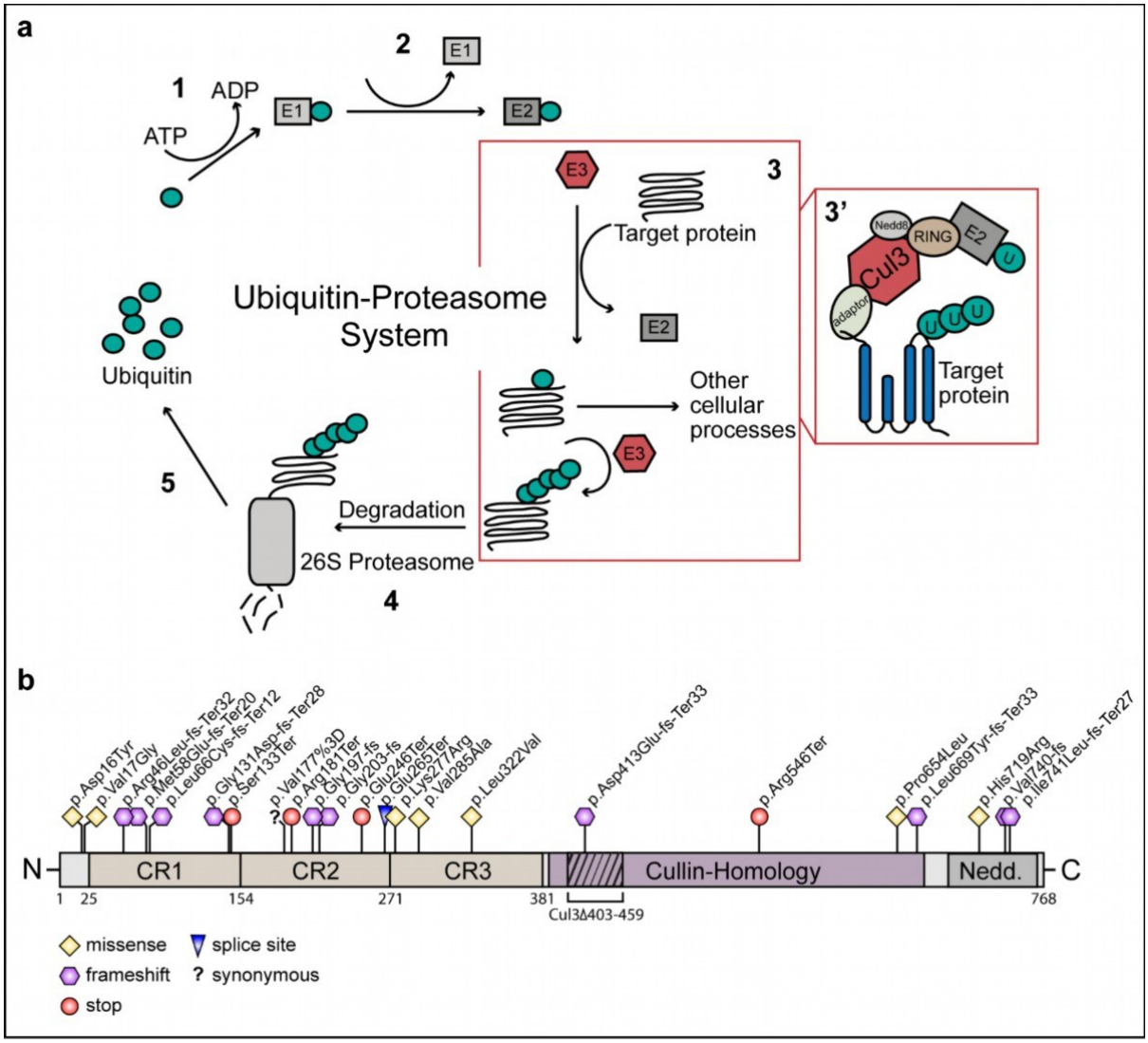

Figure 8: Cul3 in the ubiquitin-proteasome system and human pathogenic *CUL3* variants. a, Scheme of the main steps in the UPS: the highly conserved, inert 76 amino acid protein ubiquitin (U) is covalently conjugated to the ubiquitin-activation enzyme E1 (*step 1*), then it is transferred from E1 to the ubiquitin-conjugating enzyme E2 (*step 2*), the E3 ubiquitin-protein ligase complex subsequently transfers the ubiquitin from the E2 to the substrate protein (*step 3*); during this step, Cul3 operates as a scaffold, recruiting both the E2 and the substrate in a target specific fashion through interaction with e.g. a BTB-domain containing protein adaptors, to mediate ubiquitination (*3`*); After the first ubiquitin is added, the E3 can elongate the ubiquitin chain by creating ubiquitin-ubiquitin isopeptide bonds, forming a ubiquitination pattern that is subsequently recognized by shuttling factors and chaperones that bring the target protein to the proteasome (*step 4*) where it is unfolded, the ubiquitin is released (*step 5*) and the protein is cleaved into small peptide chains. **b**, In patients, several heterozygous gene variants have been described in Cul3. They include *de novo* missense (yellow), frameshift (purple), stop (red) and splice site mutations (blue) and also include one synonymous variant of unknown relevance. The *de novo* ASD and global developmental delay associated variants can be found in all the main protein domains, the N-teminal Cullin-repeat domain (CR1, CR2 and CR3), the central Cullin-homology domain and the C-terminal neddylation domain (Nedd.), and most often lead to *CUL3* haploinsufficiency. In contrast, the in-frame 57 amino acid deletion of the CUL3Δ403-459 variant acts through dominant negative effects in the kidney and causes the endocrine disorder PHA2E.

In the adult mouse, *Cul3* is expressed in most tissues, including muscles, kidney, and heart as well as, at high levels, in brain tissue [292]. Homozygous loss of *Cul3* (*Cul3*$^{-/-}$) is lethal at embryonic day (E) 7.5, due to accumulation of the cell-cycle regulator Cyclin E [292]. In

mammalian cells, Cyclin E binds to and activates the cyclin-dependent kinase Cdk2 and, through its catalytic activity, it mediates the transition from G1 to S-phase. Unbound Cyclin E has a short half-life, it gets rapidly ubiquitinated and degraded by the proteasome. Instead, Cyclin E within Cyclin E–CDK2 complexes is protected from ubiquitin-mediated degradation. This protection through CDK2, however, can be reversed in a process that involves phosphorylation of Cyclin E, which triggers its ubiquitination. These regulatory mechanisms ensure strict control over normal cell-cycle progression in mitotic cells [292]. Interestingly, Cul3 binding to Cyclin E is BTB-adaptor protein independent and mediated through the recognition of an N-terminally located degron in Cyclin E [293]. According to its cell-cycle regulatory function, *Cul3*$^{-/-}$ embryos at E7.5 are characterized by increased levels of Cyclin E and a much larger fraction of cycling cells in S-phase [293, 294]. Consequently, they show severe developmental defects, including complete disorganization of extraembryonic tissues and defective gastrulation with an absence of endo- and mesodermal cell linages [292].

This initial description of a developmental role of mammalian Cul3 *in vivo* highlights the complexity underlying its proteostatic function. First, Cul3 mediated degradation depends on its temporal and spatial co-expression with its substrate proteins and/or the respective substrate-recognition adaptors (including BTB-domain containing proteins). Second, it may depend on other regulatory modifications, such as the above mentioned phosphorylation of Cyclin E. Third, the activity of Cul3 itself is regulated through the expression of Nedd8 and its reversible conjugation with the Cul3-neddylation domain. And lastly, while Cul3 mediates substrate specificity, it can recruit more than one substrate, and conversely, substrates may be targeted by more than one E3-ligase [295]. Therefore, and despite the relatively well understood molecular function of Cul3 in regulating protein abundance [296], its specific adaptor and target proteins especially in the central nervous system, as well as its role in brain development and adult brain function still remain largely unknown.

One of the first suggested Cul3 adaptor proteins in the mammalian brain was the BTB-Kelch domain containing synaptic protein actinfilin that binds to the actin cytoskeleton [297]. In the post-synapse, actinifilin was shown to interact with the kinate receptor subunit GluR6, mediating its ubiquitination and proteasomal degradation. Furthermore, through co-immunoprecipitation experiments, myc-tagged actinfilin pulled down FLAG-tagged Cul3 in HEK293 cells [297]. Accordingly, RNAi mediated knockdown of actinfilin in primary hippocampal neurons caused and increase in synaptic GluR6 surface expression, suggesting that Cul3 may regulate the abundance of kinate receptor subunits through actinfilin in the brain [297].

Similarly, a few years later, a forward genetic screen in *Drosphila* identified the expression of the BTB-adaptor protein insomniac and Cul3 in neurons to be responsible for the regulation of sleep and wakefulness in flies, independent from the circadian clock but through a dopamine arousal pathway [298, 299].

Cul3 knockdown through RNAi in human HeLa and 293T cells, leading to an 80-90% protein reduction, identified another Cul3 target protein: the small Rho GTPase RhoA that regulates

the assembly of the contractile actin and myosin filament structures, the so called 'stress fibers'. This interaction between RhoA and Cul3 was shown to be mediated through the hBACURD (alias Kctd13) BTB-adaptor protein *in vitro* and perturbation of the Cul3/BACURD complex, by means of *xBACURD* anti-sense morpholino oligonucleotides (MO) caused gastrulation defects in *Xenopus* larvae [300]. Moreover, in a study investigating the co-expression networks of genes affected by the 16p11.2 deletion and duplication syndromes, an association between Cul3/Kctd13/ and RhoA was further hypothesized, now linking it to neuropsychiatric disorders [301]. This association was based on their spatiotemporal co-expression during cortical late mid-fetal development and suggested the involvement of these proteins in neurogenesis, neuronal migration, dendritic spine formation and maintenance. An association between *Kctd13* reduction, neurogenesis and brain size has also been described in MO- zebrafish and shRNA *in utero* electroporation (IUE) knockdown mouse models [302], however could not be confirmed later [303]. Instead, germline *Kctd13* knockout mice were shown to be hyperactive and to have reduced synaptic transmission in CA1 hippocampal neurons, but no alterations in brain size or morphology. In addition, these neurons were characterized by reduced dendritic length and complexity as well as lower spine numbers, potentially caused by increased RhoA levels, as the synaptic defects could be rescued by rhosin administration, an inhibitor of RhoA-GTP [303].

While the relevance of some of these findings still needs to be further tested functionally *in vivo* or in mammals, the above described studies strongly point to an important role of Cul3 in regulating a number of brain-related proteostasis mechanisms in a complex with, but also independently, from actinfilin and Kctd13. However, the function of Cul3 during brain development and in the adult brain, its substrate proteins in the nervous system, as well as the consequences of *Cul3* deficiency demand further investigation. This is especially true in light of the ASD-linked *CUL3* gene mutations, to understand when, how and through which cellular and molecular mechanisms these mutations are able to drive the development of ASD-related phenotypes. These questions are at the heart of this thesis and its findings might have implications not only for drug development but also for clinical trial design.

4.2. Methods

**Unless otherwise specified, experiments were performed by Jasmin Morandell.*

Mice

We thank Dr. Jeffrey Singer (Portland State University, US) for providing us with the Cul3flox (*Cul3^{fl}*) conditional mouse line in which the exons 4 to 7 are flanked by loxP sites [294]. The *Cul3* constitutive knockout mouse line (*Cul3$^{+/-}$*) was obtained by mating *Cul3^{fl}* mice with a CMV-Cre line (B6.C-Tg(CMV-cre)1Cgn/J) and back-crossings to C57BL/6J wild type animals (Fig. 9a). Genotyping for the *Cul3* knockout allele was performed using the following primers: forward GGAAACCTAAAGTTTTTATGCARG and reverse TTTGTCTGGACCAAATATGGCAGCCCAA ACC. The *Cul3 Emx1-Cre* conditional line was generated by crossing male *Cul3$^{+/fl}$* mice with a Emx1-Cre expressing line (B6.129S2 (Emx1tm1cre)Krj/J). *Cul3$^{fl/fl}$ Emx1-Cre* mutant pups were sacrificed as soon as the phenotype was clearly detectable (strongly reduced size and very weak animals) within the first week of life, to comply with ethical requirements (3R principle). Embryonic time points were determined by plug checks, defining embryonic day (E) 0.5 as the morning after copulation. Animals were housed in groups of 3-4 animals per cage and kept on a 12 hour light/dark cycle (lights on at 7:00 am), with food and water available *ad libitum*. All animal protocols were approved by the Institutional Animal Care and Use Committee at IST Austria and the Bundesministerium für Bildung, Wissenschaft und Forschung, Austria, approval number: BMWFW-66.018/0012-WF/V/3b/2017.

Behavior

All behavioral tests were performed on adult, two- to five-month-old, sex-matched littermate animals during the light period. Animal cohort sizes ranged between 8 and 20 animals per genotype and sex. Male and female cohorts were initially analyzed separately, and data was only pooled in case wild type male and wild type female data was statistically comparable, i.e. not significantly different. Before testing, animals were habituated at least for one hour to the testing room, equipment was cleaned with 70% EtOH after each animal. Different behavioral tests in the same mouse cohort were separated by at least one day of break. Tests were performed starting with the least aversive task and ending with the most aversive, and either scored automatically or by an experimenter blind to the genotype.

Hind limb clasping: During a 10 sec tail suspension period hind limb clasping severity (scores 0-1- no hindlimb clasping to 3- most severe phenotype) was assessed by the experimenter. The test was repeated 3 times per animal and the average score was calculated, scores between 0 and 1 are not considered as hindlimb clasping.

Gait analysis: Gait properties were assessed by footprint analysis as described previously [209]. Briefly, fore- and hindpaws were colored with non-toxic dye and the animals allowed crossing a white sheet of paper, 70 cm in length, in a straight line. Stride, sway and stance length, as well as paw distance were measured as indicated in Fig. 10b by the experimenter.

RotaRod: Performance on the accelerating mouse RotaRod (Ugo Basile S.R.L, Cat. No. 47650) was analyzed on 3 trials per day over three consecutive days, with an acceleration from 5 to 40 rpm over 5 min (300 sec). For each animal the latency to fall (sec) and maximum speed at the end of each trial (rpm) were automatically determined, sex-matched littermates were tested simultaneously to avoid confounding factors. Initial coordination was assessed by analyzing the first trial on the first day of training.

Open field: As previously described [183], animals were allowed to freely explore a brightly lit arena (45 x 45 x 30 cm), made out of grey Plexiglas, over a 30 min time period. Locomotor activity (distance travelled and velocity) and center crossings were recorded by a video camera and analyzed using the EthoVision XT software (Noldus).

Elevated plus maze (EPM): Mice were placed in the center of the EPM apparatus facing the open arm and left to explore the maze for 6 min. The time spent in the open and closed arms along with number of closed and open arm entries and distance travelled in each arm were determined using Ethovision XT video tracking system and software. The ratio of the time (in sec) spent on the open arm vs. the total time spent on the maze were calculated.

Three chamber sociability test: Mice were tested for sociability and social novelty preference as described previously [209]. The testing apparatus was a rectangular clear Plexiglas three chambers box (60cm (L) x 40cm (W) x 20 cm (H)). The dividing walls had doorways allowing access to each chamber. Age and sex matched C57BL/6J mice were used as stranger mice and were habituated to placement inside the wire cage. Each test animal was first placed into the center chamber with open access to both left and right chamber, each chamber containing an empty round wire cage. The wire cage (12 cm height, 11 cm diameter) allows nose contact between mice but prevents fighting. After 10 min of habituation, during the social phase, an age-matched stranger was placed in the left chamber while a novel object was placed into the right chamber. The test animal was allowed to freely explore the social apparatus for 10 min. Subsequently, each mouse was tested in a second 10 min session to evaluate the preference for a novel stranger, which was placed inside the right wire cage. Number of nose contacts (< 5cm proximity) with the caged mouse, as well as the time spent in each chamber, was calculated. Analysis was done using the Noldus EthoVison XT.

Olfaction habituation and dishabituation test (OHDH): The test was performed as previously described [304]. In brief, mice were presented with a sequence of non-social, i.e. water, almond (McCormick) and banana (McCormick) (diluted 1:100 in water), and social cotton swabs (Social A and B). Social odors were obtained by wiping the cotton swabs in a zick-zack manner through the bedding of two distinct cages, housing each three, to the test mice, sex- and age-matched wild type mice. Each cotton odor swab was presented 3 x 2 min with a 1

min break. The time the tested mouse spent sniffing each cotton swab was determined by the experimenter using a stop swatch.

Contextual fear conditioning (CFC) task: As described previously [183], mice were subjected to the CFC task in three sessions, each distanced by 24 h: a training session (day 1) and two re-exposure sessions (day 2 and day 3). On day one, mice were subjected to a single fear conditioning training session of 5 min, in which they learned to associate the conditioned stimulus (CS: context) to the unconditioned stimulus (US: a foot-shock). To this end, each mouse was placed in a fear-conditioning chamber (18 x 18 cm2, Noldus) with an electrified grid-floor. After 120 sec of free exploration, the mouse was subjected three times to a foot shock (0.5 mA; 2 sec) delivered through the grid-floor, every 1 min. Mice remained in the conditioning chamber for 1 min after the last shock delivery. On days two and three, each mouse was placed back in the conditioned chamber for 10 and 3 min, respectively, without delivering the electrical foot-shock to test their memory retention and memory extinction. Behavior during all experimental sessions was recorded by a video camera mounted above the ceiling of the cage and connected to a computer equipped with the Ethovision XT software (Noldus). Percentage of time spent freezing (absence of all but respiratory movements for at least 3 sec) was scored to assess emotional reactivity during training (day 1) and fear memory during retention test (the first 3 min of day 2 session) and extinction test (first 3 min of day 3 session). All behavioral parameters were scored by an experimenter blind to the animal experimental condition. Pairs of control-mutant littermates were randomly tested in the morning and in the afternoon to control for circadian rhythm.

Histology

Immunofluorescent staining in adults: Adult male littermate mice were deeply anesthetized and transcardially perfused with 4% paraformaldehyde (PFA). Brains were dissected, postfixed in 4% PFA, dehydrated in 30% sucrose and sliced at 40 µm on a sliding VT1200S vibratome (Leica Microsystems). Stainings on adult brains were performed on floating sections without antigen retrieval. In brief, sections were washed in 1x PBS and incubated overnight on a horizontal shaker at 4°C in primary antibody solution (14-16 hours). Primary antibodies were diluted in 0.3% Triton X-100 and 2-5% donkey serum. On the next day, the sections were washed and incubated with a species-specific secondary antibody for 2 hours at 4°C. Nuclear counterstain was performed for 10 min with 300 nM DAPI (Life Technologies) in 1x PBS before mounting in DAKO fluorescent mounting medium. To examine cortical layering, the thickness of Cux1 positive cell layer and the Ctip2 positive cell layer was measured at three defined points of each cortical hemisphere (n= 3 littermate animals per genotype, at least 4 images/animal). For interneuron, microglia and oligodendrocyte counting, positive-stained cells were counted within the somatosensory cortex and normalized to the area used (n= 3 littermate animals per genotype, at least 5 images/animal). Adult cortical sections were stained with the following primary antibodies: anti-Cux1 (Santa Cruz, sc 13024, 1:200), anti-Ctip2 (Abcam, ab18465, 1:500), anti-Parvalbumin (1:500,

Chemicon MAB1572), anti-Iba1 (1:500, Wako 019 19741), anti-GFAP (1:200, Cell Signaling 12389P).

Immunofluorescent staining in embryos and newborn pups (P0/P1): Mice were killed for analysis at E14.5 and E16.5 and P0 by decapitation. Heads were dropfixed in 4% PFA overnight, dehydrated in 30% sucrose, embedded in O.C.T. (Tissue Tek) and 18 µm sections were prepared on a Microm HM560 cryostat (Thermo Scientific). For assessment of the cellular composition of the embryonic cortex by immunofluorescent stainings, antigen retrieval was performed using 1x DAKO antigen retrieval solution (s1699) and immunofluorescent staining was performed as outlined above. The following primary antibodies were used: anti-Cux1 (Santa Cruz, sc-13024, 1:500), anti-Ctip2 (Abcam, ab18465, 1:500), anti-cleaved Caspase3 (Cell Signaling, 9661, 1:300), anti-Sox2 (Millipore, AB5603, 1:200). Analysis of Cux1/Ctip2 cell distributions at P0 was performed by counting the relative number of Cux1+ and Ctip2+ cells in each of 10 bins (bin height adjusted to cortical thickness, bin width 200 µm) in the cortex, normalized to the total number of positive cells in the respective region (n= at least 3 littermate mice per genotype, at least 4 images/animal).

BrdU based birthdate labeling for migration and proliferation analysis: For cell cycle analysis, pregnant mice were injected with 0.1 mg/g bromodeoxyuridine (BrdU) at E14.5 and E16.5 and sacrificed 2 hours later; embryos were decapitated and processed for immunostaining as described above. Cells in S-phase that incorporated BrdU were detected using anti-BrdU (BioRad, MCA2060T, 1:500). The number of BrdU+ cells was manually counted in cortical regions of 200 µm width in blinded images (n= 3 littermate animals per genotype, at least 5 images/animal). For migration analysis, pregnant females were injected with BrdU at E16.5, as described elsewhere [305]. Upon delivery (P0), pups were decapitated and tissue was processed for immunostaining as outlined above. For migration analysis, sections were stained with anti-BrdU (BioRad, MCA2060T, 1:500), and anti-Ctip2 (Abcam, ab18465, 1:500) antibodies. The P0 cortex was divided into ten bins of the same size and the relative number of BrdU+ nuclei per bin counted manually in blinded images (n= at least 3 littermate mice per genotype, at least 5 images/animal).
Imaging: Images from immunofluorescent stainings were acquired on a Zeiss LSM800 inverted confocal microscope, background corrected and adjusted for contrast and brightness, as well as analyzed in Fiji [306] using the cell counter plugin.

Nissl staining: For Nissl staining, brains from perfused adult animals were post-fixed in 4% PFA overnight, dehydrated and paraffin embedded. Sagittal and coronal sections were cut on a Microtome HM 355 at 10 µm thickness. For Nissl stainings in newborn mice, pups were decapitated at P0, brains dissected, dropfixed in 4% PFA, dehydrated in sucrose, embedded in O.C.T and cut at 18 µm on a cryostat. Nissl staining with 1% Cresyl Violet solution (Cresyl Violet Acetate, Sigma, Cat.No C 5042) was performed upon clearance of paraffin slices with RotiHistol (Carl Roth) for 10 min and rehydration of sections (absolute EtOH to water: 96%,

90%, 70%, 50%, 30%, water, 3-5 min each), or 3x 5 min washes in 1x PBS to remove the OCT. Nissl stainings of adult and P0/P1 brains were captured using a Olympus Slide scanner VS120 and analyzed using Fiji.

Golgi staining and analysis: Golgi-Cox staining was performed according to protocol using the FD Rapid GolgiStain KitTM (FD Neurotechnologies). After three weeks of Golgi impregnation, brains were cut coronally (120 µm) using a Leica Vibratome (Leica VT 1200S) and mounted onto 1% gelatin-coated slides. Slides were then dehydrated through graded ethanol steps, cleared with RotiHistol (Carl Roth) and mounted with DPX mounting medium on coverslips (#1.5). To quantitatively analyze pyramidal neurons in Golgi-stained slides, impregnated pyramidal cells (8-10 neurons per brains, n= 3 littermate brains per genotype) of layer 2/3 in the somatosensory cortex were selected and imaged with a Nikon Eclipse Ti2 using a 40x magnification. For analysis, single pyramidal neurons were manually reconstructed using Imaris analysis software (version 9.3.1). The average filament area, filament length and Sholl intersections were analyzed using the same software. Spine counting was performed using Fiji, spines that started from 100 µm distance of the apical dendrite were counted within a 100 µm segment.

**Golgi staining, imaging and analysis was performed by Lena A. Schwarz, IST Austria.*

LC-MS/MS/MS whole proteome analysis

Samples: Adult male *Cul3*$^{+/-}$ and *Cul3*$^{+/+}$ wild type littermate animals (n(cortex and hippocampus)= 4 littermate mice/genotype, n(cerebellum)= 5 littermate mice per genotype)) were deeply anesthetized and transcardially perfused with 15 ml of ice-cold 0.9% NaCl to clear the brain from blood. The cortex, hippocampus and cerebellum were rapidly dissected on ice, snap-frozen in liquid nitrogen and stored at -80° until protein extraction. Embryonic E16.5 forebrain tissue (developing cortex and hippocampus; male embryos n(constitutive)= 5 mice/genotype, n(Emx1Cre conditional)= 3 mice/genotype) was dissected on ice, meninges were removed and snap-frozen in liquid nitrogen and stored at -80° until protein extraction. Tissues were homogenized 1:5 (w:v) in modified RIPA buffer (50 mM Tris-HCl pH 7.5, 150 mM NaCl, 1% NP40, 0.5% Sodium deoxycholate, 0.1% SDS, 1mM EDTA, 10mM NaF) and freshly added protease and phosphatase inhibitors (Roche 04 693 159 001 and 04 906 837 001) and lysed for 30-45 min on ice, while occasionally being vortexed gently. Each sample was sonicated twice at 180 W in an ice-cold water bath and centrifuged at 10.000 rpm for 20 min at 4°C. Lysates were quantified using the Pierce™ BCA Protein Assay Kit (Thermo Fisher, Cat. no. 23225).

TMT Labeling and High pH reversed-phase chromatography: Aliquots of 100 µg of each sample were digested with trypsin (2.5 µg trypsin per 100 µg protein; 37°C, overnight), labeled with Tandem Mass Tag (TMT) 11plex reagents according to the manufacturer's protocol (Thermo Fisher Scientific, Loughborough, LE11 5RG, UK) and pooled. For the adult

dataset, where the number of samples exceeded the number of available TMT channel, one combined TMT sample was generated for each tissue. Pooled samples were evaporated to dryness, re-dissolved in 5% formic acid and then desalted using a SepPak cartridge according to the manufacturer's instructions (Waters, Milford, Massachusetts, USA). Eluate from the SepPak cartridge was again evaporated to dryness and re-dissolved in buffer A (20 mM ammonium hydroxide, pH 10) prior to fractionation by high pH reversed-phase chromatography using an Ultimate 3000 liquid chromatography system (Thermo Scientific). In brief, the sample was loaded onto an XBridge BEH C18 Column (130Å, 3.5 µm, 2.1 mm X 150 mm, Waters, UK) in buffer A and peptides eluted with an increasing gradient of buffer B (20 mM Ammonium Hydroxide in 90% acetonitrile, pH 10) from 0-95% over 60 min. The resulting fractions were evaporated to dryness and redissolved in 1% formic acid prior to analysis by nano-LC MSMS using an Orbitrap Fusion Lumos mass spectrometer (Thermo Scientific).

Nano-LC Mass Spectrometry: High pH RP fractions were further fractionated using an Ultimate 3000 nano-LC system in line with an Orbitrap Fusion Lumos mass spectrometer (Thermo Scientific). In brief, peptides in 1% (V/V) formic acid were injected onto an Acclaim PepMap C18 nano-trap column (Thermo Scientific). After washing with 0.5% (V/V) acetonitrile 0.1% (V/V) formic acid, peptides were resolved on a 250 mm × 75 µm Acclaim PepMap C18 reverse phase analytical column (Thermo Scientific) over a 150 min organic gradient, using 7 gradient segments (1-6% solvent B over 1min., 6-15% B over 58min., 15-32%B over 58min., 32-40%B over 5min., 40-90%B over 1min., held at 90%B for 6min and then reduced to 1%B over 1min.) with a flow rate of 300 nl min−1. Solvent A was 0.1% formic acid and Solvent B was aqueous 80% acetonitrile in 0.1% formic acid. Peptides were ionized by nano-electrospray ionization at 2.0 kV using a stainless steel emitter with an internal diameter of 30 µm (Thermo Scientific) and a capillary temperature of 275°C.
All spectra were acquired using an Orbitrap Fusion Lumos mass spectrometer controlled by Xcalibur 4.1 software (Thermo Scientific) and operated in data-dependent acquisition mode using an SPS-MS3 workflow. FTMS1 spectra were collected at a resolution of 120,000, with an automatic gain control (AGC) target of 200,000 and a max injection time of 50 ms. Precursors were filtered with an intensity threshold of 5,000, according to charge state (to include charge states 2-7) and with monoisotopic peak determination set to Peptide. Previously interrogated precursors were excluded using a dynamic window (60s +/-10ppm). The MS2 precursors were isolated with a quadrupole isolation window of 0.7 m/z. ITMS2 spectra were collected with an AGC target of 10,000, max injection time of 70 ms and CID collision energy of 35%. For FTMS3 analysis, the Orbitrap was operated at 50,000 resolution with an AGC target of 50,000 and a max injection time of 105 ms. Precursors were fragmented by high energy collision dissociation (HCD) at a normalized collision energy of 60% to ensure maximal TMT reporter ion yield. Synchronous Precursor Selection (SPS) was enabled to include up to 5 MS2 fragment ions in the FTMS3 scan.

Peptides Identification and TMT Reporter Quantitation: Acquired raw data files were processed and quantified using Proteome Discoverer software v2.1 (Thermo Scientific) and searched against the UniProt *Mus musculus* database (downloaded November 2018: 81925 sequences) using the SEQUEST algorithm. The raw files from the embryonic and adult samples were processed in two separate batches. For each, peptide precursor mass tolerance was set at 10 ppm, and MS/MS tolerance was set at 0.6 Da. Search criteria included oxidation of methionine (+15.995) and phosphorylation of serine, threonine or tyrosine (+79.966) as variable peptide modifications and carbamidomethylation of cysteine (+57.021) and the addition of the TMT mass tag (+229.163) to peptide N-termini and lysine as fixed modifications. Acetylation (+42.011) and Met-loss + Acetylation (-89.030) were included as possible modifications to the protein N-terminus. Searches were performed with full tryptic digestion and a maximum of 2 missed cleavages were allowed. The reverse database search option was enabled and all data was filtered to satisfy false discovery rate (FDR) of 5%.

Statistical Data Analysis: PSMs tables exported from Proteome discoverer were reprocessed in R using in house scripts. PSM reporter intensities were scaled by integrated precursor MS1 peak intensities and normalized (Levenberg-Marquardt procedure) across TMT channels, then summed across fractions for each peptidoform (peptide in a specific modification state). The resulting peptidoform expression matrix was then renormalized across samples using VSN normalization followed by the Levenberg-Marquardt procedure. In addition, the combined embryonic dataset was batch-corrected against the litter effect using the ComBat function from the SVA package (batch correction was skipped for the adult dataset as PCA analysis revealed only minor litter effects within tissues, and correcting for TMT batch would have removed tissue-specific variation, since each TMT sample was tissue specific). Peptidoforms were assembled into protein groups, and protein groups-level expression values calculated from those of individual peptidoforms using an in-house weighted average function (using inverse peptidoform posterior error probability as weights), excluding phosphorylated peptides and their unmodified counterpart form. Average expression values and ratios were calculated for each condition, and an F-test performed using the limma package. For both, embryonic and adult datasets, P-value significance thresholds were calculated for a pre-agreed false discovery rate level of 20 % (Benjamini-Hochberg procedure). As a second filtering step, regardless of P value, ratios were also not considered if the absolute value of their base-2 logarithm did not exceed a threshold calculated as excluding all but the 5% most extreme ratios between individual controls. For functional annotation clustering, proteins found significant for a particular condition were mapped to GO terms using the DAVID Bioinformatics Resources 6.8 online tool (done for proteins at 20% FDR, GO- terms filtered for $p < 0.01$, Benjamini adjusted p-values are reported for significantly enriched terms).

**TMT-labeling and LC-MS/MS/MS as well as peptide identification was performed at the University of Bristol Proteomics Facility, Bristol, UK under supervision of Dr. Kate Heesom. Statistical Data Analysis was performed by Dr. Armel Nicolas, IST Austria.*

Western blots

Littermate embryonic and adult animals (at least n= 3 per genotype) were decapitated, the brain was dissected on ice, snap frozen in liquid nitrogen and stored at -80°C until protein extraction. Tissues were homogenized in ice-cold RIPA buffer (50 mM Tris-HCl pH 7.5, 150 mM NaCl, 1% NP40, 0.5% Sodium deoxycholate, 0.1% SDS, 1mM EDTA, 10 mM NaF) and freshly added protease inhibitors (Roche), lysed for 45 min on ice and centrifuged at 10.000 rpm for 20 min at 4°C. Lysates were quantified using the Pierce™ BCA Protein Assay Kit (Thermo Fisher, Cat. no. 23225).

For Western Blots, 25-50 µg of proteins were mixed with 6X Laemmli buffer (375 mM Tris pH=6.8, 12% SDS, 60% glycerol, 600 mM DTT, 0.06% bromophenol blue), heat-denatured at 95°C and separated on 8-10% SDS-PAGE gels in running buffer. Proteins were transferred to a PVDF membrane (Merck) using transfer buffer in a Western blotting apparatus (Bio-Rad) for 2 h at 4°C with 300 mA constant current. The membranes were then blocked with 5% milk in 1x TBST for 1h at room temperature and incubated with primary antibodies overnight at 4°C. Secondary anti-IgG antibody coupled to horseradish peroxidase (HRP) was detected using a PierceTM enhanced chemiluminescent substrate (ThermoFisher) on a GE Healthcare Amersham machine. The following primary antibodies were used: anti-Cul3 (1:800, Cell Signaling #2759), anti-Gapdh (1:1000, Merck ABS16), anti-Pls3 (T-Plastin 1:500, Thermo Fisher PA5-27883), anti-Pls3 (T-Plastin 1:1000, Proteintech 12917-1-AP), anti-Pls1 (1:500, Novus Biologicals H00005357-M04), anti-alpha internexin (1:5000, Abcam ab40758), anti-Nischarin B3 (1:200, Santa Cruz sc-365364), anti β-actin (1:5000, Sigma A1978). Secondary antibodies used: donkey anti-rabbit IgG (1:5000, Amersham NA934), goat anti-mouse IgG (1:10000, Pierce 31432), goat anti-rabbit IgG (1:5000, Goat Dianova 111-035-045) and goat anti-mouse (1:5000, Goat Dianova 111-035-146).

RNA isolation and quantitative real time PCR (qRT-PCR) analysis

Tissue from E12.5, E14.5, E16.5, P1, P21 and adult C57BL6/J brains was used for wild type expression analysis. Tissue from *Cul3*$^{+/-}$ and wild type E16.5 embryos was used to validate up-regulated proteins identified through proteomic analyses. For RNA extraction 700 µL Trizol (Invitrogen) and 140 µL chloroform (Sigma) was used for homogenization, followed by centrifugation at 12,000 x g for 15 min at 4°C. The upper aqueous phase was transferred to a new tube and 1.5 volumes of 100% ethanol (EtOH) were added. RNA was extracted using Zymo-Spin™ IC columns (Zymo Research). In short, the aqueous phase/ethanol mixture was loaded onto the column, washed with 400 µl 70% EtOH before being treated with RQ1 DNAseI (Promega, 5 µl + 5 µl reaction buffer + 40 µl 70% EtOH) for 15 min at RT. After two washes with 70% EtOH the sample was eluted from the column with DEPC-treated H2O. RNA concentration was measured by using the NanoDrop spectrophotometer (Thermo Scientific).

500 ng of RNA were used for cDNA preparation with the RevertAid First Strand cDNA Synthesis Kit (Thermo Fisher). cDNA was diluted 1:3 and used for qPCR analysis with Lightcycler 480 Sybr green master mix (Roche) on a Real-Time PCR Roche Lightcycler 480 machine. Samples were run in duplicates or triplicates with the following intron-spanning qPCR primers for target genes: Cul3 forward: AAGGTGGTGGAGAGGGAACT and reverse TCAAACCATTTGGCACACGAC; Pls3 forward TCTAGAAGGGGAAACTCGGG and reverse GGATCACCAGAGCATCCTGC; Pls1 forward CCATGCCTACACAAGCCTGA and reverse GCGTCTGCAAGGTCACTGTA; INA forward CCAGGCACGTACCATTGAGAT and reverse CAATGCTGTCCTGGTAGCCG. As housekeeping genes Pgk1 (forward AAAGTCAGCCATGTGAGCACT and reverse ACTTAGGAGCACAGGAACCAAA) and Gapdh (forward AACGGGAAGCTCACTGGCAT and reverse GCTTCACCACCTTCTTGATG) were used. ΔCq expression levels (relative mRNA) were calculated upon normalization to housekeeper genes and plotted.

Region/Cell-type specific expression of Cul3

Brain-region specific RNA-seq data (as RPKM) were downloaded from the BrainSpan Atlas of the Developing Human Brain (http://www.brainspan.org/static/download.html). For the developmental trajectory, prefrontal cortex samples (DFC, MFC and VFC) were selected and the expression of *CUL3* was plotted for time points up to 1 year of age. For the brain region specific expression adult samples (starting at 18 years of age) were grouped according to region. After selection, the data was plotted as mean across samples with individual dots representing individual samples.

Cell-type specific data from scRNA-seq experiments and aggregated by cluster (as log2(CPM+1)) was downloaded from the Allen Cell Types Database (https://portal.brain-map.org/atlases-and-data/rnaseq, mouse: “Cell Diversity in the Mouse Cortex and Hippocampus”, human: “Cell Diversity in the Human Cortex”). Clusters were grouped according to broad cell type based on description and hierarchical relationship of the clusters and data was plotted as mean across clusters with individual dots representing individual clusters of the same broad cell type. Some clusters of rare cell types were omitted from the mouse data to simplify the plot.

**Data Analysis was performed by Christoph P. Dotter, IST Austria.*

Electrophysiology

Brain slices were obtained from *Cul3*$^{+/-}$ and wild type male littermates. Acute coronal slices (300 µm) were prepared from primary somatosensory cortex. Animals were decapitated under isoflurane anesthesia and whole brains were rapidly removed from the skull and sectioned using a VT 1200S vibratome (Leica Microsystems) in ice-cold cutting solution, containing (mM): 93 NMDG, 2.5 KCl, 1.2 NaH2PO4, 30 NaHCO3, 20 HEPES, 25 glucose, 5 sodium ascorbate, 2 thiourea, 3 sodium pyruvate, 10 MgCl2, 0.5 CaCl2 (320 mOsm, 7.2-7.4 pH). Slices were recovered at 32˚C for 12 min in the same solution and then allowed to recover

at room temperature for at least 1 hour in regular artificial cerebrospinal fluid (ACSF), containing (mM): 125 NaCl, 2.5 KCl, 1.25 NaH2PO4, 25 NaHCO3, 25 glucose, 1 MgCl2 and 2 CaCl2 (320 mOsm, 7.2–7.4 pH). The ACSF was continuously oxygenated with 95% O2 and 5% CO2 to maintain the physiological pH. Slices were visualized under infrared-differential interference contrast (IR-DIC) using a BX-51WI microscope (Olympus) with a QIClickTM charge-coupled device camera (Q Imaging Inc, Surrey, BC, Canada).
Patch pipettes (3–5 MΩ; World Precision Instruments) were pulled on a P-1000 puller (Sutter Instruments) and filled with the intracellular recording solution, containing (mM): 115 cesium methanesulphonate, 8 NaCl, 10 HEPES, 0.3 EGTA, 10 Cs4BAPTA, 4 MgATP, 0.3 NaGTP and 0.2% biocytin. Internal pH was adjusted to 7.3 with CsOH and osmolarity adjusted to 295 mOsm with sucrose. Spontaneous postsynaptic currents were recorded from pyramidal neurons in layer 2/3. Excitatory currents (sEPSC) were recorded at holding potential -70 mV, while inhibitory currents (sIPSC) at +10 mV. Signals were filtered at 2 kHz, digitized at 10 kHz and acquired using a MultiClamp 700B amplifier and a Digidata 1550A. Recorded signals were low-pass filtered at 1 kHz and analyzed using Clampfit 10 software (Molecular Devices). Both excitatory and inhibitory synaptic currents were identified by a template created for each neuron using 50-100 single events for each trace. All events recognized through the template were visualized, identified and accepted by manual analysis. Cumulative distributions for single neurons and recording conditions were obtained by pooling together 300–400 single synaptic currents.

**Electrophysiological recordings and data analysis was performed by Bernadette Basilico, IST Austria.*

Generation and culture of neural progenitor cells

Neural progenitor cells (NPCs) were generated from E13.5 mouse cortices. Briefly, cortical tissues were dissected in L15 medium (Sigma cat. nr. L5520). The tissue was dissociated using Accutase (Sigma cat. nr. A6964) for 5 min at 37°C, pelleted in basal media, re-suspended in complete media and cells plated in uncoated dishes. The next day, cells were dissociated using Accutase, pelleted and re-suspended in complete media and pooled according to their genotype (*Cul3*$^{+/+}$ and *Cul3*$^{+/-}$ NPC) for primary neurosphere formation. Two independent NPC batches were prepared and analyzed. For adherent NPC cultures, dishes were coated with 10 µg/ml Poly-L-ornithine (PLO) (Sigma cat. nr. P3655) and Laminin (3mg/ml Sigma cat. nr. L2020) and approximately 15.000 cells/cm^2 were plated. 1x10^6 cells were frozen per freezing vial using a freezing medium containing basal medium, DMSO and fetal bovine serum (FBS) (8:1:1). Composition of media: Basal medium: 1x DMEM/F12 (Gibco cat. nr. 32500-350), 2 mM Glutamax (Gibco cat. nr. 35050061), 15 mM HEPES (Sigma cat. nr. H0887), 2% D-Glucose (Sigma cat. nr. G879), Sodium bicarbonate (Sigma cat. no. S8761), 100X Penicillin/ Streptomycin (Sigma cat. nr. P4333) in sterile water. Complete medium: Basal media plus freshly added 20 ng/ml human recombinant EGF (R&D cat. nr. 236-EG) and 10 ng/ml human

recombinant bFGF (R&D cat. nr. 233-FB-025), B27TM Supplement minus VitA (Gibco cat. nr. 12587010).

**NPCs were generated by visiting scientist Dr. Emanuele Cacci and Lisa Knaus, IST Austria.*

***In vitro* migration assay and live cell imaging**

For *in vitro* migration assays, NPCs were dissociated using Accutase for 5 min at 37°C, pelleted in basal media and re-suspended in complete media. Two thousand cells were seeded per well in U-bottom 96-well ultralow attachment plates (Corning), assembled into neurospheres overnight (14-16 hours). Healthy neurospheres (defined by smooth and bright surface) were embedded under glass cover slips in 30 µl of hanging drops of 3D collagen scaffold with a final concentration of 1.7 mg/ml (obtained by mixing bovine collagen (PureCol, Advanced BioMatrix, USA) in 1X minimum essential medium eagle and 0.4 % sodium bicarbonate (both Sigma-Aldrich, USA). Collagen was let to polymerize at 37°C with 5% CO2 and humidity for 1 hour. Next, dishes were flipped around and a second layer of collagen was added on top and let polymerize for another 1 hour. Devices were covered with complete media and imaged using a 10x objective on a brightfield inverted microscope at 37°C with 5% CO2 for 72 hours every 10 min. Calibrated time course TIFF stacks were created in Fiji. Individual cells were tracked manually by an experimenter blinded to the genotype employing the Fiji plugin TrackMate [307]. Cells were chosen randomly from all sites of the sphere at the moment of their detachment and tracked until either re-joining the growing spheres or until the end of the recording. TrackMate data was then imported into R (3.6.2) environment and analyzed. The track velocity (track displacement / track duration) of detaching cells, their average instantaneous speed (average of all displacements per frame duration), track path length (sum of all displacements between frames) and persistence (track displacement / track path length) were quantified by TrackMate and with R. Finally, results were plotted with the help of ggplot2 (3.2.1), ggpubr (0.2.4) packages.

Alternatively, an adapted neurosphere migration assay was used (Schaffer et al., 2018). Spheres were embedded centrally in 40 µl of 5 mg/ml matrigel (Corning cat. nr. 356234) diluted in ice-cold basal media on PLO/Laminin coated clear bottom 96-well imaging plates (Corning cat. nr. 3603), one sphere per well. After 30 min polymerization of the matrigel at 37°C, complete media was added to the wells and images were captured using a 4x objective on a brightfield inverted microscope, to determine initial sphere sizes. Neurospheres too close to the well-border were excluded from analysis. 22 and 46 hours after embedding, radial outgrowth of NPCs from the sphere was imaged using a 4x objective on a brightfield inverted microscope and the distance (radius) from the center of the neurospheres was measured in Fiji and normalized to the initial sphere radius.

**Live-cell imaging and analysis was performed in collaboration with Saren Tascyian, IST Austria.*

B16-F1 cell culture conditions and *Pls3* knockout line generation

B16-F1 (ATCC® CRL-6323TM) mouse melanoma cells were cultivated according to standard tissue culture conditions. Cells were grown at 37°C in 5% CO2 in DMEM - high glucose (Gibco cat. nr. 11965092), GlutaMAX™ Supplement (Gibco cat. nr. 35050061), Pyruvate (Thermo Scientific) and 10% FBS (#10270-106, Thermo Scientific), 100X Penicillin/ Streptomycin (Sigma cat. nr. P4333).

Generation of *Pls3* knockout cell line using CRISPR/ Cas9: Generation of knockout cell lines was performed as previously described [308]. For the generation of Pls3 knockout cell lines (*Pls3* KO), CRISPR/ Cas9 guide design was performed using http://crispr.mit.edu by choosing a guide sequence targeting exon 3 of *Pls3*: 5'-TATCGCTAAAACCTTCCGAA-3'. The following forward and reverse oligo sequences were cloned into a pSpCas9(BB)-2A-Puro (PX459) (Addgene plasmid ID: 48138) using BbsI-mediated restriction: 5'-CACCGTATCGCTAAAACCTTCCGAA -3' and 5'- AAACTTCGGAAGGTTTTAGCGATAC -3'. The genomic DNA sequence flanking exon 3 of the *Pls3* target sequence was amplified using Phusion High-Fidelity Polymerase (NEB). Genotyping for the *Pls3* knockout allele was performed using the following primers: forward ATGCAGCACTGAATGTGTTTGG and reverse ACCAATATGTGACCCAAGACCC. Amplified DNA sequence was cloned into a Zero blunt TOPO vector (Invitrogen) according to manufacturer instructions and sequenced using the following primer: forward CAGGAAACAGCTATGAC. Clones with frameshift mutations causing stop codons downstream of the target site were selected for further characterization (Pls3 KO). Absence of Pls3 was also confirmed via Western blot.

Random migration assay: B16-F1 cells were seeded on #1.5H polymer µ-Slide 4 Well Ph+ coverslips (ibidi GmbH, Germany), which were coated with 30 µg/ml laminin (L-2020; Sigma-Aldrich) in 50 mM Tris, pH 7.4, and 150 mM NaCl buffer for 1 hour at room temperature. Brightfield time-lapse images were acquired with a 20x objective on an inverted Nikon Ti2 microscope at 37°C with 5% CO2 for 15 hours every 10 min.

**Generation of Pls3 knockout B16-F1 cells and random migration assay and analysis was performed by Georgi Dimchev, IST Austria.*

STED microscopy

Dual color labeling of neural progenitor cells (NPCs) for actin and tubulin: NPCs were seeded at a confluency of 70% on #1.5H glass coverslips coated with PLO/Laminin (Marienfeld, Lauda-Königshofen, Germany). After ~12 – 14 hours they were fixed with 4% paraformaldehyde in PBS for 15 min at room temperature (RT) followed by 3 x 2 min in PBS. Permeabilization was performed with PBS + 0.25% Triton X-100 (Sigma-Aldrich) for 10 min at RT followed by 3 x 2 min in PBS. Cells were blocked with 2% BSA (AppliChem GmbH, Darmstadt, Germany) in PBS for 30 min at RT and then incubated with anti-α-tubulin antibody (T6074, Sigma-Aldrich; 1:1000 in blocking solution) for 1 hour at RT. Samples were washed 3 x 3 min in PBS at RT. Incubation with secondary antibody and simultaneously with SiR-actin was done in blocking solution at RT for 1 hour (SiR-actin, SC001, Spirochrome, Switzerland, 1:500; goat anti-mouse

IgG, conjugated to Alexa Fluor 594, Invitrogen A11005, 1:500). Samples were washed 3 x 3 min in PBS at RT and then incubated with DAPI (D9542, Sigma-Aldrich; 1:5000) in PBS at RT for 5 min. Samples were washed 3 x 2 min in PBS, then mounted with Dako Fluorescence Mounting Medium (S3023, Agilent Technologies).

STED microscopy: STED imaging was performed on an Abberior Instruments Expert Line STED microscope. STED wavelength was 775 nm and excitation was performed at ~560 nm and ~640 nm. A 100x/1.4 NA oil immersion objective (Olympus, UPLSAPO 100XO) was used. STED pulses had a duration of ~1 ns and time gating was applied throughout. Resolution was increased in the xy-direction with a "doughnut" shaped beam and in the z-direction with an additional z-STED pattern according to the power ratio given below. Power levels are given as power at the back aperture of the objective lens with an estimated uncertainty of ~15%.

Imaging parameters:

Fig. 19b top *Cul3*$^{+/+}$: STED: pixel size 30 nm x 30 nm; pinhole size 1 Airy Unit; Excitation laser powers: 560 nm: 5.4 µW; 640 nm: 2.9 µW; STED: 90 mW with lateral/axial STED power ratio 75/25. Pixel dwell time: 15 µs with 2 scans per line for 560 nm excitation and 4 scans per line for 640 nm excitation.

Fig. 19b bottom *Cul3*$^{+/-}$: STED: pixel size 30 nm x 30 nm; pinhole size 1 Airy Unit; Excitation laser powers: 560 nm: 2.3 µW; 640 nm: 6.2 µW; STED: 90 mW with lateral/axial STED power ratio 75/25. Pixel dwell time: 15 µs with 2 scans per line for 560 nm excitation and 4 scans per line for 640 nm excitation.

Fig. 19e top *Cul3*$^{+/+}$: STED: pixel size 30 nm x 30 nm; pinhole size 1 Airy Unit; Excitation laser powers: 560nm: 5.4 µW; 640 nm: 2.9 µW; STED: 90 mW with lateral/axial STED power ratio 75/25. Pixel dwell time: 15 µs with 2 scans per line for 560 nm excitation and 4 scans per line for 640nm excitation.

Fig. 19e bottom *Cul3*$^{+/-}$: STED: pixel size 30 nm x 30 nm; pinhole size 1 Airy Unit; Excitation laser powers: 560 nm: 2.3 µW; 640 nm: 6.2 µW; STED: 90 mW with lateral/axial STED power ratio 75/25. Pixel dwell time: 15 µs with 2 scans per line for 560 nm excitation and 4 scans per line for 640nm excitation.

**NPCs staining and STED-microscopy was performed in collaboration with Caroline Kreuzinger, IST Austria.*

Orientation analysis: The orientation of actin and tubulin fibers was analyzed in custom-written Python routines using the scikit-image library (van der Walt et al., 2014) (ver. 0.16.2). We extracted the orientation distributions based on the structure tensor. The structure tensor summarizes local orientations and their coherence (degree of anisotropy) at each image location [309]. For each image of size 30 µm x 30 µm with pixel size 30 nm x 30 nm (1000 pixel²), we first normalized the raw photon counts from 16-bit integers to values in the range [0, 1] by subtracting the minimum gray value, followed by dividing with the maximum. From the structure tensor computed at Gaussian scale σ=60 nm (2 pixel), we extracted local

orientations, coherency, and energy (i.e. image gradient magnitude). Coherence yields values of 1 when the local structure is totally aligned, and 0 when there is no preferred direction. The energy measures the magnitude of the local structure (gradient). The resulting orientations were visualized in the hue, saturation, and brightness (HSB) color-space, where we set hue as the orientation angle, saturation as coherency and brightness the normalized gray-value of the source image. The distribution of orientations was built as the histogram of orientations weighted by the corresponding coherency. Image locations with a coherence or energy less than 10% of their maximum value were excluded from the histogram. Each orientation histogram was aligned to the corresponding dominant orientation angle computed from the tubulin channel. The dominant orientation is computed as the average orientation angle inside the cell. Each cell was segmented manually prior to analysis.
After alignment, we averaged all orientation histograms per group (*Cul3*$^{+/+}$, n= 43; *Cul3*$^{+/-}$, n= 43, from three independent NPC preparations respectively) and computed 95% confidence intervals per orientation angle. To test statistical significance, we measured the spread of each orientation distribution as the standard deviation of angles weighted by their occurrences. Reported p-values were computed using a two-tailed Welch's t-test using the scipy library (ver.1.3.0).

Adhesion site analysis: Adhesion sites in the actin channel were analyzed in custom-written Python routines using the scikit-image library. Each cell was segmented manually prior to analysis. For each image of size 30 µm x 30 µm with pixel size 30 nm x 30 nm (1000 pixel²), we first normalized the raw photon counts from 16-bit integers to values in the range [0, 1] by subtracting the minimum gray value, followed by dividing with the 99.9th percentile. We counted the number of adhesion sites per cell as the number of local maxima in the scale-space of a series of Laplacian of Gaussian (LoG) filters [310]. A LoG filter with scale σ is a high-pass filter with a strong response at bright, blob-like structures of radius √2σ. We computed a series of 5 LoG filters for σ = 3, 4, 5, 6, and 7 pixel (90, 120, 150, 180, and 210 nm). A local maximum was considered an adhesion site if it exceeded a threshold of 0.25 in the LoG filter response. To exclude detection at the cell boundary we removed adhesion sites closer than 1 µm from the manually segmented cell boundary. To compute the density of adhesion sites, we divided the number of detected adhesion sites by the area of the cell. To test statistical significance we used a two-tailed Welch's t-test using the scipy library (ver 1.3.0).

**STED-image analysis was performed by Dr. Christoph Sommer, IST Austria.*

Tamoxifen induced *Cul3* deletion

To induce *Cul3* deletion in adult animals double transgenic mice, *Cul3*$^{+/fl}$, *Cul3*$^{+/fl}$ *Cag-CreER* (Cag-CreER line: Jackson 04453), were injected intraperitoneally with Tamoxifen (Sigma T5648) (100 mg/kg body weight, 10 mg/ml stock solution in corn oil) or vehicle (corn oil). Animals, aged P30-P40, were injected for five consecutive days and behavior tests were performed >21 days post (last) injection (animals age P55-P65) to ensure successful

recombination, protein degradation and Tamoxifen (and its metabolites) clearance, as previously described [311]. Behavioral tests were performed as described above. After behavioral tests, animals were sacrificed, the brain dissected and the right hemisphere was used for tissue lysis and western blot analysis to determine Cul3 protein levels and success of Tamoxifen induced deletion. As described previously [312], in 5%–20% of mice treated with Tamoxifen, induction appeared to fail altogether, and no changes on Cul3 protein levels could be observed. These mice, and their corresponding control littermates, were excluded from analysis.

Statistics

Statistical analyses were performed using Microsoft ® Excel ® 2013, Origin Software (Origin Inc.) and GraphPad Prism 6/8. Shapiro–Wilk test was used to evaluate normal distribution, means and standard deviations of the data. Parametric data were analyzed for significance using unpaired two-tailed t-tests, 1¬ way or 2 way ANOVAs with Sidak's post-hoc test, using *$P < 0.05$, **$P < 0.01$, and ***$P<0.001$ for significance, and presented as bar, box and whiskers, scatter dot plots and mean ± standard error of the mean (SEM), unless otherwise specified. Data sets with non-normal distributions were analyzed using the two-tailed Mann-Whitney U test. Adjustment for multiple comparisons were made using post-hoc tests. Cumulative probability plots of the amplitude and inter-event interval of synaptic currents were compared with the Kolmogorov-Smirnov two-sample test. Experiments were replicated at least three times.

Accession code

The mass spectrometry proteomics data have been deposited to the ProteomeXchange Consortium via the PRIDE [313] partner repository with the dataset identifier PXD017040.

4.3. Results

4.3.1. Behavioral defects in *Cul3* haploinsufficient animals

To analyze ASD-linked mutations, we employed a heterozygous *Cul3* knockout (*Cul3*$^{+/-}$) mouse line, generated by crossing *Cul3* floxed mice (*Cul3*^{fl}) [294] with a CMV-Cre expressing line. Consequently, the loxP-flanked region, including exons four to seven, was excised and a constitutive *Cul3*$^{+/-}$ line was established through back-crossing with C57BL6J wild-type animals (Fig. 9a). As predicted, *Cul3*$^{+/-}$ animals show a significant decrease in Cul3 protein in the brain, to approximately 50% of wild-type levels (Fig. 9a). Importantly, Cul3 protein reduction is equal in all brain areas tested (Fig.9b), thus resembling patients with germline mutations and *CUL3* haploinsufficiency.

Although *Cul3* heterozygous mice have a slightly reduced body weight at birth and in adolescence, their weight is comparable to control animals as adults (Fig. 9c). However, the brain to body weight ratio is unaffected in mutant newborns and adults (Fig. 9d).

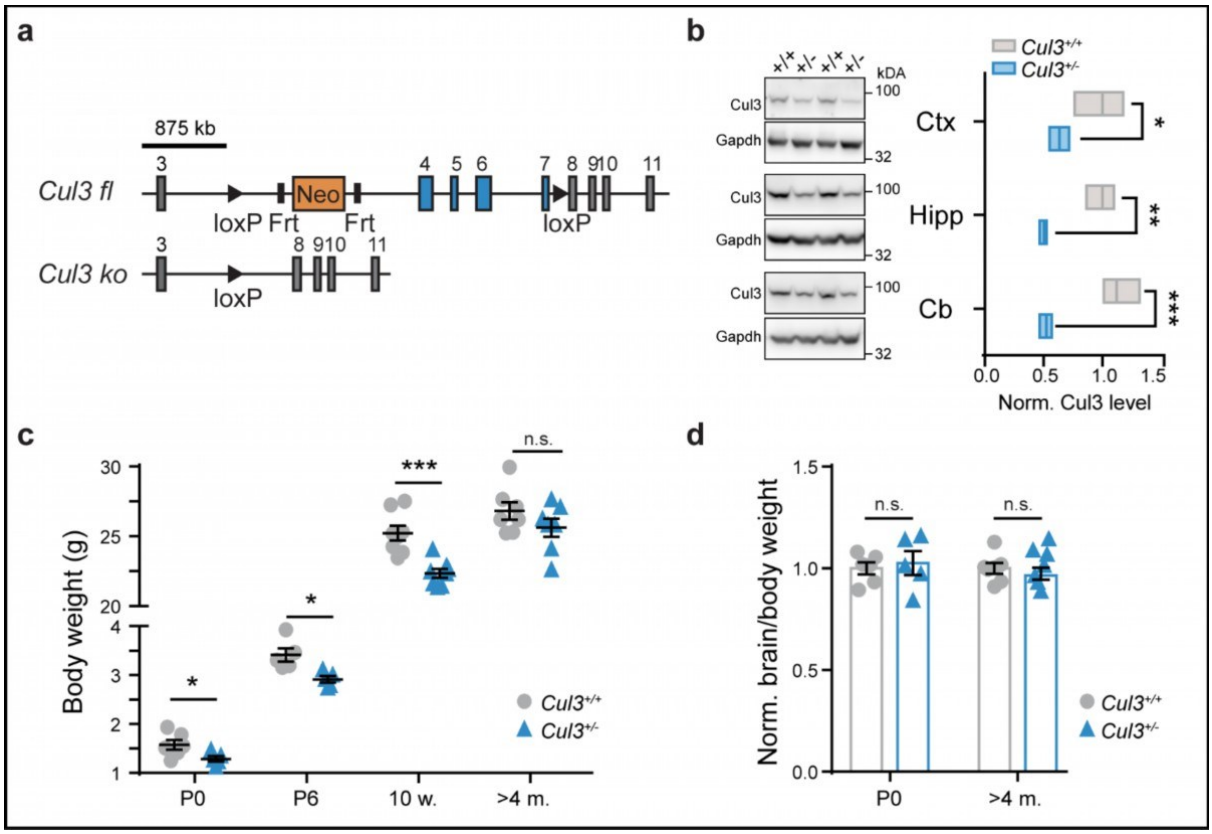

Figure 9: The conditional *Cul3* allele and its deletion in mice. a, Scheme of the conditional *Cul3* allele in mice in which exons 4-7 are flanked by two loxP sites (*Cul3*^{fl}). Cre-mediated recombination leads to genomic excision of the flanked region resulting in the *Cul3* knockout (*Cul3*^{ko}) allele. **b**, Representative Western blots and analysis of adult cortex (Ctx), hippocampus (Hipp) and cerebellum (Cb) reveal significantly decreased Cul3 levels in all brain regions of *Cul3*$^{+/-}$ mice (*n*= 3 per genotype; *P<0.05, **P<0.01, ***P<0.001; unpaired two-tailed t-tests). **c**, *Cul3*$^{+/-}$ mice are born with reduced body weight as compared to their wild-type littermates, a growth defect persisting until early adulthood (P6 and 10 weeks), but recovered at 4 month of age (*n*(P0, P6, 10w., 4m.)= 6, 5, 8, 7 per genotype respectively; *P<0.05, ***P<0.001, n.s. not significant; unpaired two-tailed t-tests). **d**, Brain to body

weight ratios, normalized to control littermates are normal at P0 and 4 month of age (*n*(P0, 4m.)= 6, 7 per genotype; n.s. not significant; unpaired two-tailed t-tests). Data is presented as mean ± SEM.

Adult *Cul3*$^{+/-}$ mice present with hindlimb clasping (Fig. 10a) and mild gait abnormalities, such as increased sway and stance length (Fig. 10b,c and Supp. Fig. 1a,b), phenotypes which are observed also in other ASD mouse models [209, 314] and indicative of cerebellar dysfunctions [315]. Further in line with motor defects, *Cul3*$^{+/-}$ mice underperform when challenged on the accelerating RotaRod (Fig. 10d,d' and Supp. Fig. 1c,c'), a task requiring formation and consolidation of a repetitive motor routine [316, 317]. Male, but not female, *Cul3* haploinsufficient mice show reduced initial coordination compared to their wild-type littermates (Fig. 10d' and Supp. Fig. 1c'). In addition, mutant mice of both sexes do not reach the same level of motor performance as their healthy counterparts by the end of the third day of trials, suggesting motor learning impairments (Fig. 10d and Supp. Fig. 1c). Motor defects of *Cul3*$^{+/-}$ mice, however, do not affect their exploratory behavior in the open field (Supp. Fig. 1d), where they travel the same distance and at the same speed as the controls. Exploration of the open arm on the elevated plus maze is also not affected: *Cul3*$^{+/-}$ animals do not show differences in anxiety-like behaviors (Supp. Fig. 1e).

Next, we subjected *Cul3*$^{+/-}$ animals to classical sociability tests in the three-chamber assay. During this paradigm, mice are first habituated to a three chambered maze, with two wire cages in the outermost chambers. Then, a stranger wild-type mouse, sex and age matched to the test mouse, is placed into one wire cage, whereas an object of similar size and shape is put into the second one. In the last phase of the test, the object is replaced with a second, stranger mouse. Automatic tracking allows the quantification of the time the test mouse is exploring either of the two wire cages, serving as a proxy for social interest and memory. In the three-chamber test, similarly to wild types, *Cul3*$^{+/-}$ mice show a preference for a mouse (M1) over an object (Ob.) (Fig. 10e). However, in the second phase of the assay, mutant mice show no preference for a stranger mouse (M2) over a familiar animal (M1), a preference displayed by control animals (Fig. 10f). We thus concluded that haploinsufficiency of the *Cul3* gene is associated with reduced social memory.

Social recognition is mainly achieved via olfaction in rodents [318, 319]. Therefore, we assessed the ability of mutant animals to distinguish and familiarize with non-social and social odors. In the odor discrimination and habituation test (ODHD) [304], both wild-type and *Cul3*$^{+/-}$ animals successfully recognize newly and already presented odors (Table S1). However, mutant mice spend significantly more time exploring odor-embedded cotton swabs, and are hyper-reactive to the presentation of social odors (Fig. 10g; Table S1). Thus, despite mutant animals spending significantly more time sniffing social odors than controls, *Cul3*$^{+/-}$ mice are able to distinguish between two different social odors, indicating that defects in social memory are not directly related to odor discrimination issues.

Finally, we employed a well-established memory test [320] to assess how *Cul3* haploinsufficiency affects learning. Contextual fear conditioning (CFC) is a paradigm in which

mice learn to associate a novel context with the delivery of an aversive stimulus in the form of a mild electric foot shock. CFC revealed normal fear acquisition and memory retention in *Cul3*$^{+/-}$ mice. However, mutant animals exhibit reduced ability to extinguish the aversive memory after extinction training, pointing towards abnormal cognition (Fig. 10h,h').

In summary, our analysis indicates that *Cul3* haploinsufficiency leads to abnormalities in several behavioral paradigms. The observed behavioral defects may be associated with dysfunction of different brain areas and/or dysfunctional brain connectivity.

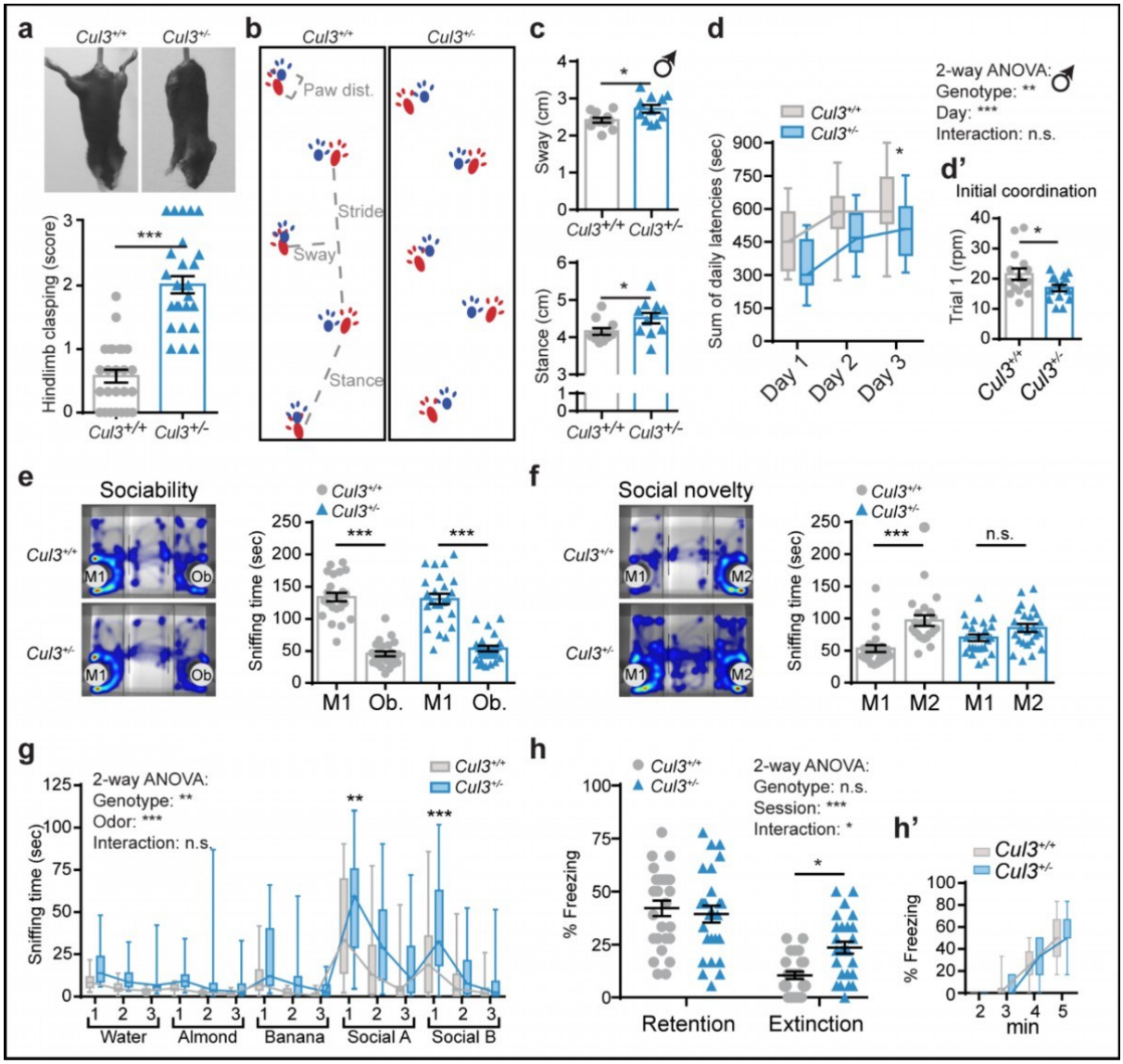

Figure 10: Behavioral defects in *Cul3* haploinsufficient mice. a, Hindlimb clasping in adult *Cul3*$^{+/-}$ mice, not observed in controls (top); scoring from 0-1 (normal) to 3 (most severe) (bottom, *n*= 25 mice, females (*n*= 11) and males (*n*= 14), per genotype; ***P<0.001; two-tailed Mann-Whitney U-test). **b**, Representative strides of *Cul3*$^{+/+}$ and *Cul3*$^{+/-}$ mice, forepaws in blue and hindpaws in red. **c**, Altered gait of *Cul3*$^{+/-}$ male mice: inter-genotype comparison of sway (top) and stance length (bottom) (*n*= 11 males per genotype; two-tailed Mann-Whitney U test or two-tailed t-test). **d**-**d'**, Accelerating RotaRod test revealing defects in motor learning and coordination in *Cul3*$^{+/-}$ mice. Shown are the sum of daily latencies of three trials per day on three consecutive days (d) and the final rpm on day one - trial 1, as measure of initial coordination (d') (*n*= 15 males per genotype; 2way ANOVA and Sidak's multiple comparison test and unpaired two-tailed t-test). Female data in Supp. Fig. 1. **e**-**f**, Heat maps

of the three-chamber social interaction test (left) and quantification of interaction times (right). Sociability: *Cul3*$^{+/-}$ and control mice spend more time with a stranger mouse (M1) than an object (Ob.) (e); Social novelty: *Cul3*$^{+/-}$ mice do not prefer a novel stranger (M2) over the familiar mouse (M1) (f) (*n*= 24 mice, females (*n*= 11) and males (*n*= 13), per genotype; 1way ANOVA and Sidak's multiple comparison test). **g**, Both genotypes distinguish and familiarize to non-social and social odors in the olfaction habituation and dishabituation test, yet *Cul3*$^{+/-}$ mutants are hyper-reactive to the presentation of social odors (*n*= 24 mice, females (*n*= 11) and males (*n*= 13), per genotype; 2way ANOVA and Sidak's multiple comparison test; details in Table S1). **h**-**h'**, Contextual fear-conditioned memory retention and extinction scored as percent freezing during a 3 min exposure to the context (h), and fear acquisition training (h') (*n*= 26 mice, females (*n*= 7) and males (*n*= 19), per genotype; 2way ANOVA interaction: (F1,100)= 6.18 p= 0.015; Sidak's multiple comparisons test: Extinction p= 0.027). Adult littermate animals were analyzed. Data presented either as mean ± SEM, as well as scatter plot (a,c,d',e,f,h) or as box and whiskers, min. to max., (d,g,h'). Significance levels: *P<0.05, **P<0.01, ***P<0.001, n.s. not significant;

4.3.2. Expression of *Cul3* in wild-type tissue

To understand when and where *Cul3* is predominantly expressed under normal conditions, we investigated Cul3 protein and mRNA levels in wild-type mouse tissues and explored available RNA sequencing (RNAseq) datasets from human post-mortem tissues for *CUL3* mRNA levels (Fig. 11).

In the mouse brain, *Cul3* expression is highest during embryonic development at E14.5 and E16.5, time-points at which neurogenesis and neural migration are peaking respectively (Fig. 11a,b). Spatially, in the adult, it is predominantly expressed in the cortex and hippocampus (Fig. 11c), and on a cellular level, in prefrontal cortex, in glutamatergic excitatory and GABAergic inhibitory neurons (Fig. 11d). These data are in line with the *CUL3* expression profile in humans. In the human brain expression peaks during early gestation and *CUL3* mRNA levels can predominantly be detected in neuronal cells, both excitatory and inhibitory, while it is less expressed in the glial linages (Fig. 11e-g).

Taken together, the expression profiles point towards an important role for *Cul3* during early brain development, as well as in the neuronal cell linages.

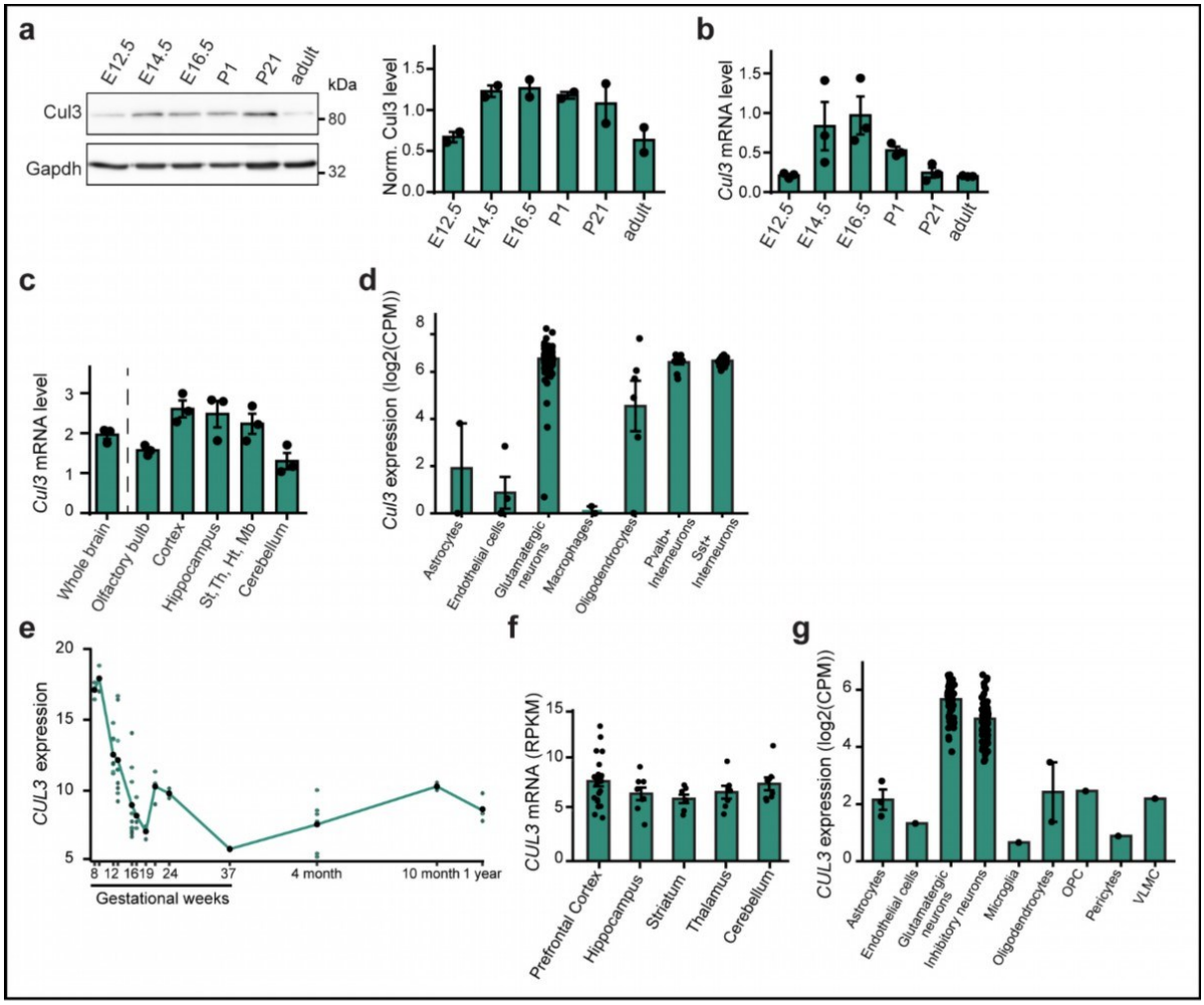

Figure 11: *Cul3* expression peaks during early development in both, mouse and humans. a, Western blot and quantification of E12.5, E14.5, E16.5, P1, P21 and adult brain lysates of C57BL/6J wild-type animals show highest Cul3 protein levels during developmental time-windows important for brain development (*n*(pooled tissue)= 3 animals per time point, *N*(WB)= 2). **b**-**c**, Quantitative real-time PCR analysis of *Cul3*, in brain development (b) and in adult brain regions (c) of C57BL/6J wild-type animals, confirms expression peaks during E14.5 and E16.5 and in cortex and hippocampal tissue. Lower *Cul3* levels were observed in the olfactory bulbs and the cerebellum (St= Striatum, Th= Thalamus, Ht= Hypothalamus, Mb= Midbrain) (*n*(tissue*)*= 3 animals, *N*(qPCR)= 3; ΔCq expression values are plotted). **d**, Normalized *Cul3* expression across cell types in the adult mouse prefrontal cortex based on data from the Allen Cell Types Database [https://portal.brain-map.org/atlases-and-data/rnaseq]. Data points indicate individual cell type clusters that were aggregated for this analysis. **e**, *CUL3* expression in cortical samples across human development based on data from the BrainSpan Atlas [http://www.brainspan.org/static/download.html]. X-axis shows age and y-axis shows expression in RPKM. Data points indicate individual samples. **f**, *CUL3* expression in RPKM across regions of the adult human brain based on data from the BrainSpan Atlas [http://www.brainspan.org/static/download.html]. Data points indicate individual samples. **g**, Normalized *CUL3* expression across cell types in the adult human brain based on data from the Allen Cell Types Database [https://portal.brain-map.org/atlases-and-data/rnaseq]. Data points indicate individual cell type clusters that were aggregated for this analysis. Data is presented as mean ± SEM.

4.3.3. *Cul3* haploinsufficiency is associated with abnormal brain development

Considering that the *Cul3* expression profiles, both in mouse and humans, point to an early developmental function of Cul3 and to understand whether the behavioral defects are accompanied by neuroanatomical changes, we performed crystal violet (Nissl) stainings of

adult coronal and sagittal brain sections obtained from *Cul3* heterozygous and wild-type mice (Fig. 12a-c and Supp. Fig. 2). Gross brain morphology appears normal but we observed a slight reduction in cortical thickness and cerebellar area (Fig. 12a,c and Supp. Fig. 2b'',b'''). To investigate this neuroanatomical phenotype more closely, we stained the somatosensory cortex for Cux1 (upper layers 2/3) and Ctip2 (lower layers 5/6) (Fig. 12d-g). Quantifications in adult mice revealed that the *Cul3* heterozygous mutation results in a mild decrease in upper and lower cortical layer thickness (Fig. 12e), a defect present already at birth (Fig. 12g). In addition, we found that the distribution of Cux1 and Ctip2 positive (Cux1+ and Ctip2+) cells is shifted toward lower cortical locations, indicative of abnormal cortical lamination (Fig. 12h).

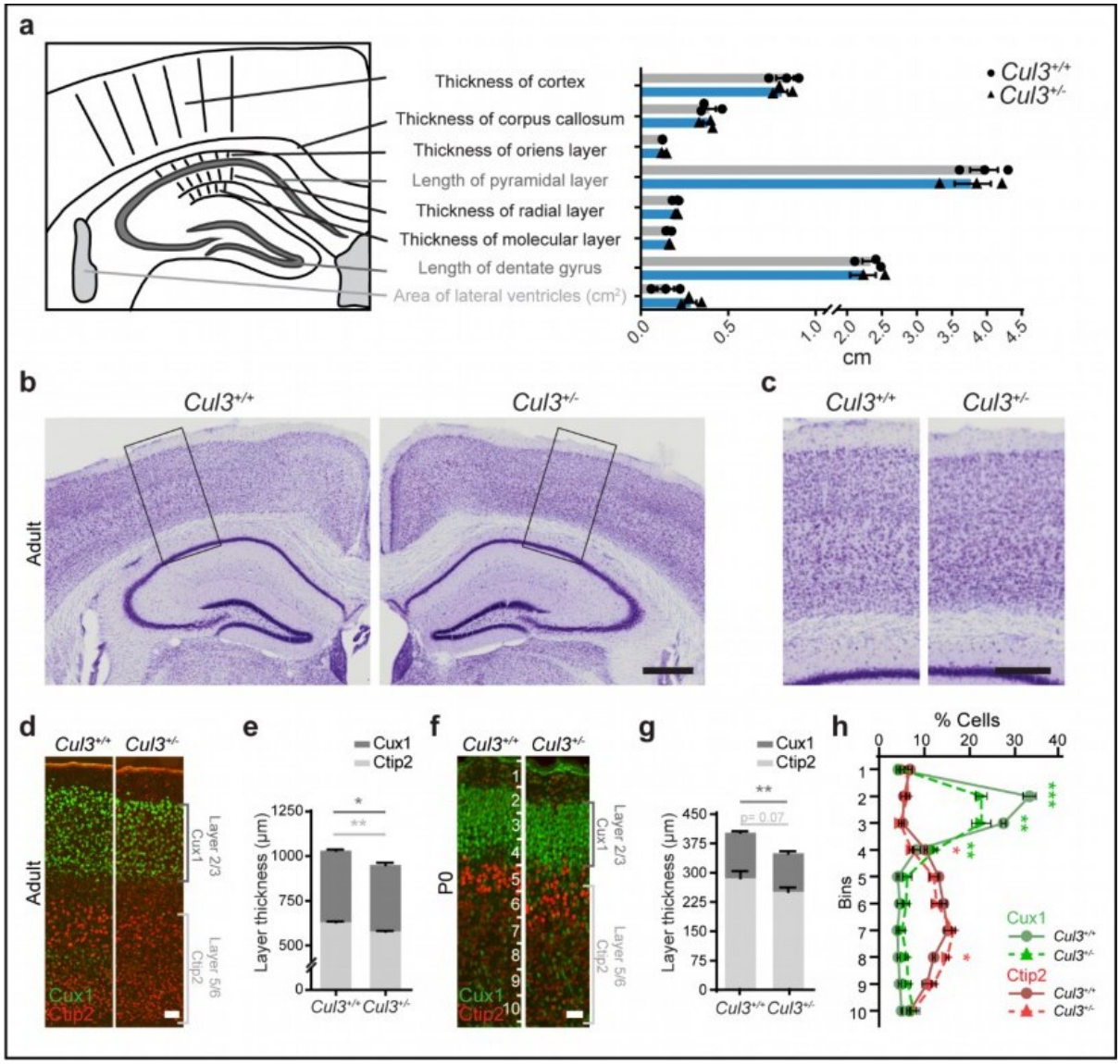

Figure 12: Abnormal lamination of the somatosensory cortex in *Cul3* mutant mice. a, Scheme of coronal forebrain sections and the measured brain features in adult *Cul3*$^{+/-}$ and *Cul3*$^{+/+}$ littermates revealed no differences between genotypes (*n*= 3 mice per genotype; unpaired two-tailed t-tests). **b**-**c**, Representative Nissl stainings of coronal forebrain sections in mutant and wild-type mice, analyzed in (a) and close-ups of cortical columns in boxed regions in (c), a slight reduction in cortical thickness can be observed. **d**-**h**, Immunofluorescent stainings for Ctip2 and Cux1 on coronal brain sections revealed laminar thinning in adults (d,e) and newborn (P0)

Cul3$^{+/-}$ animals (f,g) (*n*(adults)= 3 mice per genotype; *n*(P0)= 6 pups per genotype; 2way ANOVA and Sidak's multiple comparison test). **h**, Bin-wise comparison of relative cell numbers (%) revealed a shifted Cux1/Ctip2 layer profile, indicating laminar defects at P0 (*n*= 3 pups per genotype; 2-way ANOVA, Sidak's multiple comparison test). Data presented as mean in (a), stacked bar-plots of mean in (e,g) ± SEM and connected mean ± SEM in (h). Scale bars: 500 µm in (b), 250 µm in (c), 50 µm in (d) and 25 µm in (f); numbers in (f) indicate depth in the cortex. Significance levels: *P<0.05, **P<0.01, ***P<0.001, n.s. not significant;

We reasoned that complete loss of *Cul3* could exacerbate this phenotype and give us indications about additional *Cul3* deficiency-associated defects. Since constitutive homozygous deletion of *Cul3* is embryonically lethal, we crossed conditional *Cul3* animals with an *Emx1-Cre* expressing line, generating forebrain specific heterozygous and homozygous deletions of *Cul3* (*Cul3*$^{+/fl}$ *Emx1-Cre and Cul3*$^{fl/fl}$ *Emx1-Cre* respectively), with a strong reduction of Cul3 protein levels in cortical tissues of the latter (Fig. 13a,b). Importantly, *Emx1*-driven *Cre*-expression starts at E10.5 [321], thus inducing *Cul3* deletion at the beginning of forebrain development in radial glia progenitor cells. While *Cul3*$^{+/fl}$ *Emx1-Cre* mice are viable and fertile, like *Cul3*$^{+/-}$ animals, *Cul3*$^{fl/fl}$ *Emx1-Cre* pups are much smaller than controls (Fig. 13c) and die before weaning. In addition, *Cul3*$^{fl/fl}$ *Emx1-Cre* mice show severe brain malformations with pronounced cortical and hippocampal atrophy (Fig. 13d,e). Similar to what we observed in *Cul3*$^{+/-}$ animals, fluorescence imaging of Cux1 and Ctip2 distribution revealed lamination defects in *Cul3*$^{fl/fl}$ *Emx1-Cre* and *Cul3*$^{+/fl}$ *Emx1-Cre* mice (Fig. 13f-h). Thus, proper *Cul3* dosage is essential to guarantee correct brain development in mouse.

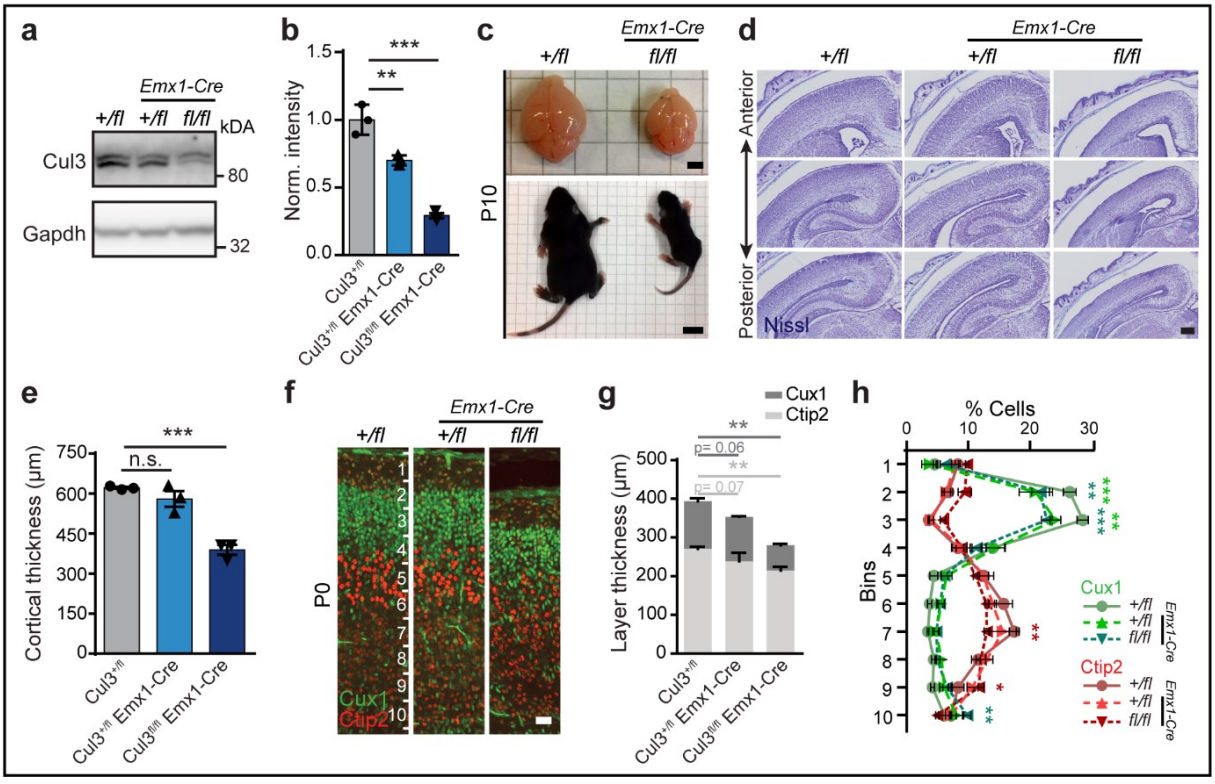

Figure 13: Severe brain malformations in *Cul3*$^{fl/fl}$ *Emx1-Cre* mice and lamination defects. a-b, Western blot (a) and quantification (b) of *Cul3*$^{+/fl}$, *Cul3*$^{+/fl}$ *Emx1-Cre* and *Cul3*$^{fl/fl}$ *Emx1-Cre* E16.5 brain lysates shows a strong

reduction of Cul3 levels in conditional homozygous embryos (*n*= 3 littermate embryos per genotype; **P<0.01, ***P<0.001; 1way ANOVA and Sidak's multiple comparisons test). **c**, Representative images of ten day-old *Cul3$^{fl/fl}$ Emx1-Cre* pups showing that mutant animals are much smaller than their *Cul3$^{+/fl}$* control littermates. While hindbrain regions are comparable, forebrain structures are severely reduced in size in the conditional homozygous animals. **d**, Nissl-staining of P0 coronal, *Cul3$^{+/fl}$*, *Cul3$^{+/fl}$ Emx1-Cre and Cul3$^{fl/fl}$ Emx1-Cre* brain sections shows severe brain malformations in *Cul3$^{fl/fl}$ Emx1-Cre* pups. **e**, Cortical thickness measured in Nissl stainings of coronal brain sections from *Cul3$^{+/fl}$*, *Cul3$^{+/fl}$ Emx1-Cre* and *Cul3$^{fl/fl}$ Emx1-Cre* newborn pups (P0), show severe cortical thinning in the latter (*n*= 3 pups per genotype; ***P<0.001, n.s. not significant; 1way ANOVA and Sidak's multiple comparisons test). **f**-**h**, Immunofluorescent stainings against Ctip2 and Cux1 reveal cortical laminar thinning in both *Cul3$^{+/fl}$ Emx1-Cre and Cul3$^{fl/fl}$ Emx1-Cre* pups and bin-wise comparison of relative cell numbers show a shifted Cux1/Ctip2 layer profile at P0 (*n*= 3 pups per genotype; 2-way ANOVA, Sidak's multiple comparison test). Littermate animals were analyzed. Data presented as mean in (b,e) or stacked bar-plots of mean in (g) ± SEM and connected mean ± SEM in (h). Scale bars: 2.5 mm in (c, top), 1 cm in (c, bottom), 200 µm in (d) and 25 µm in (f). Significance levels: *P<0.05, **P<0.01, ***P<0.001, n.s. not significant;

4.3.4. Loss of *Cul3* leads to neuronal migration defects in mice

To identify the origin of the anatomical abnormalities observed in *Cul3$^{+/-}$*, *Cul3$^{+/fl}$ Emx1-Cre* and *Cul3$^{fl/fl}$ Emx1-Cre* brains, we studied cell proliferation, apoptosis, and migration in the three different genotypes, focusing on the time window with highest *Cul3* expression (i.e. E14.5-16.5).

First, we injected pregnant females with bromodeoxyuridin (BrdU) at E14.5 and collected the brains of the *Cul3$^{+/fl}$ Emx1-Cre, Cul3$^{fl/fl}$ Emx1-Cre* and control embryos two hours after injection. BrdU is a synthetic nucleoside analog to thymidine and incorporates into the newly synthesized DNA of replicating cells, thereby labeling them permanently. Immunoflourescent staining of E14.5 forebrain sections pointed towards an increase in the number of BrdU positive (BrdU+) cells in *Cul3$^{fl/fl}$ Emx1-Cre* embryos (Fig. 14a). In addition, we observed significantly more cells in M-phase located at the ventricular surface, as identified through stainings against phospho-histone H3 (pH3) (Fig. 14b). In contrast at E16.5, by employing stainings against cleaved caspase3 (cl. Casp3) in *Cul3$^{fl/fl}$ Emx1-Cre* embryos, we found a substantial increase in apoptotic cells in the developing cortex (of which 69.75% ± 1.47 were localized in the ventricular zone), and a corresponding reduction in Sox2+ neural stem cells and cycling BrdU+ cells (after a 2 hours pulse) (Fig. 14c-f).

These observations indicate that homozygous loss of *Cul3* early during brain development initially causes an abnormal increase in cycling progenitor cells at E14.5. Later however, at E16.5, this cell-cycle defect might lead to increased cell death in the VZ and a corresponding reduction in radial glia cell numbers. While these defects most likely account for the severe brain malformations in *Cul3$^{fl/fl}$ Emx1-Cre* pups, we did not observe such anomalies in *Cul3$^{+/fl}$ Emx1-Cre* animals. This is in line with the more severe phenotype observed in *Cul3$^{fl/fl}$ Emx1-Cre* mice and with the cell cycle regulation defects described in *Cul3$^{-/-}$* animals [292].

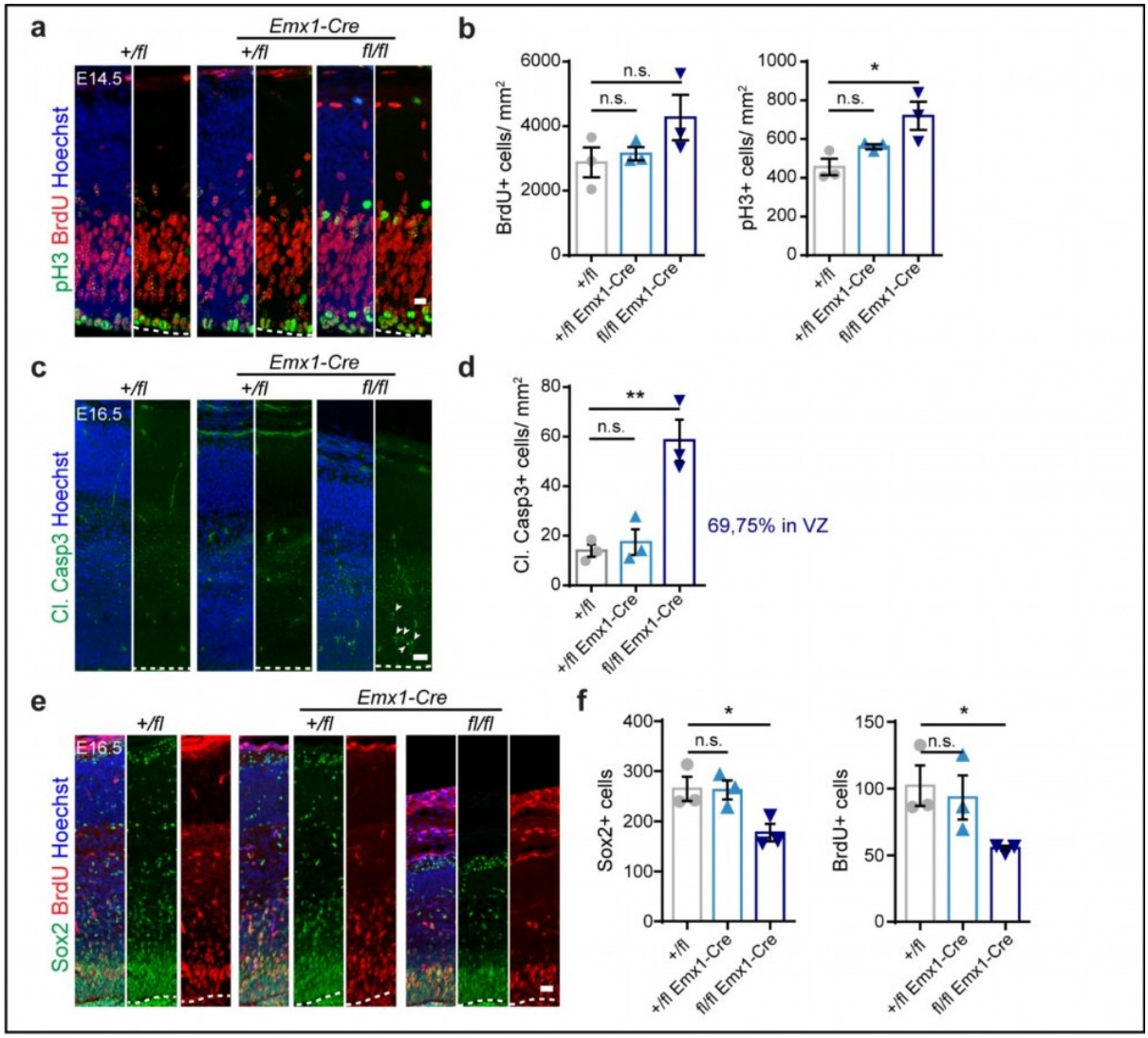

Figure 14: Severe brain malformations in *Cul3$^{fl/fl}$ Emx1-Cre* mice are caused by abnormal cell cycle regulation. **a-b**, Representative images of E14.5 cortical sections of *Cul3$^{+/fl}$*, *Cul3$^{+/fl}$ Emx1-Cre* and *Cul3$^{fl/fl}$ Emx1-Cre* embryos, stained for BrdU+ and pH3+ cells (a) and quantifications (b) (*n*= 3 littermates per genotype; *P<0.05, n.s. not significant; 1way ANOVA and Sidak's multiple comparisons tests). **c**-**d**, Immunofluorescent staining for the apoptotic marker cleaved Caspase3 shows increased cell death in the *Cul3$^{fl/fl}$ Emx1-Cre* E16.5 cortex (arrowheads: cl. Casp3+ cells) (*n*= 3 littermates per genotype; **P<0.01, n.s. not significant; 1way ANOVA and Sidak's multiple comparisons tests). **e**-**f**, Representative images of E16.5 coronal brain sections, stained for the radial glia marker Sox2 and for BrdU incorporation (2 hour pulse) in *Cul3$^{+/fl}$*, *Cul3$^{+/fl}$ Emx1-Cre* and *Cul3$^{fl/fl}$ Emx1-Cre* embryos (e) and quantification (f) (*n*= 3 littermates per genotype; *P<0.05; 1way ANOVA and Sidak's multiple comparisons tests). Data presented as mean ± SEM in (b,d,f). Scale bars: 12.5 µm in (a), and 25 µm in (c,d). Significance levels: *P<0.05, **P<0.01, ***P<0.001, n.s. not significant;

To test whether cell migration is affected in heterozygous and homozygous *Cul3* mutant mice we again pulsed E16.5 embryos with BrdU, but this time analyzed the number and position of BrdU+ cells in the cerebral cortex at P0 (Fig. 15a). We found a severe reduction in BrdU+ cells in *Cul3$^{fl/fl}$ Emx1-Cre* P0 animals compared to control samples from *Cul3$^{+/fl}$* littermates (Fig. 15b), consistent with the abovementioned increase in neural cell apoptosis in *Cul3$^{fl/fl}$ Emx1-Cre* embryos at E16.5. In addition, we found that a substantially smaller fraction of BrdU+ cells reaches the upper cortical layers and that a significant number of BrdU+ cells remain stranded

in lower cortical layers in *Cul3*$^{fl/fl}$ *Emx1-Cre* animals (Fig. 15b,c). These results suggest that complete deletion of *Cul3* in the forebrain leads to neural cell apoptosis and neuronal migration defects. Importantly, while *Cul3*$^{+/fl}$ *Emx1-Cre* samples do not show a reduction in total BrdU+ cells, suggesting normal production and survival of cortical neural cells, *Cul3*$^{+/fl}$ *Emx1-Cre* pups present a clear reduction of BrdU+ cells reaching the upper part of the cortex (Fig. 15b,c). We observed the same defect in the cerebral cortex of constitutive *Cul3*$^{+/-}$ mice (Fig. 15d,e), indicating that *Cul3* haploinsufficiency is associated with a neuronal migration phenotype, thus explaining the observed lamination defects.

Next, since we had predominantly quantified the position of glutamatergic neurons (Fig. 12h, Fig. 13h), we tested whether other cell types in the brain might be similarly affected. To this end, we counted the density of interneurons, astrocytes and microglia in the adult somatosensory cortex. Interestingly, while the number of interneurons in the cerebral cortex is significantly reduced (Fig. 15f), the amounts of astrocytes and microglia are unchanged in *Cul3* mutant animals (Fig. 15g,h). This difference may be explained by the fact that *Cul3* expression is highest in excitatory and inhibitory neurons, potentially making them more susceptible to Cul3-dependent defective protein homeostasis (Fig. 11d,g).

To better understand how *Cul3* mutations affect cell migration, we switched to an *in vitro* model system. Analysis of neural progenitor cells (NPCs) generated from E13.5 *Cul3*$^{+/+}$ and *Cul3*$^{+/-}$ cortices (Supp. Fig. 3a) confirmed abnormal cell motility *in vitro* (Fig. 15i-l; Supp. Fig. 3b). Specifically, we traced the movement of NPCs moving away from neurospheres, embedded in matrigel, over the course of several hours and found that *Cul3* mutant cells travel shorter distances than control cells (Fig. 15i,j). In addition, live imaging analysis revealed that mutant NPCs do not migrate far from the sphere, move less and have reduced migration speed, thus indicating that *Cul3* haploinsufficiency is associated with cell intrinsic defects of migration (Fig. 15k,l and Supp. Fig. 3b).

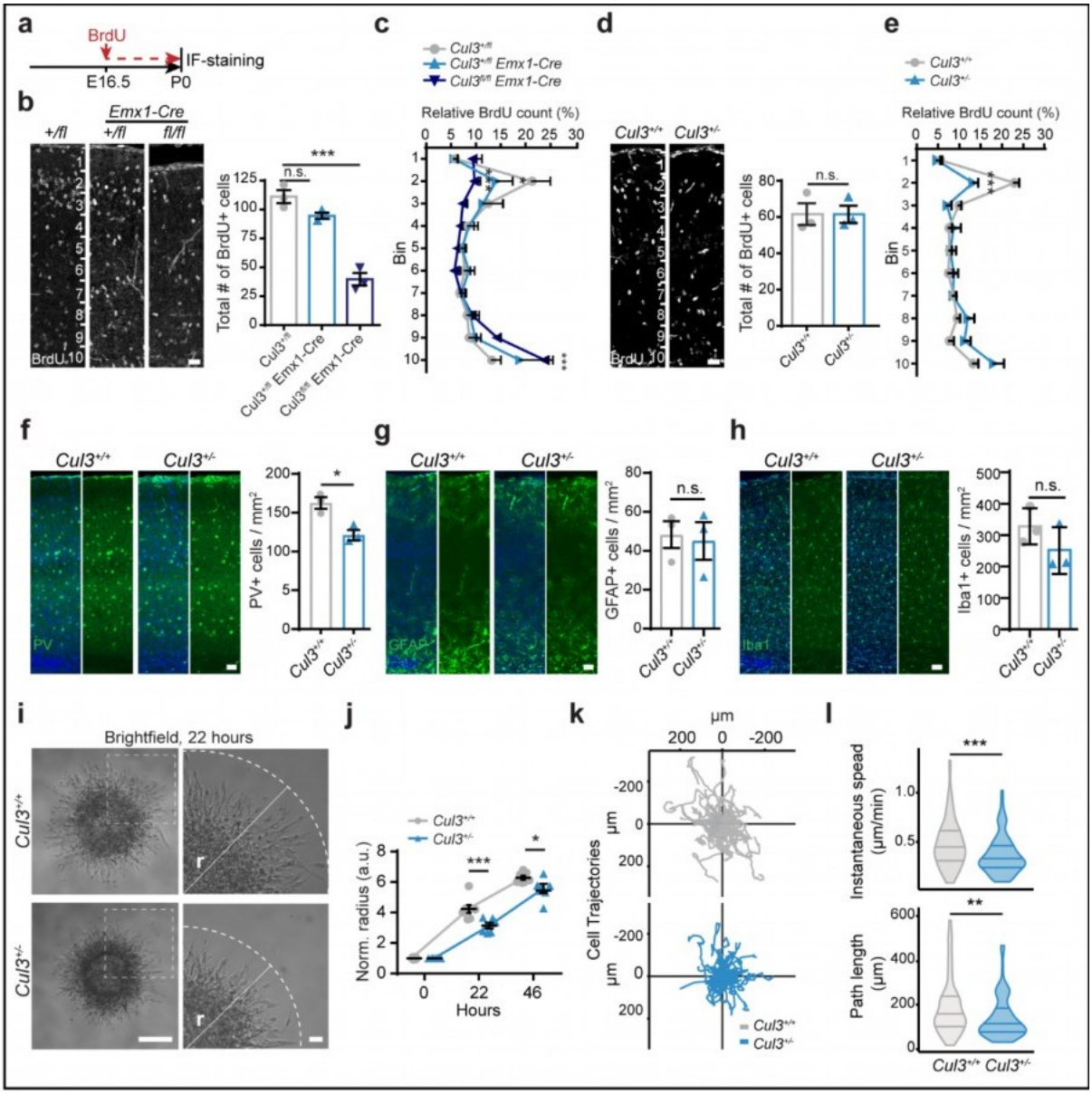

Figure 15: *Cul3* loss leads to migration deficits *in vivo* and *in vitro*. a, Scheme of the BrdU birthdate labeling experiments. **b**-**e**, Injection of BrdU at E16.5 and anti-BrdU immunofluorescent (IF-) stainings and analysis of total BrdU positive (BrdU+) cells in cortical columns at P0 show severe decreased number of BrdU+ cells in *Cul3*$^{fl/fl}$ *Emx1-Cre* brains, but not in the *Cul3*$^{+/fl}$ *Emx1-Cre* (b) and *Cul3*$^{+/-}$ (d) cortex (*n*= 3 littermate pairs pups per genotype; ***P<0.001, n.s. not significant; 1way ANOVA and Sidak's multiple comparison test and unpaired two-tailed t-test). Bin-wise analysis of relative numbers of BrdU+ cells showed decreased numbers of BrdU+ cells in upper bins and increased numbers of BrdU+ cells in lower bins of all mutant genotypes, *Cul3*$^{+/fl}$ *Emx1-Cre, Cul3*$^{fl/fl}$ *Emx1-Cre* (c) and *Cul3*$^{+/-}$ (e) (*n*= 3 littermate pairs per genotype; 2way ANOVA and Sidak's multiple comparison test). **f**-**g**, Representative images and quantification of immunofluorescent stainings against PV+ interneurons and GFAP+ astrocytes in adult coronal cortical sections, showing reduced numbers of PV+ cells (f) but not astrocytes (g) in mutant animals (*n*= 3 littermate pairs per genotype; unpaired two-tailed t-tests). **h**, No difference in the number of Iba1+ microglia in the adult *Cul3*$^{+/-}$ cortex (*n*= 3 per genotype; n.s. not significant; unpaired two-tailed t-test). **i**-**j**, *In vitro* migration assay of matrigel embedded neurospheres generated from *Cul3*$^{+/+}$ and *Cul3*$^{+/-}$ NPCs reveals decreased migratory abilities (r= radius of furthest migrated cell) 22 hours (i, representative images) and 46 hours after plating. Radius was normalized to initial sphere size; (*n*(spheres)= 7/6 *Cul3*$^{+/+}$ and *Cul3*$^{+/-}$ respectively; 2way ANOVA and Sidak's multiple comparison test). **k**-**l**, Cell tracks of *Cul3*$^{+/+}$ and *Cul3*$^{+/-}$ NPCs detaching from the neurosphere into embedding bovine collagen matrix (*n*(spheres)= 3 per genotype, *n*(cells)= 30 per replicate) imaged in a single plane. Cell trajectories of each cell fixed at origin plotted in Euclidean plane (j). Mean instantaneous speed (k, top) and total cell path length (k, bottom) quantification

(Wilcoxon rank sum test). Data presented as mean ± SEM and scatter dot plot in (b,d,f,g,h right and j), connected mean ± SEM in (c,e) or violin plots with median and first and third quartiles (l). Scale bars: 25 µm in (b,d), 50 µm in (f,g,h), 200 µm in (i, overview) and 40 µm in (i, close-up). Significance levels: *P<0.05, **P<0.01, ***P<0.001, n.s. not significant;

4.3.5. *Cul3* haploinsufficiency leads to abnormal neuronal network activity

We reasoned that defects in neural cell migration and cortical lamination could have an important impact on neuronal network activity. Indeed, other ASD-risk genes associated with defects in neuronal migration have been shown to substantially modify neuronal network activity *in vivo* [25]. To this end, we evaluated the spontaneous network activity in two-month old *Cul3*$^{+/-}$ mice, recording spontaneous postsynaptic currents (sPSC) from pyramidal neurons in layer 2/3 of the somatosensory cortex in whole-cell configuration. Both spontaneous excitatory and inhibitory post synaptic currents (sEPSC and sIPSC, respectively) are reduced in mutant animals (Fig. 16a-f). In particular, *Cul3*$^{+/-}$ mice show a strong reduction in sEPSC frequency, evidenced by an increased mean interevent interval (IEI) (Fig. 16c) compared to wild-type littermates. The effect of *Cul3* haploinsufficiency on glutamatergic current amplitudes is not evident from the average peak currents, however, the cumulative distribution shows a shift of sEPSC toward smaller amplitudes (Fig. 16b). On the other hand, GABAergic transmission is less affected. *Cul3*$^{+/-}$ and wild-type mice showed similar sIPSC peak currents even if we notice a slight shift of the cumulative distribution towards higher amplitudes (Fig. 16e) and mean frequency (Fig. 16f). Of note, sIPSC distribution is slightly shifted towards lower frequency (Fig. 16f). To test whether the observed differences in neuronal network activity are due to morphological defects, we performed Golgi stainings and analyzed the morphology of layer 2/3 pyramidal neurons in adult *Cul3*$^{+/-}$ mice (Fig. 16g-i). However, neither the dendritic length, nor the number of dendrites or spines (Fig. 16h), nor dendritic branching (Fig. 16i) are altered in Cul3 haploinsufficient mice. Altogether these results point to a tissue level reduction in network activity and global synaptic transmission, likely linked to the cortical lamination defects in *Cul3*$^{+/-}$ mice.

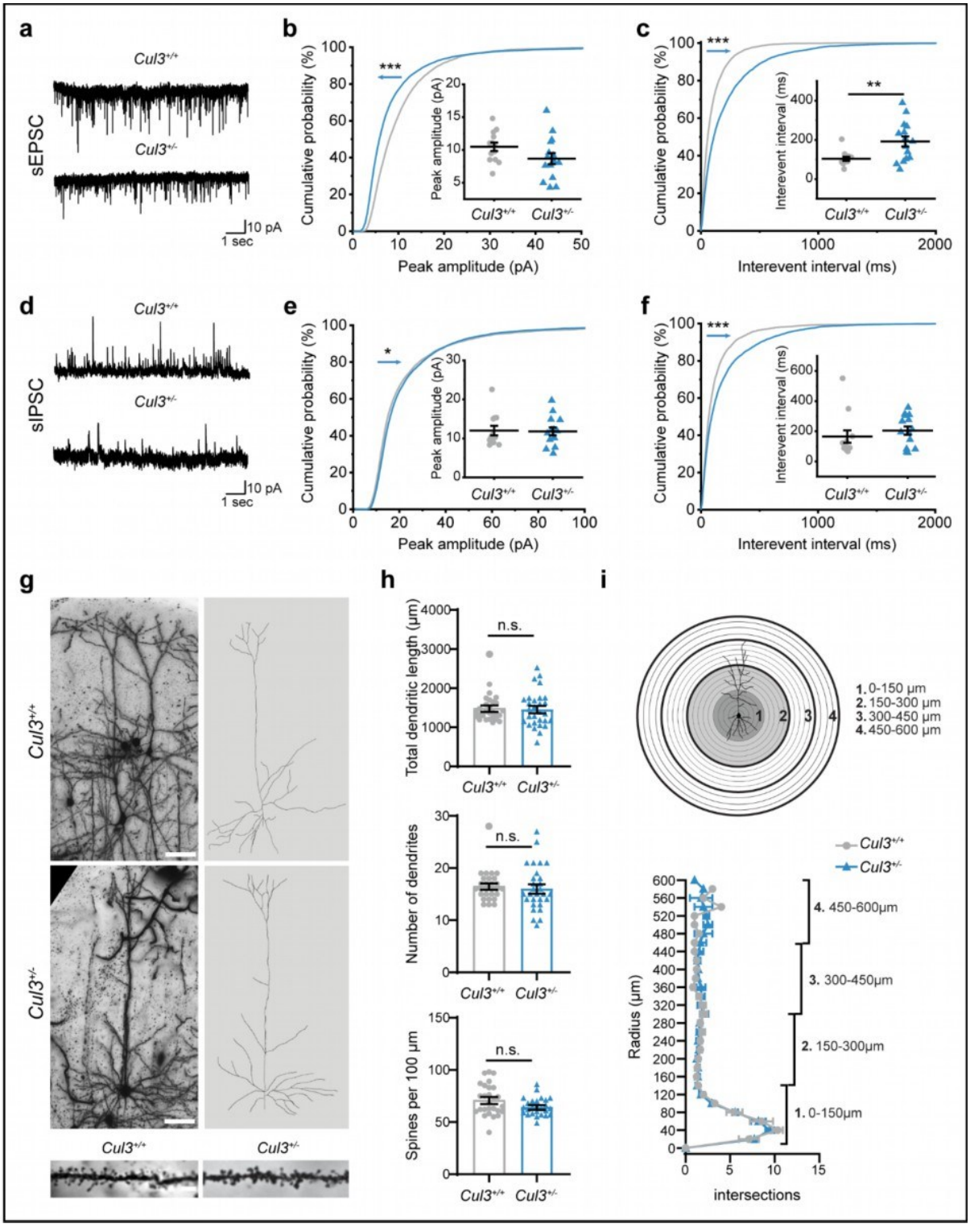

Figure 16: Reduced circuit activity in layer 2/3 pyramidal neurons of adult *Cul3*$^{+/-}$ mice, but normal neuronal morphology. a-c, Representative sEPSC traces, recorded by whole cell patch-clamp, holding potential -70 mV, layer 2/3 neurons in somatosensory cortex (a). Cumulative probability distribution and quantification of sEPSC amplitudes (Kolmogorov-Smirnov test) (b). Cumulative probability distribution and quantification of sEPSC interevent intervals (IEI) (C); (n(*Cul3*$^{+/+}$)= 12 cells, n(*Cul3*$^{+/-}$)= 15 cells from 3 mice respectively; unpaired two-tailed t-test, Kolmogorov-Smirnov test). **d-f**, Representative sIPSC traces recorded at holding potential +10 mV from layer 2/3 neurons in somatosensory cortex (d). Cumulative probability distribution and quantification of sIPSC amplitudes (Kolmogorov-Smirnov test) (e). Cumulative probability distribution and quantification of mean sIPSC IEI (F); (n(*Cul3*$^{+/+}$)= 12 cells, n(*Cul3*$^{+/-}$)= 14 cells from 3 mice respectively; Kolmogorov-Smirnov test). **g-i**, Golgi staining and analysis of the morphology and spine density of layer 2/3 pyramidal neurons in the

somatosensory cortex. Brightfield images (g, left) and Imaris reconstructions (g, right), as well as close-ups of dendrites with spines (g, bottom). Quantification did not reveal any differences in total dendritic length (h, top), number of dendrites (h, center) or spine density (H, bottom) (*n*(cells)= 27-29 from 3 mice per genotype); Sholl analysis was comparable between the mutants and wild-types (i, top- scheme; i, bottom- quantification); (*n*(mice)= 3 mice per genotype, at least 9 cells per animal; unpaired two-tailed t-tests or two-tailed Mann-Whitney U-test). Adult littermate male mice were analyzed. Data is shown as mean ± SEM and scatter plots in (b,c,e,f,h) and connected mean ± SEM in (i). Scale bars: 50 µm in (g, top) and 5 µm in (g, bottom). Significance levels: *P<0.05, **P<0.01, ***P<0.001, n.s. not significant;

4.3.6. Whole proteome analysis reveals abnormal amounts of cytoskeletal proteins in *Cul3* mutant mice

To gain insight into the molecular mechanisms underlying the observed defects, and in view of Cul3's E3 ubiquitin ligase function, we assessed the impact of *Cul3* loss on the global proteome of the developing forebrain in *Cul3*$^{+/-}$, *Cul3*$^{+/fl}$ *Emx1-Cre* and *Cul3*$^{fl/fl}$ *Emx1-Cre* mutants. Protein extracts from dissected E16.5 cortices from control and mutant animals were analyzed by quantitative proteomics (Fig. 17a).

Analysis of the total proteome of *Cul3*$^{+/-}$, *Cul3*$^{+/fl}$ *Emx1-Cre* and *Cul3*$^{fl/fl}$ *Emx1-Cre* mutants, as well as corresponding controls, resulted in the identification of 8100 protein groups. For differential protein expression analysis, protein groups were filtered based on fold change and False Discovery Rate (FDR) thresholds. Employing an FDR threshold of 20% we identified 37 up- and 40 down-regulated proteins in the *Cul3*$^{+/-}$ embryonic cortex (Fig. 17b and Table S2), and 66 up- and 51 down-regulated proteins in the *Cul3*$^{+/fl}$ *Emx1-Cre* embryonic cortex (Fig. 17c and Table S3). As expected from the more severe phenotype of *Cul3*$^{fl/fl}$ *Emx1-Cre* mutant pups, a much larger number of deregulated proteins were identified in conditional homozygous knockout embryos (178 up- and 140 down-regulated proteins, Fig. 17d and Table S4). Overall, and in agreement with previous observations [322-324], the fold changes were mild, in line with the hypothesis that the ubiquitylated isoform of a protein represents only a small fraction of the total pool of that given protein at any time point [325].

The small number of deregulated proteins in the forebrain tissue of *Cul3* haploinsufficient embryos did not justify GO-term enrichment analysis. Therefore, to get an indication of the classes of proteins affected in *Cul3* mutants, we performed GO-term enrichment analysis on the *Cul3*$^{fl/fl}$ *Emx1-Cre* data. We found that deregulated proteins were significantly enriched for DNA-directed RNA polymerase II core complex members and proteins of the proteasome core complex. In addition, deregulated proteins were functionally linked to CNS and forebrain development, the regulation of cell migration, actin- and microtubule-cytoskeleton organization, cell-cell adhesion and apoptosis (Fig. 17e and Table S5). Given the migration phenotype observed in both heterozygous and conditional homozygous *Cul3* mutant animals, we decided to investigate changes in cytoskeletal proteins further and found several of these to be misregulated also in *Cul3*$^{+/-}$ and *Cul3*$^{+/fl}$ *Emx1-Cre* embryonic tissue (Fig. 17b-d, in purple). We annotated these proteins manually, drawing on published literature and focusing on those appearing to follow a dose dependent response to *Cul3* loss, when the mean raw expression levels were fitted to a linear model (*Cul3*$^{+/fl}$ < *Cul3*$^{+/fl}$ *Emx1-Cre* and < *Cul3*$^{fl/fl}$ *Emx1-Cre*) (Fig. 17f-h and Table S6). Several have a putative or a confirmed function in cytoskeletal organization, and/or regulation of cell migration and differentiation. Some down-regulated proteins belong to a family of microtubule-associated proteins linked to abnormal brain development in humans (i.e. Tubb2b, Map2) [326, 327]. However, as Cul3 targets proteins for

degradation, we were most interested in the identified up-regulated proteins, as their up-regulation likely represents a direct consequence of *Cul3* loss. To validate the results obtained by proteomic analysis we selected two of the top up-regulated cytoskeletal-associated proteins observed in both *Cul3*$^{+/-}$ and *Cul3*$^{fl/fl}$ *Emx1-Cre* samples, Plastin 3 (Pls3) and Internexin neuronal intermediate filament protein A (INA) (Table S6), and quantified them by western blot. Indeed, we confirmed that Cul3 deficiency leads to higher amounts of Pls3 and INA in both *Cul3*$^{+/-}$ and *Cul3*$^{fl/fl}$ *Emx1-Cre* E16.5 cortical lysates (Fig. 17i,j). Furthermore, we found that the up-regulation of these proteins is not due to increased gene expression since there were no corresponding increases at the mRNA level (Fig. 17k), but rather to a translational or post-translational effect. Interestingly, *Pls3* was actually down-regulated at the mRNA level, likely a compensatory response to the accumulation of the protein, indicating a feedback loop to adjust the protein level of Pls3 and thus pointing towards a potentially important functional role of Pls3 in the brain.

In contrast to early development but in line with an important regulatory function of Cul3 mostly during early brain development, we found that in adult mutant cortical, hippocampal, and cerebellar tissues, *Cul3* deficiency results in very few deregulated proteins (at 20% FDR, cortex: 2 up-, hippocampus: 6 up- and 3 down-, and cerebellum: 3 up- and 2 down-regulated proteins; Supp. Fig. 4a-c and Table S7). Nevertheless, in samples obtained from adult animals we again found an association between *Cul3* mutations and deregulation of cytoskeletal-associated proteins, such as an up-regulation of Vimentin in the cortex, or of GFAP in the cerebellum (Supp. Fig. 4a,c). Furthermore, we found that Pls3 is also elevated in the juvenile and adult brain in constitutive *Cul3* mutants (Supp. Fig. 4d,e), supporting a tight link between Pls3 and Cul3. Interestingly, a pathogenic variant of *PLS3* has recently also been described in a patient with idiopathic osteoporosis and ASD [328].

Taken together, our analysis points to a central role of Cul3 in the homeostatic regulation of cytoskeletal proteins of which the most significant appears to be Pls3.

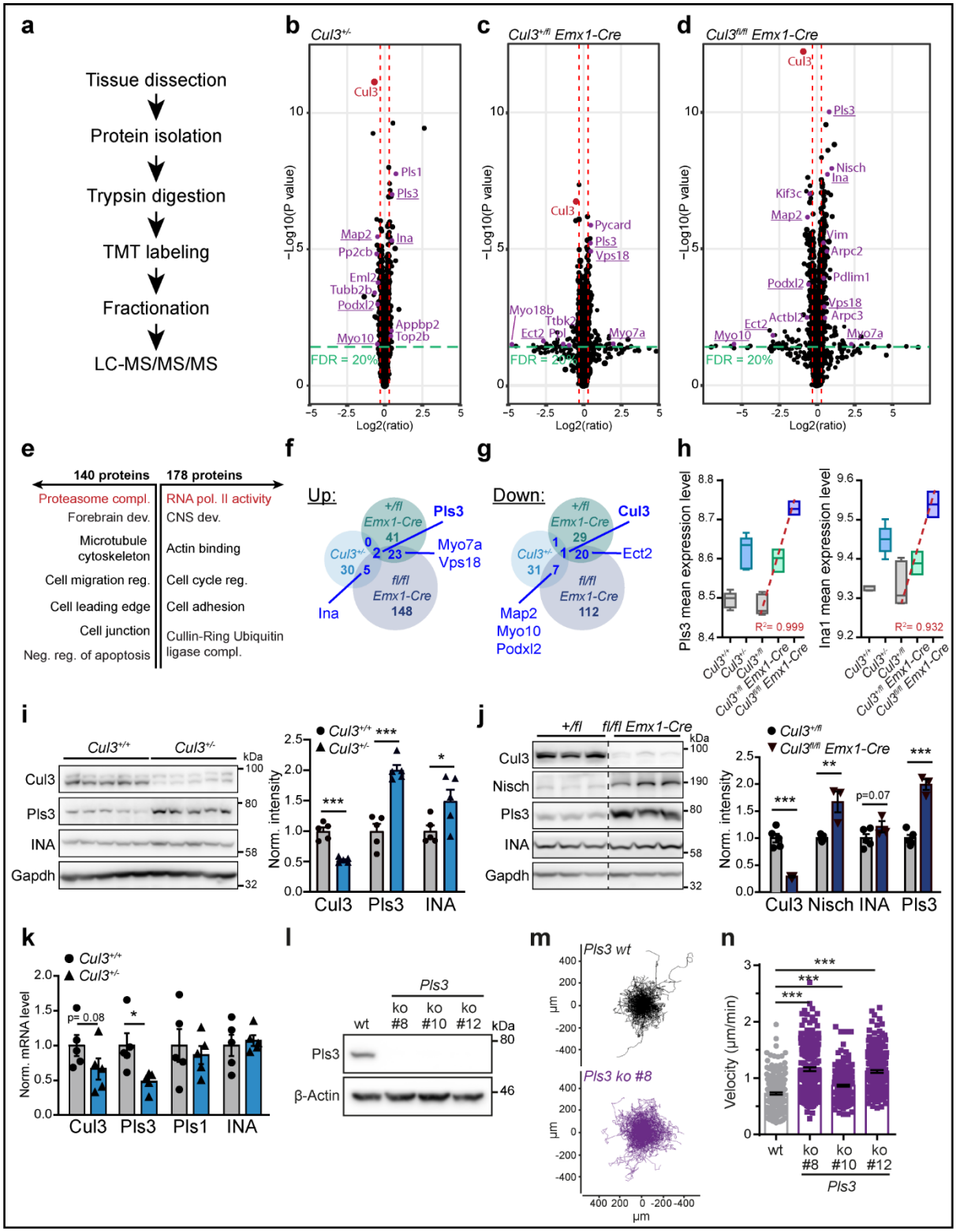

Figure 17: Deregulated cytoskeletal proteins in *Cul3* mutant embryonic forebrain tissue. a, Workflow of sample preparation for proteomic analysis ($n(Cul3^{+/-})$= 5 per genotype, $n(Cul3^{+/fl}$ *Emx1-Cre)*= 3 per genotype and $n(Cul3^{fl/fl}$ *Emx1-Cre)*= 3 per genotype; male mutant and control littermate pairs). **b**, Volcano plot of deregulated proteins at 20% FDR cut-off in the $Cul3^{+/-}$ developing cortex with 37 up- and 40 down-regulated proteins. **c**, Volcano plot of deregulated proteins in the $Cul3^{+/fl}$ *Emx1-Cre* developing forebrain with 66 up- and 51 down-regulated proteins. **d,** Volcano plot of deregulated proteins in the $Cul3^{fl/fl}$ *Emx1-Cre* developing forebrain with 178 up- and 140 down-regulated proteins; cytoskeleton related proteins are labeled in purple, proteins differently regulated in more than one dataset are underlined, Cul3 in red (b, c, d) (details in Tables S2-4). **e**, DAVID functional

annotation identified down- (left) and up- (right) regulated proteins of the *Cul3*$^{fl/fl}$ *Emx1-Cre* forebrain to be involved in regulating activity of RNA polymerase II, the proteasome core complex, neurogenesis and actin and microtubule cytoskeletal organization (selected GO-terms, significant GO-terms in red: RNA polymerase II core complex, GO:0005665, adj. p-value= 0.002; proteasome core complex GO:0005839, adj. p-value= 4.9e-07; details in Table S5). **f**-**g**, Overlap of up- and down-regulated proteins in the *Cul3*$^{+/-}$, *Cul3*$^{+/fl}$ *Emx1-Cre* and *Cul3*$^{fl/fl}$ *Emx1-Cre* cortex at 20% FDR (details in Table S6). **h,** Fitting the mean raw expression levels of Pls3 and INA to a linear regression model indicates that these proteins follow a genotype-dependent dose response (Pls3*:* R^2= 0.999; INA*:* R^2= 0.932; *Cul3*$^{+/fl}$ < *Cul3*$^{+/fl}$ *Emx1-Cre* < *Cul3*$^{fl/fl}$ *Emx1-Cre).* **i**, Western blot (left) and analysis of Gapdh normalized intensities (right) confirm increased levels of the cytoskeletal proteins Pls3 and INA in *Cul3*$^{+/-}$ lysates (*n*= 5 per genotype; *P<0.05, ***P<0.001; unpaired two-tailed t-tests). **j**, Western blot and analysis of Gapdh normalized intensities confirm increased levels of the cytoskeletal proteins Nisch, Pls3 and INA in *Cul3*$^{fl/fl}$ *Emx1-Cre* cortical lysates (samples on the same membrane cut for better visualization, *n*(*Cul3*$^{+/fl}$)= 5, *n*(*Cul3*$^{fl/fl}$ *Emx1-Cre)*= 3; **P<0.01, ***P<0.001; unpaired two-tailed t-tests). **k**, Quantitative real-time PCR analysis of mRNA levels of *Pls1*, *Pls3* and *INA* normalized to wild-type levels (ΔCq expression values; *n*= 5 per genotype; *P<0.05; unpaired two-tailed t-tests). **l**, Representative Western blot images of B16-F1 wild-type and CRISPR/Cas9 knockout cell clones confirm lack of detectable Pls3 protein in 3 independently selected *Pls3* ko clones (ko#8, #10 and #12). β-Actin as loading control. **m**-**n**, 2D random migration assay was performed over 15 hours in B16-F1 wild-type and *Pls3* ko cells. Representative cell paths/trajectories of B16-F1 wild-type (black paths) and *Pls3 ko #8* cells (purple paths), indicate larger migration area of cells upon *Pls3* knockout (m). Average migration velocity for all cell tracks per cell type was plotted on the y-axis (µm/min). Results show increased migration velocity in all *Pls3* knockout clones, relative to B16-F1 wild-type cells (n) (*n*(*wt*)= 237, *n*(*ko #8*)= 205, *n*(*ko #10*)= 222 and *n*(*ko #12*)= 212 cells respectively; Kuskal-Wallis test and Dunn's multiple correction test). Samples from male littermate embryos were analyzed (a-h). Data presented as box and whiskers, min. to max (h) and mean ± SEM in (i-k and n). Significance levels: *P<0.05, **P<0.01, ***P<0.001, n.s. not significant;

4.3.7. Abnormal actin organization in *Cul3* haploinsufficient cells

Proteomic analysis of embryonic cortices highlighted an alteration of cytoskeletal protein levels in *Cul3* mutant samples. In particular, Pls3 protein levels are consistently altered in all of our datasets. Therefore, we were curious to explore whether Pls3 does play a direct role in cell migration. To this end, we employed the murine B16-F1 melanoma cell line, a routinely used cell line model to investigate cell migration of ectodermal cells [329, 330]. As expected, CRISPR-Cas9-mediated homozygous disruption of the *Pls3* locus completely reduces *Pls3* expression (Fig. 17l). Excitingly, in a random migration assay, *Pls3* knockout cells show increased migration speed and travelled distance (Fig. 17m-n), the exact opposite phenotype displayed by *Cul3* mutant cells. Taken together our results indicate that Pls3 is an important player in the regulation of cell migration and its level is indirectly proportional to migration speed and distance.

In migrating cells, the cell front is highly organized by the cytoskeleton in general and especially by a number of different actin-filament based structures, such as lamellipodia, filopodia and stress-fibers (Fig. 18a-c). A number of the identified deregulated proteins in our proteomics dataset are involved in the organization of these actin-cytoskeletal structures, such as Arp2/3 complex members and the plastins Pls1/3 (Fig. 18b). Plastins are a highly conserved group of actin bundling proteins. They, non-covalently, cross-link multiple actin filaments into dense bundles in filopodia and stress fibers. Each plastin consists of a regulatory headpiece domain and two tandem actin-binding domains. The headpiece can bind Ca^{2+} and has a calmodulin binding motif: Ca^{2+} binding induces changes in the intramolecular interaction of the actin-binding domains and the ability to bundle F-actin decreases [331]. In addition,

Pls3 displaces cofilin from the minus-end of F-actin and inhibits its disassembly [332]. Increased levels of Pls3 might therefore impede actin turnover and decrease force generation, thereby altering actin structure and dynamics at the cell front of migrating cells.

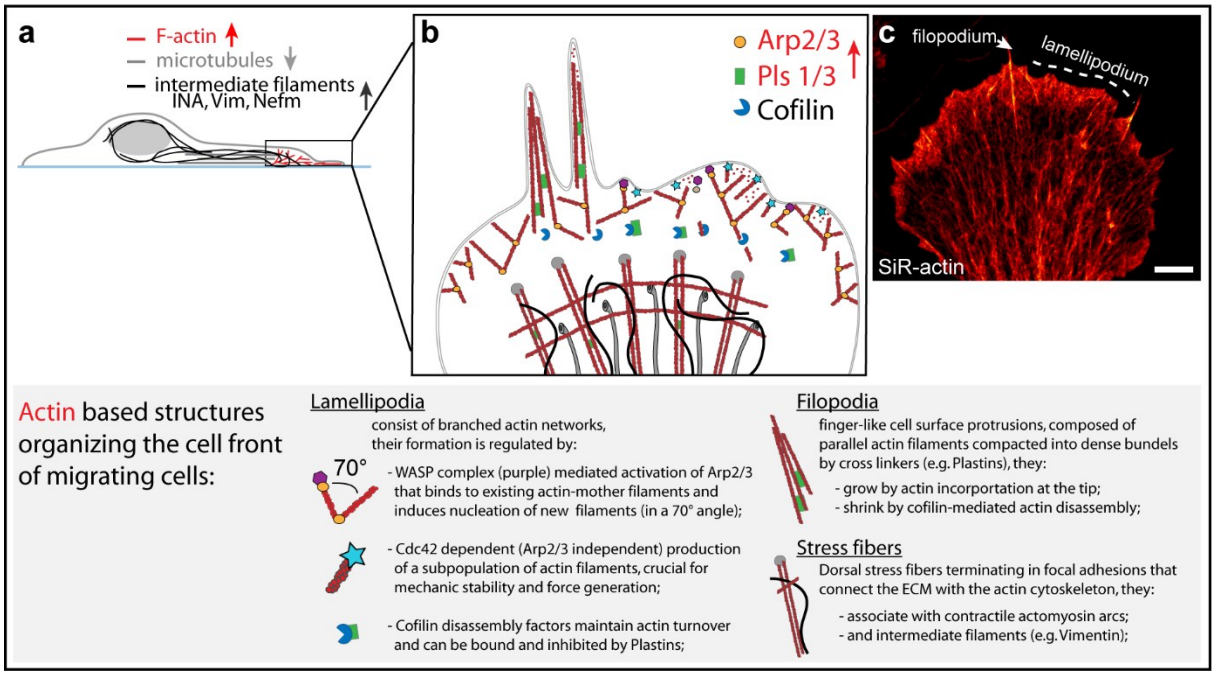

Figure 18: Cytoskeletal proteins at the cell-front of migrating cells with a focus on the actin-cytoskeleton. a, adherent migrating cells are characterized by a bipolar orientation with a leading cell-front and a trailing cell-back. Proteomic analysis of *Cul3* mutant tissues identified a number of cytoskeletal proteins to be deregulated, with actin-binding proteins (red) and intermediate filaments primarily up-regulated and microtubule associated proteins primarily down-regulated. **b**, Scheme of the cell-front of a migrating cell (top view), highlighting actin-cytoskeletal structures and the actin-interacting proteins identified by proteomics analysis in *Cul3* mutants. **c**, SiR-actin staining and STED-imaging reveals the complex actin-organization in the cell-front of adherent mouse NPCs *in vitro*. Scale bar 2.5 µm in (c); Grey box: descriptions of the actin-based structures depicted in (b) [331-335].

To assess whether abnormal homeostasis of actin-cytoskeleton proteins, in the context of *Cul3* mutations, indeed results in structural abnormalities in moving cells, we analyzed actin conformation in neural stem cells *in vitro*. We employed stimulated emission depletion (STED) super-resolution imaging to resolve the intricate actin network at the cell front of NPCs. Specifically, we stained control and *Cul3* mutant NPCs with SiR-actin, a fluorescent probe for F-actin, as well as a tubulin antibody and analyzed actin filament orientation at the leading edge in diffraction-unlimited images. We found that *Cul3* deficiency leads to a disorganized actin-architecture at the cell front of adherent *Cul3*$^{+/-}$ NPCs (Fig. 19a-d), while the microtubule organization appears normal (Fig. 19e-g). Decreased directionality of actin cables and stress fibers may in principle be caused by an increased number of focal adhesion sites, as these puncta contain all possible angles and would thereby decrease the measured dominant direction. Thus, we further analyzed the number of adhesion points in control and mutant cells. Surprisingly, adhesion site counting revealed a slight, yet significant, decrease in focal

adhesions in the mutant cells (Supp. Fig. 5). A reduction of adhesion points is also in line with our proteomic data, which identified a reduction of cell adhesion proteins (such as Podxl, Nid2 and Emb). Taken together, high resolution imaging indicates a disorganized actin cytoskeleton at the cell front, probably constituting the underlying cell biological correlate of the migration defects observed in *Cul3* mutant cells.

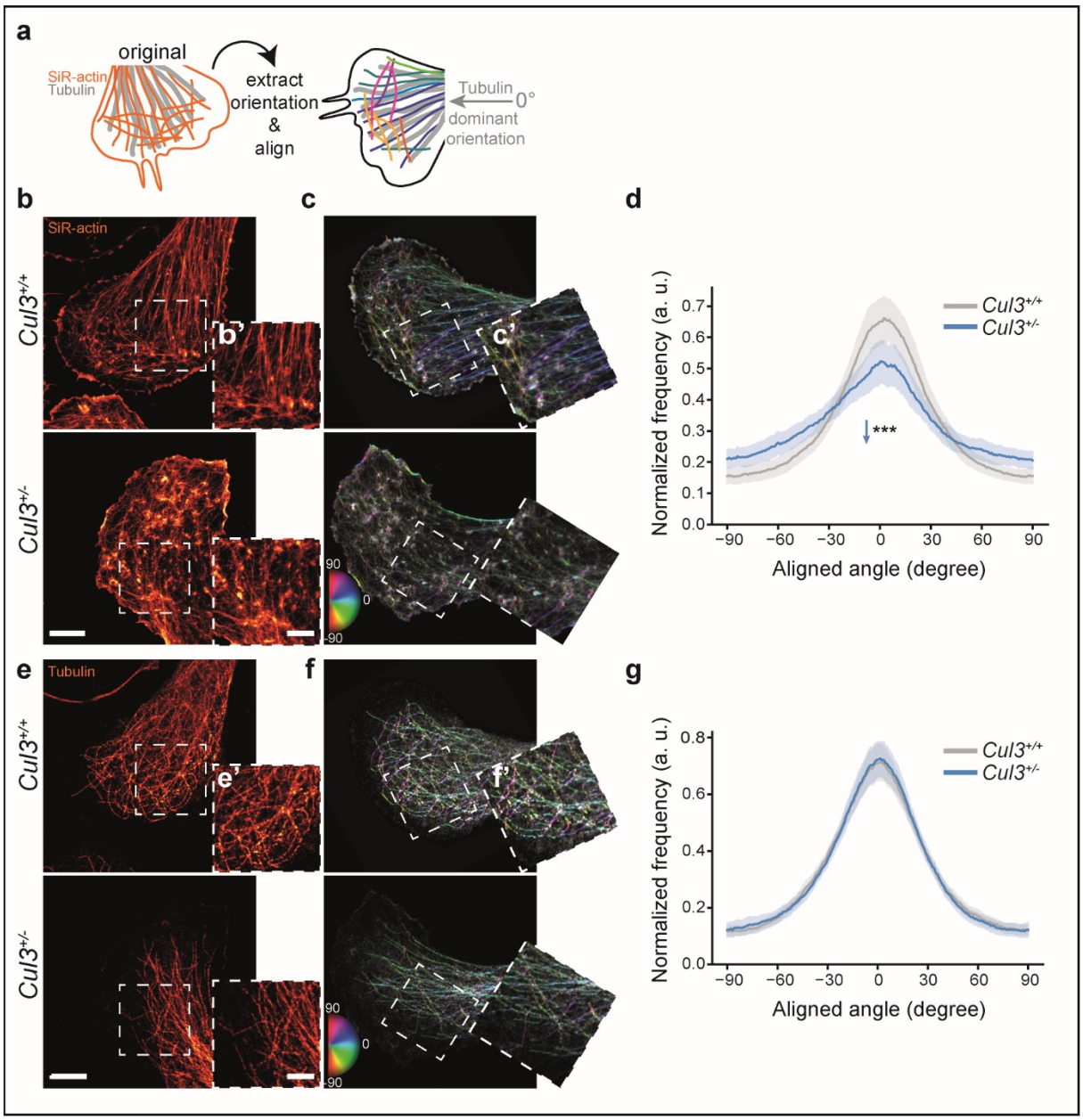

Figure 19: Actin cytoskeleton is disorganized in *Cul3* haploinsufficient NPCs. a, Scheme of the actin orientation analysis at the cell front of NPCs. **b**-**g**, NPCs cultured on Poly-L-ornithine/Laminin coated coverslips were stained using SiR-actin (b) and an anti-tubulin antibody (e). Cell protrusions were imaged employing STED-microscopy (close-up images in insets b',e'). Processed, rotated and analyzed images, color code: hue as the orientation angle, saturation as coherency, brightness represents photon counts in the STED image (c,f), close-ups in insets (c',f'). Orientation distributions for actin (d) and microtubules (g) aligned to the dominant orientation angle of microtubules are shown (*n*(cells)= 43 per genotype from three independent NPC preparations; two-tailed Welch's t-test). The dominant orientation is computed as the average orientation angle inside the cell. Plotted

is the average angle distribution per group ± 95% confidence intervals. Scale bars: 5 µm in (b,e), 2.5 µm in (insets b',e'); Significance levels: ***P<0.001, n.s. not significant;

4.3.8. Behavioral abnormalities are associated with *Cul3* developmental functions

The point(s) in time when ASD mutations exert their effects on the brain remain elusive in most cases, as is also their impact on the appearance of ASD core features. However, identifying these critical temporal windows may be essential to properly design therapeutic strategies and clinical trials. In order to understand how critical the loss of *Cul3* is at developmental stages, we investigated the link between the observed embryonic cellular defects and the appearance of mouse behavioral phenotypes by analyzing the effects of *Cul3* deletion at a later time point.

To induce deletion of *Cul3* postnatally, we crossed our conditional *Cul3* allele with animals expressing a tamoxifen-responsive Cre recombinase (*Cag-CreER*). Thus, we induced heterozygous *Cul3* deletion by tamoxifen injections of *Cul3*$^{+/fl}$ *Cag-CreER* mice between P30 and P40, and performed behavioral analysis of these animals at P55-60 (Fig. 20a). *Cul3*$^{+/fl}$ *Cag-CreER* mice injected with vehicle and *Cul3*$^{+/fl}$ mice injected with tamoxifen were used as controls for the CreER or the compound, respectively.
Consecutive daily tamoxifen injections (100 mg/kg, five days, starting at P30) significantly decrease *Cul3* protein to about half of control levels in *Cul3*$^{+/fl}$ *Cag-CreER* brain tissue (Fig. 20b,c). Of note, we observed that tamoxifen induced conditional homozygous deletion of *Cul3* caused premature lethality in *Cul3*$^{fl/fl}$ *Cag-CreER* animals, with none of them surviving for longer than 20 days after the first tamoxifen injection, while *Cul3*$^{+/fl}$ *Cag-CreER* mice show normal survival probabilities into adulthood as all the tested controls (Supp. Fig. 6a,b). This finding underscores the dose-dependent effect of *Cul3* deletion, similar as observed in our proteomics datasets and highlights the necessity of employing construct valid mouse models when investigating human pathophysiology.

Next, we performed a thorough behavioral characterization of the *Cul3*$^{+/fl}$ *Cag-CreER* animals treated with tamoxifen, testing all the paradigms in which we observed behavioral abnormalities in the constitutive adult *Cul3*$^{+/-}$ line (Fig. 10). We found that induction of *Cul3* haploinsufficiency at P30 does not result in any major behavioral defects, except for reduced motor learning abilities on the accelerating RotaRod. More specifically, while we did not observe any increase in hindlimb clasping events (Fig. 20d), abnormalities in gait (Supp. Fig. 6d) or in the initial coordination, *Cul3*$^{+/fl}$ *Cag-CreER* + TM mice significantly underperform on the third day of RotaRod training (Fig. 20e-e'). In contrast, *Cul3*$^{+/fl}$ *Cag-CreER* treated with tamoxifen behave comparably to the controls in the three chamber sociability test, with normal interest in social novelty (Fig. 20f-g). Further, they react normally to the social odors in an adapted OHDH test (Fig. 20h) and show comparable cognitive abilities in the CFC paradigm to the controls (Fig. 20i-i'). All of these behaviors were clearly perturbed in animals with germline *Cul3* haploinsufficiency but appear normal when *Cul3* is deleted at the juvenile stage. Taken together, these results indicate that developmental stages are critical for the

appearance of the vast majority of *Cul3*-associated behavioral phenotypes, especially the ASD-relevant social and cognitive defects.

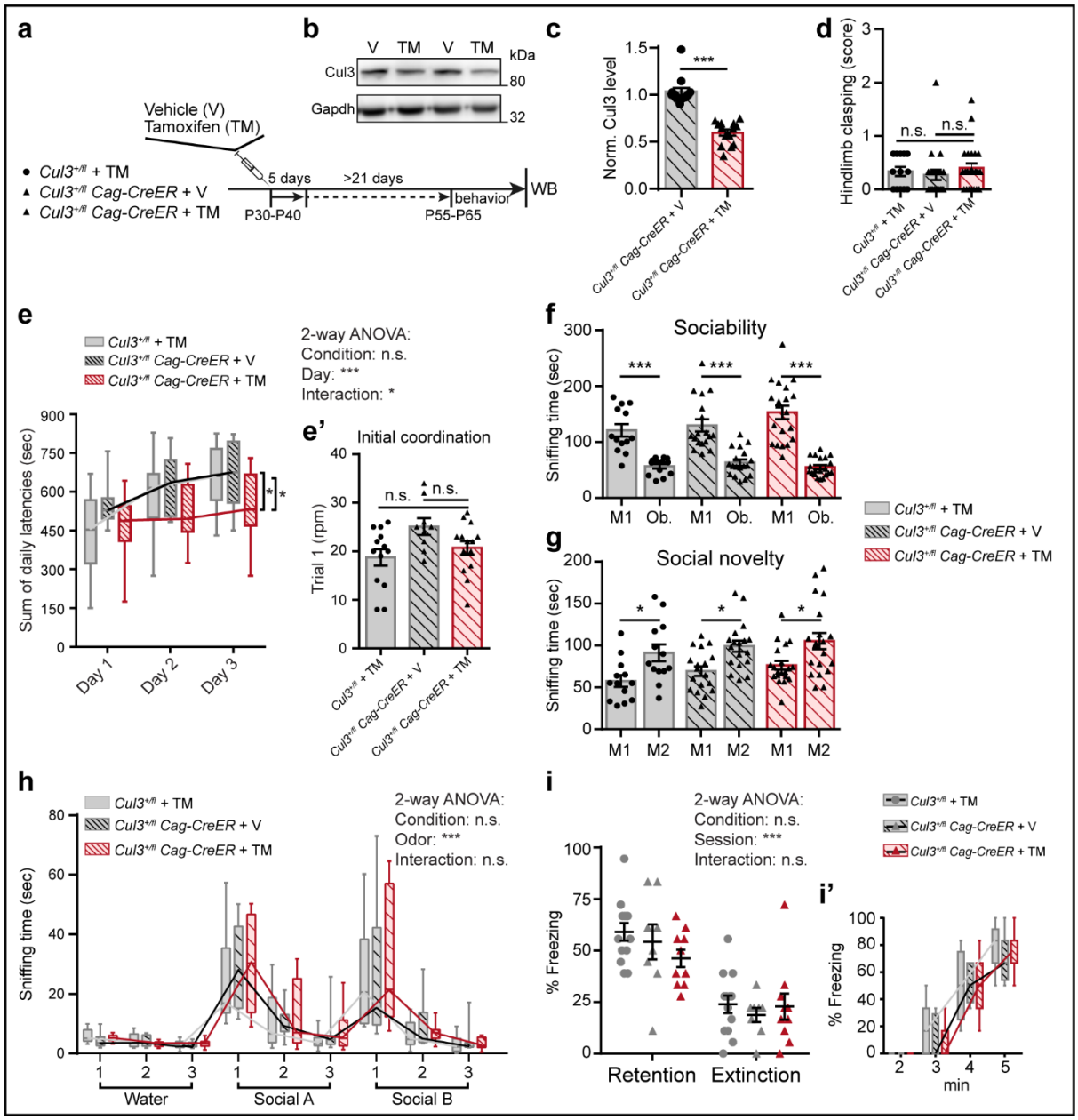

Figure 20: *Cul3* loss after completion of main developmental milestones does not lead to major behavioral abnormalities in mice. a-b, 30 to 40 day-old *Cul3*$^{+/fl}$ *Cag-CreER* double transgenic mice were injected for 5 consecutive days with either 100 mg/kg body weight tamoxifen (TM) or vehicle (V, corn oil), while *Cul3*$^{+/fl}$ animals were injected with TM to control for potential effects from the compound. Behavioral tests were performed after at least 21 days post-last injection (P55-65), followed by Western blot analysis of Cul3 levels in the brain (a, scheme and b, representative Western blot). **c**, Quantification of normalized Cul3 protein levels in the brain of tamoxifen treated mice, normalized to the levels of vehicle injected controls (*n*= 14 mice per condition; unpaired two-tailed t-test). **d**, Hindlimb clasping scoring from 0-1 (normal) to 3 (most severe) did not reveal any difference between conditions (*n(Cul3*$^{+/fl}$ + TM*)*= 13, *n(Cul3*$^{+/fl}$ *Cag-CreER* + V*)*= 22, *n(Cul3*$^{+/fl}$ *Cag-CreER* + TM*)*= 24; littermate animals, 1way ANOVA and Sidak's multiple comparison test). **e-e'**, Performance on the accelerating RotaRod of tamoxifen and vehicle treated *Cul3*$^{+/fl}$ *Cag-CreER* mice and *Cul3*$^{+/fl}$ + TM controls revealed reduced motor learning abilities in the *Cul3*$^{+/fl}$ *Cag-CreER* + TM group (e), however the initial coordination on day 1- trial 1 was comparable between *Cul3*$^{+/fl}$ *Cag-CreER* + TM mice and controls (*n(Cul3*$^{+/fl}$ +

TM)= 13, *n(Cul3$^{+/fl}$ Cag-CreER* + V)= 9, *n(Cul3$^{+/fl}$ Cag-CreER* + TM)= 14; littermate animals, 2way ANOVA (e) and 1way ANOVA (e') and Sidak's multiple comparison tests). **f**-**g**, *Cul3* loss at P30-P40 does not induce abnormal behavior in the three chamber sociability test, the tamoxifen and vehicle treated *Cul3$^{+/fl}$ Cag-CreER* mice as well as the *Cul3$^{+/fl}$* + TM controls significantly prefer a stranger mouse (M1) over the caged object (Ob.) (f), and the novel stranger (M2) over the already familiar mouse (M1) (g) (*n(Cul3$^{+/fl}$* + TM)= 13, *n(Cul3$^{+/fl}$ Cag-CreER* + V)= 22, *n(Cul3$^{+/fl}$ Cag-CreER* + TM)= 24; littermate animals, 1way ANOVA and Sidak's multiple comparison test). **h**, All test-groups distinguish and familiarize to social odors in the adapted olfaction habituation and dishabituation test, *Cul3$^{+/fl}$ Cag-CreER* + TM animals do not show hyper-reactivity to the presentation of social odors (*n(Cul3$^{+/fl}$* + TM)= 13, *n(Cul3$^{+/fl}$ Cag-CreER* + V)= 9, *n(Cul3$^{+/fl}$ Cag-CreER* + TM)= 10; littermate animals, 2way ANOVA and Sidak's multiple comparison test);. **i**-**i'**, Contextual fear-conditioned memory retention and extinction scored as percent freezing during a 3 min exposure to the context (i), and fear acquisition training (i'), reveal comparable freezing behavior between all test-groups (*n(Cul3$^{+/fl}$* + TM)= 13, *n(Cul3$^{+/fl}$ Cag-CreER* + V)= 9, *n(Cul3$^{+/fl}$ Cag-CreER* + TM)= 10; littermate animals, 2way ANOVA and Sidak's multiple comparison test). Sex-matched littermate animals were analyzed. Data presented either as mean ± SEM, as well as scatter plot (c,d,e',f,g,i) or as box and whiskers, min. to max., (e,h,i'). Significance levels: *P<0.05, **P<0.01, ***P<0.001, n.s. not significant;

4.3.9. Testing other suggested Cul3 target proteins

Recently, three studies exploring the molecular mechanisms linking *Cul3* mutations with ASD pathogenesis have been published [322, 323] or deposited on BioRxiv [336].

In the first of these studies, Rapanelli et al. employed either *Cul3$^{+/fl}$ Emx1-Cre* heterozygous adult mice or *Cul3$^{fl/fl}$* homozygous adult animals injected with a Camk2-Cre expressing virus in the PFC or the striatum, to study the effects of Cul3 depletion on behavior and the brain protein composition. *Cul3$^{+/fl}$ Emx1-Cre* animals showed increased locomotion in the open field, abnormal pre-pulse inhibition (PPI) and reduced social interest, while viral injections into the striatum and PFC triggered a subset of behavioral phenotypes, namely increased grooming in the former and reduced social interest in the latter, but normal PPI and locomotion [323]. Through proteomic and western blot analysis they detected increased levels of the histone methyl transferase Smyd3 in mutant brain lysates and proposed Smyd3 up-regulation as the main driver of *Cul3* related pathophysiology. Pharmacological and shRNA mediated Smyd3 inhibition could further rescue some of the observed phenotypes [323].

Dong and colleagues instead, made use of NEX-Cre and GFAP-Cre mediated recombination to conditionally delete *Cul3* from either post-mitotic neurons at E11.5, or radial glia cells at E13.5 in the developing forebrain [322]. Both, *Cul3$^{+/fl}$ GFAP-Cre* and *Cul3$^{+/fl}$ NEX-Cre* adult animals showed similar behavioral abnormalities, including reduced social interest in the three chamber test, increased anxiety in the open field and on the elevated plus maze but normal grooming and locomotion. In line with our findings in *Cul3$^{fl/fl}$ Emx1-Cre* mice, they observed severe brain malformations in *Cul3$^{fl/fl}$ GFAP-Cre* and *Cul3$^{fl/fl}$ NEX-Cre* pups but did not explore the consequences of *Cul3* loss on neurodevelopment any further. Instead, they identified the up-regulation of eIF4G1 as culprit driving the ASD-related pathophysiologic changes in their mouse models. Therefore, they performed intracerebroventricular injections of 4EGI-1, an inhibitor of CAP-dependent translation and could rescue some of the described phenotypes [322].

In the last of these studies, Amar et al. reported the CRISPR-Cas9 mediated generation of a mouse line, carrying the human p.E246X mutation (*Cul3*$^{+/pE246X}$), that causes *CUL3* haploinsufficiency. These mice presented with hyperactivity in the open field but normal anxiety levels, and reduced social interest in the three chamber sociability test, as well as some motor issues [336]. Magnetic resonance imaging (MRI) revealed an overall decreased brain volume, especially affecting the somatosensory cortex in P7 *Cul3*$^{+/pE246X}$ animals, brain anatomic defects further confirmed by histological analysis. *In vitro* analysis of primary neurons from these mice showed reduced length of neurites as well as reduced firing rates. The authors linked these defects with increased RhoA levels in *Cul3* mutant tissues and rescued the neuronal morphology defects, *in vitro*, via rhosin inhibition of RhoA [336].

While some overlaps can be identified, mostly regarding the described behavioral phenotypes, the main findings of these three studies, all published within a narrow timeframe of a few month, are remarkably divergent. Although a number of factors could account for these differences and will be discussed more in detail below, we nevertheless quantified the protein levels of eIF4G1, Smyd3 and RhoA in our *Cul3* haploinsufficient mouse line (Fig. 21).

First, we quantified eIF4G1 protein levels in the cerebral cortex, hippocampus and cerebellum of P14 male *Cul3*$^{+/-}$ pups (same time point and sex as in Dong et al.), employing the same antibody used by Dong and colleagues (Fig. 21a). Additionally, we investigated eIF4G1 protein levels in our adult proteomics dataset (Fig. 21b). We could not detect abnormal eIF4G1 protein levels in any of the brain areas or time points analyzed in *Cul3*$^{+/-}$ animals. These findings indicate that increased levels of eIF4G1 cannot account for the behavioral abnormalities observed in patients and mice with *Cul3* haploinsufficiency. This is not surprising since changes in eIF4G1 protein levels are not observed in any of the other recently available proteomic datasets for *Cul3* mutants [323, 336]. There are a few possible explanations for the results obtained by Dong and colleagues. For example, eIF4G1 levels could be changed due to compensatory effects. Alternatively, it is conceivable that abnormal eIF4G1 protein levels are due to the GFAP-Cre rather than to *Cul3* mutation. In fact, Dong et al. never compared *Cul3*$^{fl/+}$ *GFAP-Cre* with *Cul3*$^{+/+}$ *GFAP-Cre* controls, nor did they quantify eIF4G1 levels in the *NEX-Cre* line. Of note, certain key experiments supporting elevated protein synthesis in *Cul3*$^{fl/+}$ *GFAP-Cre* mice, such as the increased association of eIF4G1 and eIF4E, increased CAP-dependent translation by SUnSET assay, and decreased eIF4G1 ubiquitination, are solely based on a N=1, no quantification and statistics.

Second, we investigated Smyd3 levels [323], in our adult proteomic dataset and could not find any difference between wild type and mutant tissues (Fig. 21c). While 20% of the upregulated proteins in the *Cul3*$^{fl/+}$ *Emx1-Cre* cortex were cytoskeleton related proteins, Rapanelli and colleagues decided to follow up Smyd3 solely based on cited global methylation changes observed in post-mortem ASD tissues, without providing evidence of such alterations in their mouse model.

Lastly, we also investigated RhoA levels by western blot, but we could not observe any increase in protein abundance of RhoA upon *Cul3* haploinsuffisciency, at any of the tested time points and tissues (Fig. 21d,e).

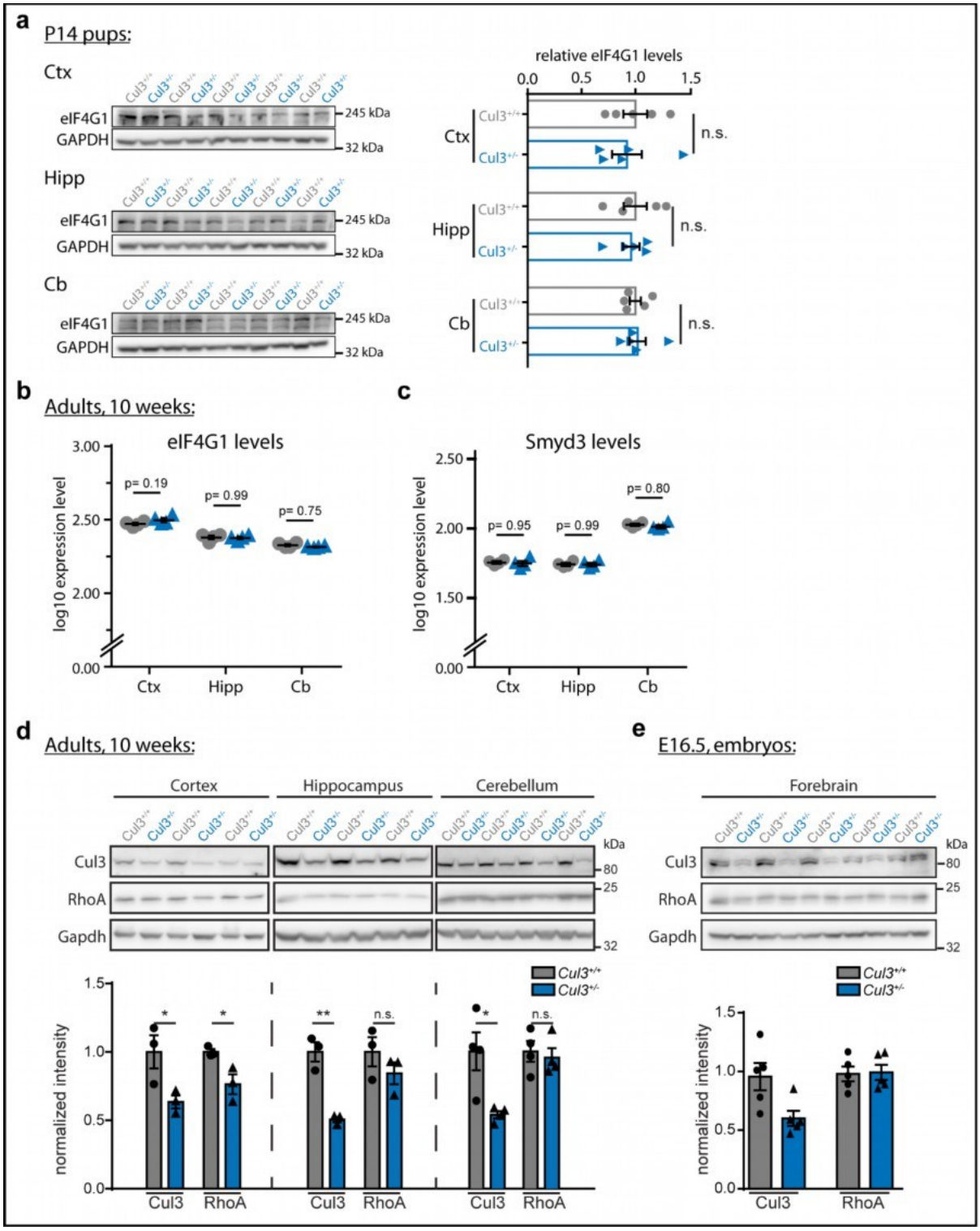

Figure 21: Western blot analysis of the proposed molecular drivers of the *Cul3* mutant phenotype. a, eIF4G1 levels are unchanged in the Cul3$^{+/-}$ P14 male cortex, hippocampus and cerebellum lysates, when probed with the anti-eIF4G1 antibody from Bethyl Lab., cat. no. A300-502A (n= 5 per genotype); **b**, eIF4G1 and **c**, Smyd3 are

not altered in the adult proteomics datasets of cortex, hippocampus and cerebellum (n= 4 per genotype, 2-way ANOVA and Sidak`s multiple comparison test). **d**-**e**, RhoA levels are comparable between $Cul3^{+/-}$ and wild type brain tissues, both in the adult (d) as well as at E16.5 (e) (n= 3-4 mice per genotype, adults; n= 5 embryos per genotype, E16.5).

In strong contrast to these contradicting results, looking into the now available proteomic data for *Cul3* mutant mice, we found that Pls3 and other cytoskeleton-related proteins are consistently up-regulated in *Cul3* mutant animals [322, 323, 336].

4.4. Summary, discussion and future directions

De novo loF mutations in *CUL3* are a relevant cause of ASD, developmental delay, motor deficits and intellectual disability in humans. Therefore, understanding the role of *CUL3* in the mammalian brain and identifying its substrate proteins is of utmost importance. While the molecular function of CUL3 in the UPS is well described, its role in the brain, particularly during development, remains largely unclear. To address these questions and model the patients' *CUL3* haploinsufficiency, we analyzed a *Cul3* heterozygous mouse model in detail, on a behavioral, histological, electrophysiological and molecular level.

We found that constitutive *Cul3* heterozygous deletion leads to several behavioral abnormalities, including sociability issues, motor dysfunctions, and olfactory hyper-reactivity in adult animals. While this confirms the necessity of maintaining correct *Cul3* dosage in the mammalian brain, it also implicates *Cul3* in the function of different brain regions, in line with the complex presentation of *CUL3* mutant patients. Importantly, for our behavioral studies we invested effort in generating and analyzing male and female cohorts separately but we did not observe major phenotypic differences between genotypes of different sexes, supporting the observation that in humans *CUL3* mutations similarly affect males and females. Thus, *CUL3* mutations do not appear to contribute to the skewed sex ratio in ASD cases [145, 146, 278, 280, 281].

Overall, in our study, we confirm the sociability problems observed in the recently published articles investigating *Cul3* deficiency in mice. However, we could not observe any hyperactivity, repetitive grooming or anxiety related issues [322, 323, 336]. Instead, our haploinsuffisciency model presents with some motor defects and growth delay, reminiscent of the human *CUL3* haploinsufficient phenotype and also confirmed in the constitutive $Cul3^{+/pE246X}$ line [336]. The divergence of these findings can be attributed to a number of factors, foremost the choice of mouse model and eventually also the genetic background. While in the heterozygous constitutive model, the 50% protein reduction of Cul3 is present from fertilization on and affects all the cell types equally, it can be speculated that conditional deletion from only a subgroup of cells and brain areas at a later time point might lead to compensatory effects and eventually overcome critical developmental time windows,

thereby masking and/or generating certain phenotypes that would not be observed in *Cul3* haploinsufficiency.

Indeed, Dong et al. employed a *GFAP-Cre* mouse line (*FVB-Tg(GFAP-cre)25Mes/J*). In this Cre-line, recombination is reported to start at embryonic day (E) 13.5 [337], suggesting that Cul3 protein levels are not reduced earlier than E14, but eventually later. Furthermore, due to the nature of the promoter, this GFAP-Cre mouse line displays Cre-mediated recombination in a mosaic fashion in the central nervous system, including the neocortex (30 to 88% of projection neurons show Cre-expression) and other brain regions. In addition, in the neocortex only a small proportion of interneurons exhibit Cre-mediated recombination (20-38% of inhibitory neurons) [337]. Due to these characteristics, the GFAP-Cre conditional mouse is rather similar to the second line employed by Dong et al., the NEX-Cre line, targeting only post-mitotic excitatory forebrain neurons [338]. The mosaicism of the GFAP-Cre line renders it unsuitable to study effects of *Cul3* loss in both the excitatory and inhibitory neurons in the forebrain since it may cover, or lead to, specific phenotypes. For example, in the piriform cortex of GFAP-Cre mice, only 66% of projection neurons and 33% of inhibitory neurons show *Cre* expression and thus may have reduced Cul3 levels. This is interesting, since it could explain why Dong et al. observed normal olfaction in *Cul3* mutants, while we detected abnormal hyper-reactivity to social odors. Indeed, the behavior in response to olfactory stimuli is strongly regulated through the piriform cortex [339]. Dong and colleagues also noted that the effect of *Cul3* deficiency on inhibitory neurons is secondary to defects in excitatory neurons. This renders it impossible to conclude whether inhibitory neurons would be similarly impacted in the context of *Cul3* germline mutations.

While we employed the Emx1-Cre line with the aim to analyze dose-dependent effects of *Cul3* loss on the excitatory cell linage of the forebrain, in addition to studying the consequences of constitutive *Cul3* heterozygous deletions, Rapanelli et al. performed their experiments exclusively either in $Cul3^{fl/+}$ *Emx1-Cre* heterozygous adult mice or in $Cul3^{fl/fl}$ homozygous animals injected with a Camk2-Cre expressing virus. Homozygous deletion of *Cul3* (in $Cul3^{fl/fl}$ *Camk2-Cre*) in a small subset of cells in the adult brain has not been described in patients and is very unlikely to occur in nature. Moreover, homozygous mutations lead to more dramatic changes, and in fact the number of deregulated proteins is much larger in $Cul3^{fl/fl}$ *Camk2-Cre* than in *Emx1-Cre* heterozygous tissue [323], in line with our observations of a dosage dependent effect of *Cul3* loss and the lethality of juvenile conditional homozygous *Cul3* deletions.

These factors render it difficult to correctly interpret the data presented by Rapanelli and colleagues and Dong et al., and demand further experimental investigation of their conclusions. To this end, it will be useful to undertake a behavioral characterization of our $Cul3^{+/fl}$ *Emx1-Cre* mice in adulthood. Indeed, preliminary analysis has shown that they do not present with the gait abnormalities and characteristic hindlimb clasping of $Cul3^{+/-}$ adult mice,

in line with a potential abnormal cerebellar function in the latter, being missed in the conditional lines (data not shown). To clarify the origins of the motor phenotypes further, it would indeed also be interesting to study the consequences of conditional heterozygous *Cul3* deletion from e.g. cerebellar Purkinje cells [340].

Furthermore, it would be important to more closely investigate the consequences of *Cul3* haploinsuffisciency on inhibitory cells. Such experiments could range from live cell imaging approaches in organotypic acute slices of embryonic mouse brains, to the utilization of Cre-lines specifically targeting the GABAergic inhibitory cell linage (eg. Dlx-Cre driver lines [341]). The obtained results would allow to better interpret the electrophysiological findings in ours as well as the other studies, shedding light on their origin and clarifying direct versus indirect effects of *Cul3* loss on excitatory and inhibitory cell linages. This is especially true since during brain development immature inhibitory neurons migrate from the proliferative VZs of the ganglionic eminences (i.e. the LGE and MGE), in a tangential fashion, into the developing cortical plate where they then integrate into the emerging networks (see also chapter 2.2.1). These cells exhibit a very characteristic saltatory migration pattern, switching from sharp periods of movement to pauses [342], paced by intermittent nuclear jumps [343]. During this process, the microtubule and actomyosin cytoskeletons are responsible for the integration of extracellular cues, guiding directed migration, and generating the forces that are required for cell movement [343]. Additionally, when invading the cortex migrating interneurons modulate the generation of age-matched projection neurons [343]. Therefore, and considering that we observe a reduction in the number of inhibitory PV+ interneurons and an overall reduced network activity in the adult somatosensory cortex of *Cul3*$^{+/-}$ animals, it is conceivable that *Cul3* deficiency might directly affect the migration and integration of inhibitory interneurons into cortical circuits. This is especially interesting, as the abnormal composition of actin-cytoskeletal proteins upon *Cul3* loss could have a deleterious effect on the actomyosin architecture and functionality, impacting the nucleokinesis and saltatory migration of the tangentially moving inhibitory cells [343].

While a gross morphological brain analysis did not reveal major abnormalities in our adult *Cul3*$^{+/-}$ mutants, we found that *Cul3* haploinsufficiency leads to cortical lamination defects and mild cortical thinning, in line with Amar et al. 2020 [336]. The lamination abnormalities in *Cul3*$^{+/-}$ animals are linked to migration defects, which lead to retention of neuronal cells in lower cortical layers. *Cul3* mutation-associated neuronal migration defects are cell-autonomous and do not depend on brain-specific cues, as we also observe migration phenotypes *in vitro*. Furthermore, our data indicate that *Cul3* deficiency does not affect the number of astrocytes and microglial cells in the cortex, thus suggesting that *Cul3* regulates neuronal-specific processes, possibly due to its much higher expression in neuronal cell types compared to other brain cells types. Lamination defects, even when subtle, can have a profound effect on the physiology of the brain and disrupt the stereotyped organization of the micro-columnar structures typical of the neocortex. Accordingly, lamination defects have

been previously associated with ASD in human and mouse models due to alteration of neuronal connectivity [25, 214]. Similarly, *Cul3* haploinsufficient mice show decreased spontaneous activity of layer 2/3 cortical excitatory and inhibitory neurons, possibly due to a reduction of total neurons reaching these upper cortical layers and an overall incorrect laminar organization. Interestingly, complete deletion of *Cul3* leads to additional phenotypes including increased apoptosis during the neural stem cell proliferation phase, possibly due to the observed defects in cell cycle regulation at E14.5. This is matched by a more severely affected proteostasis in the developing brain of Cul3$^{fl/fl}$ *Emx1-Cre* embryos. Defects of cell cycle progression were already associated with complete depletion of *Cul3* and underlie the lethality of *Cul3* null mice [292]. Thus, studying construct valid *Cul3* models, mimicking the patient's genetic architecture, is critical to understand the bases of ASD in patients, as due to its stronger effect, homozygous deletion can obscure the underlying cellular and molecular drivers of *Cul3* haploinsufficiency-linked phenotypes.

A role of *Cul3* in cell migration was already hypothesized due to its connection with *Kctd13*, one of the genes involved in the 16p11.2 deletion syndrome associated with neurological symptoms. *Kctd13* encodes a substrate-linking protein for Cul3 and was suggested to bind RhoA, a regulator of the actin-cytoskeleton, thereby targeting it for ubiquitylation and degradation [301]. However, *Kctd13* deletion does not lead to elevated RhoA until after P7 and adult *Kctd13* heterozygous knockout mice do not have major structural brain differences as assessed by MRI [303]. Thus, in agreement with a lack of RhoA increase in *Cul3*$^{+/-}$ embryonic forebrain tissue, as seen in our proteomics data and by western blot analysis, the observed migration and lamination defects are most likely caused by a more general effect of *Cul3* loss on actin-cytoskeleton-associated proteins, as indicated by our proteomics analysis at E16.5, rather than driven by RhoA. Integrity of the actin-cytoskeleton is known to be essential in multiple cell types to facilitate cell migration by generating protrusive and contractile forces [334]. Abnormal homeostasis of actin-cytoskeletal proteins likely leads to the observed disorganization of actin architecture at the leading edge of migrating cells, thus explaining the migration defects displayed by *Cul3* mutant cells *in vivo* and *in vitro*.

Importantly, the two recent studies [322, 323], analyzing the effect of *Cul3* deficiency on the adult mouse brain, fell short of studying the developmental consequences of *Cul3* mutations in detail and employed Cre-lines that may miss critical developmental issues. In contrast, here we focused on the constitutive effects of *Cul3* haploinsufficiency and discovered its crucial role in cell migration and the organization of the cortex. Interestingly however, when comparing our proteomic dataset with these recently published studies we made a few remarkable observations. First, in all datasets we found down-regulation of Map2, a microtubule associated protein and known component of the neuronal cytoskeleton. Reduced levels of Map2 may be due to the reduced cortical layer thickness and numbers of neurons. Second, we found that the only protein consistently up-regulated in mutant animals is Pls3, an under-investigated actin bundling protein [331, 332]. Pls3 is altered in the

developing and adult cortex, the adult hippocampus, but not in the adult striatum [322, 323]. Thus, although there are several discrepancies, probably due to different experimental choices (e.g. mouse model employed, time point analyzed, proteomic strategy and analysis, etc.), the combined evidence suggests a role of *Cul3* in regulating cytoskeletal organization. Furthermore, all datasets point to a potential important role of Pls3 in the brain. Our data indicate that Pls3 may act as a break of cell migration and that a tight regulation of its protein levels is critical to control cell-intrinsic migration properties. In the presence of low Pls3 levels, cells migrate faster and, consequently, travel longer distances, while in the presence of high Pls3 levels cells are moving slower and travel shorter distances.

To further strengthen the link between abnormal Pls3 accumulation and the cell migration defects in *Cul3*$^{+/-}$ neural cells, it will be interesting to explore the consequences of Pls3 overexpression in wild type NPCs. According to our proposed model, Pls3 accumulation in these cells should inhibit their migratory behavior, mimicking the effects of *Cul3* haploinsufficiency. In contrast, *Pls3* knockout through CRISPR-Cas9 and Pls3 protein reduction in the *Cul3*$^{+/-}$ NPCs might be able to rescue, at least in part, the abnormal migration in these cells. If these hypotheses hold true, performing *in utero* electroporation to deliver the Pls3 knockout- and/or overexpression-constructs into the developing forebrain of *Cul3*$^{+/+}$ and *Cul3*$^{+/-}$ embryos could further elucidate the role of Pls3 *in vivo* and clarify its potential as a therapeutic target for a personalized medicine approach. Nevertheless, the role of Pls3 in the adult brain, especially also in human tissues, and its potential involvement in regulating neuronal morphology through its actin-cytoskeleton interaction, still need to be further clarified. One strategy to address these points could be to investigate the function of Pls3 and Cul3 in human cerebral organoids, generated either from isogenic human embryonic stem cells (hESC), or induced pluripotent stem cells (iPSCs) derived from fibroblasts obtained from patients carrying *CUL3* mutations [344]. This would allow us to, not only test our findings obtained in the murine *Cul3* haploinsufficient model but also to identify potential human specific CUL3 target proteins [345].

Efforts to understand translational possibilities from mouse to human are central, when considering that many drugs, especially in the context of ASD and other psychiatric disorders, fail to be effective in human clinical trials. This might be due to human specific gene functions, but more often due to an incomplete picture about human disease pathogenesis. In the context of ASD, special attention here needs to be drawn to the developmental trajectories of certain subgroups of ASD. As discussed more in detail above (chapter 3), for some, gene function is essential in mature neurons, to maintain homeostasis and promote learning. In these ASD subgroups phenotypes can be reversed even in adulthood (as exemplified by *MECP2*), but for others, the function of the genes during brain development is essential.
Indeed, our observations point to a central role of *Cul3* in early brain development since heterozygous deletion of *Cul3* in adult animals does not cause major behavioral defects. Therefore, although a direct connection is still missing, it seems plausible that *Cul3*

haploinsufficiency associated migration defects play a central role in mediating the behavioral abnormalities associated with ASD. While some questions regarding the exact temporal trajectory remain to be answered, our findings point to a critical early developmental time window for the emergence of *Cul3* related, ASD-linked behavioral abnormalities. Further, our findings suggest that later interventions may be ineffective in patients carrying mutations in the *CUL3* gene. This is especially important when considering the results obtained by Dong et al. and Rapanelli and colleagues. Both studies did not investigate any developmental function of *Cul3*. Yet, they present treatment strategies, ameliorating some of the observed behavioral phenotypes for which it remains unclear when they arise and whether or not they may be due to compensatory effects:

First, the treatment by Rapanelli et al. decreases H3K4 di- and tri-methylation. While the authors neither present evidence for increased levels of H3K4 methylation in the *Cul3*$^{fl/+}$ *Emx1-Cre* brain, nor any data for decreased H3K4 methylation levels upon treatment in *Cul3* mutants (i.e. just in wild types), reduced levels of H3K4 di- and tri-methylation are linked to decreased gene transcription. Similar to Dong et al. (see below), broad reduction of gene transcription in a mouse model with protein degradation defects might result in the rescue of abnormal protein abundance, without targeting the underlying mechanisms. Unfortunately, no other study, including Dong et al., could replicate the findings of Smyd3 upregulation upon *Cul3* loss, so its pathophysiological relevance remains unclear.

Instead, Dong et al. pursued a rescue based on the inhibition of CAP-dependent translation. Such inhibition probably reduces/rescues the level of many proteins in an E3-ubiquitin ligase deficient mutant, independently from whether eIF4G1 is altered or not. In fact, treatment with 4EGI-1 leads to a significant reduction of a/b SNAP protein levels in control mice. By employing this inhibitor it is impossible to determine whether the rescue is due to the proteins highlighted by the authors or by reduction of the levels of any other elevated protein, potentially even Pls3. Furthermore, it has been shown previously that 4EGI-1 has an effect on protein stability independent from CAP-dependent translation, i.e. it downregulates the anti-apoptotic factor cFLIP through a proteasome specific pathway [346]. This means that 4EGI-1 pharmacological treatment will be far less specific then suggested by the authors. Importantly, the age of treatment onset, a critical point for the correct interpretation of the phenotypic rescue, is nowhere stated in the publication of Dong and colleagues.

Putting our findings into context with the recently published *Cul3* studies and identifying their overlaps but also experimental limitations, has highlighted the importance of a rigorous scientific approach. To fully understand ASD pathogenesis, already on the rare monogenic level and especially when dealing with ubiquitously expressed proteins of broad molecular function, requires the investigation of several time points, cell types and tissues. When it comes to the identification of drug targets, the specificity of the proposed treatment needs to be tightly controlled and reproducibility ensured, to avoid premature conclusions about its therapeutic effectiveness.

5. CONCLUDING REMARKS AND PERSPECTIVES

Despite significant advancements in the understanding of ASD pathogenesis over the last few years, especially with respect to monogenic ASDs, the autism research field is currently facing major roadblocks in moving promising treatment strategies from preclinical trials to successfully completed clinical trials in humans. Therefore, stratification of the very heterogeneous patient population into more defined biological subgroups will be necessary to facilitate treatment design for larger groups of patients.

Consequently, here, we provide novel insights into the pathophysiological and temporal basis of *Cul3*-linked behavioral abnormalities and show that its proteostatic function regulates the abundance of cytoskeletal proteins. More specifically, Cul3 controls actin-interacting proteins such as Pls3, for which we provide evidence that it might be a novel player regulating neuronal migration. Therefore, with respect to the concept of ASD-gene convergence, monogenic autism caused by *CUL3* mutations could be placed into the biologic ASD subgroup of proteins regulating cytoskeleton dynamics (Fig. 7). In addition, our findings that the early brain developmental defects caused by *CUL3* haploinsuffisciency might lie at the root of the phenotype manifestation in these patients, could one day inform drug development and clinical trial design.

6. SUPPLEMENTARY INFORMATION

6.1. Supplementary Figures

Supplementary Figure 1

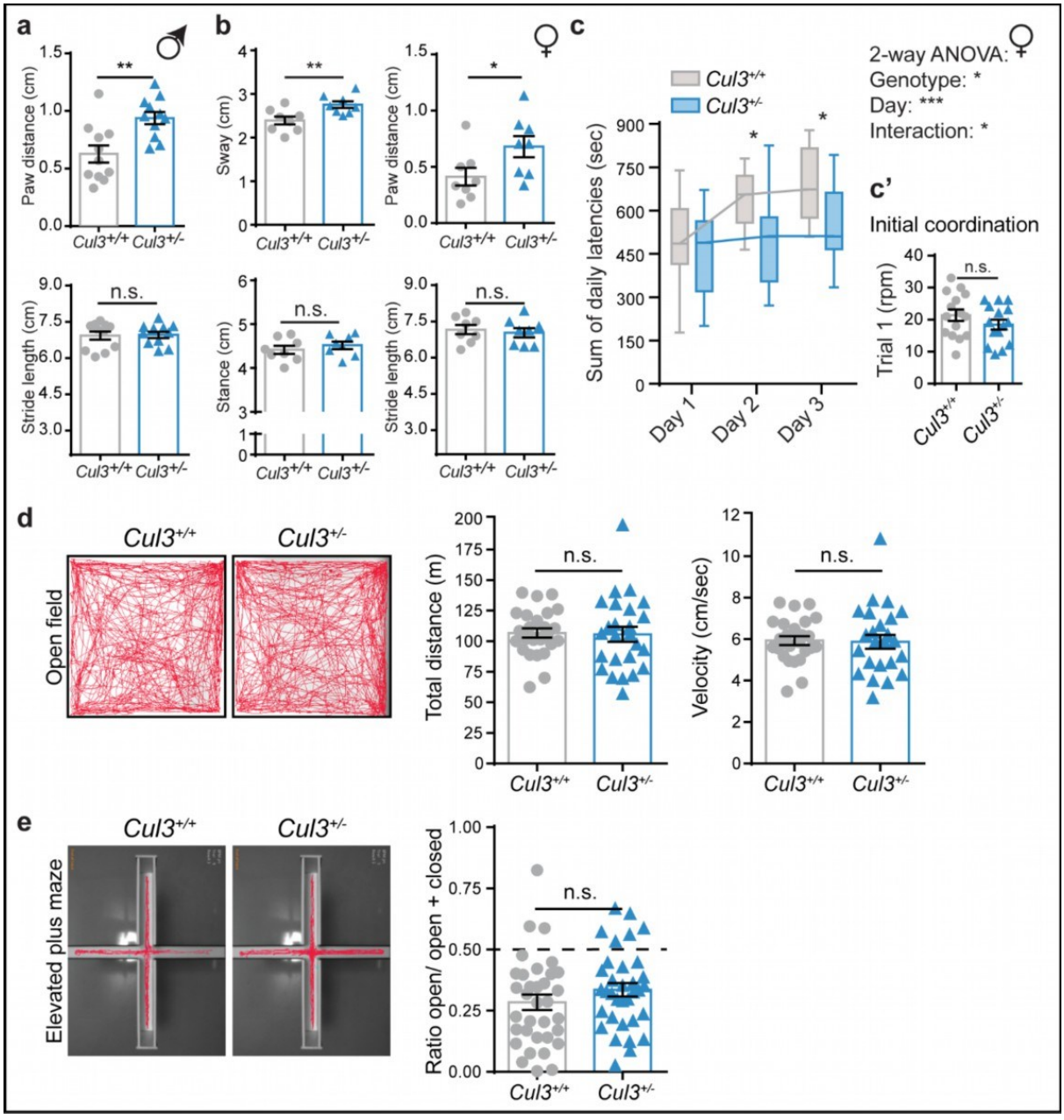

Supplementary Figure 1 (Related to Fig. 10)**: Further behavioral features of *Cul3* haploinsufficient mice. a**, Increased paw distance (top) but normal stride length (bottom) in *Cul3*$^{+/-}$ male animals (*n*= 11 male mice per genotype, littermates; **P<0.01; n.s. not significant; two-tailed Mann-Whitney U test or two-tailed t-test). **b,** Altered gait also in *Cul3* haploinsufficient female mice evidenced by inter-genotype comparison of sway (left top), stance length (left bottom), paw distance (right top) and stride length (right bottom) (*n*= 8 females per genotype, littermates; *P<0.05, **P<0.01, n.s. not significant; unpaired two-tailed t-tests). **c-c'**, Accelerating RotaRod test revealing defects in motor learning and coordination also in female *Cul3*$^{+/-}$ mice; shown are the sum of daily latencies of three trials per day on three consecutive days (c) and the final rpm on day one - trial 1, as measure of initial coordination (c') (*n*= 15 female littermate pairs per genotype; *P<0.05, n.s. not significant; 2way ANOVA and Sidak's multiple comparison test and unpaired two-tailed t-test). **d**, Normal exploratory behavior in the open field. Representative trajectories (left), and quantification of the total distance moved

(center) and velocity (right) reveal no differences between *Cul3*$^{+/+}$ and *Cul3*$^{+/-}$ mice (*n*= 25 sex-matched littermate pairs, females (*n*= 13) and males (*n*= 12); n.s. not significant; unpaired two-tailed t-tests). **e**, Performance of *Cul3*$^{+/-}$ mice in the elevated plus maze (total duration 6 min), representative trajectories (left) and quantification of the ratio of time spent on the open/ open+ closed arm (*n*= 34 sex-matched littermate pairs of wild-type and *Cul3*$^{+/-}$ animals, females (*n*= 15) and males (*n*= 19); n.s. not significant; unpaired two-tailed t-test). Data is presented as mean ± SEM.

Supplementary Figure 2

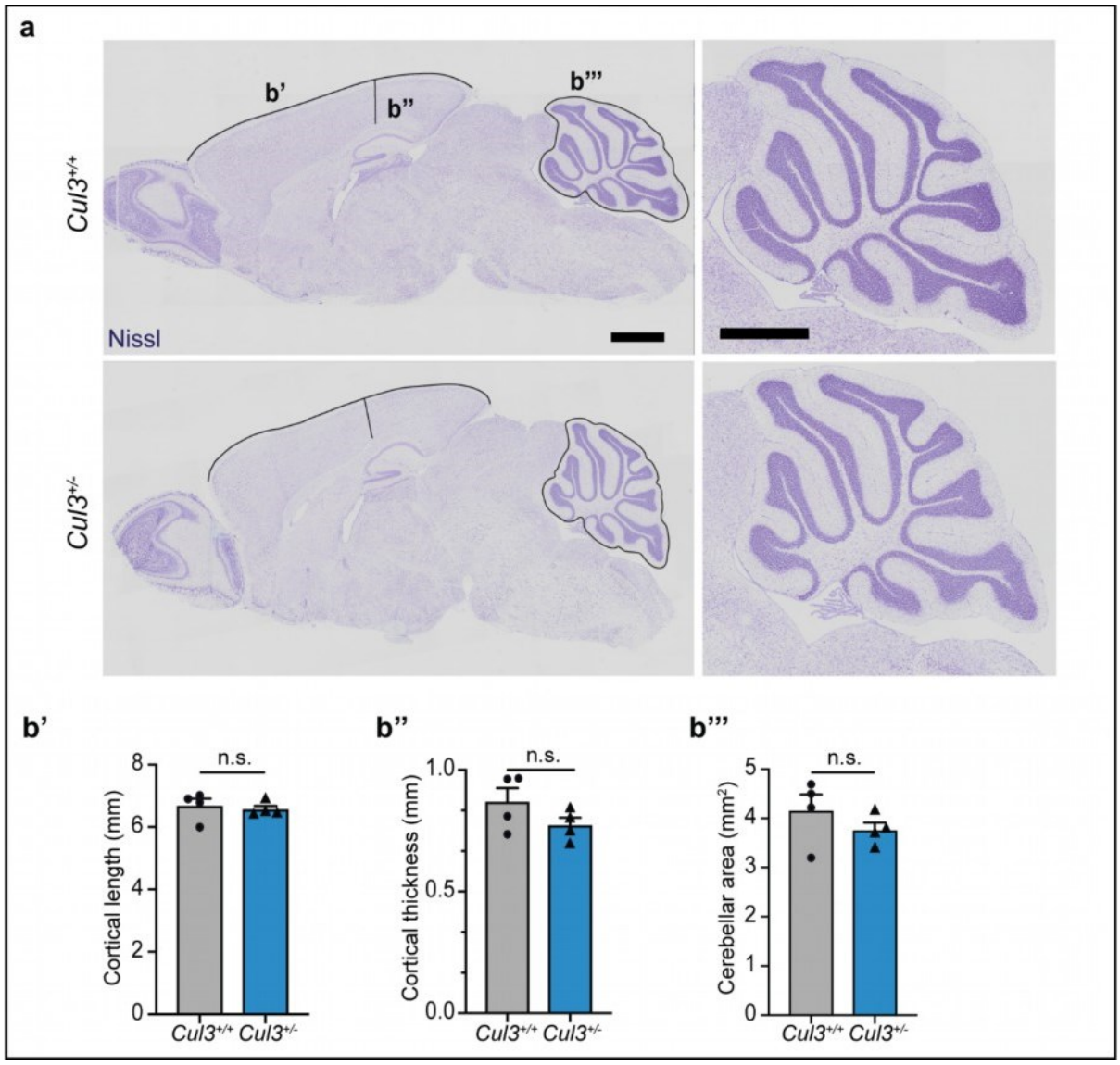

Supplementary Figure 2 (Related to Fig. 12)**: Gross brain morphology of *Cul3* haploinsufficient mice appears normal. a-b'''**, Overview (left) and cerebellar close-up (right) of Nissl stained adult sagittal brain sections and measurements of cortical length (b'), cortical thickness (b'') and cerebellar area (b''') confirmed these results, despite slight, yet not significant, decreases in the latter could be observed (*n*= 4 mice per genotype, littermates; n.s. not significant; unpaired two-tailed t-tests). Data is presented as mean ± SEM. Scale bar: 1 mm in (a, left and right).

Supplementary Figure 3

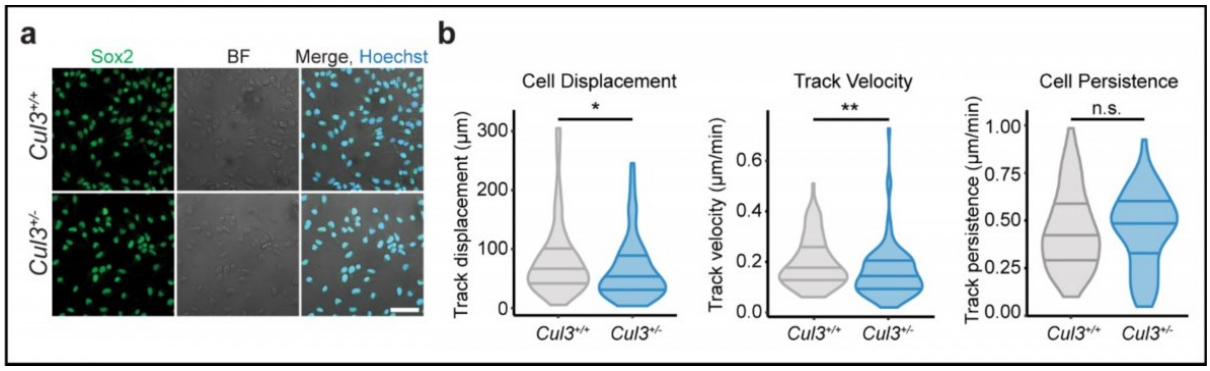

Supplementary Figure 3 (Related to Fig. 15)**: *Cul3* NPCs. a**, Representative pictures of *Cul3*$^{+/+}$ and *Cul3*$^{+/-}$ NPC preparations stained for Sox2. **b**, Cell tracks of NPCs detaching from neurosphere into embedding bovine collagen matrix imaged in a single plane. Cell displacement, cell velocity and migratory persistence were quantified in the imaging plane and compared between *Cul3*$^{+/+}$ and *Cul3*$^{+/-}$ cells (*n*(spheres)= 3 per genotype, *n*(cells)= 30 per replicate; *P<0.05; **P<0.01; Wilcoxon rank sum test). Data presented as mean ± SEM or violin plots with median and first and third quartiles. Scale bar: 25 µm in (a).

Supplementary Figure 4

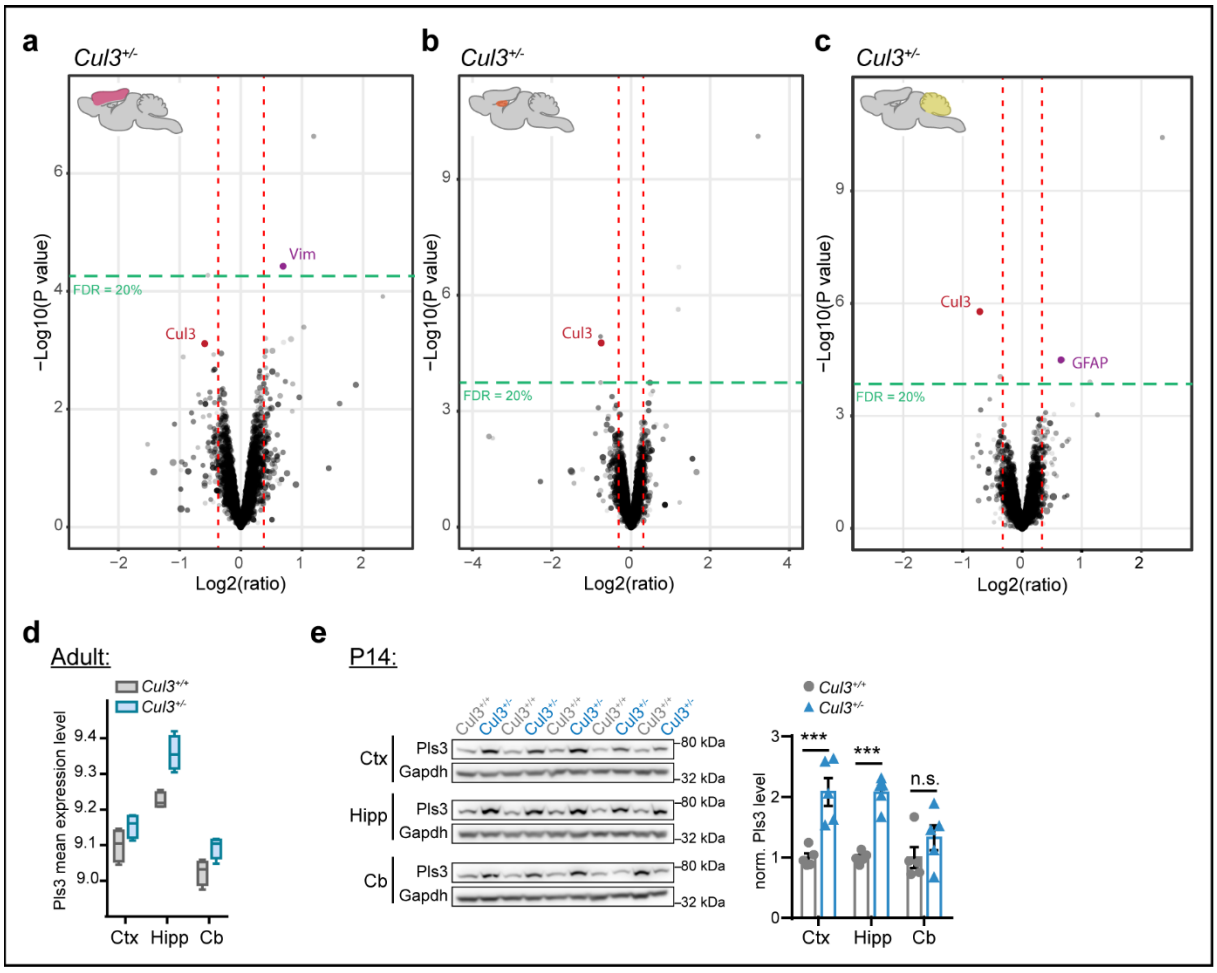

Supplementary Figure 4 (Related to Fig. 17)**: Minor protein composition alterations in the adult *Cul3*$^{+/-}$ brain.** **a**, Volcano plot of deregulated proteins at 20% FDR cut-off in the adult *Cul3*$^{+/-}$ cortex with 2 up- and 1 down-regulated protein (details in Table S7). **b**, Volcano plot of deregulated proteins at 20% FDR cut-off in the adult *Cul3*$^{+/-}$ hippocampus with 6 up- and 3 down-regulated proteins (details in Supplementary Table 8). **c**, Volcano plot of deregulated proteins at 20% FDR cut-off in the adult *Cul3*$^{+/-}$ cerebellum with 3 up- and 2 down-regulated proteins (details in Table S7). Purple: Cytoskeletal proteins, red: Cul3 (a-c). **d**, Raw protein expression levels indicate mildly elevated Pls3 levels in all analyzed adult *Cul3*$^{+/-}$ brain regions. **e**, Western blot (e, left) and analysis (e, right) of Gapdh* normalized intensities of Pls3 indicate an increase in all analyzed *Cul3*$^{+/-}$ juvenile (P14) brain regions (*n*= 5 per genotype; ***P<0.001, n.s. not significant; 2-way ANOVA and Sidak's multiple comparisons test).

Supplementary Figure 5

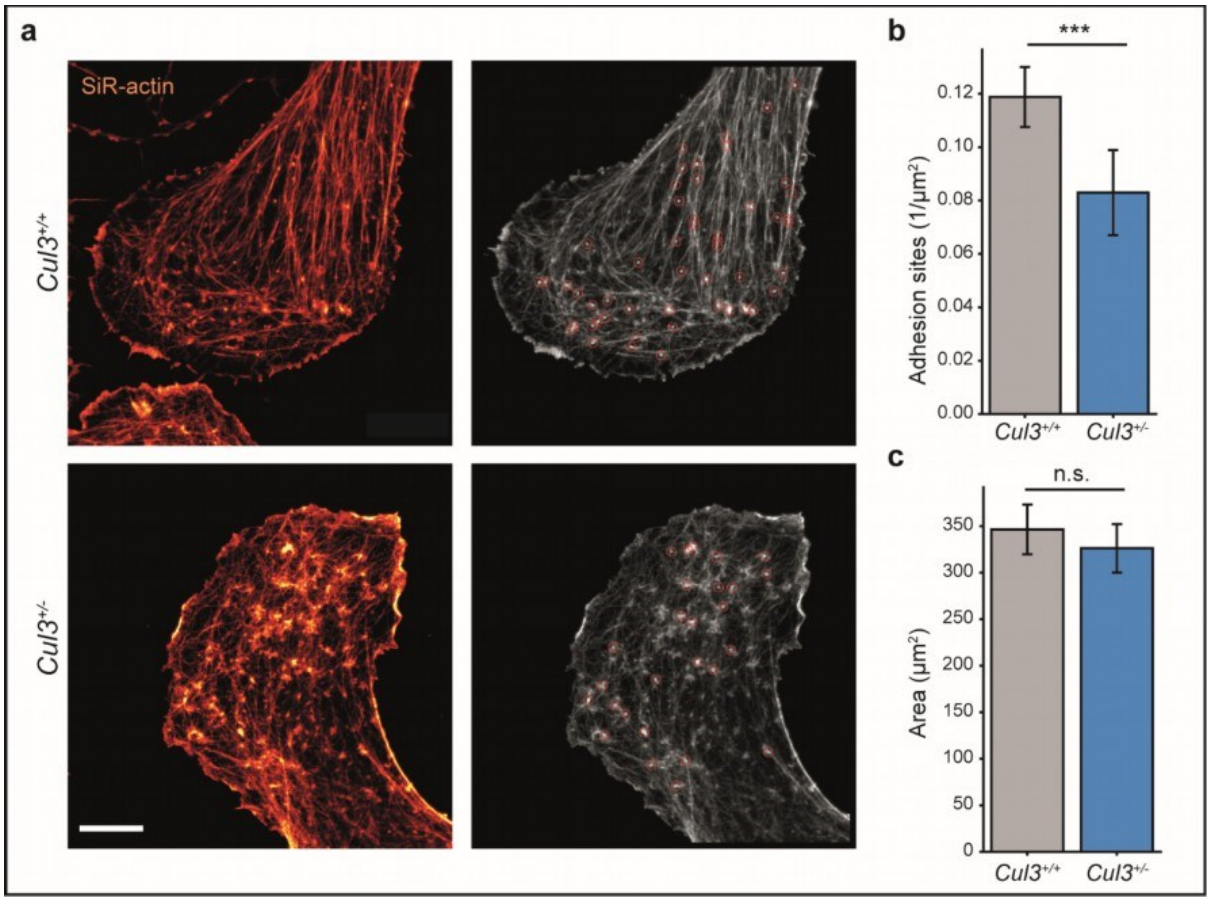

Supplementary Figure 5 (Related to Fig. 19)**: Decreased number of focal adhesions in *Cul3*$^{+/-}$ NPCs. a**, NPCs cultured on Poly-L-ornithine/Laminin were stained using SiR-actin (A) and cell protrusions were imaged employing STED-microscopy (same images as in Fig. 19). **b**, The number of bright SiR-actin puncta (red circles in a, right), putative focal adhesion sites, are reduced in *Cul3*$^{+/-}$ NPCs. Puncta were counted and normalized to the area (*n*(cells)= 43 per genotype from three independent NPCs preparations; ***P<0.001; two-tailed Welch's t-test). **c**, Analyzed areas are comparable between *Cul3*$^{+/+}$ and *Cul3*$^{+/-}$ cells (*n*(cells)= 43 per genotype from three independent NPCs preparations; n.s. not significant; two-tailed Welch's t-test). Data is presented as bar plots of mean ± SEM. Scale bar: 5 µm in (a).

Supplementary Figure 6

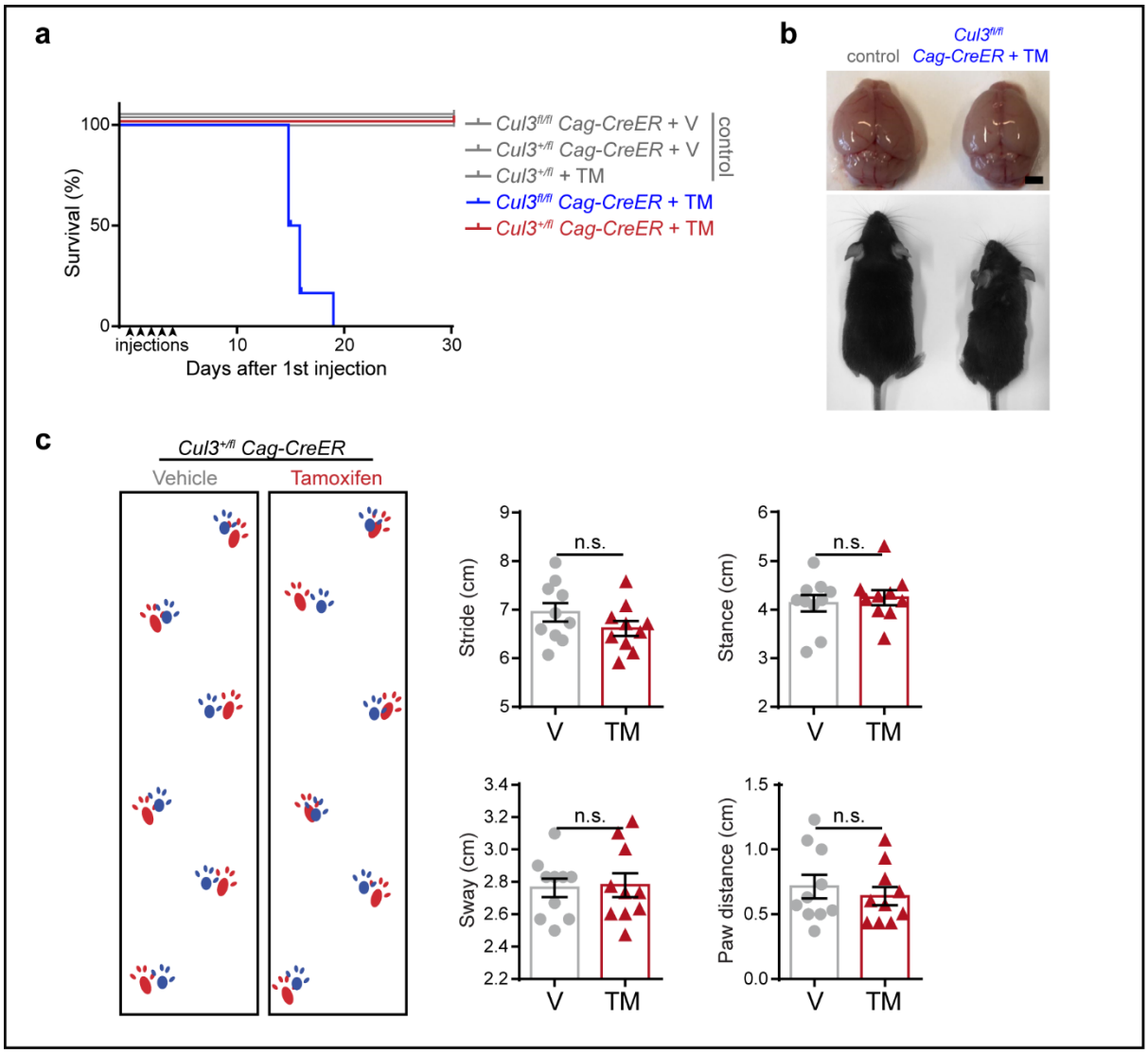

Supplementary Figure 6 (Related to Fig. 20)**: Further characterization of the conditional *Cul3* deletion in juvenile mice. a**, Mice with induced homozygous deletion of *Cul3* (*n(Cul3$^{fl/fl}$ Cag-CreER* + TM*)*= 6 mice) die within 20 days after the first tamoxifen injection. Instead, heterozygous conditional deletion (*n(Cul3$^{+/fl}$ Cag-CreER* + TM*)*= 24) does not alter the animals survival probability as compared to controls, they all survive into adulthood (*n(Cul3$^{+/fl}$* + TM*)*= 13, *n(Cul3$^{+/fl}$ Cag-CreER* + V*)*= 22, *n(Cul3$^{fl/fl}$ Cag-CreER* + V*)*= 2). **b**, Representative image of a *Cul3$^{fl/fl}$ Cag-CreER* + TM mice and a littermate control 15 days after the first TM injection (animal was found dead in the cage). **c**, Gait analysis of tamoxifen treated and vehicle treated *Cul3$^{+/fl}$ Cag-CreER* mice (representative foot-prints, left), did not reveal any difference between conditions, in stride, stance, sway or paw distance (*n*= 10 mice per condition; unpaired two-tailed t- tests). Data presented as % survival in (a) and scatter plot with mean ± SEM in (c). Scale bar: 2,5 mm in (b, top).

6.2. Supplementary Tables

Supplementary Table 1

Olfaction Habituation and Dishabituation Test (related to Fig. 10g).

Pairwise t-tests	Mean Diff.	Significant?	Summary	P Value	
Cul3+/+ wildtype					
Water-1 vs. Water-3	6,223	No	ns	0,0924	
Water-3 vs. Almond-1	-1,798	No	ns	0,6266	#
Almond-1 vs. Almond-3	3,325	No	ns	0,3682	#
Almond-3 vs. Banana-1	-10,34	Yes	**	0,0053	
Banana-1 vs. Banana-3	10,95	Yes	**	0,0031	
Banana-3 vs. Social-A-1	-37,39	Yes	****	< 0,0001	
Social-A-1 vs. Social-A-3	30,1	Yes	****	< 0,0001	
Social-A-3 vs. Social-B-1	-13,82	Yes	***	0,0002	
Social-B-1 vs. Social-B-3	18,54	Yes	****	< 0,0001	
Cul3+/- mutant					
Water-1 vs. Water-3	10,25	Yes	**	0,0057	
Water-3 vs. Almond-1	-3,949	No	ns	0,2853	#
Almond-1 vs. Almond-3	5,39	No	ns	0,1449	#
Almond-3 vs. Banana-1	-17,4	Yes	****	< 0,0001	
Banana-1 vs. Banana-3	18,69	Yes	****	< 0,0001	
Banana-3 vs. Social-A-1	-51	Yes	****	< 0,0001	
Social-A-1 vs. Social-A-3	38,68	Yes	****	< 0,0001	
Social-A-3 vs. Social-B-1	-22,9	Yes	****	< 0,0001	
Social-B-1 vs. Social-B-3	33,08	Yes	****	< 0,0001	

n.b. Almond odor did not elicit interest in either of the genotypes.

Sidak's multiple comp. test	Mean Diff.	95% CI of diff,	Significant?	Summary	Adj. P Value
Cul3+/+* vs. *Cul3+/-					
Water-1	-8,032	-20,80 to 4,741	No	ns	0,6358
Water-2	-5,366	-18,14 to 7,406	No	ns	0,9747
Water-3	-4,007	-16,78 to 8,766	No	ns	0,9987
Almond-1	-6,158	-18,93 to 6,614	No	ns	0,9229
Almond-2	-6,42	-19,19 to 6,352	No	ns	0,8962
Almond-3	-4,093	-16,87 to 8,679	No	ns	0,9983
Banana-1	-11,16	-23,93 to 1,616	No	ns	0,1463
Banana-2	-7,508	-20,28 to 5,264	No	ns	0,7345
Banana-3	-3,412	-16,18 to 9,361	No	ns	0,9998
Social-A-1	**-17,02**	**-29,79 to -4,249**	**Yes**	**	**0,0015**
Social-A-2	-12,53	-25,30 to 0,2414	No	ns	0,0593
Social-A-3	-8,444	-21,22 to 4,329	No	ns	0,5547
Social-B-1	**-17,52**	**-30,30 to -4,751**	**Yes**	***	**0,0009**
Social-B-2	-3,596	-16,37 to 9,177	No	ns	0,9996
Social-B-3	-2,984	-15,76 to 9,789	No	ns	> 0,9999

Supplementary Table 2

Deregulated proteins in the E16.5 *Cul3*$^{+/-}$ cortex (related to Fig. 17b).

Leading protein ID	Gene name	MW	Number of identified peptides	F-test: Mean log2(Ratio) - Cul3+/- vs Ctrl	F-test: Moderated -log10(Pvalue) - Cul3+/- vs Ctrl	F-test: Significant-FDR=10% - Cul3+/- vs Ctrl	F-test: Significant-FDR=20% - Cul3+/- vs Ctrl	F-test: Summary
B2RSN3	Tubb2b	50,0	46	-0,674	3,386	+	+	down, FDR = 10%
Q6ZQ84	Cul3	91,3	40	-0,696	11,126	+	+	down, FDR = 10%
F8VQC1	Srp72	74,7	32	-0,309	4,716	+	+	down, FDR = 10%
B1ATZ0	Hgs	85,8	29	-0,444	4,207	+	+	down, FDR = 10%
G3UZJ2	Map2	25,7	22	-0,493	5,466	+	+	down, FDR = 10%
P62715	Ppp2cb	35,6	18	-0,493	4,830	+	+	down, FDR = 10%
Q9CQ65	Mtap	31,1	17	-1,372	3,261	+	+	down, FDR = 10%
P51150	Rab7a	23,5	16	-0,319	2,419	+	+	down, FDR = 10%
E9QK48	Eml2	90,8	14	-0,309	3,780	+	+	down, FDR = 10%
Q91VL8	Terf2ip	43,4	13	-0,508	5,150	+	+	down, FDR = 10%
P60904	Dnajc5	22,1	13	-0,302	2,104	+	+	down, FDR = 10%
Q3TVW1	Spg20	72,7	12	-0,663	2,532	+	+	down, FDR = 10%
Q7M6Y2	Sox11	42,6	10	-0,358	2,021	+	+	down, FDR = 10%
H7BWZ3	Arpc3	19,6	9	-0,421	2,574	+	+	down, FDR = 10%
O35474	Edil3	53,7	8	-0,537	6,097	+	+	down, FDR = 10%
A2ABG4	Tbc1d16	86,5	8	-0,784	9,245	+	+	down, FDR = 10%
D3YVU4	Kdm2b	144,9	8	-0,364	3,920	+	+	down, FDR = 10%
P29699	Ahsg	37,3	7	-0,387	4,465	+	+	down, FDR = 10%
B2RPW2	Mief1	51,2	7	-0,303	3,538	+	+	down, FDR = 10%
Q3TC56	Oxa1l	48,4	6	-0,570	2,495	+	+	down, FDR = 10%
Q6P6M7	Sepsecs	55,3	5	-0,381	3,065	+	+	down, FDR = 10%
Q6P5F7	Ttyh3	57,7	5	-0,410	2,235	+	+	down, FDR = 10%
Q8BW22	Ss18l1	43,7	5	-0,358	4,983	+	+	down, FDR = 10%
A0A0G2JFS7	Ldb2	42,5	4	-0,305	3,992	+	+	down, FDR = 10%
D3YW47	Podxl2	65,0	4	-0,348	2,748	+	+	down, FDR = 10%
B2RQD1	Tmem121b	58,2	3	-0,306	2,113	+	+	down, FDR = 10%
A0A1D5RLR3	Rbm34	46,7	2	-0,363	3,024	+	+	down, FDR = 10%
E9Q2C0	Cfap46	302,6	2	-0,360	2,895	+	+	down, FDR = 10%
Q8VHZ7	Imp4	33,7	2	-0,739	3,325	+	+	down, FDR = 10%
Q499F8	Zfp445	114,7	2	-0,412	2,686	+	+	down, FDR = 10%
E0CY96	Tsen15	14,0	2	-0,373	2,436	+	+	down, FDR = 10%
Q8R2M0	Tceanc2	24,2	2	-0,325	2,210	+	+	down, FDR = 10%
Q059K7	Xk	51,1	2	-0,462	3,002	+	+	down, FDR = 10%
O35344	Kpna3	57,8	17	-0,347	1,567		+	down, FDR = 20%
Q6PCP5	Mff	32,9	14	-0,364	1,844		+	down, FDR = 20%
Q561M1	Acp1	17,9	11	-0,351	1,495		+	down, FDR = 20%
Q9QZD8	Slc25a10	31,7	9	-0,313	1,901		+	down, FDR = 20%
B2RRY4	Mpp5	77,2	8	-0,307	1,614		+	down, FDR = 20%
F8VPL2	Pik3c2a	190,7	4	-0,307	1,437		+	down, FDR = 20%

E9Q5G1	Myo10	151,6	3	-0,343	1,448		+	down, FDR = 20%
J3QNR6	Mapk8ip3	147,6	38	0,319	2,257	+	+	up, FDR = 10%
Q9Z277	Baz1b	170,7	35	0,308	2,451	+	+	up, FDR = 10%
P46660	Ina	55,4	34	0,407	5,287	+	+	up, FDR = 10%
B1AX58	Pls3	71,7	23	0,409	6,939	+	+	up, FDR = 10%
Q80XN0	Bdh1	38,3	22	0,381	2,913	+	+	up, FDR = 10%
E9QNE9	Map4k3	101,3	21	0,439	5,252	+	+	up, FDR = 10%
Q8CJF7	Ahctf1	247,6	16	0,395	4,530	+	+	up, FDR = 10%
Q3TUI3	Brd3	79,8	16	0,368	2,462	+	+	up, FDR = 10%
E9Q4P1	Wdfy1	46,2	12	2,623	9,436	+	+	up, FDR = 10%
Q6IQX8	Znf219	77,8	11	0,329	6,011	+	+	up, FDR = 10%
A0A0U1RP94	Csnk1g1	53,0	11	0,313	3,779	+	+	up, FDR = 10%
A0A1L1SR96	Ano8	124,0	11	0,352	2,753	+	+	up, FDR = 10%
B1AW58	Camk1d	42,9	10	0,433	2,507	+	+	up, FDR = 10%
D3YVW2	Golim4	79,9	9	0,937	2,797	+	+	up, FDR = 10%
Q3TYX3	Smyd5	47,1	9	0,512	5,820	+	+	up, FDR = 10%
Q6KAU3	Mrps25	19,1	8	0,352	7,153	+	+	up, FDR = 10%
A0A0A6YY64	Pfkfb3	57,3	7	0,472	7,008	+	+	up, FDR = 10%
A2NHM3	Igkc	24,2	5	0,684	5,029	+	+	up, FDR = 10%
O88845	Akap10	73,6	5	0,350	5,446	+	+	up, FDR = 10%
Q9CWR1	Wdr73	40,9	5	0,540	9,621	+	+	up, FDR = 10%
Q9ESP1	Sdf2l1	23,6	5	0,386	2,255	+	+	up, FDR = 10%
Q9CYX7	Rrp15	31,1	4	0,324	7,405	+	+	up, FDR = 10%
Q8K4F6	Nsun5	51,0	4	0,473	4,378	+	+	up, FDR = 10%
Q3V0K9	Pls1	70,4	4	0,684	7,791	+	+	up, FDR = 10%
Q3UHX9	Spout1	43,0	4	0,311	4,756	+	+	up, FDR = 10%
Q9WTV7	Rlim	66,4	3	0,363	2,124	+	+	up, FDR = 10%
Q80UW0	Hs6st2	69,2	3	0,420	4,131	+	+	up, FDR = 10%
Q059T5	Mgat5	84,6	2	0,324	3,887	+	+	up, FDR = 10%
B2RPS7	Trpc1	92,7	2	0,344	2,384	+	+	up, FDR = 10%
Q9CR60	Golt1b	15,4	2	0,722	4,581	+	+	up, FDR = 10%
Q9DB30	Phkg2	46,6	2	0,345	3,817	+	+	up, FDR = 10%
Q64511	Top2b	181,9	32	0,325	1,892		+	up, FDR = 20%
Q8C605	Pfkp	85,5	11	0,460	1,609		+	up, FDR = 20%
Q3UL50	Wdr74	37,8	6	0,362	1,824		+	up, FDR = 20%
Q9DAX9	Appbp2	66,9	4	0,342	1,949		+	up, FDR = 20%
Q9CXP8	Gng10	7,2	3	0,340	1,733		+	up, FDR = 20%
Q9CRA4	Msmo1	34,8	3	0,321	1,847		+	up, FDR = 20%

Supplementary Table 3

Deregulated proteins in the E16.5 *Cul3*$^{+/fl}$ *Emx1-Cre* cortex (related to Fig. 17c).

Leading protein ID	Gene name	MW	Number of identified peptides	F-test: Mean log2(Ratio) - Cul3+/fl Emx1-Cre vs Ctrl	F-test: Moderated -log10(Pvalue) - Cul3+/fl Emx1-Cre vs Ctrl	F-test: Significant-FDR=10% - Cul3+/fl Emx1-Cre vs Ctrl	F-test: Significant-FDR=20% - Cul3+/fl Emx1-Cre vs Ctrl	F-test: Summary
Q6ZQ84	Cul3	91,3	40	-0,497	6,751	+	+	down, FDR = 10%
Q8CI71	Vps50	111,2	33	-0,482	2,106	+	+	down, FDR = 10%
Q80TR8	Dcaf1	168,9	24	-0,336	3,807	+	+	down, FDR = 10%
A2AL50	Agps	74,3	19	-0,386	2,254	+	+	down, FDR = 10%
Q8C078	Camkk2	64,6	17	-0,344	2,991	+	+	down, FDR = 10%
Q9CW79	Golga1	87,3	16	-0,363	2,368	+	+	down, FDR = 10%
Q8K2D8	Fibp	41,9	15	-0,350	2,387	+	+	down, FDR = 10%
Q5NBY9	Patz1	74,1	14	-0,308	2,815	+	+	down, FDR = 10%
Q6DIC6	Tro	206,0	11	-0,306	4,129	+	+	down, FDR = 10%
Q6PE15	Abhd10	33,0	11	-0,327	2,285	+	+	down, FDR = 10%
D3YW42	Ccdc9	65,9	10	-0,518	6,038	+	+	down, FDR = 10%
D3YVW2	Golim4	79,9	9	-0,771	2,161	+	+	down, FDR = 10%
E9PYB1	Tbc1d14	47,6	7	-0,300	3,485	+	+	down, FDR = 10%
Q8VBV7	Cops8	23,3	7	-0,484	2,068	+	+	down, FDR = 10%
Q8K1H7	Tcp11l2	57,9	6	-0,384	2,607	+	+	down, FDR = 10%
Q99M28	Rnps1	34,2	6	-0,347	3,852	+	+	down, FDR = 10%
A2AHX9	Bcl2l1	17,1	5	-0,331	2,526	+	+	down, FDR = 10%
Q6PDJ1	Cachd1	143,8	5	-0,408	4,364	+	+	down, FDR = 10%
Q3U6N9		24,5	5	-0,312	2,488	+	+	down, FDR = 10%
O09114	Ptgds	21,1	4	-0,306	3,157	+	+	down, FDR = 10%
Q78H73	Slc35c1	40,0	2	-0,692	1,986	+	+	down, FDR = 10%
Q61753	Phgdh	56,6	23	-0,560	1,460		+	down, FDR = 20%
Q3UI30	Ewsr1	68,6	12	-0,339	1,894		+	down, FDR = 20%
Q8BKP2	Zfp189	70,5	7	-2,471	1,529		+	down, FDR = 20%
P63248	Pkia	8,0	4	-0,314	1,769		+	down, FDR = 20%
O88512	Ap1g2	87,9	4	-1,254	1,543		+	down, FDR = 20%
Q04890	Sox12	34,1	4	-1,488	1,439		+	down, FDR = 20%
E9PV66	Myo18b	288,9	3	-4,749	1,470		+	down, FDR = 20%
G5E898	Ppl	203,8	3	-1,852	1,490		+	down, FDR = 20%
Q2TL60	Znf667	70,3	3	-4,492	1,442		+	down, FDR = 20%
A2AW13	Ttbk2	96,2	3	-1,196	1,427		+	down, FDR = 20%
Q69ZR3	Galnt16	72,8	3	-0,521	1,717		+	down, FDR = 20%
Q9D0M2	Cdca7	43,8	2	-1,064	1,685		+	down, FDR = 20%
Q8VHZ7	Imp4	33,7	2	-0,660	1,963		+	down, FDR = 20%
A0A2X0SFE3	ECT2	103,4	2	-2,668	1,630		+	down, FDR = 20%
G3UZT8	Jarid2	114,1	2	-2,228	1,443		+	down, FDR = 20%

F7CJR1	Rad1	18,2	2	-0,693	1,621		+	down, FDR = 20%
E0CYY3	Ankmy1	112,6	2	-2,353	1,445		+	down, FDR = 20%
G5E8B1	Ptpn13	270,2	2	-1,804	1,493		+	down, FDR = 20%
J3QMX8	Slc30a6	51,7	2	-3,342	1,483		+	down, FDR = 20%
P14106	C1qb	26,7	2	-1,741	1,943		+	down, FDR = 20%
Q9CZ09	Mettl18	40,4	2	-0,458	1,658		+	down, FDR = 20%
P62325	Btg1	19,2	2	-2,194	1,452		+	down, FDR = 20%
D3Z3Y1	Pigg	108,5	2	-0,917	1,719		+	down, FDR = 20%
D3Z216	Tab2	60,2	2	-1,329	1,469		+	down, FDR = 20%
Q3UK98	Cbx6	42,5	2	-1,943	1,561		+	down, FDR = 20%
Q4FJY2	Ube2l6	17,7	2	-2,503	1,427		+	down, FDR = 20%
G5E8B9	Zbtb11	118,6	2	-0,642	1,637		+	down, FDR = 20%
A0A0R4J012	Fam84a	32,7	2	-1,050	1,427		+	down, FDR = 20%
B1AV66	Yipf6	21,8	2	-1,725	1,684		+	down, FDR = 20%
Q9CPV3	Mrpl42	16,5	2	-1,759	1,573		+	down, FDR = 20%
P56960	Exosc10	100,9	40	0,311	4,121	+	+	up, FDR = 10%
A0PJL3	Sarm1	77,3	36	0,416	3,130	+	+	up, FDR = 10%
Q8BRB1	Epha3	110,0	28	0,333	4,400	+	+	up, FDR = 10%
A0A1B0GSX0	Ldha	39,8	27	0,400	2,732	+	+	up, FDR = 10%
Q9Z0E0	Ncdn	78,9	26	0,311	2,240	+	+	up, FDR = 10%
B1AX58	Pls3	71,7	23	0,333	5,197	+	+	up, FDR = 10%
Q8R307	Vps18	110,2	23	0,469	4,895	+	+	up, FDR = 10%
P26369	U2af2	53,5	22	0,342	2,644	+	+	up, FDR = 10%
Q3TJL8	Pdia6	48,7	22	0,304	5,310	+	+	up, FDR = 10%
O08715	Akap1	92,2	20	0,345	2,059	+	+	up, FDR = 10%
D3Z7B5	Cip2a	102,1	20	0,311	4,780	+	+	up, FDR = 10%
Q8BW72	Kdm4a	120,3	18	0,362	2,332	+	+	up, FDR = 10%
G1UCX4	Saal1	52,8	15	0,372	2,828	+	+	up, FDR = 10%
Q3V2R3	Chn2	53,8	14	0,324	2,434	+	+	up, FDR = 10%
Q3UA06	Trip13	48,4	14	0,494	3,191	+	+	up, FDR = 10%
Q5NCR9	Nsrp1	63,8	13	0,372	3,389	+	+	up, FDR = 10%
A2AQN4	Acss2	80,4	13	0,319	2,749	+	+	up, FDR = 10%
Q3URU4	Mre11a	80,2	13	0,438	5,385	+	+	up, FDR = 10%
A0A0F6AIX5	Ldah	37,4	10	0,411	2,835	+	+	up, FDR = 10%
O70152	Dpm1	29,2	10	0,382	2,982	+	+	up, FDR = 10%
Q3TCI2	Amfr	72,8	9	0,464	3,405	+	+	up, FDR = 10%
Q6A0D4	Rftn1	61,5	9	0,351	2,488	+	+	up, FDR = 10%
Q99M01	Fars2	52,3	8	0,358	4,057	+	+	up, FDR = 10%
Q3U0V3	Ankrd13a	67,2	7	0,336	4,805	+	+	up, FDR = 10%
P12265	Gusb	74,2	7	0,402	4,365	+	+	up, FDR = 10%
Q80U04	Pja2	78,0	6	0,357	3,358	+	+	up, FDR = 10%
Q04841	Mpg	36,5	6	0,369	3,650	+	+	up, FDR = 10%
Q9QZX7	Srr	36,4	5	0,340	2,567	+	+	up, FDR = 10%
Q9CWQ0	Dph5	31,2	4	0,549	3,309	+	+	up, FDR = 10%
A0A1W2P7Y1	Ptprk	166,0	3	0,322	4,573	+	+	up, FDR = 10%
Q80Y44	Ddx10	100,7	3	0,304	5,295	+	+	up, FDR = 10%
A2AIR7	Cacna1b	261,6	3	0,749	2,005	+	+	up, FDR = 10%
O88829	St3gal5	47,4	3	0,333	4,583	+	+	up, FDR = 10%
B1AQN2	Ptprt	163,0	3	0,906	2,760	+	+	up, FDR = 10%
G5E861	Sclt1	80,5	2	0,341	2,803	+	+	up, FDR = 10%

F8WIG5	Diaph3	133,7	2	0,382	2,258	+	+	up, FDR = 10%
Q53YU5	Nol3	24,6	2	0,489	5,875	+	+	up, FDR = 10%
Q3USZ8	1190002N15Rik	49,5	2	0,541	2,934	+	+	up, FDR = 10%
E9QAQ7	Arid1a	242,7	54	0,358	1,426		+	up, FDR = 20%
Q3TMM5	Nono	54,5	41	2,955	1,686		+	up, FDR = 20%
A0A1S6GWG6	Atp6v1b2	59,3	30	0,498	1,800		+	up, FDR = 20%
E9PYT3	Atl3	60,2	14	0,403	1,581		+	up, FDR = 20%
E9Q4P1	Wdfy1	46,2	12	0,836	1,522		+	up, FDR = 20%
O35984	Pbx2	45,8	8	0,800	1,928		+	up, FDR = 20%
A0A0G2JEM5	D3Ertd254e	91,7	6	0,762	1,598		+	up, FDR = 20%
P41233	Abca1	253,9	4	0,371	1,798		+	up, FDR = 20%
A6ZI44	Aldoa	45,1	4	0,316	1,723		+	up, FDR = 20%
Q3U417	Ppfibp1	108,5	3	1,478	1,464		+	up, FDR = 20%
B7ZNA5	Phc3	102,4	3	0,575	1,522		+	up, FDR = 20%
Q8C5G2	Vash2	40,5	3	1,030	1,692		+	up, FDR = 20%
A2AH60	Klhl8	61,3	2	2,505	1,479		+	up, FDR = 20%
A0A0R4J113	Myo7a	249,8	2	2,393	1,491		+	up, FDR = 20%
O35134	Polr1a	194,1	2	0,963	1,839		+	up, FDR = 20%
A2A9V7	Slc25a19	25,3	2	0,605	1,437		+	up, FDR = 20%
Q05CS3	Cyp39a1	45,8	2	1,952	1,525		+	up, FDR = 20%
D6RG69	Ccdc167	6,2	2	1,679	1,724		+	up, FDR = 20%
Q54AA2	Pycard	21,5	2	1,702	1,814		+	up, FDR = 20%
E9PYL4	Clcn7	86,5	2	0,950	1,650		+	up, FDR = 20%
Q80XT2	Abca3	172,5	2	0,375	1,630		+	up, FDR = 20%
A2VDF7	Slc4a4	118,8	2	1,110	1,480		+	up, FDR = 20%
Q9CPV2	Anapc16	11,7	2	1,551	1,503		+	up, FDR = 20%
Q9D0F1	Ndc80	74,0	2	1,164	1,464		+	up, FDR = 20%
B1AV57	Pithd1	13,8	2	1,724	1,530		+	up, FDR = 20%
Q7TN02	Med26	64,7	2	1,071	1,652		+	up, FDR = 20%
Q8BSC6	1700084E18Rik	24,7	2	3,162	1,433		+	up, FDR = 20%
B1AUE5	Pex10	37,2	2	0,867	1,706		+	up, FDR = 20%

Supplementary Table 4

Deregulated proteins in the E16.5 *Cul3*$^{fl/fl}$ *Emx1-Cre* cortex (related to Fig. 17d).

Leading protein ID	Gene name	MW	Number of identified peptides	F-test: Mean log2(Ratio) - Cul3fl/fl Emx1-Cre vs Ctrl	F-test: Moderated -log10(Pvalue) - Cul3fl/fl Emx1-Cre vs Ctrl	F-test: Significant-FDR=10% - Cul3fl/fl Emx1-Cre vs Ctrl	F-test: Significant-FDR=20% - Cul3fl/fl Emx1-Cre vs Ctrl	F-test: Summary
A0A0A0MQ	Ttc28	270,8	41	-0,328	3,539	+	+	down, FDR = 10%
Q6ZQ84	Cul3	91,3	40	-0,914	12,225	+	+	down, FDR = 10%
A0A087WQ	Xrn1	194,3	36	-0,599	5,352	+	+	down, FDR = 10%
Q3UHF7	Hivep2	266,7	35	-0,615	7,614	+	+	down, FDR = 10%
P54227	Stmn1	17,3	32	-0,310	2,495	+	+	down, FDR = 10%
Q3TG12	Farsb	65,6	31	-0,472	6,702	+	+	down, FDR = 10%
Q61548	Snap91	91,9	30	-0,315	3,384	+	+	down, FDR = 10%
Q6DI95	Tnpo3	104,2	28	-0,384	5,455	+	+	down, FDR = 10%
P62702	Rps4x	29,6	25	-0,749	5,513	+	+	down, FDR = 10%
Q6P9P6	Kif11	118,0	24	-0,316	3,495	+	+	down, FDR = 10%
A0A0G2JEG	Amph	75,3	24	-0,496	2,250	+	+	down, FDR = 10%
G3UZJ2	Map2	25,7	22	-0,623	6,156	+	+	down, FDR = 10%
Q3U2P1	Sec24a	118,8	21	-0,347	5,397	+	+	down, FDR = 10%
Q3TN31	Psma7	27,9	18	-0,348	2,514	+	+	down, FDR = 10%
O70435	Psma3	28,4	18	-0,345	3,942	+	+	down, FDR = 10%
A2ALV3	Sh3gl2	48,3	18	-0,392	5,281	+	+	down, FDR = 10%
Q6PHU5	Sort1	91,2	18	-0,406	2,898	+	+	down, FDR = 10%
P05063	Aldoc	39,4	18	-0,326	4,902	+	+	down, FDR = 10%
Q3UGE1	Trappc12	87,7	17	-0,363	3,736	+	+	down, FDR = 10%
Q8C078	Camkk2	64,6	17	-0,387	3,990	+	+	down, FDR = 10%
Q8BHZ0	Fam49a	37,3	17	-0,374	2,810	+	+	down, FDR = 10%
Q8K0C9	Gmds	42,0	16	-0,489	2,737	+	+	down, FDR = 10%
Q9CQF3	Nudt21	26,2	15	-0,308	2,448	+	+	down, FDR = 10%
P49722	Psma2	25,9	15	-0,493	3,265	+	+	down, FDR = 10%
Q8BTG3	Tcp11l1	56,3	15	-0,332	2,714	+	+	down, FDR = 10%
P70195	Psmb7	29,9	15	-0,603	4,082	+	+	down, FDR = 10%
O35066	Kif3c	90,0	14	-0,444	7,015	+	+	down, FDR = 10%
E9PYT3	Atl3	60,2	14	-0,473	2,032	+	+	down, FDR = 10%
Q8VDK1	Nit1	35,7	14	-0,487	3,749	+	+	down, FDR = 10%
Q6P9S0	Mtss1l	76,8	14	-0,412	6,849	+	+	down, FDR = 10%
Q9R1P3	Psmb2	22,9	14	-0,312	2,940	+	+	down, FDR = 10%
A0A286YDL	Camk2g	26,0	14	-0,308	4,015	+	+	down, FDR = 10%
Q3TGR2	Fgb	54,8	13	-0,461	3,182	+	+	down, FDR = 10%
Q5NCR9	Nsrp1	63,8	13	-0,482	5,137	+	+	down, FDR = 10%
P08414	Camk4	52,6	13	-0,380	3,469	+	+	down, FDR = 10%

Q8BRG8	Tmem209	63,0	13	-0,320	2,789	+	+	down, FDR = 10%
Q14B01	Rnf113a2	38,1	13	-0,330	2,331	+	+	down, FDR = 10%
P99026	Psmb4	29,1	13	-0,429	3,438	+	+	down, FDR = 10%
Q3UU20	Hid1	88,7	12	-0,327	4,003	+	+	down, FDR = 10%
P51880	Fabp7	14,9	11	-0,316	2,877	+	+	down, FDR = 10%
Q3TCJ1	Abraxas2	46,9	11	-0,347	3,934	+	+	down, FDR = 10%
Q00896	Serpina1c	45,8	11	-0,312	5,002	+	+	down, FDR = 10%
P97314	Csrp2	20,9	11	-0,350	5,534	+	+	down, FDR = 10%
P53668	Limk1	72,8	11	-0,484	3,488	+	+	down, FDR = 10%
Q9CZV8	Fbxl20	48,4	10	-0,423	3,072	+	+	down, FDR = 10%
A0A0A0MQ	Kmt2d	600,3	10	-0,364	4,010	+	+	down, FDR = 10%
Q3TMN8	Prkag2	37,3	10	-0,370	7,028	+	+	down, FDR = 10%
Q6P3A8	Bckdhb	42,9	10	-0,327	2,378	+	+	down, FDR = 10%
A0A1D5RL9	A830010M20	190,8	9	-0,362	4,829	+	+	down, FDR = 10%
Q91YP3	Dera	35,0	9	-0,324	3,225	+	+	down, FDR = 10%
D3YVW2	Golim4	79,9	9	-0,902	2,585	+	+	down, FDR = 10%
Q71FD5	Znrf2	23,7	9	-0,334	5,337	+	+	down, FDR = 10%
Q2M3X8	Phactr1	66,3	9	-0,350	3,309	+	+	down, FDR = 10%
D3Z1C5	Ldb1	42,6	9	-0,398	3,983	+	+	down, FDR = 10%
Q9DBE9	Ftsj3	95,5	9	-0,483	4,192	+	+	down, FDR = 10%
D3YVU0	Usp46	39,5	8	-0,313	2,777	+	+	down, FDR = 10%
A0A0R4J056	Bhlhe22	35,1	8	-0,353	3,680	+	+	down, FDR = 10%
B1AS37	Ssbp3	38,2	7	-0,680	5,705	+	+	down, FDR = 10%
P29699	Ahsg	37,3	7	-0,405	4,087	+	+	down, FDR = 10%
A2RTI3	Lgmn	49,4	7	-0,383	4,957	+	+	down, FDR = 10%
A0A1W2P6I	Klhl29	87,6	7	-0,425	5,578	+	+	down, FDR = 10%
A2AG68	Atp7a	162,0	6	-0,675	5,191	+	+	down, FDR = 10%
Q3TKN7	Commd10	22,8	6	-0,302	4,483	+	+	down, FDR = 10%
A2RS63	Cuedc1	42,8	6	-0,436	3,756	+	+	down, FDR = 10%
Q80U30	Clec16a	116,2	6	-0,310	2,649	+	+	down, FDR = 10%
Q4KMS1	Trim44	38,1	5	-0,348	2,407	+	+	down, FDR = 10%
Q64322	Npdc1	35,7	5	-0,464	7,311	+	+	down, FDR = 10%
F6QM56	Pgghg	77,4	5	-0,339	2,522	+	+	down, FDR = 10%
A0A1B0GSJ1	Tti2	59,7	5	-0,452	4,284	+	+	down, FDR = 10%
A0A0R4J0Q	Trim56	79,5	5	-0,378	4,790	+	+	down, FDR = 10%
P97364	Sephs2	47,8	5	-0,626	2,502	+	+	down, FDR = 10%
Q6PDJ1	Cachd1	143,8	5	-0,710	7,109	+	+	down, FDR = 10%
A0A1B0GR8	2900026A02I	192,7	4	-0,357	2,840	+	+	down, FDR = 10%
O09114	Ptgds	21,1	4	-0,362	4,781	+	+	down, FDR = 10%
Q9JKX4	Aatf	59,5	4	-0,472	5,272	+	+	down, FDR = 10%
Q149L6	Dnajb14	42,3	4	-0,394	4,305	+	+	down, FDR = 10%
D3YW47	Podxl2	65,0	4	-0,506	3,711	+	+	down, FDR = 10%
E0CYX9	Ccdc127	27,7	3	-1,220	2,027	+	+	down, FDR = 10%
Q70IV5	Synm	173,2	3	-3,149	2,012	+	+	down, FDR = 10%
J3JS86	Cep112	117,9	3	-0,515	4,650	+	+	down, FDR = 10%
A2ANP1	Fam219a	18,7	3	-0,371	2,480	+	+	down, FDR = 10%
E9PYP2	Nbeal1	306,2	3	-0,482	4,435	+	+	down, FDR = 10%
Q8BFZ3	Actbl2	42,0	3	-0,623	2,521	+	+	down, FDR = 10%
Q8R554	Otud7a	100,8	3	-0,401	5,527	+	+	down, FDR = 10%
D3Z5V4	Fam124a	59,3	3	-0,392	5,142	+	+	down, FDR = 10%

A0A1W6AW	Nrm	22,4	2	-0,601	4,391	+	+	down, FDR = 10%
Q8R216	Sirt4	37,5	2	-0,381	4,077	+	+	down, FDR = 10%
A4FU75	Dagla	115,2	2	-0,502	4,939	+	+	down, FDR = 10%
H3BLB7	Igfbp4	18,1	2	-0,400	3,081	+	+	down, FDR = 10%
Q91XC9	Pex16	38,7	2	-0,660	2,034	+	+	down, FDR = 10%
E9PZD2	Micall2	98,8	2	-0,328	2,133	+	+	down, FDR = 10%
Q6IQX7	Chpf	85,5	2	-0,474	2,212	+	+	down, FDR = 10%
E0CY96	Tsen15	14,0	2	-0,855	4,451	+	+	down, FDR = 10%
A0A0J9YUN	Dnm1	97,3	50	-2,948	1,438		+	down, FDR = 20%
Q8VDM6	Hnrnpul1	96,0	39	-2,759	1,803		+	down, FDR = 20%
D3YXA6	Trim46	80,9	29	-0,367	1,738		+	down, FDR = 20%
Q3UE92	Xpnpep1	74,6	28	-0,303	1,427		+	down, FDR = 20%
Q80XP9	Wnk3	194,0	24	-0,663	1,465		+	down, FDR = 20%
O09012	Pex5	70,8	22	-0,386	1,815		+	down, FDR = 20%
O55234	Psmb5	28,5	17	-0,335	1,758		+	down, FDR = 20%
P60904	Dnajc5	22,1	13	-0,310	1,879		+	down, FDR = 20%
Q4KL82	Rfc2	38,7	13	-0,352	1,839		+	down, FDR = 20%
Q3T9Z2	Grhpr	35,3	12	-0,343	1,442		+	down, FDR = 20%
Q561M1	Acp1	17,9	11	-6,734	1,445		+	down, FDR = 20%
Q545G0	Psmb3	23,0	10	-0,329	1,777		+	down, FDR = 20%
A0A0R4J1D5	Fgd3	58,8	8	-0,474	1,911		+	down, FDR = 20%
O70546	Kdm6a	154,4	7	-0,408	1,426		+	down, FDR = 20%
Q8BKP2	Zfp189	70,5	7	-2,538	1,539		+	down, FDR = 20%
D3Z494	Akr1b10	32,7	7	-0,553	1,898		+	down, FDR = 20%
A0A286YDX	Kif13a	117,3	5	-1,379	1,610		+	down, FDR = 20%
E0CXS4	Grip2	107,6	4	-5,722	1,436		+	down, FDR = 20%
F6V3Y9	Atg2a	188,6	4	-0,448	1,807		+	down, FDR = 20%
Q61599	Arhgdib	22,9	4	-0,305	1,925		+	down, FDR = 20%
O88512	Ap1g2	87,9	4	-1,207	1,425		+	down, FDR = 20%
Q04890	Sox12	34,1	4	-1,641	1,691		+	down, FDR = 20%
Q9DA75	Mfsd2a	59,0	3	-0,476	1,567		+	down, FDR = 20%
G5E898	Ppl	203,8	3	-1,860	1,680		+	down, FDR = 20%
Q2TL60	Znf667	70,3	3	-4,439	1,440		+	down, FDR = 20%
A2AW13	Ttbk2	96,2	3	-1,185	1,630		+	down, FDR = 20%
E9Q5G1	Myo10	151,6	3	-5,630	1,469		+	down, FDR = 20%
Q69ZR3	Galnt16	72,8	3	-0,485	1,973		+	down, FDR = 20%
P21995	Emb	37,1	2	-2,935	1,601		+	down, FDR = 20%
O88322	Nid2	153,9	2	-0,439	1,940		+	down, FDR = 20%
Q9D0M2	Cdca7	43,8	2	-1,113	1,455		+	down, FDR = 20%
A0A2X0SFE3	ECT2	103,4	2	-2,779	1,838		+	down, FDR = 20%
A0A0R4J131	Btd	59,3	2	-1,647	1,588		+	down, FDR = 20%
G3UX33	Snx14	112,9	2	-3,067	1,427		+	down, FDR = 20%
G3UZT8	Jarid2	114,1	2	-2,256	1,583		+	down, FDR = 20%
B2RRI1	Adam17	93,1	2	-2,665	1,519		+	down, FDR = 20%
E0CYY3	Ankmy1	112,6	2	-2,146	1,450		+	down, FDR = 20%
G5E8B1	Ptpn13	270,2	2	-1,994	1,789		+	down, FDR = 20%
A7M7S2	Nprl3	60,8	2	-1,139	1,451		+	down, FDR = 20%
P62325	Btg1	19,2	2	-2,333	1,466		+	down, FDR = 20%
D3Z3Y1	Pigg	108,5	2	-0,776	1,558		+	down, FDR = 20%
B2RPS7	Trpc1	92,7	2	-2,759	1,444		+	down, FDR = 20%

Q3UK98	Cbx6	42,5	2	-2,137	1,969		+	down, FDR = 20%
Q4FJY2	Ube2l6	17,7	2	-2,592	1,510		+	down, FDR = 20%
Q8VCH6	Dhcr24	60,1	2	-2,047	1,502		+	down, FDR = 20%
Q9CPW3	Mrpl54	15,4	2	-0,567	1,465		+	down, FDR = 20%
Q9CR46	Ska2	13,7	2	-6,838	1,445		+	down, FDR = 20%
Q6PDI5	Ecpas	203,7	69	0,330	7,364	+	+	up, FDR = 10%
Q3V117	Acly	120,8	68	0,411	6,081	+	+	up, FDR = 10%
A0A0R4J0V5	Polr2a	213,5	61	0,348	5,115	+	+	up, FDR = 10%
Q3UHK5	Atp1a2	112,2	55	0,351	3,868	+	+	up, FDR = 10%
Q3TVV6	Hnrnpu	87,9	55	0,352	3,867	+	+	up, FDR = 10%
Q2PZL6	Fat4	540,3	54	0,307	3,468	+	+	up, FDR = 10%
P20152	Vim	53,7	51	0,366	5,283	+	+	up, FDR = 10%
E9PUD2	Dnm1l	79,5	51	0,397	5,441	+	+	up, FDR = 10%
Q3UH60	Dip2b	171,1	48	0,320	5,804	+	+	up, FDR = 10%
Q91ZW3	Smarca5	121,6	47	0,598	5,837	+	+	up, FDR = 10%
A2A8R7	Tut4	185,1	46	0,319	3,578	+	+	up, FDR = 10%
Q8CFI7	Polr2b	133,9	46	0,486	7,086	+	+	up, FDR = 10%
Q99JF8	Psip1	59,7	46	0,305	2,802	+	+	up, FDR = 10%
Q76MZ3	Ppp2r1a	65,3	42	0,316	4,606	+	+	up, FDR = 10%
Q68FL6	Mars	101,4	39	0,482	3,783	+	+	up, FDR = 10%
Q80TM9	Nisch	175,0	39	0,970	7,902	+	+	up, FDR = 10%
D3YXK2	Safb	105,1	39	0,360	3,020	+	+	up, FDR = 10%
A2AGR0	Madd	175,1	38	0,479	6,037	+	+	up, FDR = 10%
Q6ZQ73	Cand2	135,6	38	0,349	7,268	+	+	up, FDR = 10%
Q9Z277	Baz1b	170,7	35	0,541	4,008	+	+	up, FDR = 10%
P46660	Ina	55,4	34	0,692	7,735	+	+	up, FDR = 10%
Q7TPQ3	Shprh	191,5	30	0,315	2,832	+	+	up, FDR = 10%
Q3U8B3	Rpa1	71,4	28	0,308	6,340	+	+	up, FDR = 10%
Q05DE7	Smarca1	120,2	28	0,305	6,337	+	+	up, FDR = 10%
A0A1B0GSX	Ldha	39,8	27	0,322	2,101	+	+	up, FDR = 10%
Q3TGM7	Hbs1l	74,8	27	0,308	4,176	+	+	up, FDR = 10%
Q99PV8	Bcl11b	94,6	27	0,377	3,161	+	+	up, FDR = 10%
E9Q450	Tpm1	32,8	26	0,544	5,937	+	+	up, FDR = 10%
P10711	Tcea1	33,9	24	0,402	5,560	+	+	up, FDR = 10%
Q9CVB6	Arpc2	34,4	23	0,408	4,934	+	+	up, FDR = 10%
B1AX58	Pls3	71,7	23	0,790	10,014	+	+	up, FDR = 10%
Q8R307	Vps18	110,2	23	0,302	3,190	+	+	up, FDR = 10%
Q61753	Phgdh	56,6	23	0,696	2,154	+	+	up, FDR = 10%
Q6PCM2	Ints6	99,7	20	0,713	4,697	+	+	up, FDR = 10%
Q3TFF0	Dnaja2	45,7	20	0,507	6,793	+	+	up, FDR = 10%
D3Z7B5	Cip2a	102,1	20	0,591	9,548	+	+	up, FDR = 10%
A0A140LHW	Arhgap33	137,2	19	0,333	3,151	+	+	up, FDR = 10%
E9QK89	Mdc1	184,8	19	0,453	5,099	+	+	up, FDR = 10%
Q6ZPT1	Klhl9	69,4	19	1,009	6,182	+	+	up, FDR = 10%
O54916	Reps1	86,5	18	0,422	4,708	+	+	up, FDR = 10%
Q3TZR8	Zhx2	92,2	18	0,351	7,406	+	+	up, FDR = 10%
P12849	Prkar1b	43,2	17	0,310	5,544	+	+	up, FDR = 10%
Q60760	Grb10	70,6	17	0,717	7,057	+	+	up, FDR = 10%
B2RRX2	Ppp3ca	58,6	17	0,635	4,984	+	+	up, FDR = 10%
D3YZC8	Brd8	102,9	17	0,437	6,942	+	+	up, FDR = 10%

Q3TUI3	Brd3	79,8	16	0,605	4,032	+	+	up, FDR = 10%
A0A2X0SZ21	PIK3R2	81,5	15	0,326	4,649	+	+	up, FDR = 10%
Q5M9P3	Rps19	16,7	15	0,576	6,240	+	+	up, FDR = 10%
P97372	Psme2	27,1	15	0,513	4,576	+	+	up, FDR = 10%
Q3U3U6	Clpb	76,0	15	0,327	2,874	+	+	up, FDR = 10%
Q5SRY7	Fbxw11	62,1	15	0,384	6,642	+	+	up, FDR = 10%
Q3TE45	Sdhb	31,8	15	0,781	5,264	+	+	up, FDR = 10%
Q3UK41	Nelfa	57,6	15	0,309	3,923	+	+	up, FDR = 10%
Q32P00	Cbx3	20,8	14	0,310	3,633	+	+	up, FDR = 10%
P56959	Fus	52,7	14	0,345	2,979	+	+	up, FDR = 10%
P84244	H3f3a	15,3	14	0,424	2,309	+	+	up, FDR = 10%
O35317	Pbx3	47,2	13	0,307	5,390	+	+	up, FDR = 10%
A0A0R4J195	Rprd1b	36,8	13	0,358	7,347	+	+	up, FDR = 10%
Q5DU02	Usp22	60,0	13	0,310	2,259	+	+	up, FDR = 10%
Q3URU4	Mre11a	80,2	13	0,422	5,162	+	+	up, FDR = 10%
Q9R1S8	Capn7	92,6	13	0,395	4,047	+	+	up, FDR = 10%
G3XA34	Zfp316	110,9	12	0,471	5,040	+	+	up, FDR = 10%
E0CYH0	Wtap	44,2	12	0,444	5,699	+	+	up, FDR = 10%
G5E8N7	Pnkp	57,2	12	0,428	2,225	+	+	up, FDR = 10%
Q9D6T0	Nosip	33,2	12	0,326	4,648	+	+	up, FDR = 10%
E9QMX4	Rps6kc1	115,8	12	0,350	3,066	+	+	up, FDR = 10%
Q3V0X6	Lztr1	84,7	11	1,152	8,819	+	+	up, FDR = 10%
Q8BFX3	Kctd3	88,9	11	0,721	8,608	+	+	up, FDR = 10%
A0A0R4IZW	Trmt1	72,4	11	0,365	3,886	+	+	up, FDR = 10%
P52019	Sqle	63,8	11	0,317	2,238	+	+	up, FDR = 10%
F8WJA0	Ddx24	101,4	11	0,364	4,413	+	+	up, FDR = 10%
Q8BMJ3	Eif1ax	16,5	11	0,426	5,900	+	+	up, FDR = 10%
Q8BKT8	Haus7	40,7	11	0,505	4,340	+	+	up, FDR = 10%
Q6P5G3	Mbtd1	70,7	10	0,328	2,321	+	+	up, FDR = 10%
O88508	Dnmt3a	101,7	10	0,407	2,288	+	+	up, FDR = 10%
A0A0F6AIX5	Ldah	37,4	10	0,470	3,005	+	+	up, FDR = 10%
A0A0U1RNL	Maz	51,2	10	0,362	4,736	+	+	up, FDR = 10%
Q922M3	Kctd10	35,7	10	0,412	3,517	+	+	up, FDR = 10%
Q497T4	Klhl13	72,1	10	0,872	4,230	+	+	up, FDR = 10%
H7BWZ3	Arpc3	19,6	9	0,474	2,712	+	+	up, FDR = 10%
G3UYS3	Mettl14	44,0	9	0,451	6,117	+	+	up, FDR = 10%
O88630	Gosr1	28,5	9	0,506	4,083	+	+	up, FDR = 10%
P58544	Btbd1	53,2	9	0,914	6,975	+	+	up, FDR = 10%
Q14B21	Mrpl9	30,2	9	0,489	2,688	+	+	up, FDR = 10%
Q52L66	Ubl7	40,4	8	0,329	4,766	+	+	up, FDR = 10%
O35984	Pbx2	45,8	8	0,861	2,119	+	+	up, FDR = 10%
O35633	Slc32a1	57,4	8	0,441	5,774	+	+	up, FDR = 10%
Q9D0B0	Srsf9	25,7	8	0,409	3,192	+	+	up, FDR = 10%
Q3UGP9	Lrrc58	40,1	8	0,383	2,590	+	+	up, FDR = 10%
B8JK87	Amotl2	88,9	8	0,628	4,771	+	+	up, FDR = 10%
P17095	Hmga1	11,6	8	0,420	2,258	+	+	up, FDR = 10%
P62852	Rps25	13,7	8	0,359	5,255	+	+	up, FDR = 10%
P97760	Polr2c	31,4	8	0,329	3,800	+	+	up, FDR = 10%
B1ASA5	Zfp362	45,7	8	0,455	5,292	+	+	up, FDR = 10%
Q6PD21	Shb	54,7	8	0,312	2,916	+	+	up, FDR = 10%

Q9D0T1	Snu13	14,2	8	0,417	5,620	+	+	up, FDR = 10%
Q8K209	Adgrg1	77,3	7	0,464	3,947	+	+	up, FDR = 10%
Q3TFU7	Bad	19,0	7	0,619	2,698	+	+	up, FDR = 10%
O70400	Pdlim1	35,8	7	0,320	4,136	+	+	up, FDR = 10%
O08989	Mras	23,9	7	0,361	4,518	+	+	up, FDR = 10%
Q8BGV7	Kctd13	36,4	7	0,779	5,257	+	+	up, FDR = 10%
E9PUS2	Btbd2	56,5	7	0,471	2,340	+	+	up, FDR = 10%
P62488	Polr2g	19,3	7	0,303	2,232	+	+	up, FDR = 10%
Q9D7S9	Chmp5	24,6	7	0,324	2,644	+	+	up, FDR = 10%
O09118	Ntn1	67,8	7	0,359	3,380	+	+	up, FDR = 10%
A0A0R4J0L8	Ccdc174	54,0	7	0,317	4,796	+	+	up, FDR = 10%
P10639	Txn	11,7	7	0,406	4,918	+	+	up, FDR = 10%
A0A2X0SYS9	ARHGAP18	75,2	7	0,305	2,594	+	+	up, FDR = 10%
P62843	Rps15	17,0	7	0,373	4,263	+	+	up, FDR = 10%
P63216	Gng3	8,3	7	0,309	4,855	+	+	up, FDR = 10%
Q8R593	Rchy1	30,0	6	0,310	4,559	+	+	up, FDR = 10%
Q3U4Z0	Btbd9	69,2	6	0,532	4,448	+	+	up, FDR = 10%
Q8VEB4	Pla2g15	47,3	6	0,317	2,814	+	+	up, FDR = 10%
Q9D7M8	Polr2d	16,3	6	0,416	6,541	+	+	up, FDR = 10%
Q9JMA2	Qtrt1	44,1	6	0,368	4,041	+	+	up, FDR = 10%
Q8CE50	Snx30	49,5	6	0,335	3,035	+	+	up, FDR = 10%
Q08376	Zbtb14	50,9	6	0,379	2,330	+	+	up, FDR = 10%
P60898	Polr2i	14,5	5	0,415	3,945	+	+	up, FDR = 10%
Q8K194	Snrnp27	18,9	5	0,361	5,240	+	+	up, FDR = 10%
P09602	Hmgn2	9,4	5	0,525	2,138	+	+	up, FDR = 10%
Q9D1K2	Atp6v1f	13,4	5	0,327	5,649	+	+	up, FDR = 10%
P52927	Hmga2	11,8	5	0,641	2,474	+	+	up, FDR = 10%
E9Q8T2	Prdm15	132,9	4	0,329	5,141	+	+	up, FDR = 10%
Q9CYX7	Rrp15	31,1	4	0,306	5,849	+	+	up, FDR = 10%
Q9R1Z7	Pts	16,2	4	0,413	3,490	+	+	up, FDR = 10%
Q9CWQ0	Dph5	31,2	4	0,366	2,038	+	+	up, FDR = 10%
D3Z1T3	Zfp444	15,0	3	0,510	5,922	+	+	up, FDR = 10%
Q80UN9	Trit1	52,4	3	0,357	4,302	+	+	up, FDR = 10%
A2AWL7	Mga	328,8	3	0,476	2,681	+	+	up, FDR = 10%
Q9CRA4	Msmo1	34,8	3	0,761	4,914	+	+	up, FDR = 10%
P97299	Sfrp2	33,5	3	0,324	4,629	+	+	up, FDR = 10%
Q9CYB0	Trim13	47,0	3	0,543	4,397	+	+	up, FDR = 10%
Q8C5G2	Vash2	40,5	3	1,201	2,120	+	+	up, FDR = 10%
Q91WD9	Scgn	32,1	3	0,349	5,364	+	+	up, FDR = 10%
A0A087WRI	Gm13889	26,5	2	0,306	3,112	+	+	up, FDR = 10%
Q80TB7	Zswim6	133,1	2	0,832	3,926	+	+	up, FDR = 10%
B2RUG4	Gli3	171,7	2	0,671	2,987	+	+	up, FDR = 10%
Q54AA2	Pycard	21,5	2	1,811	2,151	+	+	up, FDR = 10%
A6H6H4	Tmsb10	5,0	2	0,570	3,192	+	+	up, FDR = 10%
A2A4Z0	Ube2c	19,6	2	0,376	4,403	+	+	up, FDR = 10%
A0A2U3TZ5	Polr2f	12,8	2	0,377	3,984	+	+	up, FDR = 10%
Q8BLI4	Dse	109,8	2	0,322	2,073	+	+	up, FDR = 10%
Q3USZ8	1190002N15I	49,5	2	0,459	2,930	+	+	up, FDR = 10%
B2KF10	Kctd20	22,5	2	0,542	3,630	+	+	up, FDR = 10%
Q7TN02	Med26	64,7	2	1,164	2,023	+	+	up, FDR = 10%

Q8BZM0	Klhl12	63,2	2	0,515	5,067	+	+	up, FDR = 10%
Q3TMM5	Nono	54,5	41	2,927	1,779		+	up, FDR = 20%
Q99JX6	Anxa6	75,3	41	1,129	1,831		+	up, FDR = 20%
Q8K2B3	Sdha	72,6	30	0,319	1,766		+	up, FDR = 20%
Q3U0S4	Ctdp1	104,5	26	0,345	1,794		+	up, FDR = 20%
Q3TST0	Pnpt1	85,7	20	0,364	1,908		+	up, FDR = 20%
Q9EPQ8	Tcf20	215,7	18	0,309	1,860		+	up, FDR = 20%
Q9QZQ8	H2afy	39,7	17	0,404	1,722		+	up, FDR = 20%
E9Q4P1	Wdfy1	46,2	12	1,199	1,971		+	up, FDR = 20%
Q8VBV7	Cops8	23,3	7	0,391	1,717		+	up, FDR = 20%
A6H619	Phrf1	184,1	5	0,335	1,506		+	up, FDR = 20%
Q9DCB1	Hmgn3	10,8	4	0,320	1,582		+	up, FDR = 20%
Q3U417	Ppfibp1	108,5	3	1,496	1,506		+	up, FDR = 20%
Q8BVR6	Rspry1	64,3	3	0,407	1,611		+	up, FDR = 20%
A2AH60	Klhl8	61,3	2	2,340	1,468		+	up, FDR = 20%
A0A0N4SW	Zfp746	69,8	2	0,354	1,591		+	up, FDR = 20%
A0A0R4J113	Myo7a	249,8	2	2,400	1,437		+	up, FDR = 20%
E0CX74	Tm7sf2	43,5	2	2,944	1,456		+	up, FDR = 20%
A0A087WQ	Pign	93,7	2	1,547	1,432		+	up, FDR = 20%
O35134	Polr1a	194,1	2	0,949	1,791		+	up, FDR = 20%
B1AUW6	Irak1	81,9	2	5,938	1,425		+	up, FDR = 20%
Q05CS3	Cyp39a1	45,8	2	1,889	1,437		+	up, FDR = 20%
A0A0N4SW5	Tmem168	35,6	2	4,772	1,439		+	up, FDR = 20%
D6RG69	Ccdc167	6,2	2	1,694	1,638		+	up, FDR = 20%
Q80XT2	Abca3	172,5	2	0,562	1,961		+	up, FDR = 20%
P57787	Slc16a3	50,4	2	0,388	1,514		+	up, FDR = 20%
Q9D0F1	Ndc80	74,0	2	1,292	1,846		+	up, FDR = 20%
D3YX64	Skor1	96,1	2	1,797	1,496		+	up, FDR = 20%
B1AV57	Pithd1	13,8	2	1,763	1,555		+	up, FDR = 20%
Q8BSC6	1700084E18R	24,7	2	3,351	1,535		+	up, FDR = 20%
Q8K0S9	Snapc1	44,6	2	0,647	1,697		+	up, FDR = 20%
O70126	Aurkb	39,4	2	0,447	1,585		+	up, FDR = 20%
B1AUE5	Pex10	37,2	2	1,137	1,509		+	up, FDR = 20%

Supplementary Table 5

DAVID functional annotation clustering of deregulated proteins detected in the *Cul3*$^{fl/fl}$ *Emx1-Cre* embryonic cortex (related to Fig. 17e).

Input:	**140 DAVID Ids (Cul3fl/fl Emx1-Cre vs. control, E16.5 cortex)- DOWN 20% FDR**
Background:	8100 identified proteins in embryonic dataset

Annotation Cluster 1	**Enrichment Score: 4,710**			
Category	**Term**	**Count**	**PValue**	**Benjamini**
GOTERM_CC_DIRECT	GO:0005839~proteasome core complex	8	2,46E-09	4,90E-07
Annotation Cluster 2	**Enrichment Score: 1,305**			
Category	**Term**	**Count**	**PValue**	**Benjamini**
GOTERM_CC_FAT	GO:0031988~membrane-bounded vesicle	42	0,021	0,741
GOTERM_CC_FAT	GO:1903561~extracellular vesicle	34	0,049	0,829
Annotation Cluster 4	**Enrichment Score: 0,795**			
Category	**Term**	**Count**	**PValue**	**Benjamini**
GOTERM_CC_FAT	GO:0031985~Golgi cisterna	4	0,044	0,870
Annotation Cluster 5	**Enrichment Score: 0,697**			
Category	**Term**	**Count**	**PValue**	**Benjamini**
GOTERM_CC_FAT	GO:0030133~transport vesicle	9	0,011	0,569
Annotation Cluster 14	**Enrichment Score: 0,464**			
Category	**Term**	**Count**	**PValue**	**Benjamini**
GOTERM_CC_FAT	GO:0015630~microtubule cytoskeleton	15	0,175	0,877
Annotation Cluster 15	**Enrichment Score: 0,459**			
Category	**Term**	**Count**	**PValue**	**Benjamini**
GOTERM_BP_FAT	GO:0036465~synaptic vesicle recycling	3	0,056	1,000
GOTERM_CC_DIRECT	GO:0045202~synapse	7	0,383	0,992
Annotation Cluster 16	**Enrichment Score: 0,456**			
Category	**Term**	**Count**	**PValue**	**Benjamini**
GOTERM_BP_FAT	GO:0021953~CNS neuron differentiation	5	0,087	1,000
GOTERM_BP_FAT	GO:0030900~forebrain development	6	0,333	1,000
GOTERM_BP_FAT	GO:0022008~neurogenesis	13	0,777	1,000
Annotation Cluster 17	**Enrichment Score: 0,448**			
Category	**Term**	**Count**	**PValue**	**Benjamini**
GOTERM_CC_DIRECT	GO:0005856~cytoskeleton	18	0,046	0,906
Annotation Cluster 28	**Enrichment Score: 0,324**			
Category	**Term**	**Count**	**PValue**	**Benjamini**
GOTERM_BP_FAT	GO:0045216~cell-cell junction organization	3	0,481	1,000
Annotation Cluster 30	**Enrichment Score: 0,319**			
Category	**Term**	**Count**	**PValue**	**Benjamini**
GOTERM_BP_DIRECT	GO:0043066~neg. reg. of apoptotic process	5	0,553	1,000
Annotation Cluster 33	**Enrichment Score: 0,283**			
Category	**Term**	**Count**	**PValue**	**Benjamini**
GOTERM_CC_FAT	GO:0031252~cell leading edge	7	0,261	0,925
GOTERM_CC_DIRECT	GO:0030027~lamellipodium	3	0,657	0,997
Annotation Cluster 36	**Enrichment Score: 0,247**			
Category	**Term**	**Count**	**PValue**	**Benjamini**
GOTERM_BP_DIRECT	GO:0048870~cell motility	3	0,012	0,834
GOTERM_BP_DIRECT	GO:0007155~cell adhesion	5	0,362	1,000
GOTERM_BP_FAT	GO:0030334~regulation of cell migration	4	0,896	1,000

Input	**178 DAVID Ids (Cul3fl/fl Emx1-Cre vs. control, E16.5 cortex)- UP 20% FDR**
Background	8100 identified proteins in embryonic dataset

Annotation Cluster 1	**Enrichment Score: 3,639**			
Category	**Term**	**Count**	**PValue**	**Benjamini**
GOTERM_CC_DIRECT	GO:0005665~DNA-directed RNA polymerase II, core comple	6	7,41E-06	0,002
GOTERM_MF_DIRECT	GO:0003899~DNA-directed RNA polymerase activity	7	2,23E-05	0,007
GOTERM_BP_DIRECT	GO:0006366~transcription from RNA polymerase II promot	7	0,0054	0,832

Annotation Cluster 2	**Enrichment Score: 3,0532**			
Category	**Term**	**Count**	**PValue**	**Benjamini**
GOTERM_MF_DIRECT	GO:0003677~DNA binding	35	6,13E-05	0,010
GOTERM_BP_DIRECT	GO:0006351~transcription, DNA-templated	38	4,84E-04	0,213

Annotation Cluster 3	**Enrichment Score: 2,304**			
Category	**Term**	**Count**	**PValue**	**Benjamini**
GOTERM_CC_DIRECT	GO:0031463~Cul3-RING ubiquitin ligase complex	6	2,96E-04	0,039
GOTERM_MF_DIRECT	GO:0004842~ubiquitin-protein transferase activity	10	0,0166	0,486
GOTERM_BP_DIRECT	GO:0016567~protein ubiquitination	10	0,0249	0,896

Annotation Cluster 4	**Enrichment Score: 1,634**			
Category	**Term**	**Count**	**PValue**	**Benjamini**
GOTERM_BP_DIRECT	GO:0043161~proteasome med. ubiquitin dep. process	7	0,013	0,876
GOTERM_BP_DIRECT	GO:0030162~regulation of proteolysis	3	0,019	0,903

Annotation Cluster 5	**Enrichment Score: 1,560**			
Category	**Term**	**Count**	**PValue**	**Benjamini**
GOTERM_CC_DIRECT	GO:0035985~senescence-associated heterochromatin focu	3	0,002	0,102
GOTERM_CC_DIRECT	GO:0000785~chromatin	6	0,038	0,679

Annotation Cluster 6	**Enrichment Score: 0,677**			
Category	**Term**	**Count**	**PValue**	**Benjamini**
GOTERM_BP_DIRECT	GO:0007049~cell cycle	12	0,224	1,000
GOTERM_BP_DIRECT	GO:0051301~cell division	8	0,291	1,000

Annotation Cluster 7	**Enrichment Score: 0,647**			
Category	**Term**	**Count**	**PValue**	**Benjamini**
GOTERM_MF_DIRECT	GO:0005200~structural constituent of cytoskeleton	5	0,026	0,573
GOTERM_MF_DIRECT	GO:0003779~actin binding	6	0,568	0,999
GOTERM_CC_DIRECT	GO:0005856~cytoskeleton	10	0,965	1,000

Annotation Cluster 8	**Enrichment Score: 0,400**			
Category	**Term**	**Count**	**PValue**	**Benjamini**
GOTERM_BP_DIRECT	GO:0000028~ribosomal small subunit assembly	3	0,056	0,983
GOTERM_MF_DIRECT	GO:0003735~structural constituent of ribosome	4	0,751	1,000
GOTERM_BP_DIRECT	GO:0006412~translation	6	0,781	1,000

Annotation Cluster 9	**Enrichment Score: 0,138**			
Category	**Term**	**Count**	**PValue**	**Benjamini**
GOTERM_MF_DIRECT	GO:0098641~cadherin binding involved in cell-cell adhesion	6	0,698	1,000
GOTERM_BP_DIRECT	GO:0098609~cell-cell adhesion	4	0,742	1,000
GOTERM_CC_DIRECT	GO:0005913~cell-cell adherens junction	6	0,746	1,000

Supplementary Table 6

Overlap E16.5 cortex datasets at 20% FDR and dose dependency (related to Fig. 17f-h).

Global DOWN-regulated proteins

Protein ID	Gene name	Occurences	Present In
Q6ZQ84	Cul3	3	HET down 20%, HOM down 20%, KO down 20%
A0A2X0SFE3	Ect2	2	HET down 20%, HOM down 20%
A2AW13	Ttbk2	2	HET down 20%, HOM down 20%
D3YVW2	Golim4	2	HET down 20%, HOM down 20%
D3YW47	Podxl2	2	HOM down 20%, KO down 20%
D3Z3Y1	Pigg	2	HET down 20%, HOM down 20%
E0CY96	Tsen15	2	HOM down 20%, KO down 20%
E0CYY3	Ankmy1	2	HET down 20%, HOM down 20%
E9Q5G1	Myo10	2	HOM down 20%, KO down 20%
G3UZJ2	Map2	2	HOM down 20%, KO down 20%
G3UZT8	Jarid2	2	HET down 20%, HOM down 20%
G5E898	Ppl	2	HET down 20%, HOM down 20%
G5E8B1	Ptpn13	2	HET down 20%, HOM down 20%
O09114	Ptgds	2	HET down 20%, HOM down 20%
O88512	Ap1g2	2	HET down 20%, HOM down 20%
P29699	Ahsg	2	HOM down 20%, KO down 20%
P60904	Dnajc5	2	HOM down 20%, KO down 20%
P62325	Btg1	2	HET down 20%, HOM down 20%
Q04890	Sox12	2	HET down 20%, HOM down 20%
Q2TL60	Znf667	2	HET down 20%, HOM down 20%
Q3UK98	Cbx6	2	HET down 20%, HOM down 20%
Q4FJY2	Ube2l6	2	HET down 20%, HOM down 20%
Q561M1	Acp1	2	HOM down 20%, KO down 20%
Q69ZR3	Galnt16	2	HET down 20%, HOM down 20%
Q6PDJ1	Cachd1	2	HET down 20%, HOM down 20%
Q8BKP2	Zfp189	2	HET down 20%, HOM down 20%
Q8C078	Camkk2	2	HET down 20%, HOM down 20%
Q8VHZ7	Imp4	2	HET down 20%, KO down 20%
Q9D0M2	Cdca7	2	HET down 20%, HOM down 20%

Global UP-regulated proteins

Protein ID	Gene name	Occurences	Present In
B1AX58	Pls3	3	HET up 20%, HOM up 20%, KO up 20%
E9Q4P1	Wdfy1	3	HET up 20%, HOM up 20%, KO up 20%
A0A0F6AIX5	Ldah	2	HET up 20%, HOM up 20%
A0A0R4J113	Myo7a	2	HET up 20%, HOM up 20%
A0A1B0GSX0	Ldha	2	HET up 20%, HOM up 20%
A2AH60	Klhl8	2	HET up 20%, HOM up 20%
B1AUE5	Pex10	2	HET up 20%, HOM up 20%
B1AV57	Pithd1	2	HET up 20%, HOM up 20%
D3Z7B5	Cip2a	2	HET up 20%, HOM up 20%
D6RG69	Ccdc167	2	HET up 20%, HOM up 20%
O35134	Polr1a	2	HET up 20%, HOM up 20%
O35984	Pbx2	2	HET up 20%, HOM up 20%
P46660	Ina	2	HOM up 20%, KO up 20%
Q05CS3	Cyp39a1	2	HET up 20%, HOM up 20%
Q3TMM5	Nono	2	HET up 20%, HOM up 20%
Q3TUI3	Brd3	2	HOM up 20%, KO up 20%
Q3U417	Ppfibp1	2	HET up 20%, HOM up 20%
Q3URU4	Mre11a	2	HET up 20%, HOM up 20%
Q3USZ8	Dipk2a	2	HET up 20%, HOM up 20%
Q54AA2	Pycard	2	HET up 20%, HOM up 20%
Q7TN02	Med26	2	HET up 20%, HOM up 20%
Q80XT2	Abca3	2	HET up 20%, HOM up 20%
Q8BSC6	1700084E18Rik	2	HET up 20%, HOM up 20%
Q8C5G2	Vash2	2	HET up 20%, HOM up 20%
Q8R307	Vps18	2	HET up 20%, HOM up 20%
Q9CRA4	Msmo1	2	HOM up 20%, KO up 20%
Q9CWQ0	Dph5	2	HET up 20%, HOM up 20%
Q9CYX7	Rrp15	2	HOM up 20%, KO up 20%
Q9D0F1	Ndc80	2	HET up 20%, HOM up 20%
Q9Z277	Baz1b	2	HOM up 20%, KO up 20%

Dose dependency:

Pls3

Cul3 fl/+	Cul3 fl/+ Emx1-Cre	Cul3 fl/fl Emx1-Cre
8,515	*8,615*	*8,746*
8,467	*8,567*	*8,712*
8,457	*8,624*	*8,723*
8,503		
8,465		

Cul3 fl/+	Cul3 fl/+ Emx1-Cre	Cul3 fl/fl Emx1-Cre	
8,48	**8,60**	**8,73**	**mean expr.**

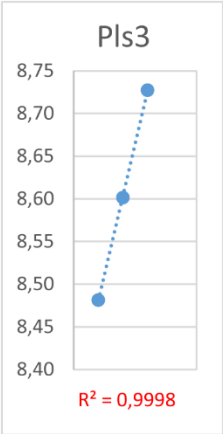

Ina

Cul3 fl/+	Cul3 fl/+ Emx1-Cre	Cul3 fl/fl Emx1-Cre
9,385	*9,387*	*9,507*
9,289	*9,418*	*9,538*
9,307	*9,361*	*9,572*
9,402		
9,286		

Cul3 fl/+	Cul3 fl/+ Emx1-Cre	Cul3 fl/fl Emx1-Cre	
9,33	**9,39**	**9,54**	**mean expr.**

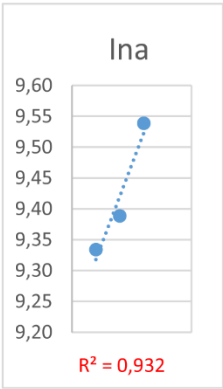

Supplementary Table 7

Deregulated proteins in the adult *Cul3*$^{+/-}$ cortex, hippocampus, and cerebellum (related to Supp. Fig. 4).

Leading protein ID	Gene name	MW	Number of identified peptides	F-test: Mean log2(Ratio) - JM_Adult_Cortex	F-test: Moderated -log10(Pvalue) - JM_Adult_Cortex	F-test: Significant-FDR=10% - JM_Adult_Cortex	F-test: Significant-FDR=20% - JM_Adult_Cortex	F-test: Regulated - JM_Adult_Cortex
P20152	Vim	53,7	38	0,693	4,433		+	up, FDR = 20%
E9Q4P1	Wdfy1	46,2	8	1,190	6,630		+	up, FDR = 20%

Leading protein ID	Gene name	MW	Number of identified peptides	F-test: Mean log2(Ratio) - JM_Adult_Hippocampus	F-test: Moderated -log10(Pvalue) - JM_Adult_Hippocampus	F-test: Significant-FDR=10% - JM_Adult_Hippocampus	F-test: Significant-FDR=20% - JM_Adult_Hippocampus	F-test: Regulated - JM_Adult_Hippocampus
Q8BKI2	Tnrc6b	192,0	13	-0,768	4,931	+	+	down, FDR = 10%
Q6ZQ84	Cul3	91,3	42	-0,755	4,773		+	down, FDR = 20%
Q3TSG4	Alkbh5	44,4	6	-0,767	3,742		+	down, FDR = 20%
E9Q4P1	Wdfy1	46,2	8	3,207	10,111	+	+	up, FDR = 10%
Q6P1J0	Maneal	51,1	3	1,192	5,633	+	+	up, FDR = 10%
Q920Q2	Rev1	137,3	2	1,208	6,729	+	+	up, FDR = 10%

Leading protein ID	Gene name	MW	Number of identified peptides	F-test: Mean log2(Ratio) - JM_Adult_Cerebellum	F-test: Moderated -log10(Pvalue) - JM_Adult_Cerebellum	F-test: Significant-FDR=10% - JM_Adult_Cerebellum	F-test: Significant-FDR=20% - JM_Adult_Cerebellum	F-test: Regulated - JM_Adult_Cerebellum
Q6ZQ84	Cul3	91,3	42	-0,717	5,767	+	+	down, FDR = 10%
Q8BGN2	D3Ertd751e	22,5	5	-0,370	4,046		+	down, FDR = 20%
E9Q4P1	Wdfy1	46,2	8	2,353	10,423	+	+	up, FDR = 10%
Q9D009	Lipt2	25,0	4	0,683	4,496	+	+	up, FDR = 10%
P03995	Gfap	49,9	37	0,646	4,485		+	up, FDR = 20%

REFERENCES

1. Baio, J., et al., *Prevalence of Autism Spectrum Disorder Among Children Aged 8 Years — Autism and Developmental Disabilities Monitoring Network, 11 Sites, United States, 2014.*, in *MMWR Surveill Summ*. 2018. p. 1–23.
2. Autism, et al., *Prevalence of autism spectrum disorders--autism and developmental disabilities monitoring network, 14 sites, United States, 2002.* MMWR Surveill Summ, 2007. **56**(1): p. 12-28.
3. Hansen, S.N., D.E. Schendel, and E.T. Parner, *Explaining the increase in the prevalence of autism spectrum disorders: the proportion attributable to changes in reporting practices.* JAMA Pediatr, 2015. **169**(1): p. 56-62.
4. Kanner, L., *Autistic disturbances of affective contact.* Nervous Child, 1943. **2**: p. 217-250.
5. Kanner, L., *Early infantile autism.* The Journal of Pediatrics, 1944. **25**(3): p. 211-217.
6. Harris, J., *Leo Kanner and autism: a 75-year perspective.* International Review of Psychiatry, 2018. **30**(1): p. 3-17.
7. Association, A.P., *Diagnostic and Statistical Manual of Mental Disorders (Fifth ed.).* 2013, Arlington: American Psychiatric Publishing.
8. Hughes, J.R. and M. Melyn, *EEG and seizures in autistic children and adolescents: further findings with therapeutic implications.* Clin EEG Neurosci, 2005. **36**(1): p. 15-20.
9. Viscidi, E.W., et al., *Clinical characteristics of children with autism spectrum disorder and co-occurring epilepsy.* PLoS One, 2013. **8**(7): p. e67797.
10. Ewen, J.B., et al., *Epilepsy and Autism Severity: A Study of 6,975 Children.* Autism Res, 2019. **12**(8): p. 1251-1259.
11. Weiss, L.A., et al., *Sodium channels SCN1A, SCN2A and SCN3A in familial autism.* Molecular Psychiatry, 2003. **8**(2): p. 186-194.
12. Sanders, S.J., et al., *Progress in Understanding and Treating SCN2A-Mediated Disorders.* Trends in Neurosciences, 2018. **41**(7): p. 442-456.
13. Shao, L.R., C.W. Habela, and C.E. Stafstrom, *Pediatric Epilepsy Mechanisms: Expanding the Paradigm of Excitation/Inhibition Imbalance.* Children (Basel), 2019. **6**(2).
14. Lee, E., J. Lee, and E. Kim, *Excitation/Inhibition Imbalance in Animal Models of Autism Spectrum Disorders.* Biological Psychiatry, 2017. **81**(10): p. 838-847.
15. Sohal, V.S. and J.L.R. Rubenstein, *Excitation-inhibition balance as a framework for investigating mechanisms in neuropsychiatric disorders.* Mol Psychiatry, 2019. **24**(9): p. 1248-1257.
16. Fombonne, E., et al., *Microcephaly and macrocephaly in autism.* J Autism Dev Disord, 1999. **29**(2): p. 113-9.
17. Wu, H., et al., *Phenotype-to-genotype approach reveals head-circumference-associated genes in an autism spectrum disorder cohort.* Clin Genet, 2020. **97**(2): p. 338-346.
18. Liaw, D., et al., *Germline mutations of the PTEN gene in Cowden disease, an inherited breast and thyroid cancer syndrome.* Nat Genet, 1997. **16**(1): p. 64-7.
19. Yasin, H., et al., *A distinct neurodevelopmental syndrome with intellectual disability, autism spectrum disorder, characteristic facies, and macrocephaly is caused by defects in CHD8.* J Hum Genet, 2019. **64**(4): p. 271-280.

20. Bahi-Buisson, N., et al., *The wide spectrum of tubulinopathies: what are the key features for the diagnosis?* Brain, 2014. **137**(Pt 6): p. 1676-700.
21. van Bon, B.W., et al., *Disruptive de novo mutations of DYRK1A lead to a syndromic form of autism and ID.* Mol Psychiatry, 2016. **21**(1): p. 126-32.
22. Scala, E., et al., *CDKL5/STK9 is mutated in Rett syndrome variant with infantile spasms.* J Med Genet, 2005. **42**(2): p. 103-7.
23. Qureshi, A.Y., et al., *Opposing brain differences in 16p11.2 deletion and duplication carriers.* J Neurosci, 2014. **34**(34): p. 11199-211.
24. Mizuno, Y., et al., *Structural brain abnormalities in children and adolescents with comorbid autism spectrum disorder and attention-deficit/hyperactivity disorder.* Transl Psychiatry, 2019. **9**(1): p. 332.
25. Pan, Y.H., N. Wu, and X.B. Yuan, *Toward a Better Understanding of Neuronal Migration Deficits in Autism Spectrum Disorders.* Front Cell Dev Biol, 2019. **7**: p. 205.
26. Thurm, A., et al., *State of the Field: Differentiating Intellectual Disability From Autism Spectrum Disorder.* Front Psychiatry, 2019. **10**: p. 526.
27. Harris, S.R., *Early motor delays as diagnostic clues in autism spectrum disorder.* Eur J Pediatr, 2017. **176**(9): p. 1259-1262.
28. Wilson, R.B., P.G. Enticott, and N.J. Rinehart, *Motor development and delay: advances in assessment of motor skills in autism spectrum disorders.* Curr Opin Neurol, 2018. **31**(2): p. 134-139.
29. Licari, M.K., et al., *Prevalence of Motor Difficulties in Autism Spectrum Disorder: Analysis of a Population-Based Cohort.* Autism Res, 2020. **13**(2): p. 298-306.
30. Wilson, R.B., et al., *What's missing in autism spectrum disorder motor assessments?* J Neurodev Disord, 2018. **10**(1): p. 33.
31. Rinehart, N.J., S. Jeste, and R.B. Wilson, *Organized physical activity programs: improving motor and non-motor symptoms in neurodevelopmental disorders.* Dev Med Child Neurol, 2018. **60**(9): p. 856-857.
32. Kasari, C., et al., *Assessing the minimally verbal school-aged child with autism spectrum disorder.* Autism Res, 2013. **6**(6): p. 479-93.
33. Mouga, S., et al., *Language Predictors in Autism Spectrum Disorder: Insights from Neurodevelopmental Profile in a Longitudinal Perspective.* J Abnorm Child Psychol, 2020. **48**(1): p. 149-161.
34. Gernsbacher, M.A., E.M. Morson, and E.J. Grace, *Language and Speech in Autism.* Annu Rev Linguist, 2016. **2**: p. 413-425.
35. van Steensel, F.J., S.M. Bogels, and S. Perrin, *Anxiety disorders in children and adolescents with autistic spectrum disorders: a meta-analysis.* Clin Child Fam Psychol Rev, 2011. **14**(3): p. 302-17.
36. Antshel, K.M. and N. Russo, *Autism Spectrum Disorders and ADHD: Overlapping Phenomenology, Diagnostic Issues, and Treatment Considerations.* Curr Psychiatry Rep, 2019. **21**(5): p. 34.
37. Fitzpatrick, S.E., et al., *Aggression in autism spectrum disorder: presentation and treatment options.* Neuropsychiatr Dis Treat, 2016. **12**: p. 1525-38.
38. DeFilippis, M., *Depression in Children and Adolescents with Autism Spectrum Disorder.* Children (Basel), 2018. **5**(9).
39. Vasa, R.A., et al., *Assessment and Treatment of Anxiety in Youth With Autism Spectrum Disorders.* Pediatrics, 2016. **137 Suppl 2**: p. S115-23.

40. Richa, S., et al., *Suicide in autism spectrum disorders.* Arch Suicide Res, 2014. **18**(4): p. 327-39.
41. Lord, C., et al., *Autism spectrum disorder.* Nature Reviews Disease Primers, 2020. **6**(1): p. 5.
42. Lockyer, L. and M. Rutter, *A five- to fifteen-year follow-up study of infantile psychosis.* Br J Psychiatry, 1969. **115**(525): p. 865-82.
43. Frith, U., *Studies in pattern detection in normal and autistic children. I. Immediate recall of auditory sequences.* J Abnorm Psychol, 1970. **76**(3): p. 413-20.
44. Folstein, S. and M. Rutter, *A Twin Study of Individuals with Infantile Autism*, in *Autism: A Reappraisal of Concepts and Treatment*, M. Rutter and E. Schopler, Editors. 1978, Springer US: Boston, MA. p. 219-241.
45. Modabbernia, A., E. Velthorst, and A. Reichenberg, *Environmental risk factors for autism: an evidence-based review of systematic reviews and meta-analyses.* Mol Autism, 2017. **8**: p. 13.
46. Landrigan, P.J., *What causes autism? Exploring the environmental contribution.* Curr Opin Pediatr, 2010. **22**(2): p. 219-25.
47. Wu, S., et al., *Advanced parental age and autism risk in children: a systematic review and meta-analysis.* Acta Psychiatr Scand, 2017. **135**(1): p. 29-41.
48. al-Haddad, B.J.S., et al., *Long-term Risk of Neuropsychiatric Disease After Exposure to Infection In Utero.* JAMA Psychiatry, 2019. **76**(6): p. 594-602.
49. Heresi Venegas, C., *[Maternal immune activation and risk of Autism Spectrum Disorder].* Rev Chil Pediatr, 2019. **90**(5): p. 555-558.
50. Taylor, L.E., A.L. Swerdfeger, and G.D. Eslick, *Vaccines are not associated with autism: an evidence-based meta-analysis of case-control and cohort studies.* Vaccine, 2014. **32**(29): p. 3623-9.
51. Devlin, B., N. Melhem, and K. Roeder, *Do common variants play a role in risk for autism? Evidence and theoretical musings.* Brain Res, 2011. **1380**: p. 78-84.
52. Sanders, S.J., et al., *De novo mutations revealed by whole-exome sequencing are strongly associated with autism.* Nature, 2012. **485**(7397): p. 237-41.
53. Dong, S., et al., *De novo insertions and deletions of predominantly paternal origin are associated with autism spectrum disorder.* Cell Rep, 2014. **9**(1): p. 16-23.
54. Willsey, A.J. and M.W. State, *Autism spectrum disorders: from genes to neurobiology.* Curr Opin Neurobiol, 2015. **30**: p. 92-9.
55. de la Torre-Ubieta, L., et al., *Advancing the understanding of autism disease mechanisms through genetics.* Nat Med, 2016. **22**(4): p. 345-61.
56. Pinto, D., et al., *Functional impact of global rare copy number variation in autism spectrum disorders.* Nature, 2010. **466**(7304): p. 368-72.
57. Gaugler, T., et al., *Most genetic risk for autism resides with common variation.* Nat Genet, 2014. **46**(8): p. 881-5.
58. Guo, H., et al., *Inherited and multiple de novo mutations in autism/developmental delay risk genes suggest a multifactorial model.* Mol Autism, 2018. **9**: p. 64.
59. Grove, J., et al., *Identification of common genetic risk variants for autism spectrum disorder.* Nat Genet, 2019. **51**(3): p. 431-444.
60. Silbereis, J.C., et al., *The Cellular and Molecular Landscapes of the Developing Human Central Nervous System.* Neuron, 2016. **89**(2): p. 248-68.
61. Gage, F.H., *Adult neurogenesis in mammals.* Science, 2019. **364**(6443): p. 827-828.

62. Spalding, K.L., et al., *Retrospective birth dating of cells in humans.* Cell, 2005. **122**(1): p. 133-43.
63. Larsen, C.C., et al., *Total number of cells in the human newborn telencephalic wall.* Neuroscience, 2006. **139**(3): p. 999-1003.
64. Sanai, N., et al., *Corridors of migrating neurons in the human brain and their decline during infancy.* Nature, 2011. **478**(7369): p. 382-6.
65. Eriksson, P.S., et al., *Neurogenesis in the adult human hippocampus.* Nat Med, 1998. **4**(11): p. 1313-7.
66. Ernst, A., et al., *Neurogenesis in the striatum of the adult human brain.* Cell, 2014. **156**(5): p. 1072-83.
67. Bystron, I., et al., *The first neurons of the human cerebral cortex.* Nature Neuroscience, 2006. **9**(7): p. 880-886.
68. Kang, H.J., et al., *Spatio-temporal transcriptome of the human brain.* Nature, 2011. **478**(7370): p. 483-489.
69. deAzevedo, L.C., et al., *Cortical radial glial cells in human fetuses: depth-correlated transformation into astrocytes.* J Neurobiol, 2003. **55**(3): p. 288-98.
70. Yeung, Maggie S.Y., et al., *Dynamics of Oligodendrocyte Generation and Myelination in the Human Brain.* Cell, 2014. **159**(4): p. 766-774.
71. Zecevic, N., *Synaptogenesis in layer I of the human cerebral cortex in the first half of gestation.* Cerebral Cortex, 1998. **8**(3): p. 245-252.
72. Peter R, H., *Synaptic density in human frontal cortex — Developmental changes and effects of aging.* Brain Research, 1979. **163**(2): p. 195-205.
73. Miller, D.J., et al., *Prolonged myelination in human neocortical evolution.* Proceedings of the National Academy of Sciences, 2012. **109**(41): p. 16480-16485.
74. Willsey, A.J., et al., *Coexpression Networks Implicate Human Midfetal Deep Cortical Projection Neurons in the Pathogenesis of Autism.* Cell, 2013. **155**(5): p. 997-1007.
75. Parikshak, N.N., et al., *Integrative functional genomic analyses implicate specific molecular pathways and circuits in autism.* Cell, 2013. **155**(5): p. 1008-21.
76. Balasco, L., G. Provenzano, and Y. Bozzi, *Sensory Abnormalities in Autism Spectrum Disorders: A Focus on the Tactile Domain, From Genetic Mouse Models to the Clinic.* Front Psychiatry, 2019. **10**: p. 1016.
77. Fuccillo, M.V., *Striatal Circuits as a Common Node for Autism Pathophysiology.* Front Neurosci, 2016. **10**: p. 27.
78. D'Mello, A.M. and C.J. Stoodley, *Cerebro-cerebellar circuits in autism spectrum disorder.* Front Neurosci, 2015. **9**: p. 408.
79. Sauer, F.C., *Mitosis in the neural tube.* The Journal of Comparative Neurology, 1935. **62**(2): p. 377-405.
80. Kosodo, Y., et al., *Asymmetric distribution of the apical plasma membrane during neurogenic divisions of mammalian neuroepithelial cells.* EMBO J, 2004. **23**(11): p. 2314-24.
81. Subramanian, L., et al., *Dynamic behaviour of human neuroepithelial cells in the developing forebrain.* Nat Commun, 2017. **8**: p. 14167.
82. Lee, H.O. and C. Norden, *Mechanisms controlling arrangements and movements of nuclei in pseudostratified epithelia.* Trends Cell Biol, 2013. **23**(3): p. 141-50.
83. Buchsbaum, I.Y. and S. Cappello, *Neuronal migration in the CNS during development and disease: insights from in vivo and in vitro models.* Development, 2019. **146**(1).

84. Angevine, J.B., Jr. and R.L. Sidman, *Autoradiographic study of cell migration during histogenesis of cerebral cortex in the mouse.* Nature, 1961. **192**: p. 766-8.
85. Nadarajah, B., et al., *Two modes of radial migration in early development of the cerebral cortex.* Nat Neurosci, 2001. **4**(2): p. 143-50.
86. Tabata, H. and K. Nakajima, *Multipolar migration: the third mode of radial neuronal migration in the developing cerebral cortex.* J Neurosci, 2003. **23**(31): p. 9996-10001.
87. Noctor, S.C., et al., *Cortical neurons arise in symmetric and asymmetric division zones and migrate through specific phases.* Nat Neurosci, 2004. **7**(2): p. 136-44.
88. Ayala, R., T. Shu, and L.H. Tsai, *Trekking across the brain: the journey of neuronal migration.* Cell, 2007. **128**(1): p. 29-43.
89. Tamamaki, N., K.E. Fujimori, and R. Takauji, *Origin and route of tangentially migrating neurons in the developing neocortical intermediate zone.* J Neurosci, 1997. **17**(21): p. 8313-23.
90. Anderson, S.A., et al., *Interneuron migration from basal forebrain to neocortex: dependence on Dlx genes.* Science, 1997. **278**(5337): p. 474-6.
91. Lavdas, A.A., et al., *The medial ganglionic eminence gives rise to a population of early neurons in the developing cerebral cortex.* J Neurosci, 1999. **19**(18): p. 7881-8.
92. Gao, P., et al., *Deterministic progenitor behavior and unitary production of neurons in the neocortex.* Cell, 2014. **159**(4): p. 775-88.
93. Llorca, A., et al., *A stochastic framework of neurogenesis underlies the assembly of neocortical cytoarchitecture.* Elife, 2019. **8**.
94. Leone, D.P., et al., *The determination of projection neuron identity in the developing cerebral cortex.* Curr Opin Neurobiol, 2008. **18**(1): p. 28-35.
95. Rowitch, D.H. and A.R. Kriegstein, *Developmental genetics of vertebrate glial–cell specification.* Nature, 2010. **468**(7321): p. 214-222.
96. Bear, M.F., B.W. Connors, and M.A. Paradiso, *Neuroscience : Exploring the Brain*. 2016: Fourth edition. Philadelphia : Wolters Kluwer, [2016] ©2016.
97. Takano, T., et al., *Neuronal polarization.* Development, 2015. **142**(12): p. 2088.
98. Petzoldt, A.G. and S.J. Sigrist, *Synaptogenesis.* Curr Biol, 2014. **24**(22): p. R1076-80.
99. Scheiffele, P., et al., *Neuroligin expressed in nonneuronal cells triggers presynaptic development in contacting axons.* Cell, 2000. **101**(6): p. 657-69.
100. Graf, E.R., et al., *Neurexins induce differentiation of GABA and glutamate postsynaptic specializations via neuroligins.* Cell, 2004. **119**(7): p. 1013-26.
101. Nam, C.I. and L. Chen, *Postsynaptic assembly induced by neurexin-neuroligin interaction and neurotransmitter.* Proceedings of the National Academy of Sciences, 2005. **102**(17): p. 6137-6142.
102. Graf, E.R., et al., *Structure function and splice site analysis of the synaptogenic activity of the neurexin-1 beta LNS domain.* J Neurosci, 2006. **26**(16): p. 4256-65.
103. Chia, P.H., P. Li, and K. Shen, *Cell biology in neuroscience: cellular and molecular mechanisms underlying presynapse formation.* J Cell Biol, 2013. **203**(1): p. 11-22.
104. Wu, Y., et al., *Microglia: Dynamic Mediators of Synapse Development and Plasticity.* Trends Immunol, 2015. **36**(10): p. 605-613.
105. Paolicelli, R.C., et al., *Synaptic pruning by microglia is necessary for normal brain development.* Science, 2011. **333**(6048): p. 1456-8.
106. Schafer, D.P., et al., *Microglia sculpt postnatal neural circuits in an activity and complement-dependent manner.* Neuron, 2012. **74**(4): p. 691-705.

107. de la Rosa, E.J. and F. de Pablo, *Cell death in early neural development: beyond the neurotrophic theory.* Trends Neurosci, 2000. **23**(10): p. 454-8.
108. Wong, F.K. and O. Marín, *Developmental Cell Death in the Cerebral Cortex.* Annual Review of Cell and Developmental Biology, 2019. **35**(1): p. 523-542.
109. Wake, H., et al., *Microglia: actively surveying and shaping neuronal circuit structure and function.* Trends Neurosci, 2013. **36**(4): p. 209-17.
110. Tremblay, M.E., R.L. Lowery, and A.K. Majewska, *Microglial interactions with synapses are modulated by visual experience.* PLoS Biol, 2010. **8**(11): p. e1000527.
111. Wake, H., et al., *Resting microglia directly monitor the functional state of synapses in vivo and determine the fate of ischemic terminals.* J Neurosci, 2009. **29**(13): p. 3974-80.
112. Christopherson, K.S., et al., *Thrombospondins are astrocyte-secreted proteins that promote CNS synaptogenesis.* Cell, 2005. **120**(3): p. 421-33.
113. Eroglu, C., et al., *Gabapentin receptor alpha2delta-1 is a neuronal thrombospondin receptor responsible for excitatory CNS synaptogenesis.* Cell, 2009. **139**(2): p. 380-92.
114. Ledda, F., et al., *GDNF and GFRalpha1 promote formation of neuronal synapses by ligand-induced cell adhesion.* Nat Neurosci, 2007. **10**(3): p. 293-300.
115. Barateiro, A., D. Brites, and A. Fernandes, *Oligodendrocyte Development and Myelination in Neurodevelopment: Molecular Mechanisms in Health and Disease.* Curr Pharm Des, 2016. **22**(6): p. 656-79.
116. Ma, Z., et al., *Cortical Circuit Dynamics Are Homeostatically Tuned to Criticality In Vivo.* Neuron, 2019. **104**(4): p. 655-664 e4.
117. Iascone, D.M., et al., *Whole-neuron synaptic mapping reveals local balance between excitatory and inhibitory synapse organization.* bioRxiv, 2018: p. 395384.
118. Bhatia, A., S. Moza, and U.S. Bhalla, *Precise excitation-inhibition balance controls gain and timing in the hippocampus.* Elife, 2019. **8**.
119. Hengen, K.B., et al., *Firing rate homeostasis in visual cortex of freely behaving rodents.* Neuron, 2013. **80**(2): p. 335-42.
120. Knoblich, J.A., *Mechanisms of asymmetric stem cell division.* Cell, 2008. **132**(4): p. 583-97.
121. Coles, C.H. and F. Bradke, *Coordinating neuronal actin-microtubule dynamics.* Curr Biol, 2015. **25**(15): p. R677-91.
122. Breuss, M. and D.A. Keays, *Microtubules and neurodevelopmental disease: the movers and the makers.* Adv Exp Med Biol, 2014. **800**: p. 75-96.
123. Breuss, M.W., et al., *Tubulins and brain development - The origins of functional specification.* Mol Cell Neurosci, 2017. **84**: p. 58-67.
124. Pacheco, A. and G. Gallo, *Actin filament-microtubule interactions in axon initiation and branching.* Brain Res Bull, 2016. **126**(Pt 3): p. 300-310.
125. Laser-Azogui, A., et al., *Neurofilament assembly and function during neuronal development.* Curr Opin Cell Biol, 2015. **32**: p. 92-101.
126. Messier, P.E., *Microtubules, interkinetic nuclear migration and neurulation.* Experientia, 1978. **34**(3): p. 289-96.
127. Kosodo, Y., et al., *Regulation of interkinetic nuclear migration by cell cycle-coupled active and passive mechanisms in the developing brain.* EMBO J, 2011. **30**(9): p. 1690-704.
128. Glotzer, M., *The 3Ms of central spindle assembly: microtubules, motors and MAPs.* Nat Rev Mol Cell Biol, 2009. **10**(1): p. 9-20.

129. Damiani, D., et al., *Lack of Diaph3 relaxes the spindle checkpoint causing the loss of neural progenitors.* Nat Commun, 2016. **7**: p. 13509.
130. Marin, O., et al., *Guiding neuronal cell migrations.* Cold Spring Harb Perspect Biol, 2010. **2**(2): p. a001834.
131. Heng, J.I., A. Chariot, and L. Nguyen, *Molecular layers underlying cytoskeletal remodelling during cortical development.* Trends Neurosci, 2010. **33**(1): p. 38-47.
132. Yee, K.T., et al., *Extension of long leading processes and neuronal migration in the mammalian brain directed by the chemoattractant netrin-1.* Neuron, 1999. **24**(3): p. 607-22.
133. Tsai, L.H. and J.G. Gleeson, *Nucleokinesis in neuronal migration.* Neuron, 2005. **46**(3): p. 383-8.
134. He, M., et al., *Leading tip drives soma translocation via forward F-actin flow during neuronal migration.* J Neurosci, 2010. **30**(32): p. 10885-98.
135. Yuan, A., et al., *Neurofilaments and Neurofilament Proteins in Health and Disease.* Cold Spring Harb Perspect Biol, 2017. **9**(4).
136. Lendahl, U., L.B. Zimmerman, and R.D. McKay, *CNS stem cells express a new class of intermediate filament protein.* Cell, 1990. **60**(4): p. 585-95.
137. Gilyarov, A.V., *Nestin in central nervous system cells.* Neurosci Behav Physiol, 2008. **38**(2): p. 165-9.
138. Yabe, J.T., et al., *Regulation of the transition from vimentin to neurofilaments during neuronal differentiation.* Cell Motil Cytoskeleton, 2003. **56**(3): p. 193-205.
139. Fliegner, K.H., et al., *Expression of the gene for the neuronal intermediate filament protein alpha-internexin coincides with the onset of neuronal differentiation in the developing rat nervous system.* J Comp Neurol, 1994. **342**(2): p. 161-73.
140. O/'Roak, B.J., et al., *Sporadic autism exomes reveal a highly interconnected protein network of de novo mutations.* Nature, 2012. **485**(7397): p. 246-250.
141. Levy, D., et al., *Rare de novo and transmitted copy-number variation in autistic spectrum disorders.* Neuron, 2011. **70**(5): p. 886-97.
142. Berg, J.M. and D.H. Geschwind, *Autism genetics: searching for specificity and convergence.* Genome Biol, 2012. **13**(7): p. 247.
143. Ben-David, E. and S. Shifman, *Combined analysis of exome sequencing points toward a major role for transcription regulation during brain development in autism.* Mol Psychiatry, 2013. **18**(10): p. 1054-6.
144. Ben-David, E., S. Shohat, and S. Shifman, *Allelic expression analysis in the brain suggests a role for heterogeneous insults affecting epigenetic processes in autism spectrum disorders.* Hum Mol Gen, 2014. **23**.
145. De Rubeis, S., et al., *Synaptic, transcriptional and chromatin genes disrupted in autism.* Nature, 2014. **515**(7526): p. 209-15.
146. Iossifov, I., et al., *The contribution of de novo coding mutations to autism spectrum disorder.* Nature, 2014. **515**.
147. Gilman, S.R., et al., *Rare de novo variants associated with autism implicate a large functional network of genes involved in formation and function of synapses.* Neuron, 2011. **70**(5): p. 898-907.
148. Gallegos, D.A., et al., *Chromatin Regulation of Neuronal Maturation and Plasticity.* Trends Neurosci, 2018. **41**(5): p. 311-324.
149. Ladd-Acosta, C., et al., *Common DNA methylation alterations in multiple brain regions in autism.* Mol Psychiatry, 2014. **19**(8): p. 862-71.

150. Wong, C.C., et al., *Methylomic analysis of monozygotic twins discordant for autism spectrum disorder and related behavioural traits.* Mol Psychiatry, 2014. **19**(4): p. 495-503.
151. Ellis, S.E., et al., *Exaggerated CpH methylation in the autism-affected brain.* Mol Autism, 2017. **8**: p. 6.
152. Corley, M.J., et al., *Epigenetic Delay in the Neurodevelopmental Trajectory of DNA Methylation States in Autism Spectrum Disorders.* Front Genet, 2019. **10**: p. 907.
153. Sun, W., et al., *Histone Acetylome-wide Association Study of Autism Spectrum Disorder.* Cell, 2016. **167**(5): p. 1385-1397 e11.
154. Zaghi, M., V. Broccoli, and A. Sessa, *H3K36 Methylation in Neural Development and Associated Diseases.* Front Genet, 2019. **10**: p. 1291.
155. Nan, X., F.J. Campoy, and A. Bird, *MeCP2 is a transcriptional repressor with abundant binding sites in genomic chromatin.* Cell, 1997. **88**(4): p. 471-81.
156. Cheng, T.L., et al., *MeCP2 suppresses nuclear microRNA processing and dendritic growth by regulating the DGCR8/Drosha complex.* Dev Cell, 2014. **28**(5): p. 547-60.
157. Young, J.I., et al., *Regulation of RNA splicing by the methylation-dependent transcriptional repressor methyl-CpG binding protein 2.* Proc Natl Acad Sci U S A, 2005. **102**(49): p. 17551-8.
158. Shahbazian, M.D., et al., *Insight into Rett syndrome: MeCP2 levels display tissue- and cell-specific differences and correlate with neuronal maturation.* Hum Mol Genet, 2002. **11**(2): p. 115-24.
159. Bedogni, F., et al., *Defects During Mecp2 Null Embryonic Cortex Development Precede the Onset of Overt Neurological Symptoms.* Cereb Cortex, 2016. **26**(6): p. 2517-2529.
160. Gulmez Karaca, K., D.V.C. Brito, and A.M.M. Oliveira, *MeCP2: A Critical Regulator of Chromatin in Neurodevelopment and Adult Brain Function.* Int J Mol Sci, 2019. **20**(18).
161. Guy, J., et al., *Reversal of neurological defects in a mouse model of Rett syndrome.* Science, 2007. **315**(5815): p. 1143-7.
162. McGraw, C.M., R.C. Samaco, and H.Y. Zoghbi, *Adult neural function requires MeCP2.* Science, 2011. **333**(6039): p. 186.
163. Kline, D.D., et al., *Exogenous brain-derived neurotrophic factor rescues synaptic dysfunction in Mecp2-null mice.* J Neurosci, 2010. **30**(15): p. 5303-10.
164. Johnson, R.A., et al., *7,8-dihydroxyflavone exhibits therapeutic efficacy in a mouse model of Rett syndrome.* J Appl Physiol (1985), 2012. **112**(5): p. 704-10.
165. Deogracias, R., et al., *Fingolimod, a sphingosine-1 phosphate receptor modulator, increases BDNF levels and improves symptoms of a mouse model of Rett syndrome.* Proc Natl Acad Sci U S A, 2012. **109**(35): p. 14230-5.
166. Castro, J., et al., *Functional recovery with recombinant human IGF1 treatment in a mouse model of Rett Syndrome.* Proc Natl Acad Sci U S A, 2014. **111**(27): p. 9941-6.
167. Sztainberg, Y., et al., *Reversal of phenotypes in MECP2 duplication mice using genetic rescue or antisense oligonucleotides.* Nature, 2015. **528**(7580): p. 123-6.
168. Gadalla, K.K.E., et al., *Development of a Novel AAV Gene Therapy Cassette with Improved Safety Features and Efficacy in a Mouse Model of Rett Syndrome.* Mol Ther Methods Clin Dev, 2017. **5**: p. 180-190.

169. Sinnett, S.E., et al., *Improved MECP2 Gene Therapy Extends the Survival of MeCP2-Null Mice without Apparent Toxicity after Intracisternal Delivery.* Mol Ther Methods Clin Dev, 2017. **5**: p. 106-115.
170. Tillotson, R., et al., *Radically truncated MeCP2 rescues Rett syndrome-like neurological defects.* Nature, 2017. **550**(7676): p. 398-401.
171. Le, T.T.H., et al., *Efficient and Precise CRISPR/Cas9-Mediated MECP2 Modifications in Human-Induced Pluripotent Stem Cells.* Front Genet, 2019. **10**: p. 625.
172. Katayama, Y., et al., *CHD8 haploinsufficiency results in autistic-like phenotypes in mice.* Nature, 2016. **537**(7622): p. 675-679.
173. Gompers, A.L., et al., *Germline Chd8 haploinsufficiency alters brain development in mouse.* Nat Neurosci, 2017. **20**(8): p. 1062-1073.
174. Durak, O., et al., *Chd8 mediates cortical neurogenesis via transcriptional regulation of cell cycle and Wnt signaling.* Nat Neurosci, 2016. **19**(11): p. 1477-1488.
175. Santen, G.W., et al., *Mutations in SWI/SNF chromatin remodeling complex gene ARID1B cause Coffin-Siris syndrome.* Nat Genet, 2012. **44**(4): p. 379-80.
176. Tsurusaki, Y., et al., *Mutations affecting components of the SWI/SNF complex cause Coffin-Siris syndrome.* Nat Genet, 2012. **44**(4): p. 376-8.
177. Wieczorek, D., et al., *A comprehensive molecular study on Coffin-Siris and Nicolaides-Baraitser syndromes identifies a broad molecular and clinical spectrum converging on altered chromatin remodeling.* Hum Mol Genet, 2013. **22**(25): p. 5121-35.
178. Celen, C., et al., *Arid1b haploinsufficient mice reveal neuropsychiatric phenotypes and reversible causes of growth impairment.* Elife, 2017. **6**.
179. Jung, E.M., et al., *Arid1b haploinsufficiency disrupts cortical interneuron development and mouse behavior.* Nat Neurosci, 2017. **20**(12): p. 1694-1707.
180. Sessa, A., et al., *SETD5 Regulates Chromatin Methylation State and Preserves Global Transcriptional Fidelity during Brain Development and Neuronal Wiring.* Neuron, 2019. **104**(2): p. 271-289 e13.
181. Mas, Y.M.S., et al., *The Human Mixed Lineage Leukemia 5 (MLL5), a Sequentially and Structurally Divergent SET Domain-Containing Protein with No Intrinsic Catalytic Activity.* PLoS One, 2016. **11**(11): p. e0165139.
182. Osipovich, A.B., et al., *Setd5 is essential for mammalian development and the co-transcriptional regulation of histone acetylation.* Development, 2016. **143**(24): p. 4595-4607.
183. Deliu, E., et al., *Haploinsufficiency of the intellectual disability gene SETD5 disturbs developmental gene expression and cognition.* Nature Neuroscience, 2018. **21**(12): p. 1717-1727.
184. Barnard, R.A., M.B. Pomaville, and B.J. O'Roak, *Mutations and Modeling of the Chromatin Remodeler CHD8 Define an Emerging Autism Etiology.* Front Neurosci, 2015. **9**: p. 477.
185. Chuang, H.C., T.N. Huang, and Y.P. Hsueh, *T-Brain-1--A Potential Master Regulator in Autism Spectrum Disorders.* Autism Res, 2015. **8**(4): p. 412-26.
186. Malishkevich, A., et al., *Activity-dependent neuroprotective protein (ADNP) exhibits striking sexual dichotomy impacting on autistic and Alzheimer's pathologies.* Transl Psychiatry, 2015. **5**: p. e501.
187. Notwell, J.H., et al., *TBR1 regulates autism risk genes in the developing neocortex.* Genome Res, 2016. **26**(8): p. 1013-22.

188. Sutton, M.A. and E.M. Schuman, *Dendritic protein synthesis, synaptic plasticity, and memory.* Cell, 2006. **127**(1): p. 49-58.
189. Buffington, S.A., W. Huang, and M. Costa-Mattioli, *Translational control in synaptic plasticity and cognitive dysfunction.* Annu Rev Neurosci, 2014. **37**: p. 17-38.
190. Louros, S.R. and E.K. Osterweil, *Perturbed proteostasis in autism spectrum disorders.* J Neurochem, 2016. **139**(6): p. 1081-1092.
191. Winden, K.D., D. Ebrahimi-Fakhari, and M. Sahin, *Abnormal mTOR Activation in Autism.* Annu Rev Neurosci, 2018. **41**: p. 1-23.
192. Ehninger, D. and A.J. Silva, *Rapamycin for treating Tuberous sclerosis and Autism spectrum disorders.* Trends Mol Med, 2011. **17**(2): p. 78-87.
193. Guertin, D.A. and D.M. Sabatini, *The pharmacology of mTOR inhibition.* Sci Signal, 2009. **2**(67): p. pe24.
194. Tsai, P.T., et al., *Autistic-like behaviour and cerebellar dysfunction in Purkinje cell Tsc1 mutant mice.* Nature, 2012. **488**(7413): p. 647-51.
195. Tsai, P.T., et al., *Sensitive Periods for Cerebellar-Mediated Autistic-like Behaviors.* Cell Rep, 2018. **25**(2): p. 357-367 e4.
196. Cox, R.L., et al., *Multiple Critical Periods for Rapamycin Treatment to Correct Structural Defects in Tsc-1-Suppressed Brain.* Front Mol Neurosci, 2018. **11**: p. 409.
197. Xing, X., et al., *Suppression of Akt-mTOR pathway rescued the social behavior in Cntnap2-deficient mice.* Sci Rep, 2019. **9**(1): p. 3041.
198. Bear, M.F., K.M. Huber, and S.T. Warren, *The mGluR theory of fragile X mental retardation.* Trends Neurosci, 2004. **27**(7): p. 370-7.
199. Dölen, G., et al., *Correction of fragile X syndrome in mice.* Neuron, 2007. **56**(6): p. 955-62.
200. Michalon, A., et al., *Chronic pharmacological mGlu5 inhibition corrects fragile X in adult mice.* Neuron, 2012. **74**(1): p. 49-56.
201. Berry-Kravis, E.M., et al., *Drug development for neurodevelopmental disorders: lessons learned from fragile X syndrome.* Nat Rev Drug Discov, 2018. **17**(4): p. 280-299.
202. Hagerman, R., et al., *Mavoglurant in Fragile X Syndrome: Results of two open-label, extension trials in adults and adolescents.* Sci Rep, 2018. **8**(1): p. 16970.
203. Youssef, E.A., et al., *Effect of the mGluR5-NAM Basimglurant on Behavior in Adolescents and Adults with Fragile X Syndrome in a Randomized, Double-Blind, Placebo-Controlled Trial: FragXis Phase 2 Results.* Neuropsychopharmacology, 2018. **43**(3): p. 503-512.
204. Davenport, M.H., et al., *Pharmacotherapy for Fragile X Syndrome: Progress to Date.* Drugs, 2016. **76**(4): p. 431-45.
205. Osterweil, E.K., et al., *Lovastatin corrects excess protein synthesis and prevents epileptogenesis in a mouse model of fragile X syndrome.* Neuron, 2013. **77**(2): p. 243-50.
206. Asiminas, A., et al., *Sustained correction of associative learning deficits after brief, early treatment in a rat model of Fragile X Syndrome.* Sci Transl Med, 2019. **11**(494).
207. Caku, A., et al., *Effect of lovastatin on behavior in children and adults with fragile X syndrome: an open-label study.* Am J Med Genet A, 2014. **164A**(11): p. 2834-42.
208. Novarino, G., et al., *Mutations in BCKD-kinase lead to a potentially treatable form of autism with epilepsy.* Science, 2012. **338**(6105): p. 394-7.

209. Tarlungeanu, D.C., et al., *Impaired Amino Acid Transport at the Blood Brain Barrier Is a Cause of Autism Spectrum Disorder.* Cell, 2016. **167**(6): p. 1481-1494 e18.
210. Garcia-Cazorla, A., et al., *Two novel mutations in the BCKDK (branched-chain keto-acid dehydrogenase kinase) gene are responsible for a neurobehavioral deficit in two pediatric unrelated patients.* Hum Mutat, 2014. **35**(4): p. 470-7.
211. Meng, L., et al., *Towards a therapy for Angelman syndrome by targeting a long non-coding RNA.* Nature, 2015. **518**(7539): p. 409-12.
212. Silva-Santos, S., et al., *Ube3a reinstatement identifies distinct developmental windows in a murine Angelman syndrome model.* J Clin Invest, 2015. **125**(5): p. 2069-76.
213. Rotaru, D.C., et al., *Adult Ube3a Gene Reinstatement Restores the Electrophysiological Deficits of Prefrontal Cortex Layer 5 Neurons in a Mouse Model of Angelman Syndrome.* J Neurosci, 2018. **38**(37): p. 8011-8030.
214. Reiner, O., et al., *Regulation of neuronal migration, an emerging topic in autism spectrum disorders.* J Neurochem, 2016. **136**(3): p. 440-56.
215. Hong, S.E., et al., *Autosomal recessive lissencephaly with cerebellar hypoplasia is associated with human RELN mutations.* Nat Genet, 2000. **26**(1): p. 93-6.
216. Folsom, T.D. and S.H. Fatemi, *The involvement of Reelin in neurodevelopmental disorders.* Neuropharmacology, 2013. **68**: p. 122-35.
217. Wasser, C.R. and J. Herz, *Reelin: Neurodevelopmental Architect and Homeostatic Regulator of Excitatory Synapses.* J Biol Chem, 2017. **292**(4): p. 1330-1338.
218. Weeber, E.J., et al., *Reelin and ApoE receptors cooperate to enhance hippocampal synaptic plasticity and learning.* J Biol Chem, 2002. **277**(42): p. 39944-52.
219. Jakob, B., et al., *Intersectin 1 is a component of the Reelin pathway to regulate neuronal migration and synaptic plasticity in the hippocampus.* Proc Natl Acad Sci U S A, 2017. **114**(21): p. 5533-5538.
220. Niu, S., et al., *Reelin promotes hippocampal dendrite development through the VLDLR/ApoER2-Dab1 pathway.* Neuron, 2004. **41**(1): p. 71-84.
221. Niu, S., O. Yabut, and G. D'Arcangelo, *The Reelin signaling pathway promotes dendritic spine development in hippocampal neurons.* J Neurosci, 2008. **28**(41): p. 10339-48.
222. Cobos, I., U. Borello, and J.L. Rubenstein, *Dlx transcription factors promote migration through repression of axon and dendrite growth.* Neuron, 2007. **54**(6): p. 873-88.
223. Mao, R., et al., *Reduced conditioned fear response in mice that lack Dlx1 and show subtype-specific loss of interneurons.* J Neurodev Disord, 2009. **1**(3): p. 224-36.
224. Gilbert, J., et al., *NEXMIF/KIDLIA Knock-out Mouse Demonstrates Autism-Like Behaviors, Memory Deficits, and Impairments in Synapse Formation and Function.* J Neurosci, 2020. **40**(1): p. 237-254.
225. Pla, R., et al., *Dlx1 and Dlx2 Promote Interneuron GABA Synthesis, Synaptogenesis, and Dendritogenesis.* Cereb Cortex, 2018. **28**(11): p. 3797-3815.
226. Adler, C.E., R.D. Fetter, and C.I. Bargmann, *UNC-6/Netrin induces neuronal asymmetry and defines the site of axon formation.* Nat Neurosci, 2006. **9**(4): p. 511-8.
227. Ning, K., et al., *PTEN depletion rescues axonal growth defect and improves survival in SMN-deficient motor neurons.* Hum Mol Genet, 2010. **19**(16): p. 3159-68.
228. Kath, C., et al., *PTEN suppresses axon outgrowth by down-regulating the level of detyrosinated microtubules.* PLoS One, 2018. **13**(4): p. e0193257.

229. Manent, J.B., et al., *Dcx reexpression reduces subcortical band heterotopia and seizure threshold in an animal model of neuronal migration disorder.* Nat Med, 2009. **15**(1): p. 84-90.
230. Fukuda, T., et al., *Rescue of CAMDI deletion-induced delayed radial migration and psychiatric behaviors by HDAC6 inhibitor.* EMBO Rep, 2016. **17**(12): p. 1785-1798.
231. Schaffer, A.E., et al., *Biallelic loss of human CTNNA2, encoding alphaN-catenin, leads to ARP2/3 complex overactivity and disordered cortical neuronal migration.* Nat Genet, 2018. **50**(8): p. 1093-1101.
232. Fife, C.M., J.A. McCarroll, and M. Kavallaris, *Movers and shakers: cell cytoskeleton in cancer metastasis.* Br J Pharmacol, 2014. **171**(24): p. 5507-23.
233. Araki, Y., et al., *Rapid dispersion of SynGAP from synaptic spines triggers AMPA receptor insertion and spine enlargement during LTP.* Neuron, 2015. **85**(1): p. 173-189.
234. Komiyama, N.H., et al., *SynGAP regulates ERK/MAPK signaling, synaptic plasticity, and learning in the complex with postsynaptic density 95 and NMDA receptor.* J Neurosci, 2002. **22**(22): p. 9721-32.
235. Kim, J.H., et al., *The role of synaptic GTPase-activating protein in neuronal development and synaptic plasticity.* J Neurosci, 2003. **23**(4): p. 1119-24.
236. Clement, J.P., et al., *SYNGAP1 links the maturation rate of excitatory synapses to the duration of critical-period synaptic plasticity.* J Neurosci, 2013. **33**(25): p. 10447-52.
237. Ozkan, E.D., et al., *Reduced cognition in Syngap1 mutants is caused by isolated damage within developing forebrain excitatory neurons.* Neuron, 2014. **82**(6): p. 1317-33.
238. Clement, J.P., et al., *Pathogenic SYNGAP1 mutations impair cognitive development by disrupting maturation of dendritic spine synapses.* Cell, 2012. **151**(4): p. 709-723.
239. Aceti, M., et al., *Syngap1 haploinsufficiency damages a postnatal critical period of pyramidal cell structural maturation linked to cortical circuit assembly.* Biol Psychiatry, 2015. **77**(9): p. 805-15.
240. Guo, X., et al., *Reduced expression of the NMDA receptor-interacting protein SynGAP causes behavioral abnormalities that model symptoms of Schizophrenia.* Neuropsychopharmacology, 2009. **34**(7): p. 1659-72.
241. Muhia, M., et al., *Disruption of hippocampus-regulated behavioural and cognitive processes by heterozygous constitutive deletion of SynGAP.* Eur J Neurosci, 2010. **31**(3): p. 529-43.
242. Michaelson, S.D., et al., *SYNGAP1 heterozygosity disrupts sensory processing by reducing touch-related activity within somatosensory cortex circuits.* Nat Neurosci, 2018. **21**(12): p. 1-13.
243. Barnes, S.A., et al., *Convergence of Hippocampal Pathophysiology in Syngap+/- and Fmr1-/y Mice.* J Neurosci, 2015. **35**(45): p. 15073-81.
244. Hu, W., et al., *Distinct contributions of Na(v)1.6 and Na(v)1.2 in action potential initiation and backpropagation.* Nat Neurosci, 2009. **12**(8): p. 996-1002.
245. Yamagata, T., et al., *Nav1.2 is expressed in caudal ganglionic eminence-derived disinhibitory interneurons: Mutually exclusive distributions of Nav1.1 and Nav1.2.* Biochem Biophys Res Commun, 2017. **491**(4): p. 1070-1076.
246. Spratt, P.W.E., et al., *The Autism-Associated Gene Scn2a Contributes to Dendritic Excitability and Synaptic Function in the Prefrontal Cortex.* Neuron, 2019. **103**(4): p. 673-685 e5.

247. Tatsukawa, T., et al., *Scn2a haploinsufficient mice display a spectrum of phenotypes affecting anxiety, sociability, memory flexibility and ampakine CX516 rescues their hyperactivity.* Mol Autism, 2019. **10**: p. 15.
248. Krueger, D.D., et al., *The role of neurexins and neuroligins in the formation, maturation, and function of vertebrate synapses.* Curr Opin Neurobiol, 2012. **22**(3): p. 412-22.
249. Cao, X. and K. Tabuchi, *Functions of synapse adhesion molecules neurexin/neuroligins and neurodevelopmental disorders.* Neurosci Res, 2017. **116**: p. 3-9.
250. Rabaneda, L.G., et al., *Neurexin dysfunction in adult neurons results in autistic-like behavior in mice.* Cell Rep, 2014. **8**(2): p. 338-46.
251. Baudouin, S.J., et al., *Shared synaptic pathophysiology in syndromic and nonsyndromic rodent models of autism.* Science, 2012. **338**(6103): p. 128-32.
252. Rothwell, P.E., et al., *Autism-associated neuroligin-3 mutations commonly impair striatal circuits to boost repetitive behaviors.* Cell, 2014. **158**(1): p. 198-212.
253. Kalbassi, S., et al., *Male and Female Mice Lacking Neuroligin-3 Modify the Behavior of Their Wild-Type Littermates.* eNeuro, 2017. **4**(4).
254. Cao, W., et al., *Gamma Oscillation Dysfunction in mPFC Leads to Social Deficits in Neuroligin 3 R451C Knockin Mice.* Neuron, 2018. **97**(6): p. 1253-1260 e7.
255. Anderson, G.R., et al., *beta-Neurexins Control Neural Circuits by Regulating Synaptic Endocannabinoid Signaling.* Cell, 2015. **162**(3): p. 593-606.
256. Martella, G., et al., *The neurobiological bases of autism spectrum disorders: the R451C-neuroligin 3 mutation hampers the expression of long-term synaptic depression in the dorsal striatum.* Eur J Neurosci, 2018. **47**(6): p. 701-708.
257. Mei, Y., et al., *Adult restoration of Shank3 expression rescues selective autistic-like phenotypes.* Nature, 2016. **530**(7591): p. 481-4.
258. Orefice, L.L., et al., *Targeting Peripheral Somatosensory Neurons to Improve Tactile-Related Phenotypes in ASD Models.* Cell, 2019. **178**(4): p. 867-886 e24.
259. Won, H., et al., *Autistic-like social behaviour in Shank2-mutant mice improved by restoring NMDA receptor function.* Nature, 2012. **486**(7402): p. 261-5.
260. Bozdagi, O., T. Tavassoli, and J.D. Buxbaum, *Insulin-like growth factor-1 rescues synaptic and motor deficits in a mouse model of autism and developmental delay.* Mol Autism, 2013. **4**(1): p. 9.
261. Lee, E.J., et al., *Trans-synaptic zinc mobilization improves social interaction in two mouse models of autism through NMDAR activation.* Nat Commun, 2015. **6**: p. 7168.
262. Sgritta, M., et al., *Mechanisms Underlying Microbial-Mediated Changes in Social Behavior in Mouse Models of Autism Spectrum Disorder.* Neuron, 2019. **101**(2): p. 246-259 e6.
263. Rhine, M.A., et al., *Hypothesis-driven investigations of diverse pharmacological targets in two mouse models of autism.* Autism Res, 2019. **12**(3): p. 401-421.
264. Wang, X., et al., *Altered mGluR5-Homer scaffolds and corticostriatal connectivity in a Shank3 complete knockout model of autism.* Nat Commun, 2016. **7**: p. 11459.
265. Vicidomini, C., et al., *Pharmacological enhancement of mGlu5 receptors rescues behavioral deficits in SHANK3 knock-out mice.* Mol Psychiatry, 2017. **22**(5): p. 689-702.
266. Kolevzon, A., et al., *A pilot controlled trial of insulin-like growth factor-1 in children with Phelan-McDermid syndrome.* Mol Autism, 2014. **5**(1): p. 54.

267. Zwanenburg, R.J., et al., *Is there an effect of intranasal insulin on development and behaviour in Phelan-McDermid syndrome? A randomized, double-blind, placebo-controlled trial.* Eur J Hum Genet, 2016. **24**(12): p. 1696-1701.
268. Qin, L., et al., *Social deficits in Shank3-deficient mouse models of autism are rescued by histone deacetylase (HDAC) inhibition.* Nat Neurosci, 2018. **21**(4): p. 564-575.
269. Gantois, I., et al., *Metformin ameliorates core deficits in a mouse model of fragile X syndrome.* Nat Med, 2017. **23**(6): p. 674-677.
270. Harony-Nicolas, H., et al., *Oxytocin improves behavioral and electrophysiological deficits in a novel Shank3-deficient rat.* Elife, 2017. **6**.
271. Andérica-Romero, A.C., et al., *Cullin 3 as a novel target in diverse pathologies.* Redox Biology, 2013. **1**(1): p. 366-372.
272. Wu, J.T., et al., *Neddylation and deneddylation regulate Cul1 and Cul3 protein accumulation.* Nat Cell Biol, 2005. **7**(10): p. 1014-20.
273. Wimuttisuk, W. and J.D. Singer, *The Cullin3 ubiquitin ligase functions as a Nedd8-bound heterodimer.* Mol Biol Cell, 2007. **18**(3): p. 899-909.
274. Krek, W., *BTB proteins as henchmen of Cul3-based ubiquitin ligases.* Nat Cell Biol, 2003. **5**(11): p. 950-1.
275. Study, D.D.D., *Large-scale discovery of novel genetic causes of developmental disorders.* Nature, 2015. **519**(7542): p. 223-8.
276. Coe, B.P., et al., *Refining analyses of copy number variation identifies specific genes associated with developmental delay.* Nat Genet, 2014. **46**(10): p. 1063-71.
277. O'Roak, B.J., et al., *Multiplex targeted sequencing identifies recurrently mutated genes in autism spectrum disorders.* Science, 2012. **338**(6114): p. 1619-22.
278. Sanders, S.J., et al., *Insights into Autism Spectrum Disorder Genomic Architecture and Biology from 71 Risk Loci.* Neuron, 2015. **87**(6): p. 1215-1233.
279. Kong, A., et al., *Rate of de novo mutations and the importance of father's age to disease risk.* Nature, 2012. **488**.
280. da Silva Montenegro, E.M., et al., *Meta-Analyses Support Previous and Novel Autism Candidate Genes: Outcomes of an Unexplored Brazilian Cohort.* Autism Res, 2020. **13**(2): p. 199-206.
281. Nakashima, M., et al., *De novo variants in CUL3 are associated with global developmental delays with or without infantile spasms.* J Hum Genet, 2020.
282. Redin, C., et al., *The genomic landscape of balanced cytogenetic abnormalities associated with human congenital anomalies.* Nat Genet, 2017. **49**(1): p. 36-45.
283. Codina-Solà, M., et al., *Integrated analysis of whole-exome sequencing and transcriptome profiling in males with autism spectrum disorders.* Molecular Autism, 2015. **6**(1): p. 21.
284. Boyden, L.M., et al., *Mutations in kelch-like 3 and cullin 3 cause hypertension and electrolyte abnormalities.* Nature, 2012. **482**(7383): p. 98-102.
285. Osawa, M., et al., *CUL3 gene analysis enables early intervention for pediatric pseudohypoaldosteronism type II in infancy.* Pediatr Nephrol, 2013. **28**(9): p. 1881-4.
286. Glover, M., et al., *Detection of mutations in KLHL3 and CUL3 in families with FHHt (familial hyperkalaemic hypertension or Gordon's syndrome).* Clin Sci (Lond), 2014. **126**(10): p. 721-6.
287. Schumacher, F.R., et al., *Characterisation of the Cullin-3 mutation that causes a severe form of familial hypertension and hyperkalaemia.* EMBO Mol Med, 2015. **7**(10): p. 1285-306.

288. Casas-Alba, D., et al., *Pseudohypoaldosteronism types I and II: little more than a name in common.* J Pediatr Endocrinol Metab, 2017. **30**(5): p. 597-601.
289. Mori, T., et al., *Comprehensive genetic testing approach for major inherited kidney diseases, using next-generation sequencing with a custom panel.* Clin Exp Nephrol, 2017. **21**(1): p. 63-75.
290. Shao, L., et al., *A novel mutation in exon 9 of Cullin 3 gene contributes to aberrant splicing in pseudohypoaldosteronism type II.* FEBS Open Bio, 2018. **8**(3): p. 461-469.
291. Ferdaus, M.Z., et al., *Mutant Cullin 3 causes familial hyperkalemic hypertension via dominant effects.* JCI Insight, 2017. **2**(24).
292. Singer, J.D., et al., *Cullin-3 targets cyclin E for ubiquitination and controls S phase in mammalian cells.* Genes Dev, 1999. **13**(18): p. 2375-87.
293. Davidge, B., et al., *Cul3 regulates cyclin E1 protein abundance via a degron located within the N-terminal region of cyclin E.* J Cell Sci, 2019. **132**(21).
294. McEvoy, J.D., et al., *Constitutive turnover of cyclin E by Cul3 maintains quiescence.* Mol Cell Biol, 2007. **27**(10): p. 3651-66.
295. Nishitani, H., et al., *Two E3 ubiquitin ligases, SCF-Skp2 and DDB1-Cul4, target human Cdt1 for proteolysis.* EMBO J, 2006. **25**(5): p. 1126-36.
296. Genschik, P., I. Sumara, and E. Lechner, *The emerging family of CULLIN3-RING ubiquitin ligases (CRL3s): cellular functions and disease implications.* Embo j, 2013. **32**(17): p. 2307-20.
297. Salinas, G.D., et al., *Actinfilin is a Cul3 substrate adaptor, linking GluR6 kainate receptor subunits to the ubiquitin-proteasome pathway.* J Biol Chem, 2006. **281**(52): p. 40164-73.
298. Stavropoulos, N. and M.W. Young, *insomniac and Cullin-3 regulate sleep and wakefulness in Drosophila.* Neuron, 2011. **72**(6): p. 964-76.
299. Pfeiffenberger, C. and R. Allada, *Cul3 and the BTB adaptor insomniac are key regulators of sleep homeostasis and a dopamine arousal pathway in Drosophila.* PLoS Genet, 2012. **8**(10): p. e1003003.
300. Chen, Y., et al., *Cullin mediates degradation of RhoA through evolutionarily conserved BTB adaptors to control actin cytoskeleton structure and cell movement.* Mol Cell, 2009. **35**(6): p. 841-55.
301. Lin, G.N., et al., *Spatiotemporal 16p11.2 protein network implicates cortical late mid-fetal brain development and KCTD13-Cul3-RhoA pathway in psychiatric diseases.* Neuron, 2015. **85**(4): p. 742-54.
302. Golzio, C., et al., *KCTD13 is a major driver of mirrored neuroanatomical phenotypes of the 16p11.2 copy number variant.* Nature, 2012. **485**(7398): p. 363-7.
303. Escamilla, C.O., et al., *Kctd13 deletion reduces synaptic transmission via increased RhoA.* Nature, 2017. **551**(7679): p. 227-231.
304. Arbuckle, E.P., et al., *Testing for odor discrimination and habituation in mice.* J Vis Exp, 2015(99): p. e52615.
305. Gstrein, T., et al., *Mutations in Vps15 perturb neuronal migration in mice and are associated with neurodevelopmental disease in humans.* Nat Neurosci, 2018. **21**(2): p. 207-217.
306. Schindelin, J., et al., *Fiji: an open-source platform for biological-image analysis.* Nat Methods, 2012. **9**(7): p. 676-82.
307. Tinevez, J.-Y., et al., *TrackMate: An open and extensible platform for single-particle tracking.* Methods, 2017. **115**: p. 80-90.

308. Xue, Z., et al., *CRISPR/Cas9 mediates efficient conditional mutagenesis in Drosophila.* G3 (Bethesda), 2014. **4**(11): p. 2167-73.
309. Seginer, A., et al., *Referenceless reconstruction of spatiotemporally encoded imaging data: principles and applications to real-time MRI.* Magn Reson Med, 2014. **72**(6): p. 1687-95.
310. Lindeberg, T., *Detecting salient blob-like image structures and their scales with a scale-space primal sketch: A method for focus-of-attention.* International Journal of Computer Vision, 1993. **11**(3): p. 283-318.
311. Jahn, H.M., et al., *Refined protocols of tamoxifen injection for inducible DNA recombination in mouse astroglia.* Scientific Reports, 2018. **8**(1): p. 5913.
312. Guenthner, C.J., et al., *Permanent genetic access to transiently active neurons via TRAP: targeted recombination in active populations.* Neuron, 2013. **78**(5): p. 773-84.
313. González-Pérez, A. and N. Lopez-Bigas, *Improving the assessment of the outcome of nonsynonymous SNVs with a consensus deleteriousness score.* Am J Hum Genet, 2011. **88**.
314. Chao, H.T., et al., *Dysfunction in GABA signalling mediates autism-like stereotypies and Rett syndrome phenotypes.* Nature, 2010. **468**(7321): p. 263-9.
315. Yang, H., et al., *One-step generation of mice carrying reporter and conditional alleles by CRISPR/Cas-mediated genome engineering.* Cell, 2013. **154**(6): p. 1370-9.
316. Bureau, G., et al., *Intrastriatal inhibition of extracellular signal-regulated kinases impaired the consolidation phase of motor skill learning.* Neurobiol Learn Mem, 2010. **94**(1): p. 107-15.
317. Buitrago, M.M., et al., *Short and long-term motor skill learning in an accelerated rotarod training paradigm.* Neurobiol Learn Mem, 2004. **81**(3): p. 211-6.
318. Popik, P., et al., *Recognition cue in the rat's social memory paradigm.* J Basic Clin Physiol Pharmacol, 1991. **2**(4): p. 315-27.
319. Noack, J., et al., *Different importance of the volatile and non-volatile fractions of an olfactory signature for individual social recognition in rats versus mice and short-term versus long-term memory.* Neurobiol Learn Mem, 2010. **94**(4): p. 568-75.
320. Rudy, J.W., N.C. Huff, and P. Matus-Amat, *Understanding contextual fear conditioning: insights from a two-process model.* Neurosci Biobehav Rev, 2004. **28**(7): p. 675-85.
321. Gorski, J.A., et al., *Cortical excitatory neurons and glia, but not GABAergic neurons, are produced in the Emx1-expressing lineage.* J Neurosci, 2002. **22**(15): p. 6309-14.
322. Dong, Z., et al., *CUL3 Deficiency Causes Social Deficits and Anxiety-like Behaviors by Impairing Excitation-Inhibition Balance through the Promotion of Cap-Dependent Translation.* Neuron, 2019.
323. Rapanelli, M., et al., *Behavioral, circuitry, and molecular aberrations by region-specific deficiency of the high-risk autism gene Cul3.* Mol Psychiatry, 2019.
324. Papizan, J.B., et al., *Cullin-3-RING ubiquitin ligase activity is required for striated muscle function in mice.* J Biol Chem, 2018. **293**(23): p. 8802-8811.
325. Swaney, D.L., et al., *Global analysis of phosphorylation and ubiquitylation cross-talk in protein degradation.* Nat Methods, 2013. **10**(7): p. 676-82.
326. Guerrini, R., et al., *Symmetric polymicrogyria and pachygyria associated with TUBB2B gene mutations.* Eur J Hum Genet, 2012. **20**(9): p. 995-8.

327. Westphal, D.S., et al., *MAP2 - A Candidate Gene for Epilepsy, Developmental Delay and Behavioral Abnormalities in a Patient With Microdeletion 2q34.* Front Genet, 2018. **9**: p. 99.
328. Balasubramanian, M., et al., *Autism and heritable bone fragility: A true association?* Bone Rep, 2018. **8**: p. 156-162.
329. Kage, F., et al., *FMNL formins boost lamellipodial force generation.* Nat Commun, 2017. **8**: p. 14832.
330. Xue, F., D.M. Janzen, and D.A. Knecht, *Contribution of Filopodia to Cell Migration: A Mechanical Link between Protrusion and Contraction.* Int J Cell Biol, 2010. **2010**: p. 507821.
331. Schwebach, C.L., et al., *The Roles of Actin-Binding Domains 1 and 2 in the Calcium-Dependent Regulation of Actin Filament Bundling by Human Plastins.* J Mol Biol, 2017. **429**(16): p. 2490-2508.
332. Giganti, A., et al., *Actin-filament cross-linking protein T-plastin increases Arp2/3-mediated actin-based movement.* J Cell Sci, 2005. **118**(Pt 6): p. 1255-65.
333. Rottner, K., et al., *Actin assembly mechanisms at a glance.* J Cell Sci, 2017. **130**(20): p. 3427-3435.
334. Schaks, M., G. Giannone, and K. Rottner, *Actin dynamics in cell migration.* Essays Biochem, 2019. **63**(5): p. 483-495.
335. Jiu, Y., et al., *Bidirectional Interplay between Vimentin Intermediate Filaments and Contractile Actin Stress Fibers.* Cell Rep, 2015. **11**(10): p. 1511-8.
336. Amar, M., et al., *Autism-linked Cullin3 germline haploinsufficiency impacts cytoskeletal dynamics and cortical neurogenesis through RhoA signaling.* bioRxiv, 2020: p. 2020.02.07.939256.
337. Zhuo, L., et al., *hGFAP-cre transgenic mice for manipulation of glial and neuronal function in vivo.* Genesis, 2001. **31**(2): p. 85-94.
338. Goebbels, S., et al., *Genetic targeting of principal neurons in neocortex and hippocampus of NEX-Cre mice.* Genesis, 2006. **44**(12): p. 611-21.
339. Meissner-Bernard, C., et al., *Encoding of Odor Fear Memories in the Mouse Olfactory Cortex.* Current Biology, 2019. **29**(3): p. 367-380.e4.
340. Sługocka, A., J. Wiaderkiewicz, and J.J. Barski, *Genetic Targeting in Cerebellar Purkinje Cells: an Update.* Cerebellum (London, England), 2017. **16**(1): p. 191-202.
341. Potter, G.B., et al., *Generation of Cre-transgenic mice using Dlx1/Dlx2 enhancers and their characterization in GABAergic interneurons.* Mol Cell Neurosci, 2009. **40**(2): p. 167-86.
342. Bellion, A., et al., *Nucleokinesis in Tangentially Migrating Neurons Comprises Two Alternating Phases: Forward Migration of the Golgi/Centrosome Associated with Centrosome Splitting and Myosin Contraction at the Rear.* The Journal of Neuroscience, 2005. **25**(24): p. 5691-5699.
343. Silva, C.G., et al., *Cell-Intrinsic Control of Interneuron Migration Drives Cortical Morphogenesis.* Cell, 2018. **172**(5): p. 1063-1078 e19.
344. Lancaster, M.A. and J.A. Knoblich, *Generation of cerebral organoids from human pluripotent stem cells.* Nat Protoc, 2014. **9**(10): p. 2329-40.
345. Nascimento, J.M., et al., *Human Cerebral Organoids and Fetal Brain Tissue Share Proteomic Similarities.* Frontiers in Cell and Developmental Biology, 2019. **7**(303).

346. Fan, S., et al., *The eIF4E/eIF4G interaction inhibitor 4EGI-1 augments TRAIL-mediated apoptosis through c-FLIP Down-regulation and DR5 induction independent of inhibition of cap-dependent protein translation.* Neoplasia, 2010. **12**(4): p. 346-56.